

https://dspace.org/

Tuning the Separation Properties of Thin-Film Nanocomposite Membranes and Aerogels by Polymeric Functionalization of Graphene Oxide Nanosheets and Cellulose Nanocrystals

Maziya, Khona Primrose

2025

University of the Witwatersrand, Johannesburg

https://hdl.handle.net/10539/48701

Maziya, Khona Primrose. (2025). Tuning the Separation Properties of Thin-Film Nanocomposite Membranes and Aerogels by Polymeric Functionalization of Graphene Oxide Nanosheets and Cellulose Nanocrystals. [PhD thesis, University of the Witwatersrand, Johannesburg]. WIReDSpace. https://hdl.handle.net/10539/48701

Downloaded from a DSpace repository. https://dspace.org/

Tuning the Separation Properties of Thin-Film Nanocomposite Membranes and Aerogels by Polymeric Functionalization of Graphene Oxide Nanosheets and Cellulose Nanocrystals

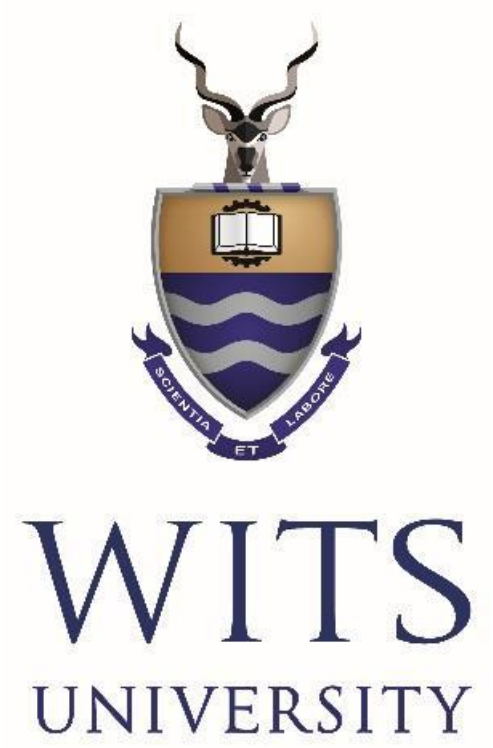

Khona Primrose Maziya

A Thesis submitted to the Faculty of Science for the degree of Doctor of Philosophy, University of the Witwatersrand, Johannesburg.

2025

DECLARATION

I declare that this thesis is my own, unaided work. It is being submitted for the Degree of Doctor of Philosophy at the University of the Witwatersrand, Johannesburg. It has not been submitted before for any degree or examination at any other University.

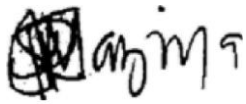

____ _____ on this _31_ day of __May 2025___

(Candidate)

DEDICATION

This work is dedicated to my dear family. As the first person in my family to pursue a PhD degree, I experience a blend of pride and challenge. I have navigated uncharted territory without a guide, and I hope my journey inspires my nieces and nephew, who look up to me. The sky is the limit; with God, ALL things are possible.

My mom, Constance Maziya, I am truly grateful for your steadfast spiritual, emotional, and financial support. Your constant love means the world to me, and I feel incredibly fortunate to have you in my life. Ngiyabonga Lushaba, Gumedze, Skhundlas'khulu.

To my sister, Dr. Khanyile Maziya, thank you for your unwavering support and belief in my dreams. Your encouragement has been a vital source of strength, and I truly would not have made it this far without you. I am grateful for the countless times you've lifted me up and inspired me to keep pushing forward.

ACKNOWLEDGEMENTS

I want to thank these individuals and entities for their counsel, patience, and support:

- God, my Father, Your love surpasses all others. Thank You for Your infinite love and granting me this incredible opportunity. Thank you for being my protector, strength, and my provider throughout my academic journey.

- I want to offer my heartfelt appreciation to my supervisors, Prof. H.L. Richards and Dr. A. Etale, for their unwavering belief in me and for inspiring me to strive for excellence. Your guidance, patience, and steadfast support have been invaluable throughout my journey. The life lessons you have imparted will remain with me forever. Prof. Richards, I especially appreciate your encouragement and the opportunities you have opened for me. Thank you both for everything you have done.

- I want to sincerely thank the WITS Environmental Analytical Chemistry research group members for their kind reception, friendship, and continued assistance. Your input has improved the overall quality of this research.

- Special thanks to Prof. A. Swarts for allowing me to work in the organomettalic laboratory; Dr. C. Joseph, I value your assistance.

- I would like to express my profound gratitude to Prof. F. Lipnizki for the opportunity to spend time at Lund University, Sweden. The experience was incredibly enriching, and I am truly thankful for the chance to learn and grow during my visit. Additionally, I want to extend my appreciation to Dr. Ahmet for your invaluable assistance throughout my time spent there.

- I am also grateful to the Microscopy and Microanalysis Unit (MMU) staff for the time they spent supporting me with TEM and SEM analysis. I truly appreciate your assistance.

- I am grateful for the opportunity to have co-supervised Sphesihle Mzobe during her honors studies. Thank you for this experience, and I appreciate the pleasure of working with such an outstanding student.

- My family and friends, I am grateful for your unwavering love and support throughout my academic career. I feel incredibly rich to have you all in my life.

- Thank you to everyone who has joined me on this journey, especially my lab, office, and school of chemistry mates who have been extremely helpful.

- Special thanks to the Volkswagen Foundation and Margaret McNamara Educational Grants for funding this research. Furthermore, I acknowledge and feel fortunate to have been supported financially by the WITS postgraduate merit award (PMA) during my studies.

PRESENTATIONS AND PUBLICATIONS

The research outlined in this thesis has been shared at various conferences and has also been submitted for publication.

Conference presentations

- Maziya K, Etale A, Richards HL. Graphene Oxide Nanosheets for the Adsorption of Heavy Metal Ions in Water, 11th International Conference of the African Materials Research Society (AMRS 2022), Dakar, Senegal, 12 – 15 December 2022.
- Maziya K, Etale A, Richards HL. Polymer brush modified graphene oxide thin film nanocomposite membranes for enhanced heavy metal adsorption, 44th South African Chemical Institute's National Convention, Stellenbosch, South Africa, 8 – 13 January 2023.
- Maziya K, Etale A, Richards HL. Polymeric functionalization of graphene oxide nanosheets for efficient dye rejection. 14th Cross Faculty Postgraduate Symposium, University of Witwatersrand, South Africa, 6 – 8 September 2023.
- Maziya K, Etale A, Richards HL. Polymer functionalized cellulose nanocrystals incorporated polyamide membranes for efficient dye separation, Analitika Conference 2024, Drakensburg, South Africa, 10 – 14 March 2024.
- Maziya K, Etale A, Richards HL. High performance TFN membranes with modified CNCs for improved dye/salt removal from water, 4th Congress of the African Membrane Society (AMSIC 2024), Addis Ababa, Ethiopia, 5 – 8 November 2024.

Publications

- Maziya K, Kotze I, Richards HL. Enhancing dye rejection and antifouling resistance of thin film nanocomposite nanofiltration membranes by the incorporation of glutamic acid functionalized graphene oxide. **Manuscript published** in Frontiers in Membrane Science and Technology.
- Maziya K, Mzobe S, Mahlangu OT, Richards HL. Enhancing dye/salt rejection and antifouling resistance of thin film nanocomposite nanofiltration membranes through the incorporation of BMEP grafted graphene oxide. **Manuscript is yet to be submitted.**
- Maziya K, Kotze I, Mahlangu OT, Richards HL. Low Pressure Thin Film Membranes with Cellulose Nanocrystals derived from Cannabis sativa for Enhanced Dye and Salt Removal. **Manuscript published** in Separation and Purification Technology.
- Maziya K, Dlamini ML, Richards HL. Polyvinyl Alcohol Cross-linked Graphene Oxide with Grafted Glutamic Acid Aerogels for Enhanced Methylene Blue Adsorption. **Manuscript submitted** to the Journal of Polymer Research.

ABSTRACT

Water contamination from dyes has emerged as a serious environmental issue, owing to their prevalent use in industries such as textiles, food, and pharmaceuticals. Yearly, billions of tons of dye-laden effluent are dumped into water systems, posing serious threats to aquatic ecosystems and public health. Untreated wastewater not only changes the color of water bodies, but it also inhibits the penetration of light, which is essential for photosynthesis in aquatic plants. Microalgae, which are essential organisms in the aquatic food chain, experience growth suppression and morphological abnormalities when exposed to these contaminants. Toxic effects travel up the food chain, affecting fish and resulting in bioaccumulation of hazardous compounds that endanger human health through contaminated water and food. In light of the significant contamination issues, numerous regions, particularly those classified as low- and middle-income, are deficient in the necessary infrastructure and regulatory systems to manage dye wastewater in an effective manner. To mitigate the severe issue of dye pollution in bodies of water, there is a need to research into possible techniques for efficient removal of such contaminants. Among the several techniques, the use of advanced materials used for separation and filtration technologies is an economical, efficient and sustainable method.

This thesis studies novel approaches to improving the performance of thin-film nanocomposite (TFN) membranes and aerogels for wastewater treatment applications. This work primarily focuses on the development of graphene oxide (GO) and cellulose nanocrystals (CNCs) based composite filler materials with poly (glutamic acid) and poly (bis[2-(methacryloyloxy)ethyl] phosphate) brushes grown on them through surface-initiated atom-transfer radical polymerization (SI-ATRP). These materials enhance thin film composite (TFC) membranes properties such as hydrophilicity, rejection rates, antifouling properties, and extend membranes longevity. All nanomaterials were synthesized and characterized using elemental Carbon, Hydrogen, Nitrogen, and Sulphur (CHNS) analysis, Fourier transform infrared spectroscopy (FTIR), X-ray diffraction (XRD), ^{13}C nuclear magnetic resonance spectroscopy (^{13}C NMR), thermogravimetric analysis (TGA), and transmission electron microscopy (TEM). Scanning electron microscopy (SEM), FTIR, atomic force microscopy (AFM) were employed to examine the fabricated membranes.

In the first study, glutamic acid brush modified GO (GO-GLU) was introduced to the selective polyamide (PA) layer. This layer was produced through interfacial polymerization (IP) of organic trimesoyl chloride (TMC) and aqueous m-phenylenediamine (MPD) on a polysulfone (PSF) support. Water permeability and dye (methyl orange (MO) and methylene blue (MB)) rejection were used to evaluate membranes performance. Contact angle measurements proved that the incorporation of these modified GO nanosheets significantly boosted the membranes' hydrophilicity and water permeability. The study revealed that at the optimal GO-GLU loading of 0.10 wt%, GO-GLU TFN membrane attained a water permeance of 14.11 L/m²h with impressive rejection rates of 99.18% for MB and 67.18% for MO. Furthermore, it displayed superior

antifouling characteristics against Bovine Serum Albumin (BSA) when compared to the virgin TFC membrane and potentially good operation stability performance after 3 cycles.

Secondly, TFN membranes were prepared through IP, incorporating bis[2-(methacryloyloxy)ethyl] phosphate (BMEP)-grafted graphene oxide (GO-PMEP) into the selective PA layer for the removal of dyes/salts in water. The results revealed that at an optimal GO-PMEP loading of 0.025 wt% (TFN-1), the membrane exhibited significantly enhanced wettability, hydrophilicity, and pure water permeability attributable to the increased oxygenated functional groups located on the membrane surface, which promote higher affinity to water molecules. Furthermore, the TFN-1 membrane demonstrated superior performance under low-pressure conditions (400 kPa), achieving a water flux of 9.32 ± 0.89 L/m²h, representing a 1.5-fold increase compared to conventional TFC membranes. Furthermore, the TFN-1 membrane demonstrated outstanding rejection rates, surpassing 80% for MO, achieving 100% for MB, and approximately 86% and 31% for $MgSO_4$ and NaCl, respectively. Moreover, the efficacy of these membranes was further validated using real water samples, confirming their potential for practical application in dye removal under environmental conditions.

Thirdly, this research explored the integration of hemp derived cellulose nanocrystals (CNCs) modified with glutamic acid (CNC-GLU) into another set of TFN membranes. The resulting CNC-GLU TFN membranes (0.10 wt%) were more hydrophilic and smoother than the comparable TFC membrane. The CNC-GLU TFN membrane outperformed pristine TFC membranes with a pure water flux of 15.45 ±1.03 L/m^2h, high dye rejection (99.83% for MB, 90.63% for MO) and salt removal ($MgSO_4$ = 86%; NaCl = 38%) under low pressure conditions (400 kPa). This was attributed to the increased hydrophilic active layer, steric hindrance, and Donnan exclusion. Furthermore, the TFN membrane effectively removed MB and MO dyes from real water samples and demonstrated good operational stability after three cycles.

Moreover, the potential application of glutamic acid modified graphene oxide (GG-PVA) aerogels fabricated through a simplistic sol gel and freeze-drying process utilizing polyvinyl alcohol (PVA) as a cross-linker in dye removal was also investigated. These aerogels exhibited a maximum adsorption capacity (q_{max}) for MB of 121.95 mg/g defined by the Langmuir Isotherm model. Maximum adsorption of the MB was favored by near neutral to alkaline conditions, reaching 88.4% efficiency and equilibrium reached in the first 30 minutes of the adsorption process. The kinetics of the MB removal followed the pseudo-second order model. Furthermore, thermodynamic studies revealed endothermic (ΔH^o = 80.598 kJ mol^{-1}) and spontaneous (ΔG^o = -8.219 kJ mol^{-1}) nature of the adsorption process.

Overall, this thesis contributes to a deeper understanding of how advanced nanocomposite materials can be utilized to create more effective and sustainable solutions for wastewater treatment, particularly in removing toxic dyes from industrial effluents. The integration of these innovative materials into membrane technology represents a significant step forward in developing efficient strategies for mitigating water contamination and promoting environmental sustainability.

TABLE OF CONTENTS

Section ***Page***

Declaration i
Dedication ii
Acknowledgements iii
Presentations and publications iv
Abstract v
Table of contents vii
List of figures ix
List of tables x
List of abbreviations xi

CHAPTER 1 : INTRODUCTION 1
1.1 Problem statement 1
1.2 Justification 2
1.3 Scientific contribution to new knowledge and novelty 4
1.4 Aim and objectives 5
1.4.1 Objectives 5
1.5 Research questions 5
1.6 Hypothesis 5
1.7 Thesis outline 6
1.8 References 8
CHAPTER 2 : LITERATURE REVIEW 14
2.1 Introduction 14
2.2 Contamination of water sources by dye effluents: Possible sources and environmental impact 14
2.2.1 Dye overview 14
2.2.2 Textile dye toxicity and their effect 15
2.3 Approaches to water treatment 16
2.3.1 Dye removal by biological methods 16
2.3.2 Dye removal by chemical methods 17
2.3.3 Dye removal by physical methods 18
2.4 Dye removal by membrane filtration technologies 19
2.4.1 Ultrafiltration (UF) 20
2.4.2 Nanofiltration and Reverse Osmosis 21
2.4.3 Advancements in Thin Film Composite Membranes: Structure, Challenges, and Innovations 22
2.4.4 Thin film nanocomposite (TFN) membranes 23
2.5 Selected nanofillers utilized for dye removal 25
2.5.1 Graphene oxide (GO) based nanomaterials 26
2.5.1.1 Graphene oxide based aerogels 29
2.5.2 Cellulose and cellulosic materials 30
2.5.3 Modification of GO and CNC surfaces 31
2.6 Polymer brushes 31

2.6.1 Synthesis of polymer brushes....32
2.6.2 Modification of GO/CNC with polymer brushes....34
2.7 Selected polymers....35
2.8 Conclusion....36
References:....37
CHAPTER 3 : EXPERIMENTAL METHODOLOGY....56
Extraction and characterization of cellulose nanocrystals derived from South African *Cannabis sativa* fibers....57
CHAPTER 4 : RESULTS AND DISCUSSION....69
4.1 Paper 1....70
4.2 Paper 2....102
4.3 Paper 3....126
4.4 Paper 4....158
CHAPTER 5 CONCLUSIONS AND RECOMMENDATIONS....184

LIST OF FIGURES

Figure ***Description*** ***Page***

Figure 2.1: Different classes of dyes and their potential industrial uses....14
Figure 2.2: Treatment of textile wastewater by biological methods....17
Figure 2.3: MF, UF, NF and RO membrane processes....20
Figure 2.4: Typical structure of TFC membrane. 22
Figure 2.5: Five categories of nanocomposite membranes. 23
Figure 2.6: Fabrication of PA thin film layer from MPD and TMC....24
Figure 2.7: Thin film nanocomposite fabrication process....25
Figure 2.8: Chemical structure of Graphene oxide. 26
Figure 2.9: Schematic representation of GO preparation process. 27
Figure 2.10: Flow of water in GO membrane systems 27
Figure 2.11: Classes of polymer brushes according to their chemical composition. 32
Figure 2.12: Three different categories of conformations of surface-attached polymers. ...32
Figure 2.13: Polymer brush fabrication methods. 33
Figure 2.14: SI-ATRP process. 34
Figure 2.15: Synthesis of surface-functionalized GO via attachment of an ATRP initiator (a-bromoisobutyryl bromide) followed by polymerization of styrene, butyl acrylate, or methyl methacrylate. 35
Figure 2.16: Structures of Glutamic acid (A), Poly(α-L-glutamic acid) (B) and Poly(γ-glutamic acid) (C). 35
Figure 2.17: Chemical structures of 2-(methacryloyloxy)ethyl phosphate (a) and bis[2-(methacryloyloxy)ethyl] phosphate (b) monomers. 36

LIST OF TABLES

Table	***Description***	***Page***
Table 2.1:	International guidelines for the release of dye effluent into the environment	15
Table 2.2:	Rate of dye removal utilizing various biological treatment methods.	17
Table 2.3:	Rate of dye removal utilizing various chemical treatment methods.	18
Table 2.4:	Rate of dye removal utilizing various physical treatment methods.	19
Table 2.5:	Summaries of different NF RO membranes, removal efficiency and working parameters.	22
Table 2.6:	Selected TFN membranes, nanofillers used, target dyes and removal efficiencies.	25
Table 2.7:	GO membrane systems, dye, testing conditions and removal efficiency.	28
Table 2.8:	Comparison of adsorption capacities of different GO based aerogels.	30

LIST OF ABBREVIATIONS

^{13}C NMR	^{13}C nuclear magnetic resonance
AFM	Atomic force microscopy
BET	Brunauer-Emmett-Teller
BIBB	α-bromoisobutyryl bromide
BMEP	bis[2-(methacryloyloxy)ethyl] phosphate
BSA	Bovine serum albumin
CHNS	Carbon, Hydrogen, Nitrogen, and Sulphur
CNC	Cellulose nanocrystals
FESEM	Field emission scanning electron microscopy
FO	Forward osmosis
FTIR	Fourier transform infrared spectroscopy
GLU	Glutamic acid
GO	Graphene oxide
IP	Interfacial polymerization
kPa	Kilopascal
MB	Methylene blue
MF	Micofiltration
MO	Methyl orange
MPD	m-phenylenediamine
NF	Nanofiltration
PA	Polyamide
PMDETA	N, N, N, N, N‴- pentamethyldiethylenetriamine
PSF	Polysulfone
PVA	Polyvinyl alcohol
PVP	Polyvinylpyrrolidone
PZC	Point of zero charge
SDS	Sodium dodecyl sulphate
SEM-EDS	Scanning electron microscopy-energy dispersive X-ray spectroscopy
SI-ATRP	Surface-initiated atom transfer radical polymerization
TEA	Triethylamine
TEM	Transmission electron microscopy
TFC	Thin film composite
TFN	Thin film nanocomposite
TGA	Thermogravimetric analysis
THF	Tetrahydrofuran
TMC	Trimesoyl chloride
UF	Ultrafiltration
UV-Vis	Ultraviolet-visible spectroscopy
WCA	Water contact angle
WIC	Water intake capacity
XRD	X-ray diffraction

CHAPTER 1
INTRODUCTION

Water contamination from dyeing effluents poses a major risk to both public health as well as aquatic ecosystems, primarily due to the inadequate treatment or complete absence of wastewater management before these pollutants are discharged into water bodies. Addressing the pollution from dyeing wastewater is crucial for preserving freshwater resources and ensuring sustainable human health and environmental integrity. This section will focus on the study's problem statement, justification, contribution to scientific knowledge, hypothesis, aim and objectives.

1.1 Problem statement

Water is crucial for human survival, yet water systems face severe challenges, particularly from pollution. A significant global issue is the contamination of freshwater systems by untreated dyeing wastewater. Dye wastewater poses a notable threat due to its high toxicity and vibrant color, even at low concentrations. The primary contributors to this pollution are industries such as textiles, paper manufacturing, food production, and automotive production.[1] The textile sector primarily employs various dye classes, including reactive, direct, azo, mordant, acid, dispersion, basic, and sulfide dyes.[2,3] Dyes used in these industries can be categorized based on their origin (natural or synthetic), structure, and intended use. Each of these categories have distinct environmental impacts that necessitate targeted management strategies to mitigate their effects on water quality and ecosystem health. Yearly, an estimated seventy million tons of synthetic dyes are manufactured globally, with more than ten thousand tons utilized within the textile sector.[4] These dyes, however, frequently fail to attach well to textiles, which causes them to be discharged into water bodies like rivers, lakes, streams, and ponds along with wastewater. There are serious ecotoxicological concerns associated with this untreated discharge, as well as negative consequences on living organisms.[5] This is owing to the difficulty of complex organic compounds to degrade when exposed to water, detergents, or other cleaning agents. Most dyes resist deterioration when subjected to oxidizing agents, high temperatures, or intense light.[1]

Dyes' ability to block light in water has a negative impact on the aquatic photic zone, resulting in diminished photosynthesis.[6] Additionally, the existence of textile pigments and dyes in wastewater causes it to be extremely colorful, fluctuate in pH, have a high total organic carbon, chemical oxygen demand (COD), suspended particles, and biological oxygen demand (BOD).[7] Excess dye in water lowers dissolved oxygen and inhibits the biological function of aquatic animals.[5,8] Fish are susceptible to a range of diseases as a result of oxygen deprivation's harmful effects on their physiological responses, mainly the immune system.[8] Due to the persistent nature of dyes, polluted fish may have a serious adverse influence on human health.[9] Also, dye effluents change the soil's chemical balance, affecting microbes and algae growth.[9] These organic contaminants also impair seed

germination and the amount of chlorophyll in plants.[10,11] Moreover, 60 – 70% of dyes are unaffected by conventional treatment procedures rendering them toxic, recalcitrant, and carcinogenic. Dermatitis and anomalies of the central nervous system are among the illnesses that have been connected to dye exposure in humans as well as in animals.[12,13] Textile dyes can irritate skin and eyes and trigger asthma attacks when consumed or inhaled.[14,15] Human lung, breast, colorectal, and bladder cancers may be caused by the pervasive use of dyes in many different industries.[16] Given their potentially hazardous qualities, dye contamination has caused numerous concerns. Additional negative effects may include mutagenesis, chromosomal damages, cancer, and pulmonary toxicity in humankind.[12] Consequently, methods and technology for removing dyes from a variety of wastewater effluents are needed.

Legislation regarding the presence of toxic colored effluent in aquatic bodies have been applied to industries.[14] Traditional wastewater treatment (chemical, physical, and biological techniques) are tailored to the effluent properties, and are extensively utilized in the industrial sector for technological and economic purposes. However, because of the persistence of the dyes chemical structure in unfavorable environments (such as oxidizing agents, light, and heat), that impedes the breakdown and metabolization of these compounds, these procedures are limited in their ability to remove dyes. Therefore, to improve dye removal efficacy, specialized treatment technologies like membrane technology may be a substantial alternative.

1.2 Justification

Several techniques have been utilized for the treatment of wastewater contaminated with dyes, including biological, flocculation and coagulation, flotation, chemical precipitation, ion exchange, electrochemical, and adsorption techniques. Despite their advantages, these methods produce sludge and toxic byproducts, while also having restricted applicability under harsh conditions such as elevated temperatures, pH, COD, BOD, color, and heavy metals, which pose significant challenges in treating textile wastewater.[5]

In contrast, membrane filtration processes have been increasingly favored owing to their numerous advantages including low cost, environmental friendliness, high removal efficacy and low energy consumption.[17] However, conventional polymeric membranes are disposed to fouling due to their hydrophobic nature which encourages the interaction of dye molecules causing rapid contaminant buildup and subsequent membrane fouling.[18,19] This significantly reduces the membranes lifespan and efficiency. Furthermore, the balance that exists amidst permeability and selectivity restricts the applicability of polymeric membranes.[20,21] Despite all these challenges, advancement in membrane technology, such as thin film nanocomposite (TFN) membranes has revolutionized dye laden wastewater treatment. TFN membranes consist of an extremely thin barrier polyamide (PA) layer infused with nanofillers, specifically nanoparticles (NPs) that are evenly distributed within the barrier layer. The inclusion of NPs into the thin PA layer atop a support to fabricate

TFN membranes has been investigated in the enhancement of selectivity, hydrophilicity, water flux and fouling properties.[22–37]

Despite these improvements, some NPs utilized in TFN membranes have been documented to be toxic to humans and the environment, thus limiting their usage in water treatment.[38] The selection of nanofiller is thus crucial to ensure both membrane performance and safety. Gaphene oxide (GO) and cellulose nanocrystals (CNCs) have drawn innumerable attention of late and are promising nanofiller materials for the future. GO has several advantages such as its hydrophilic nature, high specific surface area (~ 2600 m^2g^{-1}), and the presence of epoxy, ketones, hydroxyl and carboxyl groups, allowing for further functionalization of GO, thereby improving contaminant removal.[39–41] Multiple investigations have been published in which GO was employed to improve membrane function.[42–51] CNCs belonging to the cellulose nanomaterial family are derived from sustainable and renewable resources, resulting in lower health, environmental, and safety implications.[52,53] High aspect ratios, high negative surface charge densities, superior mechanical qualities, hydrophilicity owing to hydroxyl group abundance, and ease of synthesis are only a few of the remarkable attributes of CNCs.[54–56] Additionally, since cellulose biomass is abundant in nature and the CNC synthesis method is simple, CNC production is incredibly cost effective, making it an appealing option.[54]

However, nanoparticle aggregation and clumping at excessive concentrations leads to irregular stacking which ultimately affects membrane morphology and performance.[57–59] Nanoparticle agglomeration also decreases the hydrophilicity and water permeance of membranes.[55,60] Thus, nanofiller modification before incorporation into membranes is critical to ensure ideal dispersion and interaction with polymer matrixes. Modification using surface-initiated atom transfer radical polymerization (SI-ATRP) is a fascinating method due to its vast advantages. SI-ATRP is a controlled approach for generating polymer brushes with precise density, functionality, and thickness.[61,62] Polymer brushes have long been employed to alter the surface features of membranes, enhancing properties such as biocompatibility, corrosion resistance, and wettability due to their mechanical and chemical robustness.[63,64] The attachment of hydrophilic polymer brushes to surfaces (surface grafting) helps increase antifouling properties, repel the adsorption of nonspecific proteins and microorganisms.[65–67] These brushes consist of numerous functional groups along each polymer strand, enabling their application in improving the contaminant capture capabilities of membranes.

By leveraging the diverse functionalities of these brushes, researchers can optimize the performance of materials designed for environmental remediation and filtration processes. Of interest to this study is the use of glutamic acid (GLU) and bis-[2-(methacryloyloxy)ethyl] phosphate (BMEP) as monomers due to their numerous attractive features. Poly- (glutamic acid) (PGLU) is a linear structured, natural biopolymer, anionic, hydrophilic and non-toxic polypeptide which contains L- and D- glutamic acid units connected by amine bonds.[68,69] It has an elevated binding affinity towards a wide range of contaminants and possesses a high molecular weight making it a good candidate in wastewater purification.[69,70] Poly[2-(methacryloyloxy)ethyl]phosphate (PMEP) is a

hydrophilic polymer that contains phosphorus in its structure and is fabricated through polymerization (i.e. ATRP) using 2-(methacryloyloxy)ethyl phosphate (MEP) as a monomer. Phosphorylated polymers are biodegradable, biocompatible, pH and temperature-sensitive, catalytically active, possess ion-exchange and complexing abilities.[71,72]

In this research, the modification of TFN membranes with three novel nanofillers, namely, GO-GLU, GO-PMEP, and CNC-GLU synthesized via SI-ATRP to enhance the physiochemical properties (hydrophilicity, selectivity, surface charge, membrane structure) of the resultant membranes were examined and outcomes were presented. Moreover, aerogels containing GO-GLU were used as dye adsorbents, the results are also reported. Based on our current understanding, there are no existing studies detailing TFN membranes or aerogels modified with these nanofillers intentionally designed for the removal of organic dyes in water. By growing polymer brushes on GO/CNC NPs, we aimed to create a synergistic effect that would boost the TFN membranes' hydrophilicity, selectivity, and resistance to fouling. This could signify a considerable development in membrane technology within the field of wastewater treatment.

1.3 Scientific contribution to new knowledge and novelty

This research work introduces a pioneering approach to enhance the performance TFN membranes utilized in the removal of dyes by integrating novel nanofillers, GLU/PMEP-functionalized GO and CNCs NPs. As far as we can ascertain, no studies have been documented on TFN membranes containing GLU/PMEP-functionalized GO and CNCs NPs in PA layer, marking a noteworthy advancement in membrane technology for wastewater treatment. A key innovative aspect of this study is the strategic use of these nanofillers to overcome common challenges in traditional membranes, such as NP agglomeration and fouling. By achieving optimal dispersion of the NPs within the membrane PA structure, the study ensures enhanced nanofiller-polymer matrix compatibility, which improves water permeability, dye rejection efficiency, and fouling resistance. This approach leads to membranes that have enhanced performance and antifouling properties compared to unmodified TFC and traditional membranes.

The research demonstrates that these functionalized NPs improve membrane hydrophilicity, thermal stability, and NPs interlayer spacing within the PA layer, resulting in enhanced water permeability, reproducibility, and dye rejection capabilities in comparison to unmodified TFC membranes. The surface functionalization of the NPs enables for proper dispersion in PA layer through enhanced nanofiller-polymer matrix compatibility. Additionally, the modified surface properties contributed to reduced fouling and improved membrane longevity. Importantly, the use of NPs like GO and CNC derived from *Cannabis sativa* minimizes chemical usage and waste generation, thereby reducing the environmental footprint of water treatment processes and contributing to cost savings in compliance with environmental regulations. By also enabling low-pressure operation, the modified TFN membranes offer a reduction in operational costs. This advancement positions GO and CNC-based TFN membranes as financially viable options for wastewater

treatment applications. Furthermore, the inclusion of GO-GLU in aerogels enhanced dye adsorption capacity under varied environmental conditions.

The implications of this research are significant for industries such as textiles and water purification, as well as for remediation scientists and environmental researchers engaged in water purification efforts making them a promising solution for sustainable wastewater management.

1.4 Aim and objectives

The goal of this investigation was to develop graphene oxide and cellulose nanocrystal modified membranes and aerogels for effective removal of dyes/salts from wastewater.

1.4.1 Objectives

(i) To fabricate poly (glutamic acid) brush modified graphene oxide integrated polyamide layer thin film nanocomposite membrane.

(ii) To fabricate poly (bis[2-(methacryloyloxy)ethyl] phosphate) brush modified graphene oxide integrated polyamide layer thin film nanocomposite membrane.

(iii) To fabricate poly (glutamic acid) brush modified cellulose nanocrystals integrated polyamide layer thin film nanocomposite membrane.

(iv) To fabricate polyvinyl alcohol crosslinked poly (glutamic acid) brush modified graphene oxide aerogel.

(v) To investigate the dye removal effectiveness of the thin film nanocomposite membranes and aerogel.

1.5 Research questions

The aim and objectives were attained by tackling the subsequent study questions:

1.What is the influence of hydrophilic modification of GO and CNC on the elimination of dyes by GO/CNC thin-film nanocomposite membranes and their fouling propensity?

2.What is the consequence of modification of GO on the dye separation performance of GO aerogels?

1.6 Hypothesis

The incorporation of surface-functionalized graphene oxide (GO) and cellulose nanocrystals (CNCs) into TFN membranes will significantly enhance their performance for the rejection of MB and MO from aqueous solutions. Specifically, the functionalized nanofillers are expected to:

Improve membrane hydrophilicity: The hydrophilic functional groups on GO and CNCs, along with the grafted brushes, will increase the membrane's affinity for water, reducing fouling and improving permeate flux.

Enhance thermal stability: The rigid structure of GO and CNCs, combined with the potential for cross-linking between the nanofillers and the polymer matrix, will increase the membrane's resistance to thermal degradation.

Increased interlayer spacing: Brush growth can introduce interlayer spacing within the TFN, facilitating easier diffusion of water molecules while hindering the passage of larger dye molecules.

Tunable size and morphology: Brush grafting allows for precise control over the size and morphology of the nanofillers within the membrane, potentially optimizing pore size distribution and dye rejection capabilities.

Increase dye rejection: The synergistic effects of size exclusion, steric hindrance, and Donnan exclusion will enhance the membrane's ability to selectively reject MB and MO dyes, while allowing for the passage of smaller molecules.

Improve membrane fouling resistance: The modified surface properties and enhanced hydrophilicity of the TFN membranes will reduce the adsorption of foulants, leading to longer membrane life and reduced operating costs.

Enhance membrane recyclability: The incorporation of functionalized nanofillers may facilitate easier cleaning and regeneration of the membranes, improving their reusability and reducing environmental impact.

Moreover, for GO-GLU incorporated aerogels, the grafted brushes are expected to create additional binding sites for increased dye adsorption capacity under diverse environmental conditions. This study demonstrates the potential of GO and CNC-based TFN membranes/ aerogels as a promising technology for the efficient and sustainable treatment of wastewater contaminated with organic dyes.

1.7 Thesis outline

The layout of the thesis is outlined as follows:

Chapter 1 comprises the study's problem statement, justification, and novelty statement, as well as its addition to existing scientific knowledge. This chapter additionally outlines the study's aims, objectives, and questions.

Chapter 2 discusses the literature on dye effluent pollution of water sources, the toxicity and impact of dyes, traditional techniques to dye-contaminated water treatment, and the limitations of these methods. The use of membrane filtration technologies, notably TFN membranes, as a solution for treating dye-laden water is reviewed. Furthermore, the use of GO, CNCs, and modification via SI-ATRP are covered in depth.

Chapter 3 covers the synthetic method for CNCs derived from *Cannabis sativa* (hemp fibers). However, each of the publications provided in Chapter 4 provides more information on the synthesis of GO, GO-GLU, GO-PMEP, and CNC-GLU, as well as the subsequent TFN membranes/aerogels.

Chapter 4 offers the study's findings and discussion through a series of manuscripts. These manuscripts are either submitted or are currently being reviewed for publication.

Chapter 5 describes the study's general conclusions and gives recommendations for future consideration.

1.8 References

1. Khan MD, Singh A, Khan MZ, Tabraiz S, Sheikh J. Current perspectives, recent advancements, and efficiencies of various dye-containing wastewater treatment technologies. *J Water Process Eng*. 2023;53(December 2022):103579. doi:10.1016/j.jwpe.2023.103579
2. Dutta P, Razaya Rabbi M, Sufian MA, Mahjebin S. Effects of textile dyeing effluent on the environment and its treatment: A review. *Eng Appl Sci Lett*. 2022;5(1):1-17. doi:10.30538/psrp-easl2022.0080
3. Affat SS. Classifications, Advantages, Disadvantages, Toxicity Effects of Natural and Synthetic Dyes: A review. *Univ Thi-Qar J Sci*. 2008;8(1):130-135. http://doi.org/10.32792/utq/utjsci/v8/1/21
4. Silveira E, Marques PP, Silva SS, Lima-Filho JL, Porto ALF, Tambourgi EB. Selection of Pseudomonas for industrial textile dyes decolourization. *Int Biodeterior Biodegrad*. 2009;63(2):230-235. doi:10.1016/j.ibiod.2008.09.007
5. Al-Tohamy R, Ali SS, Li F, et al. A critical review on the treatment of dye-containing wastewater: Ecotoxicological and health concerns of textile dyes and possible remediation approaches for environmental safety. *Ecotoxicol Environ Saf*. 2022;231:113160. doi:10.1016/j.ecoenv.2021.113160
6. Alsukaibi AKD. Various Approaches for the Detoxification of Toxic Dyes in Wastewater. *Processes*. 2022;10(10). doi:10.3390/pr10101968
7. EL-SADAAWY MM, AGIB NS. Removal of Textile dyes by ecofriendly aquatic plants From wastewater: A review on Plants Species, Mechanisms, and Perspectives. *Blue Econ*. 2024;2(2). doi:10.57241/2805-2994.1023
8. Berradi M, Hsissou R, Khudhair M, et al. Textile finishing dyes and their impact on aquatic environs. *Heliyon*. 2019;5(11). doi:10.1016/j.heliyon.2019.e02711
9. Zheng X, Fu D, Cheng J, et al. Effects of hypoxic stress and recovery on oxidative stress, apoptosis, and intestinal microorganisms in Pelteobagrus vachelli. *Aquaculture*. 2021;543(December 2020):736945. doi:10.1016/j.aquaculture.2021.736945
10. Arshad H, Imran M, Ashraf M. Toxic effects of Red-S3B dye on soil microbial activities, wheat yield, and their alleviation by pressmud application. *Ecotoxicol Environ Saf*. 2020;204(July):111030. doi:10.1016/j.ecoenv.2020.111030
11. Zhu X, Chen J, Qiu K, Kuai B. Phytohormone and light regulation of chlorophyll degradation. *Front Plant Sci*. 2017;8(November):1-8. doi:10.3389/fpls.2017.01911
12. Ramamurthy K, Priya PS, Murugan R, Arockiaraj J. Hues of risk: investigating genotoxicity and environmental impacts of azo textile dyes. *Environ Sci Pollut Res*. 2024;31(23):33190-33211. doi:10.1007/s11356-024-33444-1
13. Tounsadi H, Metarfi Y, Taleb M, El Rhazi K, Rais Z. Impact of chemical substances used in textile industry on the employee's health: Epidemiological study. *Ecotoxicol Environ Saf*. 2020;197(December 2019):110594. doi:10.1016/j.ecoenv.2020.110594
14. Katheresan V, Kansedo J, Lau SY. Efficiency of various recent wastewater dye removal methods: A review. *J Environ Chem Eng*. 2018;6(4):4676-4697. doi:10.1016/j.jece.2018.06.060

15. Kathing C, Saini G. A Review of Various Treatment Methods for the Removal of Dyes from Textile Effluent. *Recent Prog Mater*. 2022;04(04):1-15. doi:10.21926/rpm.2204028
16. Singh Z, Chadha P. Textile industry and occupational cancer. *J Occup Med Toxicol*. 2016;11(1):1-6. doi:10.1186/s12995-016-0128-3
17. Mosikatsi BE, Mabuba N, Malinga SP. Thin film composite membranes consisting of hyperbranched polyethylenimine (HPEI)-cysteamine layer for cadmium removal in water. *J Water Process Eng*. 2018;(July):0-1. doi:10.1016/j.jwpe.2018.10.004
18. Karami P, Aktij SA, Khorshidi B, et al. Nanodiamond-decorated thin film composite membranes with antifouling and antibacterial properties. *Desalination*. 2022;522(August 2021):1-11. doi:10.1016/j.desal.2021.115436
19. Firouzjaei MD, Seyedpour SF, Aktij SA, et al. Recent advances in functionalized polymer membranes for biofouling control and mitigation in forward osmosis. *J Memb Sci*. 2020;596(October 2019):117604. doi:10.1016/j.memsci.2019.117604
20. Ismail AF, Goh PS, Sanip SM, Aziz M. Transport and separation properties of carbon nanotube-mixed matrix membrane. *Sep Purif Technol*. 2009;70(1):12-26. doi:10.1016/j.seppur.2009.09.002
21. Rahimi-Kashkouli Y, Rahbari-Sisakht M, Ghadami Jadval Ghadam A. Thin film nanocomposite nanofiltration membrane incorporated with cellulose nanocrystals with superior anti-organic fouling affinity. *Environ Sci Water Res Technol*. 2020;6(3):715-723. doi:10.1039/c9ew00963a
22. Fathizadeh M, Tien HN, Khivantsev K, Song Z, Zhou F. Polyamide / nitrogen-doped graphene oxide quantum dots (N-GOQD) thin film nanocomposite reverse osmosis membranes for high flux desalination. *Desalination*. 2019;451(June 2017):125-132. doi:10.1016/j.desal.2017.07.014
23. Li S, Li C, Su B, Hu MZ, Gao X, Gao C. Amino-functionalized graphene quantum dots (aGQDs) -embedded thin fi lm nanocomposites for solvent resistant nano fi ltration (SRNF) membranes based on covalence interactions. *J Memb Sci*. 2019;588(June):117212. doi:10.1016/j.memsci.2019.117212
24. Ng Z-C, Chong C-Y, Lau W-J, Mustafa K, Ismaila AF. Boron removal and antifouling properties of thin-film nanocomposite membrane incorporating PECVD-modified titanate nanotubes. *J Chem Technol Biotechnol*. 2019;94(November 2018):2772-2782. doi:10.1002/jctb.6044
25. Zhu J, Qin L, Uliana A, et al. Elevated Performance of Thin Film Nanocomposite Membranes Enabled by Modi fi ed Hydrophilic MOFs for Nano fi ltration. Published online 2017. doi:10.1021/acsami.6b14412
26. Lind ML, Ghosh AK, Jawor A, et al. Influence of zeolite crystal size on zeolite-polyamide thin film nanocomposite membranes. *Langmuir*. 2009;25(17):10139-10145. doi:10.1021/la900938x
27. Yin J, Kim ES, Yang J, Deng B. Fabrication of a novel thin-film nanocomposite (TFN) membrane containing MCM-41 silica nanoparticles (NPs) for water purification. *J Memb Sci*. 2012;423-424:238-246. doi:10.1016/j.memsci.2012.08.020

28. Shokrgozar Eslah S, Shokrollahzadeh S, Moini Jazani O, Samimi A. Forward osmosis water desalination: Fabrication of graphene oxide-polyamide/polysulfone thin-film nanocomposite membrane with high water flux and low reverse salt diffusion. *Sep Sci Technol*. 2018;53(3):573-583. doi:10.1080/01496395.2017.1398261
29. Kim ES, Hwang G, Gamal El-Din M, Liu Y. Development of nanosilver and multi-walled carbon nanotubes thin-film nanocomposite membrane for enhanced water treatment. *J Memb Sci*. 2012;394-395:37-48. doi:10.1016/j.memsci.2011.11.041
30. Rashed AO, Esawi AMK, Ramadan AR. Novel Polysulfone/Carbon Nanotube-Polyamide Thin Film Nanocomposite Membranes with Improved Water Flux for Forward Osmosis Desalination. *ACS Omega*. 2020;5(24):14427-14436. doi:10.1021/acsomega.0c00973
31. Lakhotia SR, Mukhopadhyay M, Kumari P. Separation and Puri fi cation Technology Iron oxide (FeO) nanoparticles embedded thin- fi lm nanocomposite nano fi ltration (NF) membrane for water treatment. *Sep Purif Technol*. 2019;211(September 2018):98-107. doi:10.1016/j.seppur.2018.09.034
32. Wu X, Yang L, Meng F, Shao W, Liu X, Li M. ZIF-8-incorporated thin-film nanocomposite (TFN) nanofiltration membranes : Importance of particle deposition methods on structure and performance. *J Memb Sci*. 2021;632(April):119356. doi:10.1016/j.memsci.2021.119356
33. Yin J, Deng B. Polymer-matrix nanocomposite membranes for water treatment. *J Memb Sci*. 2015;479:256-275. doi:10.1016/j.memsci.2014.11.019
34. Ghosh AK, Jeong BH, Huang X, Hoek EMV. Impacts of reaction and curing conditions on polyamide composite reverse osmosis membrane properties. *J Memb Sci*. 2008;311(1-2):34-45. doi:10.1016/j.memsci.2007.11.038
35. Lau WJ, Ismail AF, Misdan N, Kassim MA. A recent progress in thin fi lm composite membrane : A review. *DES*. 2012;287:190-199. doi:10.1016/j.desal.2011.04.004
36. Esfahani MR, Aktij SA, Dabaghian Z, et al. Nanocomposite membranes for water separation and purification: Fabrication, modification, and applications. *Sep Purif Technol*. 2019;213(December):465-499. doi:10.1016/j.seppur.2018.12.050
37. Ng ZC, Lau WJ, Matsuura T, Ismail AF. Thin film nanocomposite RO membranes : Review on fabrication techniques and impacts of nanofiller. *Chem Eng Res Des*. 2020;5:81-105. doi:10.1016/j.cherd.2020.10.003
38. Bai L, Liu Y, Ding A, Ren N, Li G, Liang H. Fabrication and characterization of thin-film composite (TFC) nanofiltration membranes incorporated with cellulose nanocrystals (CNCs) for enhanced desalination performance and dye removal. *Chem Eng J*. 2019;358(August 2018):1519-1528. doi:10.1016/j.cej.2018.10.147
39. Peng W, Li H, Liu Y, Song S. Comparison of Pb (II) adsorption onto graphene oxide prepared from natural graphites : Diagramming the Pb (II) adsorption sites. *Appl Surf Sci*. 2016;364:620-627. doi:10.1016/j.apsusc.2015.12.208
40. Gopalakrishnan A, Krishnan R, Thangavel S. Journal of Industrial and Engineering Chemistry Removal of heavy metal ions from pharma-effluents using graphene-oxide

nanosorbents and study of their adsorption kinetics. *J Ind Eng Chem*. 2015;30:14-19. doi:10.1016/j.jiec.2015.06.005

41. Li P, Li Y, Wu Y, et al. Thin-film nanocomposite NF membrane with GO on macroporous hollow fiber ceramic substrate for efficient heavy metals removal. *Environ Res*. 2021;197(November 2020):111040. doi:10.1016/j.envres.2021.111040

42. Kang Y, Obaid M, Jang J, Kim IS. Sulfonated graphene oxide incorporated thin film nanocomposite nanofiltration membrane to enhance permeation and antifouling properties. *Desalination*. 2019;470(May):114125. doi:10.1016/j.desal.2019.114125

43. Lin CS, Tung KL, Lin YL, Dong C Di, Chen CW, Wu CH. Fabrication and modification of forward osmosis membranes by using graphene oxide for dye rejection and sludge concentration. *Process Saf Environ Prot*. 2020;144:225-235. doi:10.1016/j.psep.2020.07.007

44. Abadikhah H, Naderi Kalali E, Khodi S, Xu X, Agathopoulos S. Multifunctional Thin-Film Nanofiltration Membrane Incorporated with Reduced Graphene Oxide@TiO2@Ag Nanocomposites for High Desalination Performance, Dye Retention, and Antibacterial Properties. *ACS Appl Mater Interfaces*. 2019;11(26):23535-23545. doi:10.1021/acsami.9b03557

45. Abadikhah H, Kalali EN, Behzadi S, et al. High flux thin film nanocomposite membrane incorporated with functionalized TiO2@reduced graphene oxide nanohybrids for organic solvent nanofiltration. *Chem Eng Sci*. 2019;204:99-109. doi:10.1016/j.ces.2019.04.022

46. Izadmehr N, Mansourpanah Y, Ulbricht M, Rahimpour A, Omidkhah MR. TETA-anchored graphene oxide enhanced polyamide thin film nanofiltration membrane for water purification; performance and antifouling properties. *J Environ Manage*. 2020;276(October 2019):111299. doi:10.1016/j.jenvman.2020.111299

47. Zhao DL, Jin H, Zhao Q, et al. Smart integration of MOFs and CQDs to fabricate defect-free and self-cleaning TFN membranes for dye removal. *J Memb Sci*. 2023;679(January):121706. doi:10.1016/j.memsci.2023.121706

48. Li Y, Li C, Li S, Su B, Han L, Mandal B. Graphene oxide (GO)-interlayered thin-film nanocomposite (TFN) membranes with high solvent resistance for organic solvent nanofiltration (OSN). *J Mater Chem A*. 2019;7(21):13315-13330. doi:10.1039/c9ta01915d

49. Tang K, Zhu LS, Lan P, et al. Regulating the thickness of nanofiltration membranes for efficient water purification. *Nanoscale Adv*. 2023;5(18):4770-4781. doi:10.1039/d3na00110e

50. Zhang C, Wei K, Zhang W, Bai Y, Sun Y, Gu J. Graphene Oxide Quantum Dots Incorporated into a Thin Film Nanocomposite Membrane with High Flux and Antifouling Properties for Low-Pressure Nanofiltration. *ACS Appl Mater Interfaces*. 2017;9(12):11082-11094. doi:10.1021/acsami.6b12826

51. Jee H, Jang J, Kang Y, et al. Enhancing the Dye-Rejection Efficiencies and Stability of Graphene Oxide-Based Nanofiltration Membranes via Divalent Cation Intercalation and Mild Reduction. *Membranes (Basel)*. 2022;12(4). doi:10.3390/membranes12040402

52. Moon RJ, Martini A, Nairn J, Simonsen J, Youngblood J. *Cellulose Nanomaterials Review: Structure, Properties and Nanocomposites*. Vol 40.; 2011. doi:10.1039/c0cs00108b

53. Bai L, Liu Y, Bossa N, et al. Incorporation of Cellulose Nanocrystals (CNCs) into the Polyamide Layer of Thin-Film Composite (TFC) Nanofiltration Membranes for Enhanced Separation Performance and Antifouling Properties. *Environ Sci Technol*. 2018;52(19):11178-11187. doi:10.1021/acs.est.8b04102

54. Asempour F, Emadzadeh D, Matsuura T, Kruczek B. Synthesis and characterization of novel Cellulose Nanocrystals-based Thin Film Nanocomposite membranes for reverse osmosis applications. *Desalination*. 2018;439(December 2017):179-187. doi:10.1016/j.desal.2018.04.009

55. Liu Y, Bai L, Zhu X, et al. The role of carboxylated cellulose nanocrystals placement in the performance of thin-film composite (TFC) membrane. *J Memb Sci*. 2021;617(August 2020):118581. doi:10.1016/j.memsci.2020.118581

56. Xu C, Chen W, Gao H, Xie X, Chen Y. Cellulose nanocrystal/silver (CNC/Ag) thin-film nanocomposite nanofiltration membranes with multifunctional properties. *Environ Sci Nano*. 2020;7(3):803-816. doi:10.1039/c9en01367a

57. Unimpeded Permeation of Water Through Helium-Leak–Tight Graphene-Based Membranes. *Science (80-)*. 2012;335(January):442-444. doi:10.1126/science.1211694

58. Anand A, Unnikrishnan B, Mao JY, Lin HJ, Huang CC. Graphene-based nanofiltration membranes for improving salt rejection, water flux and antifouling–A review. *Desalination*. 2018;429(December 2017):119-133. doi:10.1016/j.desal.2017.12.012

59. Feng X, Peng D, Zhu J, Wang Y, Zhang Y. Recent advances of loose nanofiltration membranes for dye/salt separation. *Sep Purif Technol*. 2022;285(November 2021):120228. doi:10.1016/j.seppur.2021.120228

60. Peltzer M, Pei A, Zhou Q, Berglund L, Jiménez A. Surface modification of cellulose nanocrystals by grafting with poly(lactic acid). *Polym Int*. 2014;63(6):1056-1062. doi:10.1002/pi.4610

61. Chen M, Qin L, Liu Y, Zhang F. Controllable preparation of polymer brushes from mesoporous silica SBA-15 via surface-initiated ARGET ATRP. *Microporous Mesoporous Mater*. 2018;263(12):158-164. doi:10.1016/j.micromeso.2017.12.019

62. Pranantyo D, Xu LQ, Neoh K, Kang E, Ng YX, Teo SL. Tea Stains-Inspired Initiator Primer for Surface Grafting of Antifouling and Antimicrobial Polymer Brush Coatings. Published online 2015. doi:10.1021/bm501623c

63. Ma S, Zhang X, Yu B, Zhou F. Brushing up functional materials. *NPG Asia Mater*. 2019;11(1). doi:10.1038/s41427-019-0121-2

64. Jeyaprakash JD, Samuel S, Dhamodharan R, Rühe J. Polymer brushes via ATRP: Role of activator and deactivator in the surface-initiated ATRP of styrene on planar substrates. *Macromol Rapid Commun*. 2002;23(4):277-281. doi:10.1002/1521-3927(20020301)23:4<277::AID-MARC277>3.0.CO;2-U

65. Ladd J, Zhang Z, Chen S, Hower JC, Jiang S. Zwitterionic Polymers Exhibiting High Resistance to Nonspecific Protein Adsorption from Human Serum and Plasma. *ACS Biomacromolecules*. 2008;9(5).
66. Zdyrko B, Klep V, Li X, et al. Polymer brushes as active nanolayers for tunable bacteria adhesion. *Mater Sci Eng C*. 2009;29(3):680-684. doi:10.1016/j.msec.2008.12.017
67. Uttley OF, Brummitt A, Worrall SD. Accessible and sustainable Cu(0)-mediated radical polymerisation for the functionalisation of surfaces. *Polym Chem*. Published online 2020:3831-3840. doi:10.1039/d0py00516a
68. Shih I, Van Y-T. The production of poly-(y -glutamic acid) from microorganisms and its various applications. 2001;79.
69. Pandey K, Pandey AK, Sirohi R, Pandey S. *Production and Applications of Polyglutamic Acid*. INC; 2021. doi:10.1016/B978-0-12-821888-4.00021-6
70. Li M, Zhu X, Yang H, et al. Treatment of potato starch wastewater by dual natural fl occulants of chitosan and poly-glutamic acid. 2020;264. doi:10.1016/j.jclepro.2020.121641
71. Głowińska A, Trochimczuk AW, Jakubiak-marcinkowska A. Novel acrylate / organophosphorus-based hydrogels for agricultural applications . New outlook and innovative concept for the use of 2- (methacryloyloxy) ethyl phosphate as a multi-purpose monomer. *Eur Polym J*. 2019;110(August 2018):202-210. doi:10.1016/j.eurpolymj.2018.11.020
72. Zhou F, Huck WTS. Three-stage switching of surface wetting using phosphate-bearing polymer brushes. 2005;(i):5999-6001. doi:10.1039/b512106j

CHAPTER 2
LITERATURE REVIEW

2.1 Introduction

The contamination of water is a major global concern, with wastewater being dumped into freshwater systems. Among the several types of wastewaters, dyeing wastewater deserves special consideration since it is a threat to the environment because of its color and high toxicity at low levels. This chapter will look at dyes in broad terms, wastewater treatment procedures, and dye removal techniques. It also emphasizes the literature on the synthesis of thin film nanocomposite (TFN) membranes and aerogels for dye wastewater treatment.

2.2 Contamination of water sources by dye effluents: Possible sources and environmental impact

2.2.1 Dye overview

Dyes are organic chemical compounds which are used to add color to items in a variety of sectors. Dye molecules contain chromophores that impart color, and auxochromes, which enhance the intensity of that color.[1] The various colors of dyes are influenced by specific wavelengths of light that are absorbed by both the auxochromes and chromophores.[1] Dyes are usually divided into classes based on their source (natural or synthetic), structure, and application (**Figure 2.1**). In dyes, the structural variations are classed as (i) anionic, (ii) cationic, and (iii) non-ionic dyes.[2] Azo, mordant, direct, basic, reactive, acid, sulfide, and dispersion dyes are all extensively utilized in the textile industry.[3]



Figure 2.1: Different classes of dyes and their potential industrial uses.[5]

Synthetic dyes are produced globally at a rate of approximately 7×10^7 tons per year, with textile industries using over 10,000 tons.[4] Textile dyes inadequately adhere to fabric thus

released as effluent with wastewater into aquatic systems, including streams, ponds, rivers, and lakes,without prior treatment, resulting in significant ecotoxicological risks and detrimental effects on living species.[5] Dyes are complex organic compounds that do not disintegrate when exposed to water, detergents, or other washing agents. Even when subjected to severe heat, oxidizing chemicals, or intense light, dye molecules can defy deterioration.[1] Industries have been subject to legislation about the discharge of harmful colored wastewater in water bodies.[6] **Table 2.1** shows the international acceptable standards for the discharge of pollutants in dye effluents.

Table 2.1: International guidelines for the release of dye effluent into the environment.[6]

Factor	Standard allowed
Chemical oxygen demand	< 50 ppm
Biological oxygen demand	< 30 ppm
pH	Between 6 – 9
Colour	< 1 ppm
Temperature	< 42 °C
Suspended solids	< 20 ppm
Toxic pollutants	Not permitted to be released

2.2.2 Textile dye toxicity and their effect

The discharge of dye contaminated water by humans has had a severe impact on the natural environment. The shielding effect of light by dyes in water negatively affects aquatic photic zone resulting in decreased photosynthesis.[7] Furthermore, the existence of textile pigments and dyes in wastewater causes it to be extraordinarily colorful, fluctuate in pH, have an elevated level of biological oxygen demand (BOD), suspended particles, chemical oxygen demand (COD), and total organic carbon.[8] These suspended particulates hinder the passage of water along fish gills, impeding gaseous exchange and, as a result, lowering growth rates in fish and in some cases death.[5] Prolonged exposure to dye effluents causes a reduction in fish feed intake, which in turn results in decreased levels of fat, protein, and carbohydrates.[9] Excessive quantities of dye in water lower oxygen availability and hinder the biological functions of aquatic animals.[5,10] As such, fish are vulnerable to a variety of diseases due to the negative consequences of oxygen deprivation on their functional reactions, notably the immune system.[11] Massive amounts of dyes are dumped into seas, oceans, lakes, and rivers, which have a negative influence on algae development. Dye effluents also alter the soils chemical balance thus negatively impacting microorganisms.[12] These organic pollutants also damage plant germination and chlorophyll content.[13] Moreover, 60 – 70% of dyes are carcinogenic, recalcitrant, toxic, and unsusceptible to decomposition by means of conventional remediation methods.[10]

Dyes have sparked widespread concern due to their hazardous properties. Dye exposed fish have significant harmful impact on human health.[11] Dye exposure has been linked to ailments in animals and humans, including dermatitis and central nervous system abnormalities.[14,15] When textile colors are ingested or inhaled, this can lead to irritation of skin and eyes, as well as respiratory issues such as asthma.[6,16] The extensive application of

dyes in many sectors raises concerns over their potential link to cancers, including breast, lung, bladder, and colorectal cancers in humans.[17] Mutagenesis, chromosomal fractures, carcinogenesis, and pulmonary toxicity have all been reported as negative repercussions.[14] Accordingly, methods and technology for removing dyes from a variety of wastewater streams are needed.

2.3 Approaches to water treatment

Textile manufacturers utilize tremendous volumes of water in their dyeing operations, making it difficult to treat the massive amounts of wastewater discharged. The latter contains a variety of inorganic and organic contaminants. As a result, numerous countries have implemented restrictions to ensure that effluent meets a standard before it is discharged into the ecosystem or repurposed (**Table 2.1**). In order to accomplish this, chemical, physical, and biological techniques have been utilized to safeguard the environment and human health from discharge concerns. To achieve effective outcomes, these methods could be employed alone or in combination. Although various dye removal procedures have been studied over the last thirty years, relatively few are currently used by the relevant industries due to the restrictions provided by the majority of the approaches.

2.3.1 Dye removal by biological methods

Biological remediation is the employment of biological species or techniques to eliminate contaminants from industrial effluent (**Figure 2.2**).[18] This technique aims to provide an efficient mechanism for disposing of breakdown products. Microorganisms responsible for biodegradation employ several techniques such as adsorption, bioaccumulation, biosorption, elimination, alleviation, or mineralization of the hazardous wastewater molecules into non-harmful or even valuable compounds.[19] Biological alternatives to wastewater purification are simpler to use, energy savers, employs less chemical reagents, eco-friendlier, produces no sludge, and non-toxic by-products.[20] Microbes like algae, yeast, bacteria, filamentous fungi, along with their enzymes, have garnered significant interest owing to their abundant availability, affordability, and impressive effectiveness in degrading a diverse range of dyes and transforming dye molecules into simpler non-toxic compounds.[21] Due to their genetic diversity and flexibility, biological techniques are successful for reducing and mineralizing wastewater pollutants.[22] However, the biological technique has significant drawbacks, such as long operating periods and the inability to function against hazardous compounds.[19] **Table 2.2** displays the findings of numerous investigations on biological approaches for dye degradation.

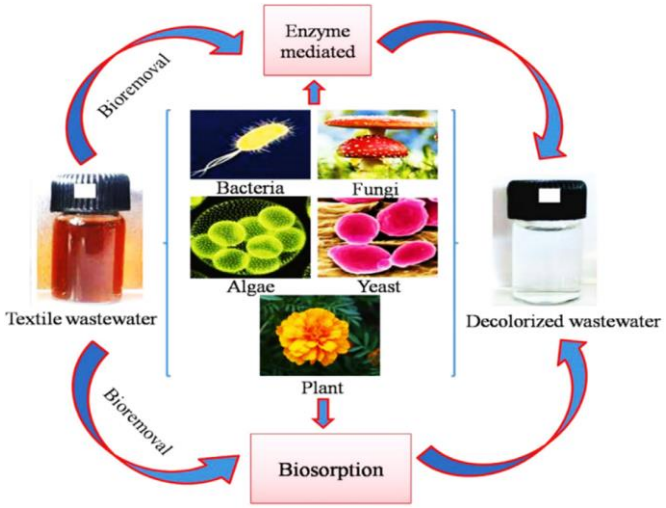

Figure 2.2: Treatment of textile wastewater by biological methods.[18]

Table 2.2: Rate of dye removal utilizing various biological treatment methods.

Species	Dye	Decolorization / Removal (%)	References
Corynebacterium glutamicum (bacteria)	Reactive black 5	93%	23
Trametes versicolor (fungus)	Direct blue 1	95 %	24
Azolla filiculoides (algae)	Acid blue 15	43%	25
Pseudomonas extremorientalis BU118 (bacteria)	Congo red	36 – 94	26
Scheffersomyces spartinae TLHS-SF1(yeast)	Acid Scarlet 3R	98.14	27
Magnusiomyces ingens LH-F1 (yeast)	Acid Red B	97.37	28
Galactomyces geotrichum MTCC 1360 (yeast)	Methyl Red	100	29
Peroneutypa scoparia (fungi)	Acid Red 97	75	30

2.3.2 Dye removal by chemical methods

This method involves utilizing chemical principles to remove dyes. Chemical methods of dye removal include coagulation, flocculation, electrochemical destruction, ozonation, advanced oxidation, fenton reagents, ultraviolet (UV) and photochemical irradiation.[6,31] Chemical dye removal methods have various disadvantages that make them unsuitable for commercial application such as the requirement of proper equipment, enormous electrical energy requirements for reactors, and the use of large amounts of chemicals.[31] Moreover, the formation of unstable toxic by-products as well as carcinogenic aromatic amines, sludge generation, high cost, and pH sensitivity are significant constraints of chemical techniques use in treating dye contaminated effluents from industrial applications.[32] **Table 2.3** displays the various chemical methods utilized in the removal of dye.

Table 2.3: Rate of dye removal utilizing various chemical treatment methods.

Treatment method	Dye	Condition	Dye removal (%)	References
Coagulation–flocculation (aluminum-based water treatment residuals)	disperse blue 79	concentration = 25, 50, 75 mg/L dosage = 3,000 mg/L Initial pH = 3	88	33
Catalytic ozonation (MgO nanocrystals)	reactive red 198	pH = 8 catalyst dose = 5 g/L concentration = 200 mg/L Time = 9 min	100	34
Catalytic ozonation (Fe/activated carbon catalyst)	crystal violet	concentration = 400 mg/L time = 30 min dosage = 2.5 g/L pH = 7 Ozone dosage = 4.44 mg/min, Catalyst	>96	35
Photocatalytic Degradation (TiO_2)	MB	concentration = 20 mg /L	100	36
coagulation-Photocatalytic treatment (UVA/synthesized MgO nanoparticles)	acid red 73	MgO nanoparticles = 0.8 g/L, reaction time = 60 min, pH = 5	100	37
Electrocoagulation (aluminum sacrificial anode)	crystal violet	Electrolysis time = 1 hour pH = 5.4	100	38
Advanced oxidation process (AOP)	reactive green 19	time = 20 min		39

2.3.3 Dye removal by physical methods

Physical dye elimination techniques are relatively straightforward procedures that exploit the mass transfer mechanism and are increasingly used in dye removal.[6] When contrasted with chemical or biological dyes removal procedures, this method requires fewer chemicals.[40] This approach is considered to be more reliable than the other two color removal procedures because it does not employ any live organisms or chemicals.[40] Membrane filtration, ion exchange and adsorption are common physical approaches. The highest removal percentage for physical dye removal processes is 86.8 – 99%. Physical techniques provide various advantages, such as simplicity, affordability, minimal chemical demands, and no inhibiting influence from toxic compounds.

Adsorption is an efficient strategy in physical treatment methods. Adsorption is a technique that uses physical and chemical forces to adhere dissolved molecules to the surface of an adsorbent substance.[7] Numerous adsorbents, such as alumina, zeolites, activated carbon, and silica gel, have been extensively employed to remove dyes from industry.[5,41] The ion exchange process has drawn significant attention in recent decades for treating wastewater containing dyes owing to its advantages, i.e. simplicity, flexibility,

regeneration, and effectiveness, however it is costly.[18] Dye removal through ion exchange is centered on strong interactions between charges of dye molecules and functional resins.[41] **Table 2.4** displays the various physical methods utilized in the removal of dye.

Table 2.4: Rate of dye removal utilizing various physical treatment methods.

Treatment method	Dye	Condition	Dye removal (%)/ adsorption capacity (mg/g)	References
Adsorption (mesoporous carbon material)	rhodamine B acid yellow 17	ST-A CWZ-22	83–100, 35–53 58–87, 46–71	42
Adsorption (*Curcuma caesia* based activated carbon)	malachite green	fixed bed column	38.16	43
Adorption (bentonite – alginate Composite)	crystal violet	70 °C langmuir parameter, q_{max} Freundlich parameter, K_F	 601.9339 36.3399	44
Ion Exchange (based on waste cotton)	acid black	Native Cotton Aminated cotton	23.83 147.27	45
Membrane photocatalytic Reactor (0.3 g/L ZnO-PVP-St)	congo red	photocatalysis nanofiltration	65 ± 1.0 100 ± 0.5	46
Electro-Fenton treatment	reactive red 195	Fe_3O_4/ rGO catalyst	93.34	47

However, there are significant disadvantages to these technologies, including the generation of hazardous byproducts and sludge, along with their restricted use.[1] Also, high temperatures, heavy metals, COD, BOD, color, and pH, typically limit their usage in textile wastewater treatment.[5] The use of membrane filtration techniques to remove dyes is particularly relevant to this study due to its vast advantages including high efficacy and will be explored in greater detail in the upcoming section.

2.4 Dye removal by membrane filtration technologies

Membrane separation is a sophisticated physical method utilized in wastewater treatment, where wastewater is filtered through a permeable membrane. Semi-permeable membranes in pressure driven settings act as sieves to selectively exclude contaminants from permeate through Donnan, size exclusion and/or adsorption mechanisms.[48,49] The utilization of membrane filtration technologies for the elimination of dyes in water has been researched vastly owing to its numerous benefits including high removal efficacy, low cost and energy consumption.[50] Furthermore, this technique concentrates and, more importantly, eradicates color from wastewater in real time. It has numerous special features that are incomparable with other techniques, such as resistance to chemical toxicity, temperature, and microbial attack.[18] This filtration technique is beneficial for water recycling in textile dye manufacturing.

The porosity, pore sizes and surface charge are crucial in membrane selectivity and permeability.[51–53] These can be tuned via method of fabrication, choice of polymers, nanofillers and solvents used. The addition of filler materials into negatively charged membrane surfaces enhances the electrostatic repulsion based rejection of negatively charged dyes.[53] When the hydrated dye ions surpass the size of the membrane's pores, the size exclusion mechanism can effectively prevent their passage. Typically, the rejection of dyes is often accomplished by the combination size and charge exclusion.[54] As dye molecules clump together in water, size exclusion effect intensifies. For dyes possessing low molecular weights, the Donnan exclusion effect tends to take precedence over the size exclusion effect. Therefore, it is crucial to leverage the inherent dye charge in their hydrated state to adjust the surface charge of the porous membranes.[54] Pressure driven membrane systems are extensively utilized in wastewater treatment and fall into four categories depending on their pore size; Reverse osmosis (RO), Nanofiltration (NF), Ultrafiltration (UF), and Microfiltration (MF) as summarized in **Figure 2.3**. Microfiltration (MF) filtration entails passing a liquid through a membrane with pore diameters ranging from 0.1 to 10 µm. This approach retains bacteria and suspended solids, allowing smaller solutes through the membrane. It is ineffective for dye removal since dyes are usually smaller than the pores and hence pass through the membrane. The membrane processes that are widely used for dye removal are UF, NF and RO due to the pore sizes.

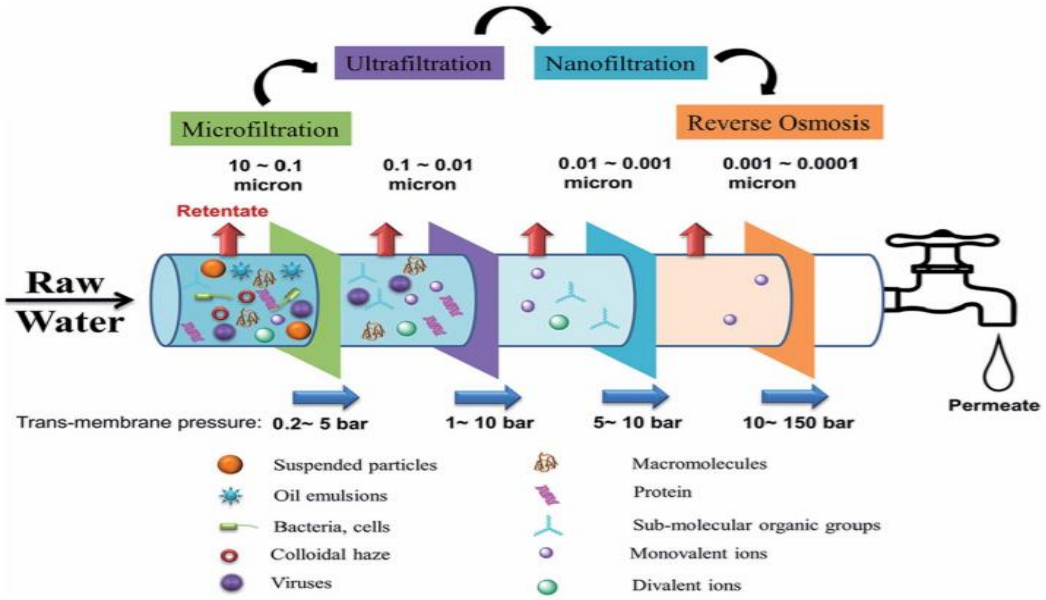

Figure 2.3: MF, UF, NF and RO membrane processes.[55]

2.4.1 Ultrafiltration (UF)

This is a separation process that relies on pressure and utilizes filtration membranes with typical pore sizes between 0.01 – 0.1 µm.[56] Species that have a higher molecular weight are retained whilst low molecular weight and dissolved salts flow through the membrane.[57] Ultrafiltration is used as a pretreatment process in wastewater treatment processes.[58] Ultrafiltration membranes are normally fabricated using phase inversion which result in membranes with wide pore size distribution.[59] This eventually leads to low flux and high

fouling rates.[60,61] Subsequently, dye rejection due to ultrafiltration alone rarely exceeds 90%. To achieve a higher rejection, Micellar enhanced ultrafiltration membranes were proposed. Micellar enhanced and polyelectrolyte enhanced ultrafiltration membranes utilize surfactants i.e. Sodium dodecyl sulfate (SDS), which are dispersed to wastewater until a critical micelle concentration (CMC) is reached.[62]

2.4.2 Nanofiltration and Reverse Osmosis

Nanofiltration (NF) membrane system involves the filtration of a liquid through a membrane that has a nominal pore size ranging from ~1 to 2 nm in a pressure driven setup.[61] These membranes generally possess a high rejection rate for most dissolved organic solutes which possess a molecular weight (MW) exceeding 100 – 200 Da, divalent ions from water and salt with salt concentrations below 1000 – 2000 ppm.[63] These membranes are generally intermediates between UF and RO and their separation is through sieving and electrostatic interactions of the membrane and pollutant.[55,64,65] Nanofiltration membranes have been researched vastly in the elimination dyes from wastewater and have shown great removal efficiency as summarized in **Table 2.5**. These membranes are favored owing to their simplicity, low energy usage and high efficiency in contaminant rejection.[66]

The reverse osmosis (RO) process utilizes a membrane with pore sizes between 0.1 and 1 nm to eliminate contaminants from water, operating under high hydraulic pressures (0.7 – 5.5 MPa).[58] Typically, the feed is transported against the natural flow in a concentrated solution to a dilute solution under high pressure to overcome the osmotic pressure of salt via the membrane.[58,67] It is normally used for the production of freshwater from saltwater in a desalination process.[68] This filtration process is able to remove a wide range of dissolved species in water but it suffers from scaling, removal of brine and boron.[58]

An emerging separation technique is forward osmosis (FO). This separation technology entails the use of a semi-permeable membrane through which water molecules moves from low to high osmotic pressure without the use of hydraulic pressure.[69] Forward osmosis has several advantages i.e. low energy consumption, environmentally friendly, low fouling tendency which is suspected to extend the lifespan of the membrane.[69,70] However, because RO and FO are commonly used in desalination, there has been limited research on dye removal using these processes.

Table 2.5: Summaries of different NF RO membranes, removal efficiency and working parameters.

Membrane	Dye	Experiment conditions	Removal efficiency (%)	Reference
SiO_2 modified polyethyleneimine-based NF	crystal violet	0.1wt% SiO_2 nanoparticles	100	71
carboxymethyl chitosan coated Fe_3O_4 nanoparticles NF	direct Red 16	4 bar; pH = 6; concentration =30 mg/L	99	72
M-PEI and M-PIP NF	reactive black 5	0.6 MPa; concentration = 0 – 3 g/L; room temperature	>95	73
Toray, NF 270, Desal 5 L	setazol red dye	6 – 15 bar; concentration = 100 mg/L; pH = 8	97 – 98	74
RO membrane	reactive orange acid red reactive black reactive blue	8 bar; concentration = 65 mg/L; temperature = 39°C;	96 – 99 97.2% 99.58% 99.9%	75
PA@GO loose NF	trypan blue	0.3 bar; concentration = 20 ppm; PA@GO-60	99.8	76
Polysulfone - functionalized graphene oxide (f-GO) NF	congo red MB	2wt% f-GO; concentration = 25 ppm	>99	77
polyphenol/polyethyleneimine NF	MB victoria blue B	TA/PEI mass ratio of 1:2	>92	78

2.4.3 Advancements in Thin Film Composite Membranes: Structure, Challenges, and Innovations

RO and NF membranes mostly have thin film composite (TFC) structures developed through interfacial polymerization (IP) technique. TFC membranes feature a thin selective layer, commonly made from polyamide (PA) or polyimide, supported by a porous substrate such as ultrafiltration polysulfone (PSF) or polyethersulfone (PES) (**Figure 2.4).**[79,80] These membranes are extensively utilized in wastewater treatment applications owing to their ability to tolerate a broad range of pH levels, high water flux, exceptional stability, and strong resistance to pressure-induced compaction. However, they face challenges such as fouling and degradation from chlorine exposure, which require comprehensive pretreatment processes to mitigate fouling and ensure the production of high-quality permeate.[81,82]

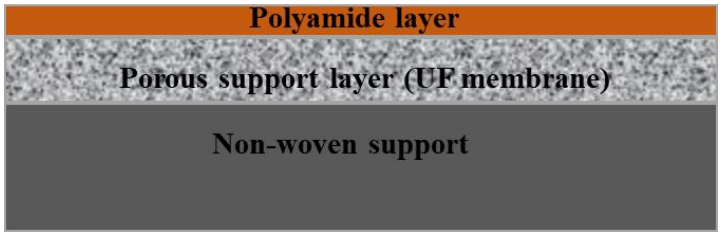

Figure 2.4: Typical structure of TFC membrane.

To address these limitations, researchers are exploring advanced materials to increase the antifouling attributes of PA-TFC membranes, aiming to lower operational costs and enhance performance. Approaches such as grafting, electrostatic deposition, and surface coating have been employed to boost properties like fouling resistance, durability, and energy efficiency (**Figure 2.5**).[83] Furthermore, optimizing the PA layer has been a focal point for reducing foulant accumulation, increasing permeability, and improving energy efficiency, driving advancements in high-performance TFC membranes. [81,82]

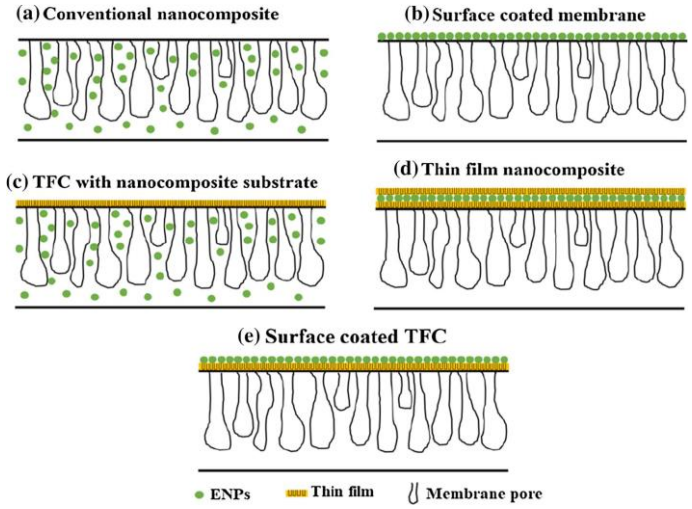

Figure 2.5: Five categories of nanocomposite membranes. [83]

The structural design of PA-TFC membranes provides extensive opportunities for customization, particularly through the incorporation of nanofillers into the PA layer. The advent of thin film nanocomposite (TFN) membranes, which contains nanoparticles into the PA layer, has opened up new paths for increasing membrane performance and permeability. This innovation not only improves water flux and antifouling attributes but also preserves the membrane's rejection efficiency, paving the way for more efficient and durable membrane technologies.[84,85] Furthermore, the nanostructured materials possessing a hydrophilic outer layer and a hydrophobic inner layer are envisaged to significantly improve water permeability. The hydrophobic inner layer facilitates the seamless transport of water molecules across frictionless channels, whilst the hydrophilic outer layer diminishes surface tension and capillary forces, thereby enhancing overall water flow efficiency.[86,87]

2.4.4 Thin film nanocomposite (TFN) membranes

To improve water flux, selectivity and antifouling properties, the dispersion of nanomaterials i.e. graphene oxide (GO), titanite nanotubes, metallic organic framework (MOF), zeolites, silica (SiO_2), iron oxide (FeO) nanoparticles, nanosilver, multi-walled carbon nanotube (MWCNT) into the ultra-thin barrier (PA layer) to fabricate TFN membranes has been studied.[88–98] In-situ interfacial polymerization (IP) process between trimesoyl chloride (TMC) organic solution and aqueous m- phenylenediamine (MPD) is the most common method of fabrication (**Figures 2.6 and 2.7**).[99] The nanofillers are

dispersed either in organic or in aqueous phase.[100] During in-situ IP process, the PA layer is produced by submerging the substrate in an aqueous solution of MPD and then in an organic solution of TMC. The polymerization takes place at the boundary where the two monomers meet.[101] During this process, the monomers and their chemical characteristics have a vital role in the control of the membranes hydrophilicity, thickness, roughness, film density and chemical resistance of the active layer.[101]

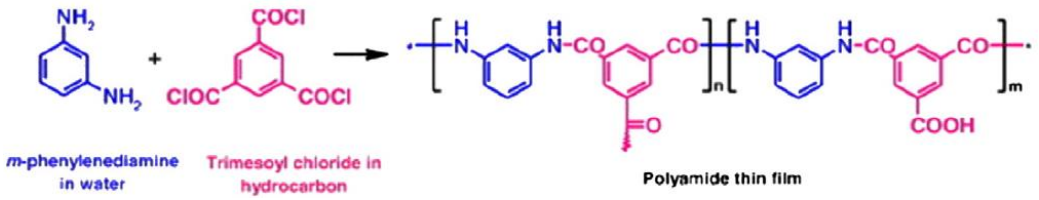

Figure 2.6: Fabrication of PA thin film layer from MPD and TMC. [99]

During TFN fabrication, water permeability and selectivity trade off need to be balanced. With the introduction and increase of nanoparticles (NP) in the PA layer, the hydrophilicity has been seen to improve evidenced by the decline in water contact angle which aids in water solubilization and diffusion.[102] The nanomaterial size, surface and internal characteristics need to be optimized to ensure proper interfacial interactions between them and polymer matrices. Modification of nanomaterial before embedding it in the active layer is also common to improve the dispersal as well as the interaction between nanomaterial and polymer matrix. Large nanomaterials i.e. NPs can ruin the barrier layer.[102] Besides hydrophilicity, thin film layer thickness plays a key role in water permeability.[103] Generally, a thinner thin film layer coupled with a lower degree of cross linking is associated with a higher water permeability. The cross-linking in the PA layer is likely reduced with the integration of nanoparticles in the PA matrix. This is due to the amine and acryl chloride groups reaction disturbance and the formation of nanovoids surrounding the interfaces between the PA matrix and nanofillers.[102] The removal of dyes using TFN membranes has been reported (**Table 2.6**). Ghaemi et al. (2018) investigated the effects of introducing nano-porous SAPO-34 (silicoaluminophosphate nano-porous zeolite) NPs into the PA layer of TFN membranes on membrane permeability and performance.[104] Upon the introduction and growth of NPs into the PA layer, the pure water flux improved from 10.9 to 35.2 kg/m^2h. The membrane's performance was evaluated in the removal of dyes (acid blue 193, methyl violet 6B, and reactive blue 4) in water, and the modified membranes efficiently rejected 100% of all dyes (feed solution concentration = 50 ppm).[104]

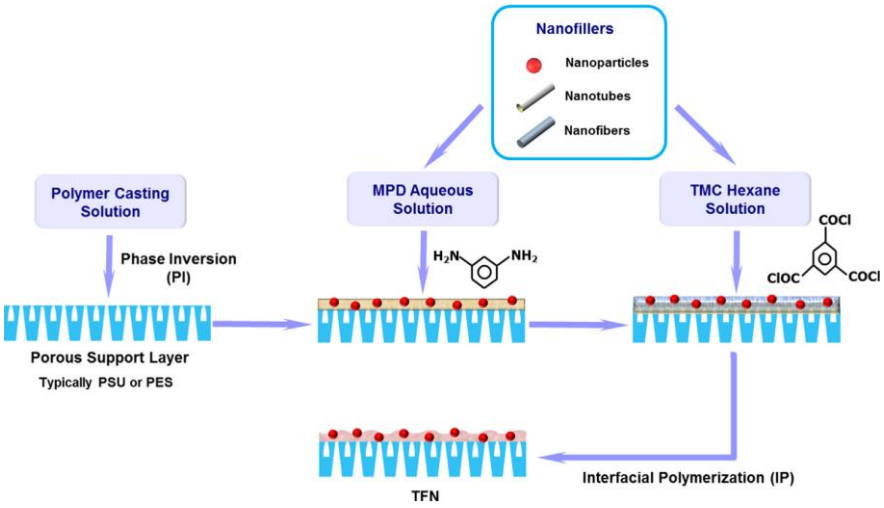

Figure 2.7: Thin film nanocomposite fabrication process. [102]

Table 2.6: Selected TFN membranes, nanofillers used, target dyes and removal efficiencies.

Nanofiller embedded on PA layer	Dye	Operational conditions	Rejection (%)	References
EBAX®1657/chitosan-wrapped multiwalled carbon nanotubes	malachite green	2 bar; concentration = 30 mg/L; 1 wt% and 0.1 wt% CWNT	~98.7	105
Zr-MOFs (PVP-UiO-66-NH_2)	congo red; methyl blue; direct red 23; reactive Black 5	0.3 wt%	99.89 ~ 100	106
UiO-66-NH_2 and carbon quantum dots (CQDs)	MB; methyl orange; direct red 23; methyl blue	0.2 wt% of UiO-66-NH_2/CQD	82.23; 96.10; 99.82; 99.66	107
Cellulose nanocrystals	rose bengal; MO; congo red; MB; crystal violet	0.150 wt%	>99	108
AA-functionalized GO	rhodamine B; acid red 1; rose bengal	concentration = 50 ppm	> 98	109
UiO-66-NH_2	malachite green	0.02 wt%; concentration=100 ppm	91.90 ± 3	110

2.5 Selected nanofillers utilized for dye removal

The choice of nanomaterials for dye removal is pivotal as they enhance various properties such as selectivity, hydrophilicity, and physico-chemical characteristics. Graphene oxide and cellulose nanocrystals stand out as promising nanomaterials. The next sections delve

into the benefits of these nanomaterials, as well as their fabrication and application in dye removal.

2.5.1 Graphene oxide (GO) based nanomaterials

GO is a 2-dimensional nanomaterial consisting of a single layer of carbon atoms organized in a hexagonal pattern, similar to a structure of honeycomb, with sp^2 hybridization (**Figure 2.8**).[111,112] Graphene oxide, an oxidized form of graphene contains epoxy, hydroxyl, ketones and carboxyl groups which are linked to its high negative charge and hydrophilicity.[113,114] It has numerous advantages including its large surface area (specific area ~ 2600 m^2g^{-1}) since it conserves the basic framework of graphene, outstanding mechanical, thermal and electrical properties.[115–118] Graphene oxide has a high affinity for contaminants and is considered to be a promising adsorbent owing to its large surface area, hydrophilicity, high negative charge density, surface hydrophobic $\pi - \pi$ interaction and abundant nature of graphite.[114]

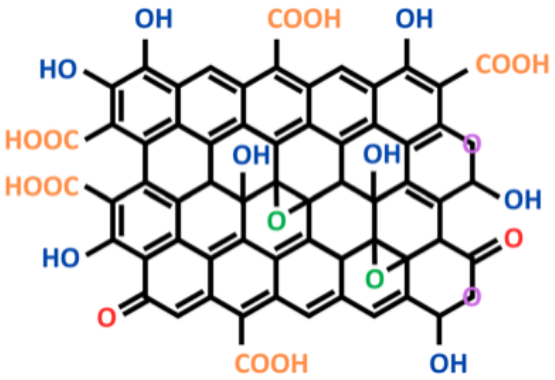

Figure 2.8: Chemical structure of Graphene oxide.[119]

Preparation of GO is via two steps: oxidation of graphite and the exfoliation of graphite oxide as shown in **Figure 2.9**.[120] There are several methods of preparation such as Hummers, Brodies, Staudenmaiers and Hoffmans. The derivatives of Hummers method are prominently used due to the higher yield, more organized structure of graphene and no production of toxic gas.[121] Improved Hummers method involves the use of mixed acids (H_2SO_4/H_3PO_4, 9:1) and a strong oxidizing agent, $KMnO_4$.[121]

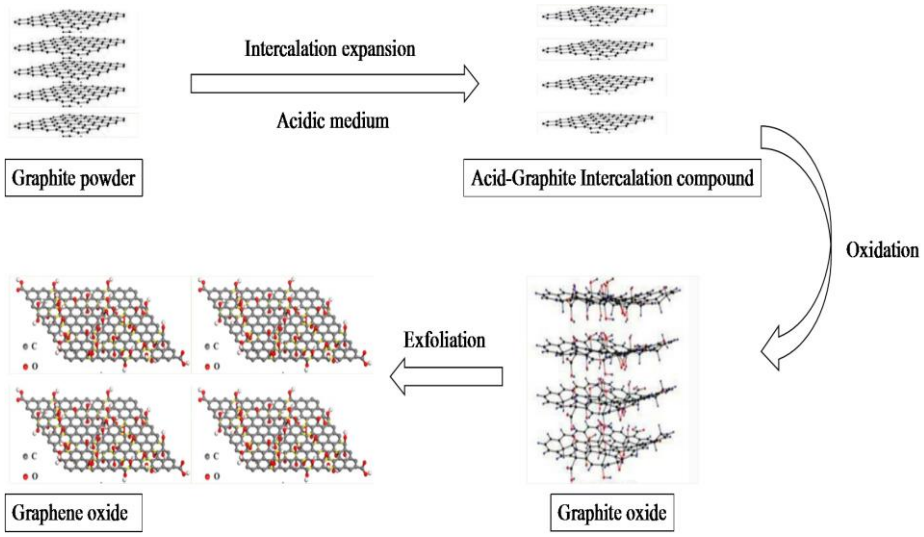

Figure 2.9: Schematic representation of GO preparation process.[120]

Outstanding perfomances have been reported on the application of GO and its derivatives in energy conversion and storage, sensors, electrochemistry, photocatalysis and water purification processes (i.e. membrane technology). In filtration membrane processes, the stacking of GO makes it possible to have an increased water passage and rejection of contaminants in GO membranes through size exclusion, electrostatic interactions and ion adsorption as portrayed in **Figure 2.10**.[122] Water molecules (H_2O) are typically stable and neutral but can form hydronium (H_3O^+) or hydroxide (OH^-) ions in acidic or basic conditions through proton transfer. Dye molecules also change their charge depending on the solution's pH. Since water molecules are small and neutral, they easily pass through the membrane. In contrast, charged ions are surrounded by hydration shells, making them larger and less permeable. Electrostatic interactions between membranes and dye molecules based on their charges affect dye adsorption, aggregation, and overall membrane separation efficiency and fouling.

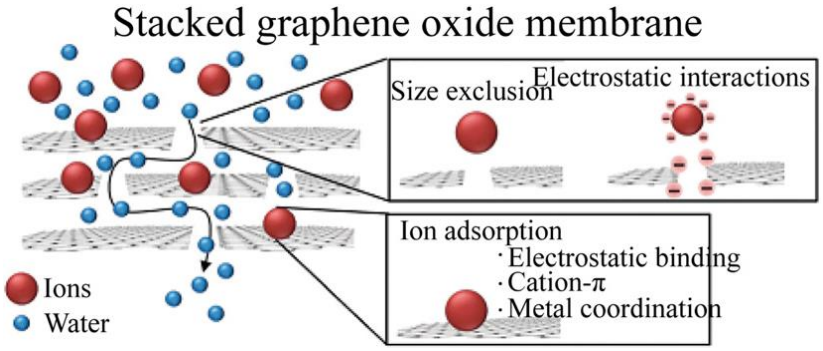

Figure 2.10: Flow of water in GO membrane systems.[122]

There have been several reports on the use of GO based membranes in water for dye rejection (**Table 2.7**). Zhao et al. (2019) explored the effects of GO quantum dots on membrane performance.[123] Graphene oxide quantum dots were introduced into the TFN PA layer via surface coating, and membrane rejection against methyl orange (MO) and methylene blue (MB) was assessed.[123] MO rejection increased from 89.2 to 97% after PA

layer modification with graphene oxide quantum dots due to electrostatic repulsion. However, there was a decrease in MB rejection (75.4 – 71%), which was caused by the adsorption of positively charged MB onto the membrane, reducing water flux and rejection.[123] However, two major challenges impede the implementation of GO-functionalized membranes in water treatment to date. Agglomeration of GO at high concentrations affects membrane performance and also decreases the membranes hydrophilicity and water flux. Secondly, the stacking of the GO nanosheets limits the passage of water through the membrane thus reducing its permeability.[124–126] To enhance the membrane performance, it is crucial to address these issues by modifying GO nanosheets by attaching various functional groups prior to membrane fabrication. Seah et al. (2022) investigated the effects of modified GO TFN membranes on salt/dye removal.[127] Accordingly, the PA layer was prepared using a mist-based IP approach in order to fabricate TFN membrane with improved characteristics. GO was modified with acrylic acid (AA) via plasma-enhanced chemical vapor deposition. The acrylic acid-modified GO increased the pure water permeability (PWP) of the TFN membrane by 6.6%, resulting in a PWP of 11.34 L/m^{2}h·bar compared to the control GO TFN. These membranes were comparatively assessed for Rhodamine B, Acid Red, and Rose Bengal dye rejection, achieving rejection rates of more than 98%.[127]

Table 2.7: GO membrane systems, dye, testing conditions and removal efficiency.

Membrane	Nanocomposite	Dye	Testing conditions	Removal (%)	References
TFN	triethylenetetramine-modified graphene oxide (GO-TETA)	direct red; congo red	6 bar; 50 ppm	99.6	128
TFN	GO	congo red; brilliant yellow; crystal violet; disperse blue 1	6 bar; 10 ppm GO solution; Dye concentration = 50 ppm	99.82; 99.02; 98.99; 99.97	129
TFN	chitosan-tailored graphene oxide (CSGO)-embedded poly(ether-b-amide)	malachite green	2 bar; 0.1 -1 wt%	98.54 99.63	130
Nanocomposite membrane (PVDF)	GO	MB; rhodamine B; crystal violet; MO; reactive red; eosin Y	concentration =100 ppm	~99	131
MF membranes (PES)	GO/PEI	blue corazol	3 bar; 10 ppm; pH = ~6	97.8	132
NF	magnetic graphene oxide/metformin hybrid	direct red 16	4 bar; 0.5 wt% MMGO; concentration =30 mg/L	~99	133

Mixed matrix membranes (UF)	(MMGO) GO nanoparticles	acid black; rose bengal	3 bar; 0.5 wt% GO; pH = ~5; concentration = 50 ppm	~99	53
MF membrane	isophorone diisocyanate modified of GO	MB; MO; rhodamine B; congo red	1 bar; pH = 7	98.5; 97.7; 96.1; 99.3	134

2.5.1.1 Graphene oxide based aerogels

Aerogels are a category of three-dimensional light materials distinguished by an extremely porous, air-filled structure with high specific surface area, thermal conductivity and low density.[135] Aerogels can be generated from a range of materials, including inorganic, organic, and hybrid molecular starting materials, allowing for a variety of morphologies with different dimensions and pore size distributions.[135,136] Apart from aerogels made of a single substance, the fabrication of composites made of various substances is intriguing because it offers the opportunity to modify and enhance the characteristics of aerogels, such as their mechanical resistance, water affinity, and performance to suit specific uses.[137–139] Due to their special properties, aerogels are attractive for a number of applications, such as packaging, energy storage, thermal insulation, drug delivery, and catalysis.[136] Additionally, due to their remarkable adsorption capacity, aerogels have emerged as one of the greatest adsorbents for eliminating contaminants from both air and water.[140]

Aerogels have been seen to be easily recyclable, are chemically and physically stable in water and have high adsorptive capacity.[141,142] This makes them a promising adsorption candidate for wastewater purification. Pharmaceuticals, dyes, oils and solvents, heavy metals, and radioactive elements are just a few of the contaminants that aerogels have been effectively employed to remove.[143–150] The three steps involved in developing aerogel are gel formation, solvent exchange, and drying. During gel formation, the aerogel's shape is established. This procedure also makes it possible to determine the aerogel's microstructure.[151] For the aerogel to maintain its shape, solvent exchange and drying procedures are crucial. Supercritical conditions or low pressure and a temperature below the melting point (freeze-drying) are two possible methods for the drying process.[151] Although several types of aerogels have been presented so far for the treatment of air and water, the most widely used ones are those based on cellulose, chitosan, GO, and silica.[152]

The most popular 3D graphene structures are GO-based aerogels, which have remarkable qualities like light weight, high surface area, electrical conductivity, superior mechanical and thermal resistance, and adsorption capacity. Due to GO's vast surface area and abundance of oxygenated groups, this material has the capacity to remove pollutants from wastewater. The direct use of GO sheets to remove pollutants is, however, restricted by an array of reasons. First, due to its strong planar interactions, it tends to aggregate layer by layer, which may reduce its adsorption capacity; second, the oxygenated groups of GO are not very stable when they coordinate with pollutants; and lastly, the insufficient groups needed to achieve adsorption on the aerogel's surface make it difficult to achieve targeted adsorption, which further restricts its range of use.[135,153,154] Thus, it is crucial to

functionalize the nanomaterials to increase contaminant capture.[155] **Table 2.8** displays various GO aerogels efficiency in removing dyes from water.

Table 2.8: Comparison of adsorption capacities of different GO based aerogels.

Aerogel type	Dyes	Best fitted isotherm and model	Maximum adsorption capacity, Qe (mg/g)	References
GO/poly(ethyleneimine)	MO	pseudo-second-order	331.0; 249.6	156
Partly reduced GO aerogels induced by proanthocyanidins	MB	Langmuir, pseudo-second-order	460.83	157
Cellulose nanofibers (CNFs) /GO	MB	pseudo-second-order	9.94	158
Biologically reduced GO/poly(vinyl alcohol)	MB;	Langmuir	135.17	159
	congo red	Freundlich	134.24	
GO doped silica	acid green 25; crystal violet	Langmuir, pseudo-second-order	20.56; 41.46	160
Tannic acid (TA)-GO, acrylic acid (AA) and sodium p-styrenesulfonate (SSS)	MB	Langmuir, quasi-second-order	1782.5	161
alginate/ graphene aerogel	MB; neutral red	Langmuir, pseudo-second-order	1091.9; 813.2	162

2.5.2 Cellulose and cellulosic materials

The utilization of cellulosic materials for the removal of pollutants such as dyes, heavy metals and oil in water has been gladly received. Cellulose is a natural, widely available organic polymer available on earth.[163] It is generally found in cell walls of numerous plants and in a diverse set of living organisms i.e. fungi, bacteria, algae, and tunicates. Cellulose is a tough, water insoluble and a fibrous polymer that serves a key function in maintaining the plants cell wall structure.[164] It is also a biocompatible, biodegradable and renewable polymer that has a broad spectrum of application in environmental engineering.[165] It is made up of a linear homopolysaccharide comprising of β-1,4-linked glucopyranose units.[165] The focus of researchers has shifted to the use of cellulose nanocrystals (CNCs) owing to its attractive features i.e. outstanding mechanical strength, high specific surface area, wide availability, renewability, ease of modification, biocompatibility and biodegradability.[166,167] Cellulose nanocrystals are rigid, rod shaped nanomaterials derived from cellulose with an average diameter of ~10 nm and a length of ~100 nm depending on the cellulose source.[168] Strong acid driven hydrolysis results in CNCs, with sulfuric acid as the most utilized acid, which selectively degenerates the amorphous regions of the cellulose resulting in nanoparticles with high uniformity and crystallinity.[165,169] The carboxylic groups on the CNC renders the molecule hydrophilic. Though, the packing of

the cellulose chains within CNC particles can sometimes lead to a hydrophobic crystal plane which results in amphiphilic properties as such these nanomaterials are able to stabilize foams and emulsions.[165] Several researchers have reported on the utilization of cellulose based materials in the elimination of dyes in aqueous medium.[170–176] Bai et al. (2019) investigated membrane performance following the incorporation of CNCs (0.005 - 0.200 wt%) in polyamide layer generated via interfacial polymerization in TFC membranes.[177] The developed membranes demonstrated excellent divalent salt rejection (98%) and 97.5% for $MgSO_4$ and Na_2SO_4.[177] The membranes also demonstrated superior dye removal (rose bengal, congo red, crystal violet, methyl orange, and methylene blue), with the 0.150 wt% CNC membrane surpassing the others with 99.0% removal for all dyes.[177]

2.5.3 Modification of GO and CNC surfaces

Despite being shown to increase membrane performance, the aggregation of GO and CNCs continues to hinder their broader application in water treatment membranes.[135,153–155,178,179] Modification of GO/CNCs to overcome these shortcomings is crucial, since it also enhances water permeability, dye removal, thermal and mechanical stabilities, and antifouling properties. One of the strategies that can be explored is polymerization that involves taking advantage of GOs surface located oxygenated functional groups to increase interlayer spacing of the GO sheets which also allows for holding together of the sheets.

The abundance of carboxylic groups on CNCs make surface modification possible thus the CNCs interaction with surroundings is altered.[180] Surface modification such as polymer grafting endows the CNC molecule with either positive or negative electrostatic charges and also enhances compatibility in hydrophobic polymer matrixes.[165] Depending on the type of monomer used to form polymer brushes, the tuning of the materials hydrophilicity, stimuli-responsiveness, colloidal stability, adhesive and rheological behavior is allowed.[181]

2.6 Polymer brushes

Polymer brushes refer to a class of polymeric macromolecular materials that have abundant polymer chains either anchored at one end or to a substrate through its backbone.[182] Polymer chains can either be grafted to a polymer backbone or to an inorganic or organic surface material and these polymer brushes are formed at high grafting densities (i.e chains/nm^2).[182,183] Thus, polymer chains extend out from the interface owing to excluded volume interactions and the space between the chains is smaller than the polymers radius of gyration.[184–186] Polymer brush height range is usually 10 – 100 nm.[187] The architecture, chemical configuration, thickness, responsiveness to external stimuli and density owes to their potential applications in numerous research fields, which can be tuned down to nanoscale due to their ease in preparation.[188–190] The presence of polymer brushes traditionally have been used to tailor membrane surface wettability, biocompatibility, and corrosion resistance due to their mechanical and chemical robustness.[188,191] Surface grafting of hydrophilic polymer brushes helps increase antifouling properties, repel the adsorption of nonspecific proteins and microorganisms.[192–194] The use of films

functionalized with polymer brushes has potential application prospects in the fields of separation, antifouling studies, drug delivery, sensors and catalysis.[188,195] Polymer brushes have abundant functional groups per strand, therefore can be used to increase contaminant capture of adsorbents.

Polymer brushes are classified as either homo-, mixed homo-, random copolymer and block copolymer brushes based on their chemical composition (**Figure 2.11**).[196] Homopolymer brushes have same repeating polymer chains, mixed homopolymer brushes have a combination of two or more homopolymer brushes grafted on the same surface.[196] With random copolymer brushes, there is a random polymerization of two or more differing monomers forming the polymer chains and lastly, block copolymer brushes consist of different units of homopolymers that are covalently linked together.[196]

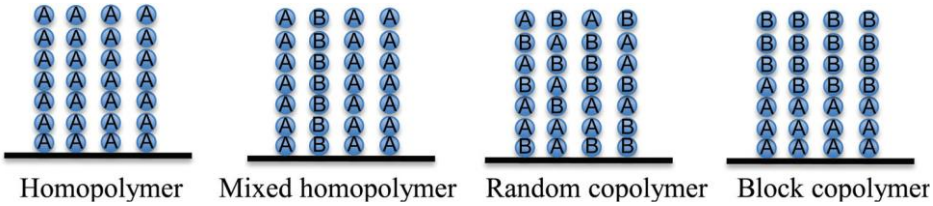

Figure 2.11: Classes of polymer brushes according to their chemical composition.[196]

Surface grafted polymer brushes are also classified based on their morphological/conformational state: pancake or mushroom polymer brushes are formed at low grafting density whilst brush like polymers are formed at high grafting density (**Figure 2.12**).[197] This can also be caused by their molecular weight.

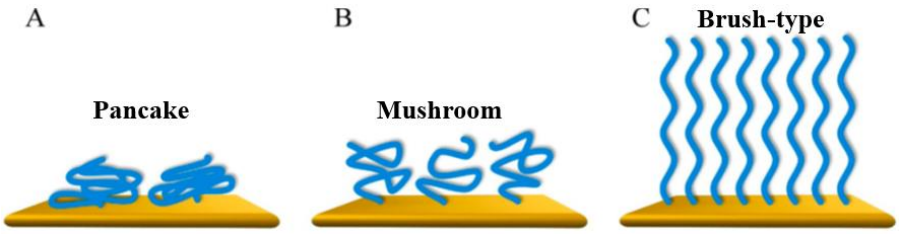

Figure 2.12: Three different categories of conformations of surface-attached polymers. [197]

2.6.1 Synthesis of polymer brushes

There are two approaches by which surfaces can be modified with polymers: Physisorption and chemisorption (**Figure 2.13**). Physisorption is an easy preparation technique that entails the usage of van der Waals forces, electrostatic forces, and, hydrogen bonding to anchor the polymer brushes to the surfaces.[196,198] This suffers from several challenges such as the instability in bonding, reversible adsorption nature and polymer brushes formed are rarely densely grafted.[196]

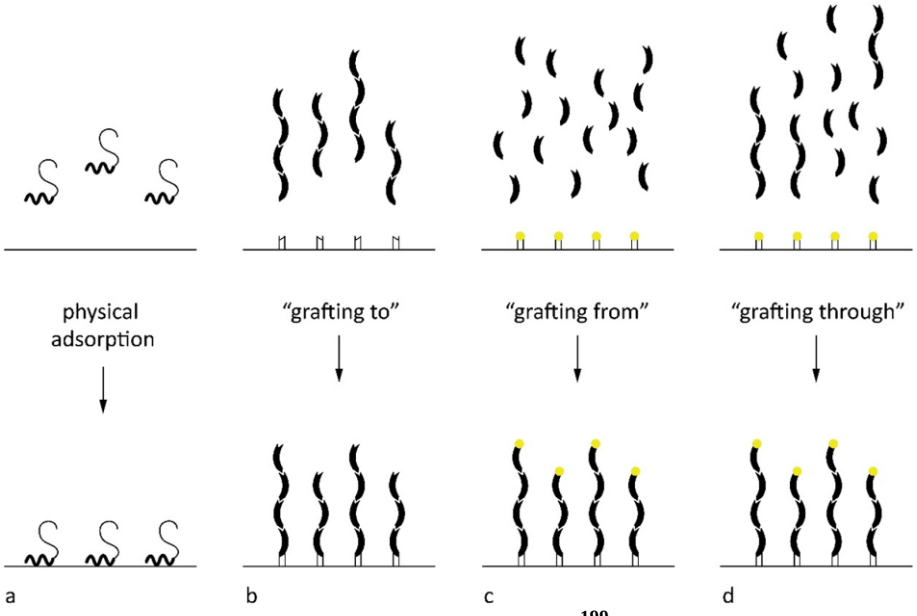

Figure 2.13: Polymer brush fabrication methods.[199]

Chemisorption (or covalent attachment) involves the covalent interaction of the surface and polymers. There are three techniques that are used: grafting to, grafting from and grafting through. The grafting to method entails the surface immobilization of polymers through reactions of (end-) functionalized polymers with corresponding surface functionalities.[200] However, this procedure suffers from shortcomings like increased reaction time, poor grafting densities (surface coverage) owing to the steric effect especially in high molecular weight chains, limited film thickness and unfavorable reactions between the functional groups and surface anchors.[187,200–202] Grafting through process involves anchoring polymer chains to a substrate that has been immobilized with a double bond-containing chemical.[182] In this method, the polymer chains are introduced on the substrate from the backbone.[182] The favored method is the grafting from approach (or surface initiated polymerization, SIP) which involves growing polymer chains on the surface. The initiator molecules are immobilized on the surface, then the polymer layer grows from the surface as monomers are repetitively added to the developing chain (polymerization).[203,204] The polymer chains grow from the surface as they reduce their free energy to form brush-looking polymer chains. This method has several advantages such as control over graft density (high grafting density), architecture and thickness of polymer brushes.[205,206] A number of polymerization techniques exists i.e. atom transfer radical polymerization (ATRP), nitroxide-mediated radical polymerization (NMP), ring-opening polymerization (ROP), and reversible addition fragmentation chain transfer (RAFT) polymerization. The frequently employed SIP is surface initiated-ATRP (SI-ATRP) for the production of homo- and copolymers brushes because it produces well defined polymer brushes, control over polymer growth, easy initiator synthesis and commercially available reagents.[207–210] In this process, the surface of the material is immobilized with the initiator species that initiates the polymerization under specific reaction conditions leading to the formation of polymer brushes.[211–213] Certain parameters have an effect on polymerization of SI-ATRP such as initiator, type of catalyst, monomer concentration, solvent and

ligand.[214] **Figure 2.14** details the grafting polymerization process whereby the activator (i.e. Cu (I) complex) removes the halogen atom from either the immobilized initiator or grown latent chain, resulting in a growing radical, to which additional monomer units are subsequently added till it is capped forming a latent chain.[215] This frequent and random process occurs on the surfaces of halogenated sites, thus the chains grow simultaneously in a controlled manner.[215]

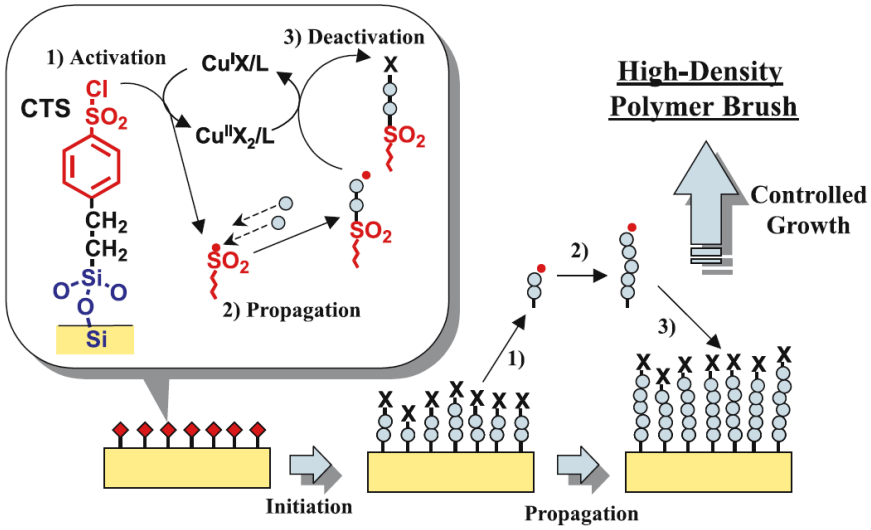

Figure 2.14: SI-ATRP process. [215]

2.6.2 Modification of GO/CNC with polymer brushes

The modification of GO and cellulose with polymers has been vastly studied. [211,216–236] As reported by Lee et al. (2010), GO was modified with methyl methacrylate, styrene, and butyl acrylate via SI-ATRP (**Figure 2.15**).[237] The morphological results revealed that GO and polymers maintained the structural properties observed in unmodified samples.[237] Various techniques such as XPS, solubility tests, Raman spectroscopy confirmed the attachment of the polymers to GO.[237] Functionalization significantly increased the solubility of the resulting materials.[237]

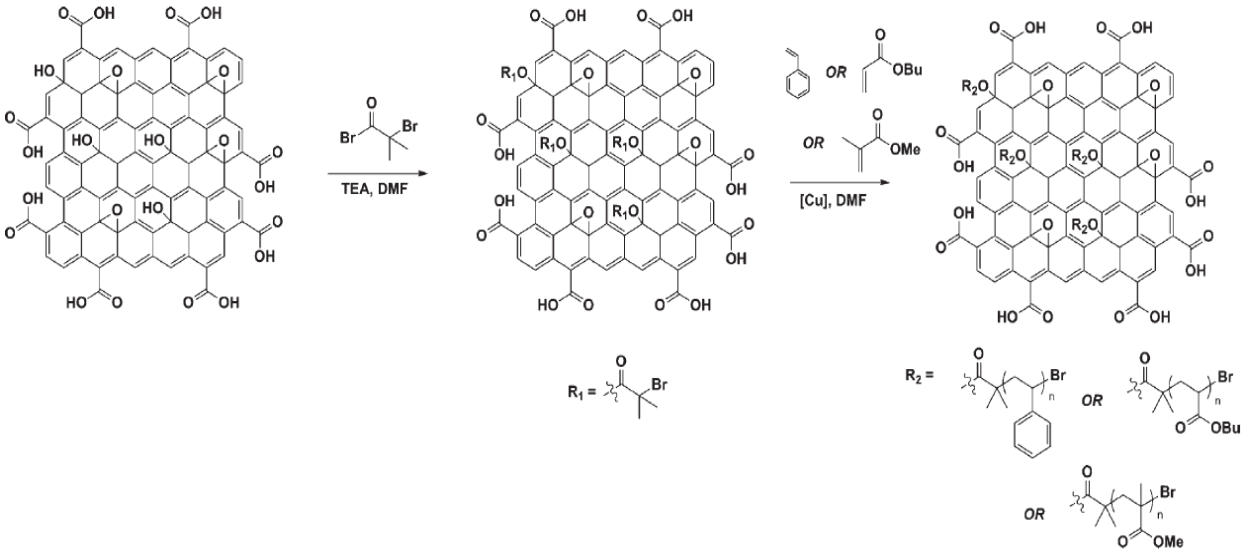

Figure 2.15: Synthesis of surface-functionalized GO via attachment of an ATRP initiator (a-bromoisobutyryl bromide) followed by polymerization of styrene, butyl acrylate, or methyl methacrylate.[237]

2.7 Selected polymers

Of interest to this study are the following polymers: poly (glutamic acid (PGLU), and poly[2-(methacryloyloxy)ethyl] phosphate (PMEP). Poly(glutamic acid) (PGLU) is a linear structured, natural biopolymer, anionic, hydrophilic and non-toxic polypeptide which contains L- and D- glutamic acid units connected by amine bonds.[238,239] It has a high binding affinity toward contaminants and possesses a high molecular weight making it a good candidate in wastewater purification.[239,240] It has two isoforms: poly(γ-glutamic acid), and poly(α-L-glutamic acid), owing to the chemical links between the carboxyl and amino groups as shown on **Figure 2.16**. Poly(α-L-glutamic acid) is produced through the nucleophile-initiated polymerization of the γ-protected *N* -carboxyanhydride derived from L- glutamic acid.[241] The amide bonds form between the α-carboxylic acid and α- amino groups of the L-glutamic acid units, creating peptide bonds similar to those found in proteins.[241] Poly(γ-glutamic acid), however, is produced by bacteria (*Bacillus* species).[242] Studies have detailed its use in medicine, food and wastewater treatment processes.[243–249]

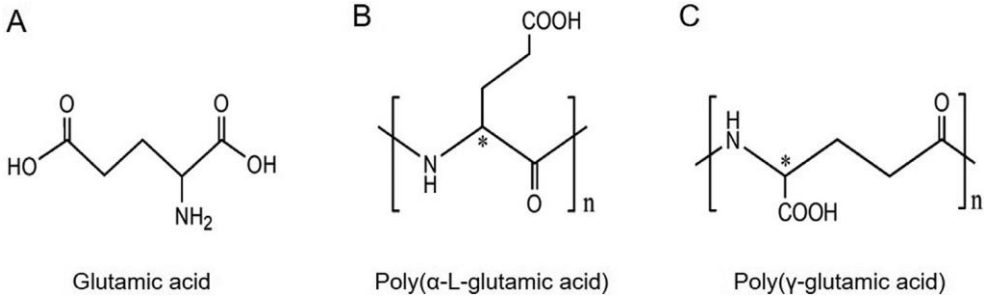

Figure 2.16: Structures of Glutamic acid (A), Poly(α-L-glutamic acid) (B) and Poly(γ-glutamic acid) (C).[241]

Poly[2-(methacryloyloxy)ethyl]phosphate (PMEP) is a hydrophilic polymer that contains phosphorus in its structure and is fabricated through polymerization (i.e. ATRP) using 2-(methacryloyloxy)ethyl phosphate (MEP) as a monomer (**Figure 2.17**). Phosphorylated polymers are biodegradable, biocompatible, pH and temperature-sensitive, catalytically active, possess ion-exchange and complexing abilities.[250,251]

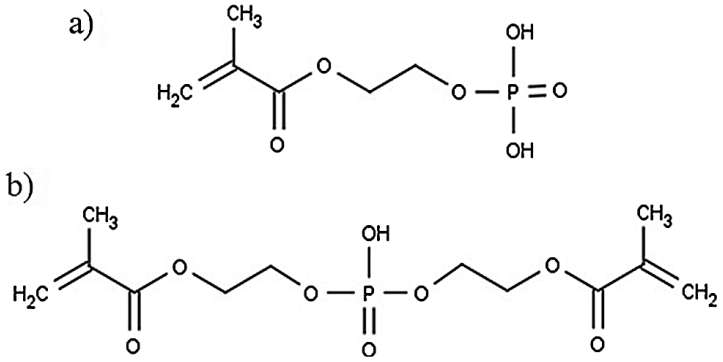

Figure 2.17: Chemical structures of 2-(methacryloyloxy)ethyl phosphate (a) and bis[2-(methacryloyloxy)ethyl] phosphate (b) monomers.[250]

2.8 Conclusion

The reviewed literature covers the issue of dye toxicity in wastewater and explores feasible water remediation solutions, with a focus on membrane technology. Dyes are major pollutants that endanger aquatic ecosystems and human health, needing effective treatment solutions. TFN membranes outperform standard membranes due to the integration of nanofillers such as graphene oxide (GO) and cellulose nanocrystals (CNCs). These materials boost membrane flux, selectivity, and antifouling qualities while retaining high dye rejection rates. This section further highlights the significant role of SI-ATRP in modifying nanofillers to effectively enhance membrane performance, underscoring its importance in advancing membrane technology. TFN membranes with enhanced nanofillers and unique modification techniques offer potential alternatives for successful dye removal in wastewater treatment, paving the path for more environmentally friendly water management practices.

References:

1. Khan MD, Singh A, Khan MZ, Tabraiz S, Sheikh J. Current perspectives, recent advancements, and efficiencies of various dye-containing wastewater treatment technologies. *J Water Process Eng*. 2023;53(December 2022):103579. doi:10.1016/j.jwpe.2023.103579
2. Affat SS. Classifications, Advantages, Disadvantages, Toxicity Effects of Natural and Synthetic Dyes: A review. *Univ Thi-Qar J Sci*. 2008;8(1):130-135. http://doi.org/10.32792/utq/utjsci/v8/1/21
3. Dutta P, Razaya Rabbi M, Sufian MA, Mahjebin S. Effects of textile dyeing effluent on the environment and its treatment: A review. *Eng Appl Sci Lett*. 2022;5(1):1-17. doi:10.30538/psrp-easl2022.0080
4. Silveira E, Marques PP, Silva SS, Lima-Filho JL, Porto ALF, Tambourgi EB. Selection of Pseudomonas for industrial textile dyes decolourization. *Int Biodeterior Biodegrad*. 2009;63(2):230-235. doi:10.1016/j.ibiod.2008.09.007
5. Al-Tohamy R, Ali SS, Li F, et al. A critical review on the treatment of dye-containing wastewater: Ecotoxicological and health concerns of textile dyes and possible remediation approaches for environmental safety. *Ecotoxicol Environ Saf*. 2022;231:113160. doi:10.1016/j.ecoenv.2021.113160
6. Katheresan V, Kansedo J, Lau SY. Efficiency of various recent wastewater dye removal methods: A review. *J Environ Chem Eng*. 2018;6(4):4676-4697. doi:10.1016/j.jece.2018.06.060
7. Alsukaibi AKD. Various Approaches for the Detoxification of Toxic Dyes in Wastewater. *Processes*. 2022;10(10). doi:10.3390/pr10101968
8. EL-SADAAWY MM, AGIB NS. Removal of Textile dyes by ecofriendly aquatic plants From wastewater: A review on Plants Species, Mechanisms, and Perspectives. *Blue Econ*. 2024;2(2). doi:10.57241/2805-2994.1023
9. Carney Almroth B, Cartine J, Jönander C, et al. Assessing the effects of textile leachates in fish using multiple testing methods: From gene expression to behavior. *Ecotoxicol Environ Saf*. 2021;207(July 2020). doi:10.1016/j.ecoenv.2020.111523
10. Berradi M, Hsissou R, Khudhair M, et al. Textile finishing dyes and their impact on aquatic environs. *Heliyon*. 2019;5(11). doi:10.1016/j.heliyon.2019.e02711
11. Zheng X, Fu D, Cheng J, et al. Effects of hypoxic stress and recovery on oxidative stress, apoptosis, and intestinal microorganisms in Pelteobagrus vachelli. *Aquaculture*. 2021;543(December 2020):736945. doi:10.1016/j.aquaculture.2021.736945
12. Arshad H, Imran M, Ashraf M. Toxic effects of Red-S3B dye on soil microbial activities, wheat yield, and their alleviation by pressmud application. *Ecotoxicol Environ Saf*. 2020;204(July):111030. doi:10.1016/j.ecoenv.2020.111030
13. Zhu X, Chen J, Qiu K, Kuai B. Phytohormone and light regulation of chlorophyll degradation. *Front Plant Sci*. 2017;8(November):1-8. doi:10.3389/fpls.2017.01911
14. Ramamurthy K, Priya PS, Murugan R, Arockiaraj J. Hues of risk: investigating genotoxicity and environmental impacts of azo textile dyes. *Environ Sci Pollut Res*. 2024;31(23):33190-33211. doi:10.1007/s11356-024-33444-1

15. Tounsadi H, Metarfi Y, Taleb M, El Rhazi K, Rais Z. Impact of chemical substances used in textile industry on the employee's health: Epidemiological study. *Ecotoxicol Environ Saf*. 2020;197(December 2019):110594. doi:10.1016/j.ecoenv.2020.110594
16. Kathing C, Saini G. A Review of Various Treatment Methods for the Removal of Dyes from Textile Effluent. *Recent Prog Mater*. 2022;04(04):1-15. doi:10.21926/rpm.2204028
17. Singh Z, Chadha P. Textile industry and occupational cancer. *J Occup Med Toxicol*. 2016;11(1):1-6. doi:10.1186/s12995-016-0128-3
18. Shabir M, Yasin M, Hussain M, et al. A review on recent advances in the treatment of dye-polluted wastewater. *J Ind Eng Chem*. 2022;112:1-19. doi:10.1016/j.jiec.2022.05.013
19. Slama H Ben, Bouket AC, Pourhassan Z, et al. Diversity of synthetic dyes from textile industries, discharge impacts and treatment methods. *Appl Sci*. 2021;11(14):1-21. doi:10.3390/app11146255
20. Hayat H, Mahmood Q, Pervez A, Bhatti ZA, Baig SA. Comparative decolorization of dyes in textile wastewater using biological and chemical treatment. *Sep Purif Technol*. 2015;154:149-153. doi:10.1016/j.seppur.2015.09.025
21. Khan MD, Singh A, Khan MZ, Tabraiz S, Sheikh J. Current perspectives, recent advancements, and efficiencies of various dye-containing wastewater treatment technologies. *J Water Process Eng*. 2023;53(February):103579. doi:10.1016/j.jwpe.2023.103579
22. Kumari S, Singh R, Jahangeer J, Garg MC. Innovative Strategies for Dye Removal from Textile Wastewater : A Comprehensive Review of Treatment Approaches and Challenges. *Water, Air, Soil Pollut*. Published online 2024:1-29. doi:10.1007/s11270-024-07532-4
23. Vijayaraghavan K, Yun YS. Utilization of fermentation waste (Corynebacterium glutamicum) for biosorption of Reactive Black 5 from aqueous solution. *J Hazard Mater*. 2007;141(1):45-52. doi:10.1016/j.jhazmat.2006.06.081
24. Bayramoğlu G, Yakup Arica M. Biosorption of benzidine based textile dyes "Direct Blue 1 and Direct Red 128" using native and heat-treated biomass of Trametes versicolor. *J Hazard Mater*. 2007;143(1-2):135-143. doi:10.1016/j.jhazmat.2006.09.002
25. Padmesh TVN, Vijayaraghavan K, Sekaran G, Velan M. Biosorption of Acid Blue 15 using fresh water macroalga Azolla filiculoides: Batch and column studies. *Dye Pigment*. 2006;71(2):77-82. doi:10.1016/j.dyepig.2005.06.003
26. Neifar M, Chouchane H, Mahjoubi M, Jaouani A, Cherif A. Pseudomonas extremorientalis BU118: a new salt-tolerant laccase-secreting bacterium with biotechnological potential in textile azo dye decolourization. *3 Biotech*. 2016;6(1):1-9. doi:10.1007/s13205-016-0425-7
27. Tan L, He M, Song L, Fu X, Shi S. Aerobic decolorization, degradation and detoxification of azo dyes by a newly isolated salt-tolerant yeast Scheffersomyces spartinae TLHS-SF1. *Bioresour Technol*. 2016;203:287-294. doi:10.1016/j.biortech.2015.12.058

28. Tan L, Li H, Ning S, Xu B. Aerobic decolorization and degradation of azo dyes by suspended growing cells and immobilized cells of a newly isolated yeast Magnusiomyces ingens LH-F1. *Bioresour Technol*. 2014;158:321-328. doi:10.1016/j.biortech.2014.02.063
29. Waghmode TR, Kurade MB, Govindwar SP. Time dependent degradation of mixture of structurally different azo and non azo dyes by using Galactomyces geotrichum MTCC 1360. *Int Biodeterior Biodegrad*. 2011;65(3):479-486. doi:10.1016/j.ibiod.2011.01.010
30. Pandi A, Marichetti Kuppuswami G, Numbi Ramudu K, Palanivel S. A sustainable approach for degradation of leather dyes by a new fungal laccase. *J Clean Prod*. 2019;211:590-597. doi:10.1016/j.jclepro.2018.11.048
31. Solayman HM, Hossen MA, Abd Aziz A, et al. Performance evaluation of dye wastewater treatment technologies: A review. *J Environ Chem Eng*. 2023;11(3):109610. doi:10.1016/j.jece.2023.109610
32. Fatima M, Farooq R, Lindström RW, Saeed M. A review on biocatalytic decomposition of azo dyes and electrons recovery. *J Mol Liq*. 2017;246:275-281. doi:10.1016/j.molliq.2017.09.063
33. Gadekar MR, Ahammed MM. Coagulation/flocculation process for dye removal using water treatment residuals: modelling through artificial neural networks. *Desalin Water Treat*. 2016;57(55):26392-26400. doi:10.1080/19443994.2016.1165150
34. Moussavi G, Mahmoudi M. Degradation and biodegradability improvement of the reactive red 198 azo dye using catalytic ozonation with MgO nanocrystals. *Chem Eng J*. 2009;152(1):1-7. doi:10.1016/j.cej.2009.03.014
35. Wu J, Gao H, Yao S, Chen L, Gao Y, Zhang H. Degradation of Crystal Violet by catalytic ozonation using Fe/activated carbon catalyst. *Sep Purif Technol*. 2015;147:179-185. doi:10.1016/j.seppur.2015.04.022
36. Šíma J, Hasal P. Photocatalytic degradation of textile dyes in aTiO2/UV system. *Chem Eng Trans*. 2013;32(1999):79-84. doi:10.3303/CET1332014
37. Jorfi S, Barzegar G, Ahmadi M, et al. Enhanced coagulation-photocatalytic treatment of Acid red 73 dye and real textile wastewater using UVA/synthesized MgO nanoparticles. *J Environ Manage*. 2016;177:111-118. doi:10.1016/j.jenvman.2016.04.005
38. Mbacké MK, Kane C, Diallo NO, et al. Electrocoagulation process applied on pollutants treatment- experimental optimization and fundamental investigation of the crystal violet dye removal. *J Environ Chem Eng*. 2016;4(4):4001-4011. doi:10.1016/j.jece.2016.09.002
39. Zuorro A, Lavecchia R. Evaluation of UV/H2O2 advanced oxidation process (AOP) for the degradation of diazo dye Reactive Green 19 in aqueous solution. *Desalin Water Treat*. 2014;52(7-9):1571-1577. doi:10.1080/19443994.2013.787553
40. Valli Nachiyar C, Rakshi AD, Sandhya S, Britlin Deva Jebasta N, Nellore J. Developments in treatment technologies of dye-containing effluent: A review. *Case Stud Chem Environ Eng*. 2023;7(March):100339. doi:10.1016/j.cscee.2023.100339

41. Dutta S, Gupta B, Srivastava SK, Gupta AK. Recent advances on the removal of dyes from wastewater using various adsorbents: A critical review. *Mater Adv*. 2021;2(14):4497-4531. doi:10.1039/d1ma00354b
42. Jedynak K, Wideł D, Rędzia N. Removal of rhodamine b (A basic dye) and acid yellow 17 (an acidic dye) from aqueous solutions by ordered mesoporous carbon and commercial activated carbon. *Colloids and Interfaces*. 2019;3(1). doi:10.3390/colloids3010030
43. Arora C, Kumar P, Soni S, Mittal J, Mittal A, Singh B. Efficient removal of malachite green dye from aqueous solution using curcuma caesia based activated carbon. *Desalin Water Treat*. 2020;195:341-352. doi:10.5004/dwt.2020.25897
44. Fabryanty R, Valencia C, Soetaredjo FE, et al. Removal of crystal violet dye by adsorption using bentonite – alginate composite. *J Environ Chem Eng*. 2017;5(6):5677-5687. doi:10.1016/j.jece.2017.10.057
45. Waly AI, Khedr MA, Ali HM, Riad BY, Ahmed IM. Synthesis and characterization of ion exchanger based on waste cotton for dye removal from wastewater. *Egypt J Chem*. 2019;62(3):451-468. doi:10.21608/EJCHEM.2018.4885.1435
46. Hairom NHH, Mohammad AW, Kadhum AAH. Effect of various zinc oxide nanoparticles in membrane photocatalytic reactor for Congo red dye treatment. *Sep Purif Technol*. 2014;137:74-81. doi:10.1016/j.seppur.2014.09.027
47. Nazari P, Setayesh SR. Effective degradation of Reactive Red 195 via heterogeneous electro-Fenton treatment: theoretical study and optimization. *Int J Environ Sci Technol*. 2019;16(10):6329-6346. doi:10.1007/s13762-018-2048-5
48. Osman AI, Chen Z, Elgarahy AM, et al. Membrane Technology for Energy Saving: Principles, Techniques, Applications, Challenges, and Prospects. *Adv Energy Sustain Res*. 2024;5(5). doi:10.1002/aesr.202400011
49. Suhalim NS, Kasim N, Mahmoudi E, et al. Rejection Mechanism of Ionic Solute Removal by Nanofiltration Membranes: An Overview. *Nanomaterials*. 2022;12(3). doi:10.3390/nano12030437
50. Mosikatsi BE, Mabuba N, Malinga SP. Thin film composite membranes consisting of hyperbranched polyethylenimine (HPEI)-cysteamine layer for cadmium removal in water. *J Water Process Eng*. 2018;(July):0-1. doi:10.1016/j.jwpe.2018.10.004
51. Roberge H, Moreau P, Couallier E, Abellan P. Determination of the key structural factors affecting permeability and selectivity of PAN and PES polymeric filtration membranes using 3D FIB/SEM. *J Memb Sci*. 2022;653(March):120530. doi:10.1016/j.memsci.2022.120530
52. He M, Zhang S, Su Y, Zhang R, Liu Y, Jiang Z. Manipulating membrane surface porosity and pore size by in-situ assembly of Pluronic F127 and tannin. *J Memb Sci*. 2018;556(March):285-292. doi:10.1016/j.memsci.2018.03.087
53. Kadhim RJ, Al-Ani FH, Al-Shaeli M, Alsalhy QF, Figoli A. Removal of dyes using graphene oxide (Go) mixed matrix membranes. *Membranes (Basel)*. 2020;10(12):1-24. doi:10.3390/membranes10120366
54. Lim YJ, Lee SM, Wang R, Lee J. Emerging materials to prepare mixed matrix membranes for pollutant removal in water. *Membranes (Basel)*. 2021;11(7):1-25.

doi:10.3390/membranes11070508

55. Liao Y, Loh CH, Tian M, Wang R, Fane AG. Progress in electrospun polymeric nanofibrous membranes for water treatment: Fabrication, modification and applications. *Prog Polym Sci*. 2018;77:69-94. doi:10.1016/j.progpolymsci.2017.10.003
56. Warsinger DM, Chakraborty S, Tow EW, et al. A review of polymeric membranes and processes for potable water reuse. Published online 2018. doi:10.1016/j.progpolymsci.2018.01.004.A
57. Al Aani S, Mustafa TN, Hilal N. Ultrafiltration membranes for wastewater and water process engineering: A comprehensive statistical review over the past decade. *J Water Process Eng*. 2020;35(March):101241. doi:10.1016/j.jwpe.2020.101241
58. Selatile MK, Ray SS, Ojijo V, Sadiku R. Recent developments in polymeric electrospun nanofibrous membranes for seawater desalination. *RSC Adv*. 2018;8(66):37915-37938. doi:10.1039/C8RA07489E
59. Zazouli MA, Kalankesh LR. Removal of precursors and disinfection byproducts (DBPs) by membrane filtration from water; a review. *J Environ Heal Sci Eng*. 2017;15(1):1-10. doi:10.1186/s40201-017-0285-z
60. Mohamad SH, Idris MI, Abdullah HZ, Ismail AF. Short review of ultrafiltration of polymer membrane as a self-cleaning and antifouling in the wastewater system. *Adv Mater Res*. 2013;795:318-323. doi:10.4028/www.scientific.net/AMR.795.318
61. Garba MD, Usman M, Mazumder MAJ, Al-Ahmed A, Inamuddin. Complexing agents for metal removal using ultrafiltration membranes: a review. *Environ Chem Lett*. 2019;17(3):1195-1208. doi:10.1007/s10311-019-00861-5
62. Mungray AA, Kulkarni S V., Mungray AK. Removal of heavy metals from wastewater using micellar enhanced ultrafiltration technique: A review. *Cent Eur J Chem*. 2012;10(1):27-46. doi:10.2478/s11532-011-0134-3
63. Abdullah N, Rahman MA, Othman MHD, Jaafar J, Ismail AF. *Membranes and Membrane Processes: Fundamentals*. Elsevier Inc.; 2018. doi:10.1016/B978-0-12-813549-5.00002-5
64. Arora R. Adsorption of heavy metals-a review. *Mater Today Proc*. 2019;18(1):4745-4750. doi:10.1016/j.matpr.2019.07.462
65. Oatley-Radcliffe DL, Walters M, Ainscough TJ, Williams PM, Mohammad AW, Hilal N. Nanofiltration membranes and processes: A review of research trends over the past decade. *J Water Process Eng*. 2017;19(April):164-171. doi:10.1016/j.jwpe.2017.07.026
66. Fu F, Wang Q. Removal of heavy metal ions from wastewaters: A review. *J Environ Manage*. 2011;92(3):407-418. doi:10.1016/j.jenvman.2010.11.011
67. Ezugbe EO, Rathilal S. Membrane technologies in wastewater treatment: A review. *Membranes (Basel)*. 2020;10(5). doi:10.3390/membranes10050089
68. Volkov V V, Federation R, Deville S. *Encyclopedia of Membranes.*; 2016. doi:10.1007/978-3-662-44324-8
69. Muhamad N, Nurfatin S, Mohd N, et al. Journal of Water Process Engineering Composite zeolite hollow fiber membrane for the removal of nickel using forward

osmosis. *J Water Process Eng*. 2021;40(March 2020):101806. doi:10.1016/j.jwpe.2020.101806

70. Liu C, Lei X, Wang L, et al. Investigation on the removal performances of heavy metal ions with the layer-by-layer assembled forward osmosis membranes. *Chem Eng J*. 2017;327:60-70. doi:10.1016/j.cej.2017.06.070
71. Kebria MRS, Jahanshahi M, Rahimpour A. SiO2 modified polyethyleneimine-based nanofiltration membranes for dye removal from aqueous and organic solutions. *Desalination*. 2015;367:255-264. doi:10.1016/j.desal.2015.04.017
72. Zinadini S, Zinatizadeh AA, Rahimi M, Vatanpour V, Zangeneh H, Beygzadeh M. Novel high flux antifouling nanofiltration membranes for dye removal containing carboxymethyl chitosan coated Fe3O4 nanoparticles. *Desalination*. 2014;349:145-154. doi:10.1016/j.desal.2014.07.007
73. Cao XL, Yan YN, Zhou FY, Sun SP. Tailoring nanofiltration membranes for effective removing dye intermediates in complex dye-wastewater. *J Memb Sci*. 2020;595(September 2019). doi:10.1016/j.memsci.2019.117476
74. Agtaş M, Ormancı-Acar T, Keskin B, Türken T, Koyuncu I. Nanofiltration membranes for salt and dye filtration: effect of membrane properties on performances. *Water Sci Technol*. 2021;83(9):2146-2159. doi:10.2166/wst.2021.125
75. Abid MF, Zablouk MA, Abid-Alameer AM. Experimental study of dye removal from industrial wastewater by membrane technologies of reverse osmosis and nanofiltration. *J Environ Heal Sci Eng*. 2012;9(1):1-9.
76. Zhan X, Ge R, Huo T, Lu J, Li J. Highly permeable PA@GO loose nanofiltration membranes enabled by hierarchical transport channels for efficient dye removal. *Chem Eng J*. 2023;476(October):146831. doi:10.1016/j.cej.2023.146831
77. Abdelhamid AE, El-Sayed AA, Khalil AM. Polysulfone nanofiltration membranes enriched with functionalized graphene oxide for dye removal from wastewater. *J Polym Eng*. 2020;40(10):833-841. doi:10.1515/polyeng-2020-0141
78. Yang X, You F, Zhao Y, Bai Y, Shao L. Confinedly Assembling Surface Nanocoating to Manipulate Nanofiltration Membranes for Highly-efficient Dye Removal. *ES Energy Environ*. Published online 2018:106-113. doi:10.30919/esee8c142
79. Yu C, Li H, Zhang X, et al. Polyamide thin-film composite membrane fabricated through interfacial polymerization coupled with surface amidation for improved reverse osmosis performance. *J Memb Sci*. 2018;566(August):87-95. doi:10.1016/j.memsci.2018.09.012
80. Karami P, Khorshidi B, McGregor M, Peichel JT, Soares JBP, Sadrzadeh M. Thermally stable thin film composite polymeric membranes for water treatment: A review. *J Clean Prod*. 2020;250. doi:10.1016/j.jclepro.2019.119447
81. Kadhom M. A review on the polyamide thin film composite (TFC) membrane used for desalination: Improvement methods, current alternatives, and challenges. *Chem Eng Res Des*. 2023;191:472-492. doi:10.1016/j.cherd.2023.02.002
82. Tayel A, Abdelaal AB, Esawi AMK, Ramadan AR. Thin-Film Nanocomposite (TFN) Membranes for Water Treatment Applications: Characterization and

Performance. *Membranes (Basel)*. 2023;13(5):1-25. doi:10.3390/membranes13050477

83. Wen Y, Yuan J, Ma X, Wang S, Liu Y. Polymeric nanocomposite membranes for water treatment: a review. *Environ Chem Lett*. 2019;17(4):1539-1551. doi:10.1007/s10311-019-00895-9
84. Jhaveri JH, Murthy ZVP. A comprehensive review on anti-fouling nanocomposite membranes for pressure driven membrane separation processes. *Desalination*. 2016;379:137-154. doi:10.1016/j.desal.2015.11.009
85. Liu L, Xie X, Qi S, et al. Thin film nanocomposite reverse osmosis membrane incorporated with UiO-66 nanoparticles for enhanced boron removal. *J Memb Sci*. 2019;580(February):101-109. doi:10.1016/j.memsci.2019.02.072
86. Može M, Vajc V, Zupančič M, Golobič I. Hydrophilic and hydrophobic nanostructured copper surfaces for efficient pool boiling heat transfer with water, water/butanol mixtures and novec 649. *Nanomaterials*. 2021;11(12). doi:10.3390/nano11123216
87. Shi Y, Kim K. Fabrication of hydrophilic and hydrophobic membranes inspired by the phenomenon of water absorption and storage of cactus. *Front Mater*. 2022;9(September):1-11. doi:10.3389/fmats.2022.966692
88. Fathizadeh M, Tien HN, Khivantsev K, Song Z, Zhou F. Polyamide / nitrogen-doped graphene oxide quantum dots (N-GOQD) thin film nanocomposite reverse osmosis membranes for high flux desalination. *Desalination*. 2019;451(June 2017):125-132. doi:10.1016/j.desal.2017.07.014
89. Li S, Li C, Su B, Hu MZ, Gao X, Gao C. Amino-functionalized graphene quantum dots (aGQDs) -embedded thin fi lm nanocomposites for solvent resistant nano fi ltration (SRNF) membranes based on covalence interactions. *J Memb Sci*. 2019;588(June):117212. doi:10.1016/j.memsci.2019.117212
90. Ng Z-C, Chong C-Y, Lau W-J, Mustafa K, Ismaila AF. Boron removal and antifouling properties of thin-film nanocomposite membrane incorporating PECVD-modified titanate nanotubes. *J Chem Technol Biotechnol*. 2019;94(November 2018):2772-2782. doi:10.1002/jctb.6044
91. Zhu J, Qin L, Uliana A, et al. Elevated Performance of Thin Film Nanocomposite Membranes Enabled by Modi fi ed Hydrophilic MOFs for Nano fi ltration. Published online 2017. doi:10.1021/acsami.6b14412
92. Lind ML, Ghosh AK, Jawor A, et al. Influence of zeolite crystal size on zeolite-polyamide thin film nanocomposite membranes. *Langmuir*. 2009;25(17):10139-10145. doi:10.1021/la900938x
93. Yin J, Kim ES, Yang J, Deng B. Fabrication of a novel thin-film nanocomposite (TFN) membrane containing MCM-41 silica nanoparticles (NPs) for water purification. *J Memb Sci*. 2012;423-424:238-246. doi:10.1016/j.memsci.2012.08.020
94. Shokrgozar Eslah S, Shokrollahzadeh S, Moini Jazani O, Samimi A. Forward osmosis water desalination: Fabrication of graphene oxide-polyamide/polysulfone thin-film nanocomposite membrane with high water flux and low reverse salt

diffusion. *Sep Sci Technol*. 2018;53(3):573-583. doi:10.1080/01496395.2017.1398261

95. Kim ES, Hwang G, Gamal El-Din M, Liu Y. Development of nanosilver and multi-walled carbon nanotubes thin-film nanocomposite membrane for enhanced water treatment. *J Memb Sci*. 2012;394-395:37-48. doi:10.1016/j.memsci.2011.11.041
96. Rashed AO, Esawi AMK, Ramadan AR. Novel Polysulfone/Carbon Nanotube-Polyamide Thin Film Nanocomposite Membranes with Improved Water Flux for Forward Osmosis Desalination. *ACS Omega*. 2020;5(24):14427-14436. doi:10.1021/acsomega.0c00973
97. Lakhotia SR, Mukhopadhyay M, Kumari P. Separation and Puri fi cation Technology Iron oxide (FeO) nanoparticles embedded thin- fi lm nanocomposite nano fi ltration (NF) membrane for water treatment. *Sep Purif Technol*. 2019;211(September 2018):98-107. doi:10.1016/j.seppur.2018.09.034
98. Wu X, Yang L, Meng F, Shao W, Liu X, Li M. ZIF-8-incorporated thin-film nanocomposite (TFN) nanofiltration membranes : Importance of particle deposition methods on structure and performance. *J Memb Sci*. 2021;632(April):119356. doi:10.1016/j.memsci.2021.119356
99. Lau WJ, Ismail AF, Misdan N, Kassim MA. A recent progress in thin fi lm composite membrane : A review. *DES*. 2012;287:190-199. doi:10.1016/j.desal.2011.04.004
100. Ng ZC, Lau WJ, Matsuura T, Ismail AF. Thin film nanocomposite RO membranes : Review on fabrication techniques and impacts of nanofiller. *Chem Eng Res Des*. 2020;5:81-105. doi:10.1016/j.cherd.2020.10.003
101. Esfahani MR, Aktij SA, Dabaghian Z, et al. Nanocomposite membranes for water separation and purification: Fabrication, modification, and applications. *Sep Purif Technol*. 2019;213(December):465-499. doi:10.1016/j.seppur.2018.12.050
102. Yin J, Deng B. Polymer-matrix nanocomposite membranes for water treatment. *J Memb Sci*. 2015;479:256-275. doi:10.1016/j.memsci.2014.11.019
103. Ghosh AK, Jeong BH, Huang X, Hoek EMV. Impacts of reaction and curing conditions on polyamide composite reverse osmosis membrane properties. *J Memb Sci*. 2008;311(1-2):34-45. doi:10.1016/j.memsci.2007.11.038
104. Ghaemi N, Safari P. Nano-porous SAPO-34 enhanced thin-film nanocomposite polymeric membrane: Simultaneously high water permeation and complete removal of cationic/anionic dyes from water. *J Hazard Mater*. 2018;358(May):376-388. doi:10.1016/j.jhazmat.2018.07.017
105. Mousavi SR, Asghari M, Mahmoodi NM. Chitosan-wrapped multiwalled carbon nanotube as filler within PEBA thin film nanocomposite (TFN) membrane to improve dye removal. *Carbohydr Polym*. 2020;237(February):116128. doi:10.1016/j.carbpol.2020.116128
106. Zhao P, Li R, Wu W, Wang J, Liu J, Zhang Y. In-situ growth of polyvinylpyrrolidone modified Zr-MOFs thin-film nanocomposite (TFN) for efficient dyes removal. *Compos Part B Eng*. 2019;176(April):107208. doi:10.1016/j.compositesb.2019.107208

107. Zhao DL, Jin H, Zhao Q, et al. Smart integration of MOFs and CQDs to fabricate defect-free and self-cleaning TFN membranes for dye removal. *J Memb Sci*. 2023;679(April):121706. doi:10.1016/j.memsci.2023.121706
108. Bai L, Liu Y, Ding A, Ren N, Li G, Liang H. Fabrication and characterization of thin-film composite (TFC) nanofiltration membranes incorporated with cellulose nanocrystals (CNCs) for enhanced desalination performance and dye removal. *Chem Eng J*. 2019;358(October 2018):1519-1528. doi:10.1016/j.cej.2018.10.147
109. Seah MQ, Lau WJ, Goh PS, Ismail AF. Greener synthesis of functionalized-GO incorporated TFN NF membrane for potential recovery of saline water from salt/dye mixed solution. *Desalination*. 2022;523(October 2021):115403. doi:10.1016/j.desal.2021.115403
110. Borpatra Gohain M, Karki S, Yadav D, et al. Development of Antifouling Thin-Film Composite/Nanocomposite Membranes for Removal of Phosphate and Malachite Green Dye. *Membranes (Basel)*. 2022;12(8). doi:10.3390/membranes12080768
111. Zunita M, Irawanti R, Koesmawati T, Lugito G. Graphene Oxide (Go) Membrane In Removing Heavy Metals From Wastewater : Graphene Oxide (GO) Membrane in Removing Heavy Metals from Wastewater : a Review. 2020;(October). doi:10.3303/CET2082070
112. Kausar A. Applications of polymer/graphene nanocomposite membranes: A review. *Mater Res Innov*. 2019;23(5):276-287. doi:10.1080/14328917.2018.1456636
113. Saleem H, Zaidi SJ. Nanoparticles in reverse osmosis membranes for desalination : A state of the art review. *Desalination*. 2020;475(October 2019):114171. doi:10.1016/j.desal.2019.114171
114. Peng W, Li H, Liu Y, Song S. Comparison of Pb (II) adsorption onto graphene oxide prepared from natural graphites : Diagramming the Pb (II) adsorption sites. *Appl Surf Sci*. 2016;364:620-627. doi:10.1016/j.apsusc.2015.12.208
115. Peer FE, Bahramifar N, Younesi H. Removal of Cd (II), Pb (II) and Cu (II) ions from aqueous solution by polyamidoamine dendrimer grafted magnetic graphene oxide nanosheets. *J Taiwan Inst Chem Eng*. 2018;87:225-240. doi:10.1016/j.jtice.2018.03.039
116. Yan M, Liang Q, Wan W, Han Q, Tan S, Ding M. Amino acid-modified graphene oxide magnetic nanocomposite for the magnetic separation of proteins. *RSC Adv*. 2017;7(48):30109-30117. doi:10.1039/c7ra05114j
117. Jilani SM, Gamot TD, Banerji P. Thin-film transistors with a graphene oxide nanocomposite channel. *Langmuir*. 2012;28(48):16485-16489. doi:10.1021/la303554z
118. Zhao G, Li J, Ren X, Chen C, Wang X. Few-layered graphene oxide nanosheets as superior sorbents for heavy metal ion pollution management. *Environ Sci Technol*. 2011;45(24):10454-10462. doi:10.1021/es203439v
119. Tan YY, Abdul Raman AA, Zainal Abidin MII, Buthiyappan A. *A Review on Sustainable Management of Biomass: Physicochemical Modification and Its Application for the Removal of Recalcitrant Pollutants—Challenges, Opportunities, and Future Directions*. Vol 31. Springer Berlin Heidelberg; 2024.

doi:10.1007/s11356-024-33375-x

120. Ma J, Ping D, Dong X. Recent developments of graphene oxide-based membranes: A review. *Membranes (Basel)*. 2017;7(3). doi:10.3390/membranes7030052
121. Yih J, Mubarak NM, Abdullah EC, Nizamuddin S. Recent trends in the synthesis of graphene and graphene oxide based nanomaterials for removal of heavy metals — A review. *J Ind Eng Chem*. 2018;66:29-44. doi:10.1016/j.jiec.2018.05.028
122. Huang L, Zhang M, Li C, Shi G. Graphene-Based Membranes for Molecular Separation. Published online 2015. doi:10.1021/acs.jpclett.5b00914
123. Zhao G, Hu R, He Y, Zhu H. Physically Coating Nanofiltration Membranes with Graphene Oxide Quantum Dots for Simultaneously Improved Water Permeability and Salt/Dye Rejection. *Adv Mater Interfaces*. 2019;6(5):1-11. doi:10.1002/admi.201801742
124. Unimpeded Permeation of Water Through Helium-Leak–Tight Graphene-Based Membranes. *Science (80-).* 2012;335(January):442-444. doi:10.1126/science.1211694
125. Anand A, Unnikrishnan B, Mao JY, Lin HJ, Huang CC. Graphene-based nanofiltration membranes for improving salt rejection, water flux and antifouling–A review. *Desalination*. 2018;429(December 2017):119-133. doi:10.1016/j.desal.2017.12.012
126. Feng X, Peng D, Zhu J, Wang Y, Zhang Y. Recent advances of loose nanofiltration membranes for dye/salt separation. *Sep Purif Technol*. 2022;285(November 2021):120228. doi:10.1016/j.seppur.2021.120228
127. Seah MQ, Lau WJ, Goh PS, Ismail AF. Greener synthesis of functionalized-GO incorporated TFN NF membrane for potential recovery of saline water from salt/dye mixed solution. *Desalination*. 2022;523(July 2021):115403. doi:10.1016/j.desal.2021.115403
128. Izadmehr N, Mansourpanah Y, Ulbricht M, Rahimpour A, Omidkhah MR. TETA-anchored graphene oxide enhanced polyamide thin film nanofiltration membrane for water purification; performance and antifouling properties. *J Environ Manage*. 2020;276(October 2019):111299. doi:10.1016/j.jenvman.2020.111299
129. Austria HFM, Young JO, Setiawan O, et al. Thin film nanocomposite loose nanofiltration membranes with graphene oxide interlayer for textile wastewater treatment. *Sep Purif Technol*. 2025;354(P5):129053. doi:10.1016/j.seppur.2024.129053
130. Mousavi SR, Asghari M, Mahmoodi NM, Salahshoori I. Water decolorization and antifouling melioration of a novel PEBA1657/PES TFC membrane using chitosan-decorated graphene oxide fillers. *J Environ Chem Eng*. 2023;11(3):109955. doi:10.1016/j.jece.2023.109955
131. Khansanami M, Esfandiar A. High flux and complete dyes removal from water by reduced graphene oxide laminate on Poly Vinylidene Fluoride/graphene oxide membranes. *Environ Res*. 2021;201(June):111576. doi:10.1016/j.envres.2021.111576
132. Homem NC, de Camargo Lima Beluci N, Amorim S, et al. Surface modification of

a polyethersulfone microfiltration membrane with graphene oxide for reactive dyes removal. *Appl Surf Sci*. 2019;486(May):499-507. doi:10.1016/j.apsusc.2019.04.276

133. Abdi G, Alizadeh A, Zinadini S, Moradi G. Removal of dye and heavy metal ion using a novel synthetic polyethersulfone nano fi ltration membrane modi fi ed by magnetic graphene oxide / metformin hybrid. *J Memb Sci*. 2018;552(July 2017):326-335. doi:10.1016/j.memsci.2018.02.018
134. Zhang P, Gong JL, Zeng GM, et al. Cross-linking to prepare composite graphene oxide-framework membranes with high-flux for dyes and heavy metal ions removal. *Chem Eng J*. 2017;322:657-666. doi:10.1016/j.cej.2017.04.068
135. Franco P, Cardea S, Tabernero A, De Marco I. Porous aerogels and adsorption of pollutants fromwater and air: A review. *Molecules*. 2021;26(15):1-35. doi:10.3390/molecules26154440
136. Nguyen NTT, Nguyen TTT, Nguyen DTC, Tran T Van. Fruit waste-derived aerogels for the removal of dyes, heavy metals and oils in water: a review. *Environ Chem Lett*. 2024;22(1):419-443. doi:10.1007/s10311-023-01667-2
137. Adavan Kiliyankil V, Fugetsu B, Sakata I, Wang Z, Endo M. Aerogels from copper (II)-cellulose nanofibers and carbon nanotubes as absorbents for the elimination of toxic gases from air. *J Colloid Interface Sci*. 2021;582:950-960. doi:10.1016/j.jcis.2020.08.100
138. Hu J, Zhu J, Ge S, et al. Biocompatible, hydrophobic and resilience graphene/chitosan composite aerogel for efficient oil−water separation. *Surf Coatings Technol*. 2020;385(January):125361. doi:10.1016/j.surfcoat.2020.125361
139. Nawaz M, Khan AA, Hussain A, Jang J, Jung HY, Lee DS. Reduced graphene oxide−TiO2/sodium alginate 3-dimensional structure aerogel for enhanced photocatalytic degradation of ibuprofen and sulfamethoxazole. *Chemosphere*. 2020;261:127702. doi:10.1016/j.chemosphere.2020.127702
140. Maleki H. Recent advances in aerogels for environmental remediation applications: A review. *Chem Eng J*. 2016;300:98-118. doi:10.1016/j.cej.2016.04.098
141. Hong H, Ban G, Seo H, Su H, Sang M. Fabrication of cylindrical 3D cellulose nano fibril (CNF) aerogel for continuous removal of copper (Cu2+) from wastewater. *Chemosphere*. 2021;278:130288. doi:10.1016/j.chemosphere.2021.130288
142. Huang C, Cai B, Zhang L, Zhang C, Pan H. Journal of Solid State Chemistry Preparation of iron-based metal-organic framework @ cellulose aerogel by in situ growth method and its application to dye adsorption. *J Solid State Chem*. 2021;297(February):122030. doi:10.1016/j.jssc.2021.122030
143. Dan H, Li N, Xu X, et al. Mechanism of sonication time on structure and adsorption properties of 3D peanut shell/graphene oxide aerogel. *Sci Total Environ*. 2020;739:139983. doi:10.1016/j.scitotenv.2020.139983
144. Esmaeili Z, Izadyar S, Hamzeh Y, Abdulkhani A. Preparation and Characterization of Highly Porous Cellulose Nanofibrils/Chitosan Aerogel for Acid Blue 93 Adsorption: Kinetics, Isotherms, and Thermodynamics Analysis. *J Chem Eng Data*. 2021;66(2):1068-1080. doi:10.1021/acs.jced.0c00872
145. Rahmani Z, Rashidi AM, kazemi A, Samadi MT, Rahmani AR. N-doped reduced

graphene oxide aerogel for the selective adsorption of oil pollutants from water: Isotherm and kinetic study. *J Ind Eng Chem*. 2018;61:416-426. doi:10.1016/j.jiec.2017.12.041

146. Huo J bo, Yu G, Wang J. Adsorptive removal of Sr(II) from aqueous solution by polyvinyl alcohol/graphene oxide aerogel. *Chemosphere*. 2021;278:130492. doi:10.1016/j.chemosphere.2021.130492
147. Zhou S, Liu P, Wang M, Zhao H, Yang J, Xu F. Sustainable, Reusable, and Superhydrophobic Aerogels from Microfibrillated Cellulose for Highly Effective Oil/Water Separation. *ACS Sustain Chem Eng*. 2016;4(12):6409-6416. doi:10.1021/acssuschemeng.6b01075
148. Gao C, Wang XL, An Q Da, Xiao ZY, Zhai SR. Synergistic preparation of modified alginate aerogel with melamine/chitosan for efficiently selective adsorption of lead ions. *Carbohydr Polym*. 2021;256(August 2020):117564. doi:10.1016/j.carbpol.2020.117564
149. He J, Zhao H, Li X, et al. Superelastic and superhydrophobic bacterial cellulose/silica aerogels with hierarchical cellular structure for oil absorption and recovery. *J Hazard Mater*. 2018;346:199-207. doi:10.1016/j.jhazmat.2017.12.045
150. Prasanna VL, Mamane H, Vadivel VK, Avisar D. Ethanol-activated granular aerogel as efficient adsorbent for persistent organic pollutants from real leachate and hospital wastewater. *J Hazard Mater*. 2020;384(October 2019):121396. doi:10.1016/j.jhazmat.2019.121396
151. Korkmaz S, Kariper A. Graphene and graphene oxide based aerogels: Synthesis, characteristics and supercapacitor applications. *J Energy Storage*. 2020;27(December 2019). doi:10.1016/j.est.2019.101038
152. Mariana M, Abdul Khalil HPS, Yahya EB, et al. Recent trends and future prospects of nanostructured aerogels in water treatment applications. *J Water Process Eng*. 2022;45(October 2021):102481. doi:10.1016/j.jwpe.2021.102481
153. Gao B, Feng X, Zhang Y, et al. Graphene-based aerogels in water and air treatment: A review. *Chem Eng J*. 2024;484(December 2023):149604. doi:10.1016/j.cej.2024.149604
154. Rong N, Chen C, Ouyang K, Zhang K, Wang X, Xu Z. Adsorption characteristics of directional cellulose nanofiber / chitosan / montmorillonite aerogel as adsorbent for wastewater treatment. *Sep Purif Technol*. 2021;274(March):119120. doi:10.1016/j.seppur.2021.119120
155. Zhou Y, Apul OG, Karanfil T. Adsorption of halogenated aliphatic contaminants by graphene nanomaterials. *Water Res*. 2015;79:57-67. doi:10.1016/j.watres.2015.04.017
156. Zhao Q, Zhu X, Chen B. Stable graphene oxide/poly(ethyleneimine) 3D aerogel with tunable surface charge for high performance selective removal of ionic dyes from water. *Chem Eng J*. 2018;334(August 2017):1119-1127. doi:10.1016/j.cej.2017.11.053
157. Liu C, Liu H, Zhang K, et al. Partly reduced graphene oxide aerogels induced by proanthocyanidins for efficient dye removal. *Bioresour Technol*.

2019;282(January):148-155. doi:10.1016/j.biortech.2019.03.012
158. Nguyen VT, Ha LQ, Nguyen TDL, Ly PH, Nguyen DM, Hoang D. Nanocellulose and Graphene Oxide Aerogels for Adsorption and Removal Methylene Blue from an Aqueous Environment. *ACS Omega*. 2022;7(1):1003-1013. doi:10.1021/acsomega.1c05586
159. Han M, Xu B, Zhang M, et al. Preparation of biologically reduced graphene oxide-based aerogel and its application in dye adsorption. *Sci Total Environ*. 2021;783:147028. doi:10.1016/j.scitotenv.2021.147028
160. Sharma SK, Ranjani P, Mamane H, Kumar R. Preparation of graphene oxide-doped silica aerogel using supercritical method for efficient removal of emerging pollutants from wastewater. *Sci Rep*. 2023;13(1):1-19. doi:10.1038/s41598-023-43613-w
161. Zhao S, Jing K, Liu H. Facile construction of pH-responsive graphene oxide-based aerogel and its efficient and selective adsorption performance toward methylene blue. *Chem Eng Res Des*. 2024;208(March):1-14. doi:10.1016/j.cherd.2024.06.036
162. Liu H, Wang B, Liu H, et al. Multi-crosslinked robust alginate/polyethyleneimine modified graphene aerogel for efficient organic dye removal. *Colloids Surfaces A Physicochem Eng Asp*. 2024;683(December 2023):133034. doi:10.1016/j.colsurfa.2023.133034
163. Lu P, Hsieh Y. Preparation and properties of cellulose nanocrystals : Rods , spheres , and network. *Carbohydr Polym*. 2010;82(2):329-336. doi:10.1016/j.carbpol.2010.04.073
164. Trache D, Hussin MH, Thakur VK. Recent progress in cellulose nanocrystals: sources and production. Published online 2017:1763-1786. doi:10.1039/c6nr09494e
165. George J. Cellulose nanocrystals : synthesis , functional properties , and applications. Published online 2015:45-54.
166. Song K, Zhu X, Zhu W, Li X. Preparation and characterization of cellulose nanocrystal extracted from Calotropis procera biomass. *Bioresour Bioprocess*. Published online 2019. doi:10.1186/s40643-019-0279-z
167. Han Y, Zhang X, Wu X, Lu C. Flame Retardant, Heat Insulating Cellulose Aerogels from Waste Cotton Fabrics by in Situ Formation of Magnesium Hydroxide Nanoparticles in Cellulose Gel Nanostructures. Published online 2015. doi:10.1021/acssuschemeng.5b00438
168. Tian C, Fu S, Chen J, Meng Q, Lucia LA. Graft polymerization of ε-caprolactone to cellulose nanocrystals and optimization of grafting conditions utilizing a response surface methodology. 2014;29(1).
169. Razali SA, Azwadi N, Sidik C, Koten H. Cellulose Nanocrystals : A Brief Review on Properties and General Applications. 2019;1(1):1-15.
170. Balcik-Canbolat C, Van der Bruggen B. Efficient removal of dyes from aqueous solution: the potential of cellulose nanocrystals to enhance PES nanocomposite membranes. *Cellulose*. 2020;27(9):5255-5266. doi:10.1007/s10570-020-03157-y
171. Daraei P, Ghaemi N, Sadeghi Ghari H. An ultra-antifouling polyethersulfone membrane embedded with cellulose nanocrystals for improved dye and salt removal

from water. *Cellulose*. 2017;24(2):915-929. doi:10.1007/s10570-016-1135-3
172. Rafieian F, Jonoobi M, Yu Q. A novel nanocomposite membrane containing modified cellulose nanocrystals for copper ion removal and dye adsorption from water. *Cellulose*. 2019;26(5):3359-3373. doi:10.1007/s10570-019-02320-4
173. Mohammed N, Lian H, Islam MS, et al. Selective adsorption and separation of organic dyes using functionalized cellulose nanocrystals. *Chem Eng J*. 2021;417(December 2020):129237. doi:10.1016/j.cej.2021.129237
174. Ibrahim MA, Salama A, Zahran F, et al. Fabrication of cellulose nanocrystals/carboxymethyl cellulose/zeolite membranes for methylene blue dye removal: understanding factors, adsorption kinetics, and thermodynamic isotherms. *Front Chem*. 2024;12(February):1-18. doi:10.3389/fchem.2024.1330810
175. Amiri M, Jafarbeigi E, Salimi F. Fabrication of modified nanofiltration membranes by functionalized cellulose nanocrystals with high anti-fouling capability in removing dye from water and wastewater. *Korean J Chem Eng*. 2022;39(3):616-627. doi:10.1007/s11814-021-0952-8
176. Karim Z, Mathew AP, Grahn M, Mouzon J, Oksman K. Nanoporous membranes with cellulose nanocrystals as functional entity in chitosan: Removal of dyes from water. *Carbohydr Polym*. 2014;112:668-676. doi:10.1016/j.carbpol.2014.06.048
177. Bai L, Liu Y, Ding A, Ren N, Li G, Liang H. Fabrication and characterization of thin-film composite (TFC) nanofiltration membranes incorporated with cellulose nanocrystals (CNCs) for enhanced desalination performance and dye removal. *Chem Eng J*. 2019;358(August 2018):1519-1528. doi:10.1016/j.cej.2018.10.147
178. Liu Y, Bai L, Zhu X, et al. The role of carboxylated cellulose nanocrystals placement in the performance of thin-film composite (TFC) membrane. *J Memb Sci*. 2021;617(August 2020):118581. doi:10.1016/j.memsci.2020.118581
179. Peltzer M, Pei A, Zhou Q, Berglund L, Jiménez A. Surface modification of cellulose nanocrystals by grafting with poly(lactic acid). *Polym Int*. 2014;63(6):1056-1062. doi:10.1002/pi.4610
180. Xu X, Liu F, Jiang L, Zhu JY, Haagenson D, Wiesenborn DP. Cellulose Nanocrystals vs. Cellulose Nano fi brils: A Comparative Study on Their Microstructures and E ff ects as Polymer Reinforcing Agents. Published online 2013.
181. Geurds L, Lauko J, Rowan AE, Amiralian N. Tailored nanocellulose-grafted polymer brush applications. Published online 2021:17173-17188. doi:10.1039/d1ta03264j
182. Eskandari P, Abousalman-Rezvani Z, Roghani-Mamaqani H, Salami-Kalajahi M, Mardani H. Polymer grafting on graphene layers by controlled radical polymerization. *Adv Colloid Interface Sci*. 2019;273:102021. doi:10.1016/j.cis.2019.102021
183. Polanowski P, Jeszka JK, Matyjaszewski K. Polymer brushes in pores by ATRP: Monte Carlo simulations. *Polymer (Guildf)*. 2020;211:123124. doi:10.1016/j.polymer.2020.123124
184. Psarra E, Foster E, Ko U, et al. Growth Factor-Bearing Polymer Brushes - Versatile

Bioactive Substrates In fl uencing Cell Response. *ACS Biomacromolecules*. Published online 2015. doi:10.1021/acs.biomac.5b00967

185. Bunsow J, Kelby T, Huck WTS. Polymer Brushes : Routes toward Mechanosensitive Surfaces. Published online 2010.
186. Coad BR, Lu Y, Glattauer V, Meagher L. Substrate-Independent Method for Growing and Modulating the Density of Polymer Brushes from Surfaces by ATRP. Published online 2012.
187. Ayres N. Polymer brushes: Applications in biomaterials and nanotechnology. *Polym Chem*. 2010;1(6):769-777. doi:10.1039/b9py00246d
188. Ma S, Zhang X, Yu B, Zhou F. Brushing up functional materials. *NPG Asia Mater*. 2019;11(1). doi:10.1038/s41427-019-0121-2
189. Ko U, Mu M, Bittrich E, et al. In Situ Monitoring of Linear RGD-Peptide Bioconjugation with Nanoscale Polymer Brushes. *ACS Omega*. Published online 2017. doi:10.1021/acsomega.6b00450
190. Ionov L, Minko S. Mixed Polymer Brushes with Locking Switching. *ACS Appl Mater Interfaces*. Published online 2012.
191. Jeyaprakash JD, Samuel S, Dhamodharan R, Rühe J. Polymer brushes via ATRP: Role of activator and deactivator in the surface-initiated ATRP of styrene on planar substrates. *Macromol Rapid Commun*. 2002;23(4):277-281. doi:10.1002/1521-3927(20020301)23:4<277::AID-MARC277>3.0.CO;2-U
192. Ladd J, Zhang Z, Chen S, Hower JC, Jiang S. Zwitterionic Polymers Exhibiting High Resistance to Nonspecific Protein Adsorption from Human Serum and Plasma. *ACS Biomacromolecules*. 2008;9(5).
193. Zdyrko B, Klep V, Li X, et al. Polymer brushes as active nanolayers for tunable bacteria adhesion. *Mater Sci Eng C*. 2009;29(3):680-684. doi:10.1016/j.msec.2008.12.017
194. Uttley OF, Brummitt A, Worrall SD. Accessible and sustainable Cu(0)-mediated radical polymerisation for the functionalisation of surfaces. *Polym Chem*. Published online 2020:3831-3840. doi:10.1039/d0py00516a
195. Bhairamadgi NS, Pujari SP, Leermakers FAM, Rijn CJM Van, Zuilhof H. Adhesion and Friction Properties of Polymer Brushes: Fluoro versus Nonfluoro Polymer Brushes at Varying Thickness. *Langmuir*. Published online 2014.
196. Avincula RC, Brittain WJ, Caster KC, Ruhe J. Polymer brushes. *IEEE Electr Insul Mag*. 2006;22(5):50-51. doi:10.1109/MEI.2006.1705866
197. Zoppe JO, Ataman NC, Mocny P, Wang J, Moraes J, Klok H. Surface-Initiated Controlled Radical Polymerization: State-of-the-Art , Opportunities , and Challenges in Surface and Interface Engineering with Polymer Brushes. *Chem Rev*. Published online 2017. doi:10.1021/acs.chemrev.6b00314
198. Li B, Yu B, Ye Q, Zhou F. Tapping the Potential of Polymer Brushes through Synthesis. Published online 2015.
199. Wójcik AJ, Wolski K, Zapotoczny S. Double-stranded surface-grafted polymer brushes with ladder-like architecture. *Eur Polym J*. 2021;155(June). doi:10.1016/j.eurpolymj.2021.110577

200. Iv JJK, Imbrogno J, Belfort G. Polymer Brushes for Membrane Separations: A Review. *ACS Appl Mater Interfaces*. Published online 2016. doi:10.1021/acsami.6b09068
201. Rastogi A, Paik MY, Tanaka M, Ober CK. Direct Patterning of Intrinsically. 2010;4(2):771-780.
202. Railian S, Haven JJ, Maes L, et al. Photo-induced copper-mediated (meth)acrylate polymerization towards graphene oxide and reduced graphene oxide modification. *Eur Polym J*. 2020;134(December 2019):109810. doi:10.1016/j.eurpolymj.2020.109810
203. Azzaroni O. Polymer brushes here, there, and everywhere: Recent advances in their practical applications and emerging opportunities in multiple research fields. *J Polym Sci Part A Polym Chem*. 2012;50(16):3225-3258. doi:10.1002/pola.26119
204. Zhao B, Zhu L. Mixed Polymer Brush-Grafted Particles : A New Class of Environmentally Responsive Nanostructured Materials. Published online 2009:9369-9383. doi:10.1021/ma902042x
205. Chen M, Qin L, Liu Y, Zhang F. Controllable preparation of polymer brushes from mesoporous silica SBA-15 via surface-initiated ARGET ATRP. *Microporous Mesoporous Mater*. 2018;263(12):158-164. doi:10.1016/j.micromeso.2017.12.019
206. Pranantyo D, Xu LQ, Neoh K, Kang E, Ng YX, Teo SL. Tea Stains-Inspired Initiator Primer for Surface Grafting of Antifouling and Antimicrobial Polymer Brush Coatings. Published online 2015. doi:10.1021/bm501623c
207. Gruszkiewicz A, Słowikowska M, Grześ G, et al. Enhancement of the growth of polymer brushes via ATRP initiated from ions-releasing indium tin oxide substrates. *Eur Polym J*. 2019;112(October 2018):817-821. doi:10.1016/j.eurpolymj.2018.11.004
208. Yan J, Yuan L, Hong-wen Z, Rong Z. Grafting β -CD Copolymer Metal Complex from Silicon Gel by SI-ATRP. 2013;29(6):1029-1031. doi:10.1007/s40242-013-3322-1
209. Textor M, Clark RL, Carolina N. Monitoring kinetics of surface initiated atom transfer radical polymerization by quartz crystal microbalance with dissipation. 2006;(March):35-39. doi:10.1116/1.2190697
210. Rutnakornpituk B, Wichai U. Surface-initiated atom transfer radical polymerization of poly (4-vinylpyridine) from magnetite nanoparticle. Published online 2011:6847-6857. doi:10.1007/s11051-011-0592-8
211. Aguilar-Bolados H, Yazdani-Pedram M, Quinteros-Jara E, et al. Synthesis of sustainable, lightweight and electrically conductive polymer brushes grafted multi-layer graphene oxide. *Polym Test*. 2021;93(July 2020):0-8. doi:10.1016/j.polymertesting.2020.106986
212. Raghuraman GK, Ruhe J, Dhamodharan R. Grafting of PMMA brushes on titania nanoparticulate surface via surface-initiated conventional radical and ‘“ controlled ”’ radical polymerization (ATRP). Published online 2008:415-427. doi:10.1007/s11051-007-9268-9
213. Fukazawa K, Nakao A, Maeda M, Ishihara K. Photoreactive Initiator for Surface-

Initiated ATRP on Versatile Polymeric Substrates. Published online 2016:6-10. doi:10.1021/acsami.6b07145

214. Yang W, Zhou F. Polymer brushes for antibiofouling and lubrication. *Biosurface and Biotribology*. 2017;3(3):97-114. doi:10.1016/j.bsbt.2017.10.001
215. Tsujii Y, Ohno K, Yamamoto S, Goto A. Structure and Properties of High-Density Polymer Brushes Prepared by Surface-Initiated Living Radical Polymerization. 2006;(January):1-45.
216. Wang J, Chen H, Ma Y, et al. Grafting high content of imidazolium polymer brushes on graphene oxide for nanocomposite membranes with enhanced anion transport. *React Funct Polym*. 2020;146(December 2019):104447. doi:10.1016/j.reactfunctpolym.2019.104447
217. Kumar A, Bansal A, Behera B, Jain SL, Ray SS. Ternary hybrid polymeric nanocomposites through grafting of polystyrene on graphene oxide-TiO2 by surface initiated atom transfer radical polymerization (SI-ATRP). *Mater Chem Phys*. 2016;172:189-196. doi:10.1016/j.matchemphys.2016.01.064
218. Mogha NK, Gosain S, Masram DT. Lanthanum oxide nanoparticles immobilized reduced graphene oxide polymer brush nanohybrid for environmental vitiation of organic dyes. *Arab J Chem*. 2020;13(1):1367-1376. doi:10.1016/j.arabjc.2017.11.008
219. Ilcikova M, Galeziewska M, Mrlik M, et al. The effect of short polystyrene brushes grafted from graphene oxide on the behavior of miscible PMMA/SAN blends. *Polymer (Guildf)*. 2020;211(August):123088. doi:10.1016/j.polymer.2020.123088
220. Zhao X, Liu P. Hydrophobic-Polymer-Grafted Graphene Oxide Nanosheets as an Easily Separable Adsorbent for the Removal of Tetrabromobisphenol A. Published online 2014.
221. Kan L, Xu Z, Gao C. General Avenue to Individually Dispersed Graphene Oxide-Based Two-Dimensional Molecular Brushes by Free Radical Polymerization. Published online 2011:444-452. doi:10.1021/ma102371d
222. Guo C, Zhao X, Zhang W, et al. Preparation of polymer brushes grafted graphene oxide by atom transfer radical polymerization as a new support for trypsin immobilization and efficient proteome digestion. *Anal Bioanal Chem*. 2017;409(20):4741-4749. doi:10.1007/s00216-017-0417-4
223. Ohno K, Zhao C, Nishina Y. Polymer-Brush-Decorated Graphene Oxide: Precision Synthesis and Liquid-Crystal Formation. *Langmuir*. 2019;35(33):10900-10909. doi:10.1021/acs.langmuir.9b01747
224. Hu J, Li M, Wang L, Zhang X. Polymer brush-modified graphene oxide membrane with excellent structural stability for effective fractionation of textile wastewater. *J Memb Sci*. 2021;618(July 2020):118698. doi:10.1016/j.memsci.2020.118698
225. Ata S, Banerjee SL, Singha NK. Polymer nano-hybrid material based on graphene oxide/POSS via surface initiated atom transfer radical polymerization (SI-ATRP): Its application in specialty hydrogel system. *Polymer (Guildf)*. 2016;103:46-56. doi:10.1016/j.polymer.2016.09.035
226. Kloser E, Gray DG. Surface Grafting of Cellulose Nanocrystals with Poly (ethylene

oxide) in Aqueous Media. 2010;26(21):13450-13456. doi:10.1021/la101795s
227. Kan KHM, Li J, Wijesekera K, Cranston ED. Polymer-Grafted Cellulose Nanocrystals as pH-Responsive Reversible Flocculants. Published online 2013.
228. Abousalman-rezvani Z, Eskandari P, Roghani-mamaqani H. Grafting light- , temperature , and CO 2 -responsive copolymers from cellulose nanocrystals by atom transfer radical polymerization for adsorption of nitrate ions. *Polymer (Guildf)*. 2019;182(August):121830. doi:10.1016/j.polymer.2019.121830
229. Lizundia E, Fortunati E, Dominici F, et al. PLLA-grafted cellulose nanocrystals : Role of the CNC content and grafting on the PLA bionanocomposite film properties. *Carbohydr Polym*. 2016;142:105-113. doi:10.1016/j.carbpol.2016.01.041
230. Malmstr E, Destarac M. SI-RAFT / MADIX polymerization of vinyl acetate on cellulose nanocrystals for nanocomposite applications phane Mazi e. *Polymer (Guildf)*. 2016;99:240-249. doi:10.1016/j.polymer.2016.07.013
231. Hatton FL, Kedzior SA, Cranston ED, Carlmark A. Grafting-from cellulose nanocrystals via photoinduced Cu-mediated reversible-deactivation radical polymerization. *Carbohydr Polym*. 2017;157:1033-1040. doi:10.1016/j.carbpol.2016.10.064
232. Zhang Z, Tam KC, Sèbe G, Wang X. Convenient characterization of polymers grafted on cellulose nanocrystals via SI-ATRP without chain cleavage. *Carbohydr Polym*. 2018;199(July):603-609. doi:10.1016/j.carbpol.2018.07.060
233. Anirudhan TS, Rejeena SR, Binusree J. Adsorptive Separation of Myoglobin from Aqueous Solutions Using Iron Oxide Magnetic Nanoparticles Modified with Functionalized Nanocrystalline Cellulose. Published online 2013.
234. Anirudhan TS, Deepa JR. Synthesis and characterization of multi-carboxyl-functionalized nanocellulose/nanobentonite composite for the adsorption of uranium (VI) from aqueous solutions : Kinetic and equilibrium profiles. *Chem Eng J*. 2015;273:390-400. doi:10.1016/j.cej.2015.03.007
235. Spinella S, Raquez J, Mccallum SA, Gross R, Dubois P. Green and Efficient Synthesis of Dispersible Cellulose Nanocrystals in Biobased Polyesters for Engineering Applications. Published online 2016. doi:10.1021/acssuschemeng.5b01611
236. Anirudhan TS, Deepa JR, Christa J. Nanocellulose/nanobentonite composite anchored with multi-carboxyl functional groups as an adsorbent for the effective removal of Cobalt (II) from nuclear industry wastewater samples. *J Colloid Interface Sci*. 2016;467:307-320. doi:10.1016/j.jcis.2016.01.023
237. Lee SH, Dreyer DR, An J, et al. Polymer brushes via controlled, surface-initiated atom transfer radical polymerization (ATRP) from graphene oxide. *Macromol Rapid Commun*. 2010;31(3):281-288. doi:10.1002/marc.200900641
238. Shih I, Van Y-T. The production of poly-(y -glutamic acid) from microorganisms and its various applications. 2001;79.
239. Pandey K, Pandey AK, Sirohi R, Pandey S. *Production and Applications of Polyglutamic Acid*. INC; 2021. doi:10.1016/B978-0-12-821888-4.00021-6
240. Li M, Zhu X, Yang H, et al. Treatment of potato starch wastewater by dual natural fl

occulants of chitosan and poly-glutamic acid. 2020;264. doi:10.1016/j.jclepro.2020.121641

241. Park S, Sung M, Uyama H, Keun D. Progress in Polymer Science Poly (glutamic acid): Production , composites , and medical applications of the next-generation biopolymer. *Prog Polym Sci*. 2021;113:101341. doi:10.1016/j.progpolymsci.2020.101341
242. Kim HC, Lee JN, Kim E, Kim MH, Park WH. Self-healable poly(y-glutamic acid)/chitooligosaccharide hydrogels via ionic and p-interactions. *Mater Lett*. 2021;297:129987. doi:10.1016/j.matlet.2021.129987
243. Hajdu I, Bodnár M, Csikós Z, Wei S, Daróczi L, Kovács B. Combined nano-membrane technology for removal of lead ions. 2012;410:44-53. doi:10.1016/j.memsci.2012.03.011
244. Bhattacharyya D, Hestekin JA, Brushaber P, Cullen L, Bachas LG, Sikdar SK. Novel poly-glutamic acid functionalized micro ® ltration membranes for sorption of heavy metals at high capacity. 1998;141:121-135.
245. Karimi M, Tabatabaee F, Ali S, Shahabi-ghahfarrokhi I, Chamani J. Development of active antimicrobial poly (L -glutamic) acid-poly (L -lysine) packaging material to protect probiotic bacterium. *Polym Test*. 2020;83(January):106338. doi:10.1016/j.polymertesting.2020.106338
246. Liang J, Shi W. Poly- γ -glutamic acid improves water-stable aggregates , nitrogen and phosphorus uptake efficiency , water-fertilizer productivity , and economic benefit in barren desertified soils of Northwest China. *Agric Water Manag*. 2021;245(March 2020):106551. doi:10.1016/j.agwat.2020.106551
247. Song HK, Toste B, Ahmann K, Hoffman-Kim D, Palmore GTR. Micropatterns of positive guidance cues anchored to polypyrrole doped with polyglutamic acid: A new platform for characterizing neurite extension in complex environments. *Biomaterials*. 2006;27(3):473-484. doi:10.1016/j.biomaterials.2005.06.030
248. Hareesha N, Manjunatha JG, Amrutha BM, Sreeharsha N. Colloids and Surfaces A : Physicochemical and Engineering Aspects A fast and selective electrochemical detection of vanillin in food samples on the surface of poly (glutamic acid) functionalized multiwalled carbon nanotubes and graphite composite paste . 2021;626(June).
249. Zeng W, Hu W, Li H, et al. Preparation and Characterization of Poly (y-glutamic acid) Hydrogels as potential tissue engineering scaffolds. 2014;32(11):1507-1514. doi:10.1007/s10118-014-1536-4
250. Głowińska A, Trochimczuk AW, Jakubiak-marcinkowska A. Novel acrylate / organophosphorus-based hydrogels for agricultural applications . New outlook and innovative concept for the use of 2- (methacryloyloxy) ethyl phosphate as a multi-purpose monomer. *Eur Polym J*. 2019;110(August 2018):202-210. doi:10.1016/j.eurpolymj.2018.11.020
251. Zhou F, Huck WTS. Three-stage switching of surface wetting using phosphate-bearing polymer brushes. 2005;(i):5999-6001. doi:10.1039/b512106j

CHAPTER 3
EXPERIMENTAL METHODOLOGY

This study endeavored to synthesize GO, CNC, GO-GLU, GO-PMEP, and CNC-GLU and then incorporate them onto TFN membranes for dye/salt removal in water. The materials, procedures, and characterization are detailed in the manuscripts contained in Chapter 4.

This section explores the synthesis of CNCs from *Cannabis sativa* (hemp fibers).

Extraction and characterization of cellulose nanocrystals derived from South African *Cannabis sativa* fibers

Khona Maziya, Anita Etale, Heidi Lynn Richards

Molecular Sciences Institute, School of Chemistry, University of the Witwatersrand, Private Bag X3, Johannesburg, 2050, South Africa

Abstract

Cellulose nanocrystals (CNCs) were extracted from South African industrial hemp (*Cannabis sativa*) fibers via chemical pretreatments followed by sulphuric acid hydrolysis. The impact of acid concentration on the shape of the CNCs obtained was examined. Raw hemp fibers, bleached fibers, and cellulose nanocrystals were analyzed for chemical composition, size, crystallinity, and thermal characteristics using FTIR, SEM, TEM, XRD, and TGA to gain insight into changes that occur during reactions. At the optimum acid concentration (60 wt%), the CNCs exhibited a needle-like morphology with an average length of 4.909 ± 1.611 nm. The CNCs crystallinity degree rose to 79% from 61% crystallinity of raw hemp fiber, while the chemical structure was preserved following sulfuric acid hydrolysis and exhibited improved thermal stability. These promising results demonstrate that industrial hemp fibers are invaluable resources for the extraction of CNCs with successive possible implementation in various industries.

1. Introduction

Recently, there has been a surge of global emphasis on eco-friendly materials and production practices in the medical, pharmaceutical, packaging, electrical, manufacturing and fuel sectors. As the globe confronts the difficulties of climate change and depleted natural resources, the search for alternative, eco-friendly materials has become critical. In this context, cellulose nanocrystals (CNCs) produced from renewable and sustainable biomass sources have emerged as a possible option for developing innovative materials with improved characteristics and a lower environmental footprint.

Industrial hemp is a highly sustainable and versatile crop that can be used to produce cellulose-rich fibers for various applications such as textile processing, cosmetics, medicine, reinforcements of building materials, and pharmaceuticals manufacturing.[1,2] Industrial hemp is widely used since it is inexpensive, biodegradable, renewable, and environmentally friendly.[3,4] With the increase in production of industrial hemp (*Cannabis sativa*) in South Africa due to the legalization for cannabis commercialization, agricultural hemp waste has increased. Hemp production generates a large amount of solid waste, including bast fibers and woody core fibers (hurds). Hemp fibers have numerous attractive features including, outstanding antibacterial properties, strong adsorption, excellent permeability, anti-odor capabilities, heat transfer properties and high cellulose content.[5,6] Hemp bast fibers are made up of 74% cellulose, 14% hemicellulose, 1% pectin, 5% lignin, and 6% miscellaneous compounds.[4] Natural hemp fibers are an excellent substitute to synthetic fibers, and cellulose source given their rapid growth.

Cellulose is a naturally occurring biopolymer, comprising of D-glucopyranose subunits connected with a 1,4-β glycosidic bond.[7,8] It is an important component of a plant that has been recognized as a major constituent of a cell wall.[9,10] The linear arrangement of cellulose is preserved in the form of a cellulose chain, thanks to hydrogen bonds that connect the oxygen atom and hydroxyl groups.[9] It is an exceptional material that possesses numerous hydroxyl groups and can undergo esterification, oxidation and other reactions.[11] Cellulose also possesses excellent properties such as biodegradability, thermal stability, and recyclability.[11]

As nanotechnology advances, one emerging domain of cellulose use is the development of nanomaterials, specifically cellulose nanocrystals (CNCs). Given that the cellulose chain can exhibit amorphous and crystalline areas, different nanomaterials can be obtained by hydrolysis of the amorphous section.[12] CNCs are typically rod shaped particles of nanoscale length (50 – 500 nm).[12] CNCs have emerged as a versatile and sustainable nanomaterial utilized in an array of applications owing to their multiple benefits, including thermal, mechanical, and optical features, high stiffness, large surface area, low density, and an abundance of surface hydroxyl groups.[13–15] A well-known and simplest method used to produce CNCs is via hydrolysis of the cellulose with an acid i.e. Sulphuric acid, results in the removal of armophous regions retaining the crystalline portions of the cellulose.[16,17] Acid hydrolysis results in distinct rod-shaped nanofibers with anionic sulfate ester groups at their surface.[18] Several researches have been conducted using this technique of CNC isolation from various plant sources such as *Calotropis procera*, corncobs, garlic,

pine cone, etc.[19–34] This present work was conducted to firstly extract cellulose fibers from industrial hemp and to further examine the usage of sulphuric acid in the synthesis of CNCs. The impact of acid concentration on CNC morphology was also explored.

2. Experimental section

2.1 Materials

All chemicals utilized were of analytical grade. Glacial acetic acid (CH_3COOH), sulphuric acid (H_2SO_4), sodium hydroxide (NaOH), and sodium chlorite ($NaClO_2$), were sourced from Sigma-Aldrich (Johannesburg, South Africa. Solutions utilized were produced using double-deionized water, and hemp fibers were acquired locally. Prior to use, polypropylene vials and glassware were thoroughly cleaned by soaking in 1 M nitric acid (HNO_3) for a minimum of 24 hours, followed by rinsing with deionized water.

2.2 Cellulose fibers extraction from *Cannabis sativa* (hemp) plants

The cellulose fibers were extracted following a method reported by Mhlongo et al, 2022.[35] Dried hemp branches and stems were steeped overnight in water, to facilitate the peeling of the bark from woody cores. Following this, the bark underwent a treatment with 4 wt% sodium hydroxide (NaOH) for two hours at a temperature of 80°C. This alkaline treatment was repeated three times. Subsequently, the bark was bleached using a mixture of acetate buffer at pH 4.8 and sodium chlorite (1.7 wt% $NaClO_2$). This bleaching process was conducted for one hour at 100°C until the fibers achieved a white appearance. The fibers were subsequently allowed to air dry after being properly rinsed with distilled water.

2.3 Synthesis of cellulose nanocrystals from hemp cellulose fibers

Sulphuric acid (45, 60, and 65 wt%) was added to the bleached fibers. In summary, cellulose fibers were hydrolyzed with sulfuric acid (20 mL/g acid/pulp ratio). Dropwise, sulphuric acid was added with vigorous stirring while keeping the temperature below 30°C. The reaction mixtures temperature was raised to 45°C once the acid addition was finished. The reaction was kept at this temperature for an hour while being constantly stirred. The hydrolysis process was terminated by introducing 200 mL of cold water (about 2x the volume of acid solution). To obtain a precipitate, the diluted sample was centrifuged (10 minutes; 11,000 rpm). The precipitate was resuspended in water and centrifuged after vigorous agitation. This continued till the pH of the suspension reached 5, at which point dialysis was performed for three days to ensure that the pH remained constant. The suspension was then sonicated using an ultrasonic homogenizer to distribute the nanofibers in water. [36]

2.4 Characterization

The CNCs morphology was analyzed using a FEI Tecnai G2 Spirit transmission electron microscope (TEM) from Hillsboro, USA, operating at an acceleration voltage of 120 kV. CNC suspensions (10 µL) were deposited on carbon-coated copper grids for TEM examination and allowed to adsorb for 60 seconds. A filter paper was used to carefully remove excess liquid. The adsorbed specimen was then negatively stained using a drop of negative stain (2 wt% uranyl acetate) and blotting. Fourier transform infrared (FTIR)

spectra ranging from 4000 to 500 cm^{-1} was obtained by means of a Tensor 27 Infrared Spectrometer from Massachusetts, USA. The thermal stability of the CNCs was evaluated by means of a thermogravimetric analysis (TGA) conducted on a thermogravimetric analyser over a temperature span of 35 – 900 °C, with a heating rate of 20 °C/min in a nitrogen environment (Perkin Elmer). For scanning electron microscopy (SEM), raw hemp and bleached fibers were initially coated (carbon and Pd/Au) and examined (accelerating voltage = 20 kV). X-ray diffraction (XRD) was conducted utilizing a Bruker D2 Phaser diffractometer equipped with a Cu-Kα source (Johannesburg, South Africa). The analysis covered a scan ranging from 5 – 90 degrees (2θ), employing a step size of 0.026 degrees and a duration of 37 seconds per step. The crystallinity index was computed following the Segal empirical method as presented in **Equation (1)**[37]:

$$CrI = \frac{I200 - Iam}{I200} \times 100\% \quad \ldots\ldots\ldots\ldots\ldots\ldots\ldots\ldots\ldots\ldots\ldots\ldots (1)$$

where, I_{200} is the magnitude of crystallites peak at approximately 2θ = 22.7º and I_{am} is the least intensity between the peaks at 110 and 200 at 2θ =18 – 19º.

3. Results and discussion

3.1 Morphological structure and size distribution

The surface morphology of raw hemp and cellulose fibers was examined using SEM (**Figure 1**). The raw hemp fiber surface consists of lignin and other non-cellulosic components which results in an uneven and rough surface (**Figure 1 (a)**). During alkali treatment, the high temperatures hydrolyzed the hemicellulose thus became water soluble and the lignin was partially depolymerized.[18] A bleaching process further removed the residual lignin causing further separation to elementary fibers (**Figure 1 (b)**) with diameter average of 10.73 ± 4.34 µm.

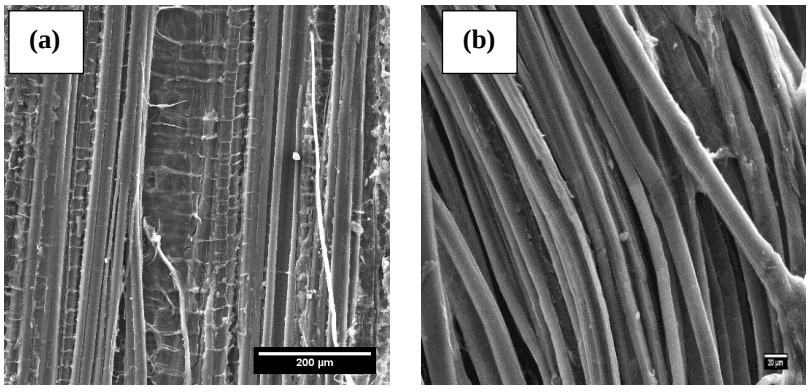

Figure 1: SEM images of raw hemp fiber (a) and bleached fibers (b).

TEM analysis was employed to assess particle size and morphology, as shown in **Figure 2**. The cellulose fibers treated with 45 wt% H_2SO_4 formed nanofibers possessing an average diameter of 4.474 ± 1.709 nm **(Figure 2(a))**. However, at greater concentrations (65 wt%), both crystalline and amorphous regions of cellulose were degraded into sugars **(Figure 2(c))**. To achieve nanocrystals, the acid concentration must be effectively optimized**,** the ideal concentration was determined to be 60 wt%, resulting in nanocrystals with needle-

like morphology having an average diameter of 4.909 ± 1.611 nm **(Figure 2(b)).** The crystalline particles are left behind after the amorphous portions that act as structural flaws are eliminated during acid hydrolysis.

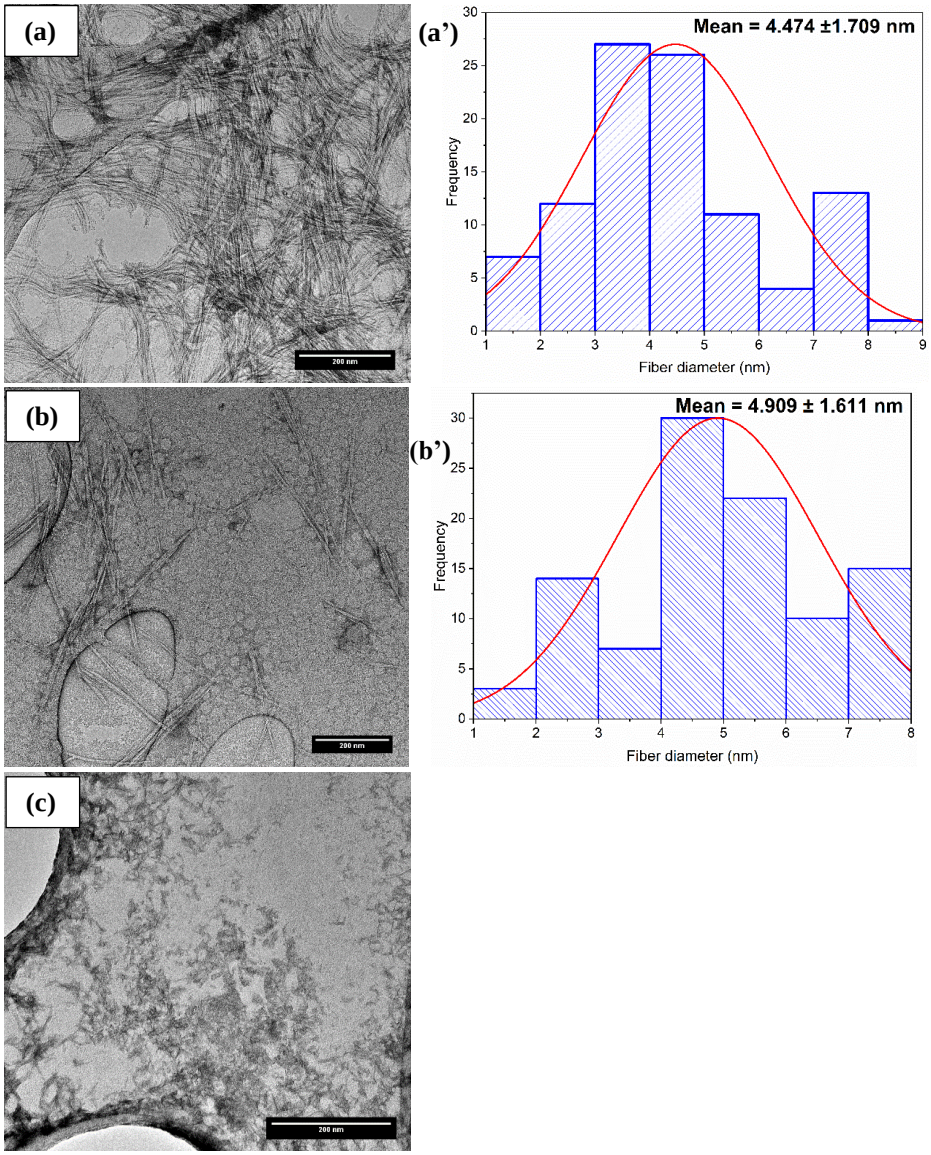

Figure 2: TEM images of bleached cellulose fibers exposed to 45 wt% (a), 60 wt%, 65 wt% sulphuric acid and corresponding histograms.

3.2 FTIR analysis

Figure 3 exhibits the FTIR spectra of hemp fibers, bleached fibers, and CNCs, with the appropriate functional group determining the cellulose extraction outcome as well as lignin and pectin removal. The peaks at 3313 and 2907 cm^{-1} correspond to the O-H and C-H stretching of polysaccharide aliphatic groups, respectively.[38] The stretching vibration of the carbonyl group (C=O) linked with acetyl and uronic ester groups found in pectin, hemicellulose, as well as the ester linkage of carboxylic groups like ferulic and p-coumaric acids present in lignin and/or hemicelluloses was observed at 1730 cm^{-1} for the raw hemp fiber spectrum. [19,39] In the raw hemp fiber spectrum, the peak at 1239 cm^{-1} is accredited to

the C-O stretching vibration associated with the aryl or acetyl groups in lignin.[23] The peak at 1645 cm^{-1} is credited to the O-H bending of absorbed water and cellulose molecules.[40] Following the alkali and bleaching processes, the peak at 1239 cm^{-1} dissapears indicating that the majority of the lignin was removed, leading to an increased cellulose content.[22]
The peaks at 1110 cm^{-1} and 891 cm^{-1} in all samples were primarily attributable to the vibration of ether groups (C-O-C) and rocking motion of C-H bonds associated with the β-glycosidic bonds between the β-D-glucopyranose units in cellulose.[40] Also, a peak at 1364 cm^{-1} attributed to the bending of C–H linkage in the native cellulose was also observed.[41] Commonly, the presence of these peaks indicates that the native cellulose structure was preserved at all stages of the isolation procedure. The peak at 1030 cm^{-1} corresponds to the skeletal vibration of the C-O-C pyranose ring, and its intensity steadily rose from raw fiber to CNC, with cellulose nanocrystals exhibiting the maximum intensity.[21] These findings show that the cellulose structure remained intact after the chemical treatments.

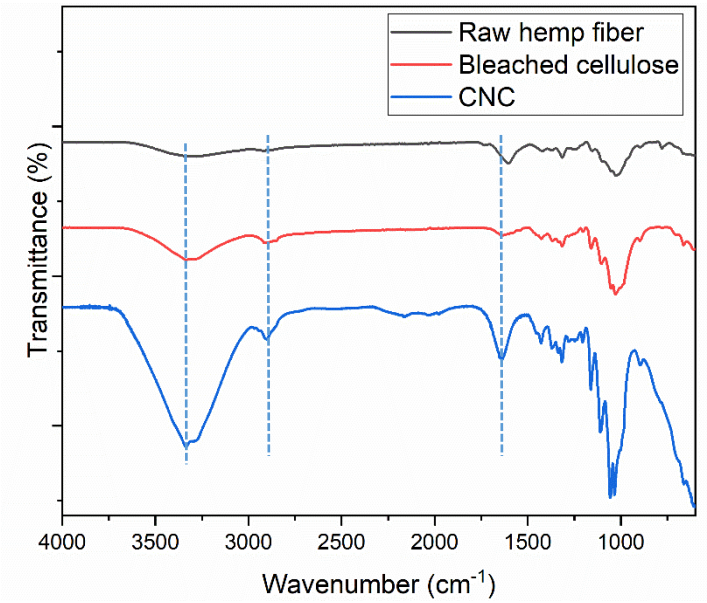

Figure 3: FTIR spectrum of raw hemp fiber, bleached fibers and CNCs.

3.3 XRD

To examine the crystalline structure and prove bleaching and acid hydrolysis of raw hemp fibers, bleached fibers and CNCs, XRD analysis was conducted (**Figure 4**). The diffractograms displayed a broad amorphous hump with crystalline peaks, characteristic of a semi-crystalline material. Three crystalline peaks associated with cellulose I was observed at approximately 2θ = 15.5° (110), 22.7° (002) and 34.6° (004).[24,42] As anticipated, the sizes of these crystalline peaks amplified upon cellulose purification and elimination of amorphous regions (hemicellulose and lignin). Raw hemp, bleached fibers, and CNCs had CrI values of 61, 73, and 79%, respectively. The rise in CrI is brought about by the elimination of amorphous areas during acid hydrolysis.

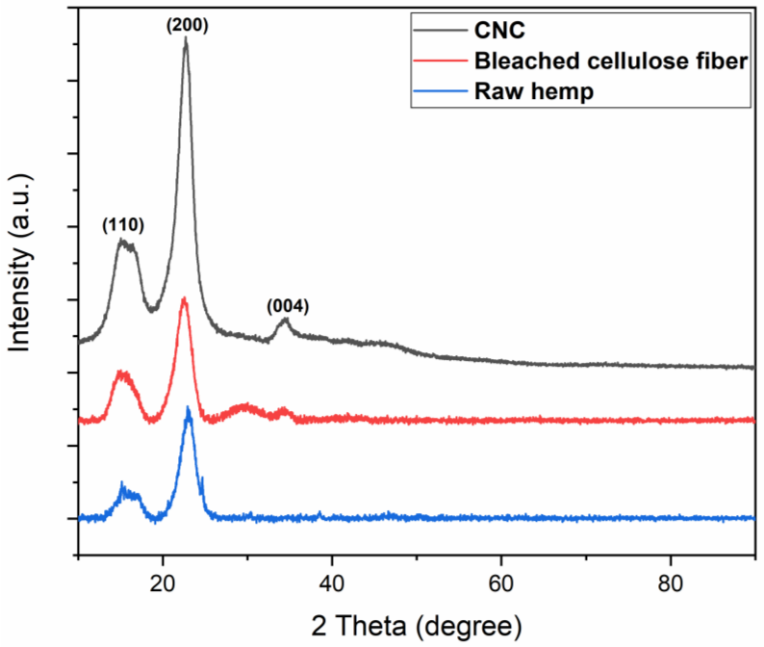

Figure 4: XRD patterns of raw hemp fibers, bleached fibers, and CNCs derived from *Cannabis sativa* plants.

3.4 Thermal analysis

Raw hemp fibers, bleached fibers and synthesized CNCs thermal stability was investigated and shown in **Figure 5**. The materials displayed three stages of disintegration; the first one at 50 – 200°C which is caused by the loss of absorbed water.[43] The second stage at 210 – 400°C, is a major degradation step caused by the depolymerization of hemicellulose, lignin and the breakdown of glycosidic bonds of cellulose.[43] The last stage is observed above 400°C which is due to additional breakdown of thermal degradation intermediates.[20]

However, the degrading behavior of these materials differed significantly. This is because the chemical compositions of lignin, hemicellulose, and cellulose differ, resulting in varied decomposition rates at various temperatures.[21] Raw hemp and bleached fibers had more significant early thermal stability than CNCs, with T_{onset} values of 262°C and 275°C, respectively. At roughly 213°C, the CNCs started to degrade. The delayed thermal decomposition of raw hemp and bleached fibers is accredited to the high contents lignin and hemicellulose, which inhibits degradation.[2,44,45] CNCs' decreased thermal stability can be ascribed to the enlarged surface area, that exposes them to more heat, and negatively charged sulfate groups introduced into their outer surfaces after sulphuric acid hydrolysis, that reduces the activation energy for degradation.[22] The final residual weights were found to be 14.3%, 9.9% and 18.6% for raw hemp fibers, bleached fibers and CNCs, respectively. The increased residual weight of CNCs is as a result to the occurrence of sulfonated groups likely to act as flame retardants.[23]

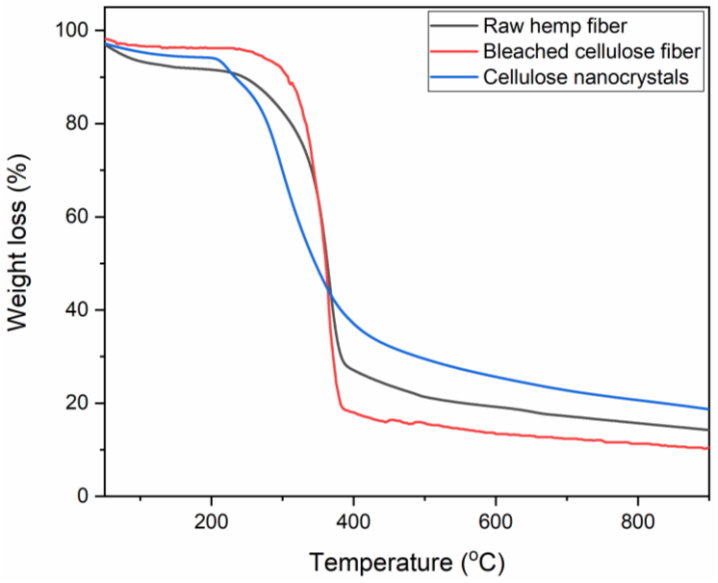

Figure 5: TGA graphs of Raw hemp fibers, bleached cellulose fiber and CNCs.

4. Conclusion

CNCs were successfully extracted from industrial hemp fibers via acid hydrolysis, following an alkaline and subsequent bleaching process. The effects of acid concentration on the isolation of CNCs were investigated and 60 wt% proved to be the optimum concentration. Lignin and hemicellulose were successfully removed after chemical treatment, as such, the crystallinity of needle-shaped CNCs increased. Furthermore, the CNCs exhibited an enhanced thermal stability than raw hemp fibers. This work demonstrates that CNCs may be successfully synthesized from hemp fibers using acid hydrolysis, promoting their utilization as a green alternative for the generation CNC for a variety of applications.

5. References

1. Salami A, Raninen K, Heikkinen J, et al. Complementary chemical characterization of distillates obtained from industrial hemp hurds by thermal processing. *Ind Crops Prod*. 2020;155(June):112760. doi:10.1016/j.indcrop.2020.112760

2. Mhlongo JT, Nuapia Y, Tlhaole B, Mahlangu OT, Etale A. Optimization of Hemp Bast Microfiber Production Using Response Surface Modelling. *Processes*. 2022;10(6):1-20. doi:10.3390/pr10061150

3. Jarabo R, Fuente E, Monte MC, Savastano H, Mutjé P, Negro C. Use of cellulose fibers from hemp core in fiber-cement production. Effect on flocculation, retention, drainage and product properties. *Ind Crops Prod*. 2012;39(1):89-96. doi:10.1016/j.indcrop.2012.02.017

4. Väisänen T, Batello P, Lappalainen R, Tomppo L. Modification of hemp fibers (Cannabis Sativa L.) for composite applications. *Ind Crops Prod*. 2018;111(September 2017):422-429. doi:10.1016/j.indcrop.2017.10.049

5. Xia W, Anwar A, Wang L, et al. Microwave-assisted solid-state pretreatment for fabrication of hemp fibres using ethanolamine at low temperature. *Carbohydr Polym*. 2024;332(January):121906. doi:10.1016/j.carbpol.2024.121906

6. Zhao S, Qin Z, Zhang R, et al. The physical and chemical properties of hemp fiber prepared by alkaline pectinase–xylanase system. *Cellulose*. 2022;29(18):9569-9581. doi:10.1007/s10570-022-04858-2

7. Prabsangob N. Plant-based cellulose nanomaterials for food products with lowered energy uptake and improved nutritional value-a review. *NFS J*. 2023;31(January):39-49. doi:10.1016/j.nfs.2023.03.002

8. Cranston ED, Gray DG. Morphological and optical characterization of polyelectrolyte multilayers incorporating nanocrystalline cellulose. *Biomacromolecules*. 2006;7(9):2522-2530. doi:10.1021/bm0602886

9. Naomi R, Idrus RBH, Fauzi MB. Plant-vs. Bacterial-derived cellulose for wound healing: A review. *Int J Environ Res Public Health*. 2020;17(18):1-25. doi:10.3390/ijerph17186803

10. Selvaraj S, Chauhan A, Dutta V, et al. A state-of-the-art review on plant-derived cellulose-based green hydrogels and their multifunctional role in advanced biomedical applications. *Int J Biol Macromol*. 2024;265(P2):130991. doi:10.1016/j.ijbiomac.2024.130991

11. Zhang Y, Gong S, Lu R, et al. Fresh water collection strategy: Invasive plant-based cellulose aerogels for highly efficient interfacial solar evaporation. *Chem Eng J*. 2024;480(October 2023):148121. doi:10.1016/j.cej.2023.148121

12. Sinha A, Martin EM, Lim K-T, et al. Cellulose Nanocrystals as Advanced "Green" Materials for Biological and Biomedical Engineering. *J Biosyst Eng*. 2015;40(4):373-393. doi:10.5307/jbe.2015.40.4.373

13. Zulu B, Oyewo OA, Sithole B, Leswifi TY. Functionalized Sawdust-Derived Cellulose Nanocrystalline Adsorbent for Efficient Removal of Vanadium From Aqueous Solution. 2020;8(July):1-11. doi:10.3389/fenvs.2020.00056

14. Rashid A Bin, Hoque ME, Kabir N, et al. Synthesis, Properties, Applications, and Future Prospective of Cellulose Nanocrystals. *Polymers (Basel)*. 2023;15(20). doi:10.3390/polym15204070
15. Schiavi D, Ronchetti R, Di Lorenzo V, et al. Sustainable Protocols for Cellulose Nanocrystals Synthesis from Tomato Waste and Their Antimicrobial Properties against Pseudomonas syringae pv. tomato. *Plants*. 2023;12(4). doi:10.3390/plants12040939
16. Domingues RMA, Gomes ME, Reis RL. The potential of cellulose nanocrystals in tissue engineering strategies. *Biomacromolecules*. 2014;15(7):2327-2346. doi:10.1021/bm500524s
17. Islam MS, Chen L, Sisler J, Tam KC. Cellulose nanocrystal (CNC)-inorganic hybrid systems: Synthesis, properties and applications. *J Mater Chem B*. 2018;6(6):864-883. doi:10.1039/c7tb03016a
18. Rahman NHA, Chieng BW, Ibrahim NA, Rahman NA. Extraction and characterization of cellulose nanocrystals from tea leaf waste fibers. *Polymers (Basel)*. 2017;9(11):1-11. doi:10.3390/polym9110588
19. Song K, Zhu X, Zhu W, Li X. Preparation and characterization of cellulose nanocrystal extracted from Calotropis procera biomass. *Bioresour Bioprocess*. Published online 2019. doi:10.1186/s40643-019-0279-z
20. Sadare OO, Mabunda N, Ikegwu UM, Keitemoge MK, Daramola MO, Moothi K. Parametric optimization of the production of cellulose nanocrystals (CNCs) from South African corncobs via an empirical modelling approach. *Sci Rep*. 2022;12(1):1-15. doi:10.1038/s41598-022-22865-y
21. Fortunati E, Puglia D, Monti M, et al. Extraction of Cellulose Nanocrystals from Phormium tenax Fibres. *J Polym Environ*. 2013;21(2):319-328. doi:10.1007/s10924-012-0543-1
22. Gupta V, Ramakanth D, Verma C, Maji PK, Gaikwad KK. Isolation and characterization of cellulose nanocrystals from amla (Phyllanthus emblica) pomace. *Biomass Convers Biorefinery*. 2023;13(17):15451-15462. doi:10.1007/s13399-021-01852-9
23. Kargarzadeh H, Ahmad I, Abdullah I, Dufresne A, Zainudin SY, Sheltami RM. Effects of hydrolysis conditions on the morphology, crystallinity, and thermal stability of cellulose nanocrystals extracted from kenaf bast fibers. *Cellulose*. 2012;19(3):855-866. doi:10.1007/s10570-012-9684-6
24. Huang S, Zhou L, Li MC, Wu Q, Zhou D. Cellulose nanocrystals (CNCs) from corn stalk: Activation energy analysis. *Materials (Basel)*. 2017;10(1). doi:10.3390/ma10010080
25. Lusiana SE, Srihardyastutie A, Masruri M. Cellulose nanocrystal (CNC) produced from the sulphuric acid hydrolysis of the pine cone flower waste (Pinus merkusii Jungh et de Vriese). *J Phys Conf Ser*. 2019;1374(1). doi:10.1088/1742-6596/1374/1/012023
26. Wulandari WT, Rochliadi A, Arcana IM. Nanocellulose prepared by acid hydrolysis of isolated cellulose from sugarcane bagasse. *IOP Conf Ser Mater Sci Eng*. 2016;107(1). doi:10.1088/1757-899X/107/1/012045

27. Pereira ALS, Nascimento DMD, Souza Filho MDSM, et al. Improvement of polyvinyl alcohol properties by adding nanocrystalline cellulose isolated from banana pseudostems. *Carbohydr Polym*. 2014;112:165-172. doi:10.1016/j.carbpol.2014.05.090
28. Fortunati E, Puglia D, Luzi F, Santulli C, Kenny JM, Torre L. Binary PVA bio-nanocomposites containing cellulose nanocrystals extracted from different natural sources: Part I. *Carbohydr Polym*. 2013;97(2):825-836. doi:10.1016/j.carbpol.2013.03.075
29. Rosli NA, Ahmad I, Abdullah I. Isolation and characterization of cellulose nanocrystals from agave angustifolia fibre. *BioResources*. 2013;8(2):1893-1908. doi:10.15376/biores.8.2.1893-1908
30. Chieng BW, Lee SH, Ibrahim NA, Then YY, Loo YY. Isolation and characterization of cellulose nanocrystals from oil palm mesocarp fiber. *Polymers (Basel)*. 2017;9(8):1-11. doi:10.3390/polym9080355
31. Kusmono, Listyanda RF, Wildan MW, Ilman MN. Preparation and characterization of cellulose nanocrystal extracted from ramie fibers by sulfuric acid hydrolysis. *Heliyon*. 2020;6(11):e05486. doi:10.1016/j.heliyon.2020.e05486
32. Prasad Reddy J, Rhim JW. Isolation and characterization of cellulose nanocrystals from garlic skin. *Mater Lett*. 2014;129:20-23. doi:10.1016/j.matlet.2014.05.019
33. Li Y, Li G, Zou Y, Zhou Q, Lian X. Preparation and characterization of cellulose nanofibers from partly mercerized cotton by mixed acid hydrolysis. *Cellulose*. 2014;21(1):301-309. doi:10.1007/s10570-013-0146-6
34. Rosa MF, Medeiros ES, Malmonge JA, et al. Cellulose nanowhiskers from coconut husk fibers: Effect of preparation conditions on their thermal and morphological behavior. *Carbohydr Polym*. 2010;81(1):83-92. doi:10.1016/j.carbpol.2010.01.059
35. Mhlongo JT, Dlamini ML, Nuapia Y, Etale A. Synthesis and application of cationized cellulose for adsorption of anionic dyes. *Mater Today Proc*. 2022;62(February):S133-S140. doi:10.1016/j.matpr.2022.02.100
36. Fahma F, Iwamoto S, Hori N, Iwata T, Takemura A. Isolation, preparation, and characterization of nanofibers from oil palm empty-fruit-bunch (OPEFB). *Cellulose*. 2010;17(5):977-985. doi:10.1007/s10570-010-9436-4
37. Segal L, Creely JJ, Martin AE, Conrad CM. An Empirical Method for Estimating the Degree of Crystallinity of Native Cellulose Using the X-Ray Diffractometer. *Text Res J*. 1959;29(10):786-794. doi:10.1177/004051755902901003
38. Mondragon G, Fernandes S, Retegi A, et al. A common strategy to extracting cellulose nanoentities from different plants. *Ind Crops Prod*. 2014;55:140-148. doi:10.1016/j.indcrop.2014.02.014
39. Kassab Z, Syafri E, Tamraoui Y, Hannache H, Qaiss AEK, El Achaby M. Characteristics of sulfated and carboxylated cellulose nanocrystals extracted from Juncus plant stems. *Int J Biol Macromol*. 2020;154:1419-1425. doi:10.1016/j.ijbiomac.2019.11.023
40. Mahur BK, Ahuja A, Singh S, Maji PK, Rastogi VK. Different nanocellulose morphologies (cellulose nanofibers, nanocrystals and nanospheres) extracted from Sunn hemp (Crotalaria Juncea). *Int J Biol Macromol*. 2023;253(P1):126657. doi:10.1016/j.ijbiomac.2023.126657

41. Lamaming J, Hashim R, Leh CP, Sulaiman O. Properties of cellulose nanocrystals from oil palm trunk isolated by total chlorine free method. *Carbohydr Polym*. 2017;156:409-416. doi:10.1016/j.carbpol.2016.09.053
42. Hemmati F, Jafari SM, Kashaninejad M, Barani Motlagh M. Synthesis and characterization of cellulose nanocrystals derived from walnut shell agricultural residues. *Int J Biol Macromol*. 2018;120:1216-1224. doi:10.1016/j.ijbiomac.2018.09.012
43. Rana SS, Gupta MK. Isolation of nanocellulose from hemp (Cannabis sativa) fibers by chemo-mechanical method and its characterization. *Polym Compos*. 2020;41(12):5257-5268. doi:10.1002/pc.25791
44. Kamelnia E, Divsalar A, Darroudi M, Yaghmaei P, Sadri K. Production of new cellulose nanocrystals from Ferula gummosa and their use in medical applications via investigation of their biodistribution. *Ind Crops Prod*. 2019;139(March):111538. doi:10.1016/j.indcrop.2019.111538
45. Hancock J, Osei-Bonsu R, Hoque M, Samuels L, Foster EJ. Valorization of cannabis green waste to cellulose nanomaterials via phosphoric acid hydrolysis. *Ind Crops Prod*. 2023;201(January):116888. doi:10.1016/j.indcrop.2023.116888

CHAPTER 4
RESULTS AND DISCUSSION

Chapter 4 presents published articles and manuscripts submitted for publication consideration. Each manuscript's references are formatted in accordance with the specific guidelines of the journal to which it was submitted or is being reviewed. Consequently, the structure, as well as the sections, subsections, and citation styles, may vary across all documents.

4.1 Paper 1

This paper entitled "**Enhancing dye rejection and antifouling resistance of thin film nanocomposite nanofiltration membranes by the incorporation of glutamic acid functionalized graphene oxide**" has been published in Frontiers in Membrane Science and Technology.

Front. Membr. Sci. Technol., 14 May 2025

Sec. Membrane Formation and Structure

Volume 4 - 2025 | https://doi.org/10.3389/frmst.2025.1571459

This article evaluated the potential of glutamic acid functionalized graphene oxide modified TFN membranes in the removal of dyes in water.

Khona Maziya – Principal author

Contribution: principal author, conceptualization, performed experiments, data collection/analysis, methodology, formal analysis, research, visualization and writing - original draft.

Enhancing dye rejection and antifouling resistance of thin film nanocomposite nanofiltration membranes by the incorporation of glutamic acid functionalized graphene oxide

Khona Maziya, Izak Kotze, Heidi Lynn Richards

Molecular Sciences Institute, School of Chemistry, University of the Witwatersrand, Private Bag X3, Johannesburg, 2050, South Africa

Graphical abstract

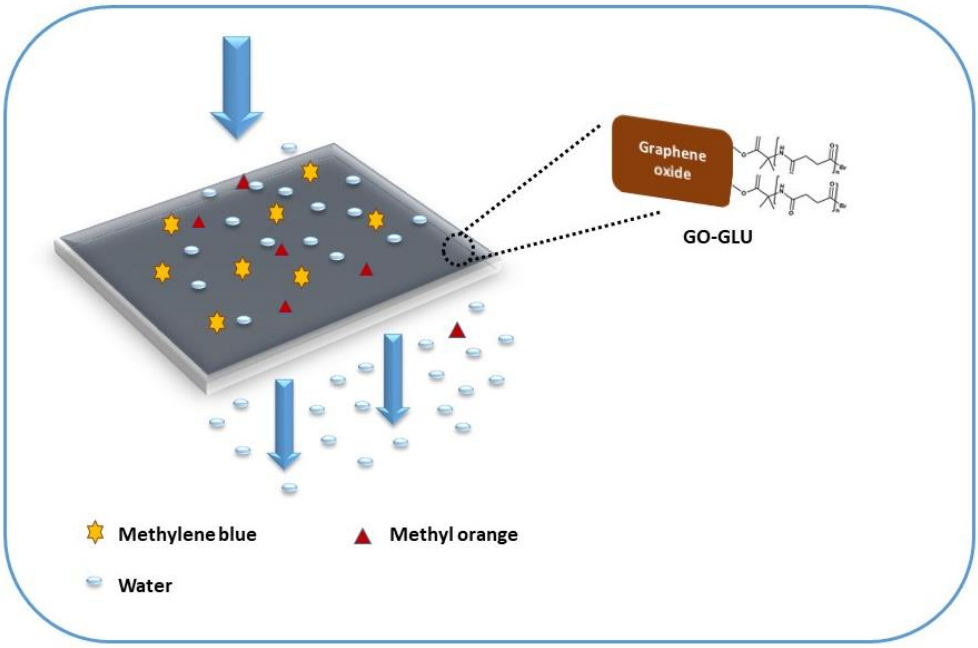

*Corresponding author: Email address: heidi.richards@wits.ac.za

Abstract

To enhance membrane performance of nanofiltration (NF) membranes for dye wastewater treatment, thin film nanocomposite (TFN) membranes embedded with glutamic acid brush modified graphene oxide (GO-GLU) were fabricated. In this current study, GO-GLU was introduced to the selective polyamide (PA) layer which was prepared via interfacial polymerization of organic trimesoyl chloride (TMC) and aqueous m-phenylenediamine (MPD) on a polysulfone (PSF) support. Water permeability and dye rejection with methyl orange (MO) and methylene blue (MB) were used to evaluate membranes performance. The evaluation of TFN membranes via WCA, FTIR, SEM, and AFM demonstrated that GO-GLU nanosheets enhanced hydrophilicity. The fabricated GO-GLU TFN membrane attained a water permeance of 14.11 L/m^2h at the optimal GO-GLU dosage of 0.10 wt%, with 99.18% MB rejection and 67.18% MO rejection. Furthermore, it displayed superior antifouling characteristics against Bovine Serum Albumin (BSA) than the virgin TFC membrane and potentially good operation stability performance after 3 cycles. The results proved that addition of GO-GLU nanosheets enhanced membrane performance. The TFN membranes provide excellent performance in effectively removing of dyes from both synthetic and river water samples, rendering them a suitable alternative for wastewater treatment. The study sheds fresh light on the construction of NF membranes by using GO-GLU nanosheets to boost the membranes hydrophilicity and antifouling properties.

Keywords: Thin film nanocomposite membranes; Graphene oxide; Glutamic acid; Dyes.

1. Introduction

The growing contamination of water sources with harmful organic compounds discharged by the textile and dyeing industries is a worldwide concern. Due to their widespread use in the textile industry, untreated dye wastewater is one of the leading causes of water pollution [1]. Synthetic dyes including methyl orange (MO) and methylene blue (MB) have been found in textile wastewater. MB is a cationic dye containing adjacent aromatic rings that is utilized in the dyeing of cotton and wool. MO, on the other hand, is an anionic dye with a double bond N=N in its structure that is commonly utilized in printing, textile, and pharmaceutical sectors [2]. Even in low concentrations, these hues in bodies of water are highly visible and have serious adverse effects [2-3]. One of the main effects is a reduction in sunlight infiltration, which negatively influences photosynthesis in living organisms and, as a result, the rate of dissolved oxygen [4-5]. Furthermore, prolonged direct contact with this pollutant class may be detrimental, resulting in digestive, liver, cancer, and other health problems since they are persistent and bioaccumulate in living organisms [6-7].

In order to eliminate dyes from wastewater, physical, biological, and chemical approaches have been examined [8]. However, membrane separation techniques have been favored for the removal of dyes from water sources owing to their multiple benefits such as cost effectiveness, environmental friendliness, excellent removal efficacy as well as low energy consumption [8-9]. Among various membranes, thin film nanocomposite (TFN) membranes prepared using interfacial polymerization (IP) technique on a porous support have demonstrated a high efficacy in the removal of dyes in water [10-13]. Ormanci-Acar et al. (2018) studied dye removal efficacy of TFN membranes containing halloysite nanotubes (HNTs) [14]. In their investigation, HNTs were added to the organic phase during IP to create nanofiltration (NF) membranes that had excellent pH and temperature tolerance [14]. Filtration performance experiments were performed using dyes, NaCl and $MgSO_4$ solutions [14]. At 0.04 wt% of HNTs, $MgSO_4$, NaCl, Reactive orange and Setazol red reactive dyes were rejected at 94.4, 49, 99.7, and 99.7%, respectively [14]. Yang et al. (2022) studied the effects of polydopamine functionalized cellulose nanocrystals (CNCs) TFN membranes for the removal of dye and salt from textile effluent [15]. The TFN membranes displayed exceptional salt permeability of 99.33%, an excellent Congo red (CR) removal of 99.91%, and an outstanding pure water permeability (PWP) of 128.4 LMH bar^{-1} [15].

TFN membranes are characterized by the inclusion of nanofillers in the polyamide (PA) layer which enhance selectivity, antifouling properties, and water flux. The choice of nanofiller is critical to the TFN membranes' fabrication. Unique nanofillers such as halloysite nanotubes (HNTs), cellulose nanocrystals, carbon nanotubes, graphene quantum dots, and metallic organic frameworks (MOFs) have been introduced to the PA layer to boost the membranes' performance [13-14, 16-20]. Graphene oxide (GO) has recently attracted a lot of attention due to its several appealing properties, such as its large specific surface area (~ 2600 m^2g^{-1}), hydrophilic nature, and the presence of epoxy, ketones, carboxyl and hydroxyl groups. These allow for further functionalization of GO, thereby

improving contaminant removal [21-23]. Several studies have been reported where GO was used to boost membrane performance [24-33]. Zhao et al. (2019) examined the impact of GO quantum dots (GQDs) on the performance of the membrane [34]. The GQDs were embedded into the TFN PA layer via surface coating, and membrane rejection against MO and MB dyes was assessed [34]. MO rejection increased from 89.2 to 97% after PA layer modification with GQDs due to electrostatic repulsion [34]. There was a decrease in MB rejection (75.4 -71%), ascribed to the adsorption of positively charged MB onto the membrane, thus reducing water flux and rejection [34].

However, two key issues impede the usage of GO-functionalized membranes in water treatment to date. Agglomeration of GO at high concentrations affects membrane performance and also decreases the membranes water flux and hydrophilicity. Secondly, the stacking of GO nanosheets limits the movement of water through the membrane thus reducing the its permeability [35-37]. Therefore, in an effort to improve membrane performance, it is crucial to address these issues by modifying GO nanosheets via attaching various functional groups prior to membrane fabrication. Seah et al. (2022) examined the effects of modified GO TFN membranes on salt/dye removal [38]. Accordingly, they prepared a PA layer using a mist-based IP approach in order to fabricate TFN membrane with improved characteristics [38]. GO was modified with Acrylic acid (AA) by plasma-enhanced chemical vapor deposition [38]. The acrylic acid-modified GO increased the PWP of TFN membranes by 6.6%, attaining 11.34 $L/m^2h{\cdot}bar$ compared to the control GO TFN. These membranes were comparatively assessed for Rhodamine B, Acid Red, and Rose Bengal dye rejection, achieving rejection rates of more than 98% [38]. Modification of GO to overcome these shortcomings is crucial, since it also enhances water permeability, dye removal, thermal and mechanical stabilities, and antifouling properties. One of the strategies that can be explored is polymerization that involves taking advantage of the functional groups that contain oxygen on the surface of GO to enhance interlayer spacing of the GO sheets which also allows for holding together of the sheets. GO modification via surface-initiated atom transfer radical polymerization (SI-ATRP) is a flexible polymerization technique that results in high grafting density and control over the brushes architecture and thickness. This method involves immobilizing an initiator on the substrates surface, subsequent to the growth phase through the repetitive addition of monomers on the growing chain (polymerization) [39-40]. This functionalization results in multifunctional materials with end group functionalities [41].

In this study, we present the synthesis of GLU polymerized GO (GO-GLU) via SI-ATRP and its subsequent inclusion into TFN membranes for the rejection of MO and MB dyes in water. The incorporation of GO-GLU nanosheets represents an innovative modification of the PA layer, leveraging the functional properties of GO combined with GLU brushes. This functionalization improves water flux, dye rejection efficiency, and antifouling characteristics while maintaining membrane stability over multiple cycles at low operational pressure. The study also evaluates performance against environmental samples (river water), showcasing practical applicability.

2. Materials and Methods

2.1 Materials

Graphite powder, ethanol (CH_3-CH_2-OH), diethyl ether (CH_3-CH_2-O-CH_2-CH_3), phosphoric acid (H_3PO_4), methylene blue ($C_{16}H_{18}ClN_3S$), potassium permanganate ($KMnO_4$), α-bromoisobutyryl bromide (BiBB) (98%), hydrogen peroxide (H_2O_2), chloroform, methanol (CH_3OH), tetrahydrofuran (THF), dimethylformamide (DMF), polysulphone (PSF) pellets (MW= 35 K g/mol), trimesoyl chloride (TMC), glutamic acid, N,N,N ,N ,N‴- pentamethyldiethylenetriamine (PMDETA, 99%), sulphuric acid (H_2SO_4), methyl orange ($C_{14}H_{14}N_3NaO_3S$), triethylamine (TEA, 99%), m-phenylenediamine (MPD), copper(I) bromide (CuBr) and Polyvinylpyrrolidone (PVP) (Mw = 30 – 70 K; 87 – 90%) were obtained from Sigma-Aldrich. De-ionized (DI) water possessing a resistance of 18 mΩ cm was used in all experiments (Milli-Q system, Millipore).

2.2 GO nanosheets synthesis

GO was synthesized by the improved Hummers method [42]. Briefly, graphite powder (1 g) followed by $KMnO_4$ (6g) was added to a concentrated mixture of H_2SO_4 and H_3PO_4 in a 9:1 ratio. For 12 hours, the mixture was stirring in an oil bath set to 50 ℃. After the reaction was completed, it was allowed to cool to ambient temperature before being transferred to 400 mL of ice with 1 mL of 30% hydrogen peroxide (H_2O_2). When the mixture had reached room temperature, it was centrifuged at 4000 rpm for 30 minutes and the supernatant was carefully decanted. The precipitate was washed twice with DI water before being rinsed with 30% HCl and ethanol. After this thorough washing, the residual material was coagulated with 200 mL diethyl ether. The resulting solid was then placed under vacuum and dried overnight at ambient temperature. Finally, the dried solid was pulverized with a mortar and pestle.

2.3 Synthesis of initiator-attached GO (GO-Br)

The modification of GO was performed using an altered approach described by Kumar et al., 2016 [43]. To prepare the colloidal suspension, typically, GO was placed in a round-bottom flask comprising of 30 mL DMF and subjected to sonication for an hour. After adding TEA (4 mL) to the flask, BIBB was gradually added to the mixture which was stirred in an ice bath (24 hours). GO-Br was recovered using centrifugation and washed with chloroform and DI water prior to being vacuum dried for 12 hours.

2.4 SI-ATRP of glutamic acid on initiator attached GO (GO-Br)

The polymerization of GO-Br was performed using a modified approach described by Kumar et al., 2016 [43]. Briefly, sonication was used to disperse 50 mg GO-Br in DMF. Cu(I)Br (0.2 mmol) with various quantities of glutamic acid (50, 100, and 200 mmol) was placed into sealed vials and degassed using nitrogen purging. To the reaction mixture, 0.2 mmol of PMDETA (ligand) was added, followed by 24 hours of polymerization at 70 ℃. Methanol was utilized to precipitate polymer composites by pouring reaction mixture to it. To remove the occluded monomer, the product (GO-GLU 50/100/200) was washed numerous times with chloroform, centrifuged, and vacuum dried for 24 hours.

2.5 Membrane synthesis

Polysulfone (PSF) support preparation

The PSF substrate was produced through the phase inversion technique. To make the PSF membrane casting solution, 1 wt% PVP and 16 wt% PSF were allowed to dissolve in DMF solvent. To ensure homogeneity, the solution was stirred for 12 hours at 50 ℃. To perform solvent/non-solvent exchange (wet phase inversion), the solution was degassed, cast on a glass plate with a thickness of 100 μm, and submerged in a water coagulation bath at ambient temperature. The electrometer 4843 automatic film applicator (Manchester, UK) was used for casting. To eliminate any remaining DMF, the membranes were washed with fresh distilled water and then stored in distilled water until use.

Preparation of polyamide (PA) selective layer

The membranes' PA layer was synthesized atop a PSF support membrane employing the traditional interfacial polymerization (IP) process. Pre-treatment of the PSF support membranes involved soaking them in an overnight solution of 0.5% sodium dodecyl sulphate (SDS). After that, membranes were rinsed for an hour with distilled water. The PSF membrane was then secured between a glass plate and a frame. A 20 mL aqueous solution containing 2 w/v% MPD was poured onto the porous substrate. Following a 2-minute contact period, surplus MPD solution was eliminated from the surface by vertically positioning it for 1 minute. The PSF substrate was then exposed to an organic phase containing a 0.2 wt% TMC-hexane solution for a minute before being removed from the membrane surface. To increase crosslinking, the treated membrane was dried for 8 minutes at 60 ℃ before being rinsed with distilled water. The fabrication technique of GO-GLU TFN membranes resembled that used for TFC membranes, with the exception that GO nanosheets (modified) were first added to an aqueous solution of MPD (**Table 1**). Prior to interfacial polycondensation reaction, all MPD/additives solutions were sonicated for 30 minutes [44].

Table 1: TFN membranes GO-GLU 100 loading.

Membrane	GO-GLU 100 loading (wt%)
TFC	-
TFN-1	0.025
TFN-2	0.05
TFN-3	0.10

2.6 Characterization

An FEI Tecnai G2 Spirit transmission electron microscope (Hillsboro, USA) with a 120 kV acceleration voltage was utilized to study the morphological characteristics of GO nanosheets. Bruker D2 phaser diffractometer (Cu-Ka) (Johannesburg, South Africa) was utilized for X-ray diffraction investigations, with a scanning range of 5 - 90 (2θ). A Tensor 27 Infrared Spectrometer (Massachusetts, USA) was employed to acquire Fourier transform infrared (FTIR) spectra ranging from 500 to 4000 cm^{-1} for the GO nanosheets

and membranes (OPUS software). The magic-angle solid state ^{13}C nuclear magnetic resonance (^{13}C MAS NMR) spectra of GO and GO-GLU were recorded on an AVANCE-III-500 (Bruker, Germany) machine. Direct polarization high power broad band ^{1}H decoupling and Cross-polarization MAS was acquired using 4mm zirconium rotors with 8 or 10 kHz MAS spin-rate. ^{13}C NMR chemical shifts were externally referenced with adamantane as described by Hoffman (2022) [45]. VarioELcube v4.0.13 (Elementar, Germany) was used for elemental study of carbon, hydrogen, nitrogen, and sulfur (CHNS). The thermal properties of GO and its derivatives was studied using thermogravimetric analysis (TGA), which was performed in an inert (nitrogen) environment on a thermogravimetric analyzer through a temperature ranging from 35 - 900 ℃ (heating rate = 20°C/min) (Perkin Elmer). Cross-sectional and surface morphologies of the produced membranes were studied by means of scanning electron microscopy (SEM-EDS) (Tescan Vega). TFN membranes were initially coated (carbon and Pd/Au) and examined under SEM (accelerating voltage = 20 kV). To assess membranes hydrophilicity, contact angle instrument (DataPhysics Instruments GmbH, Filderstadt, Germany) was used to measure the contact angles using the sessile-drop method. Each membrane sample (dried) was measured ten times at various regions using the sessile-drop method.

GO and derivatives' pH point of zero charge (pH PZC) was obtained through the use the salt titration method [46]. Briefly, 0.1g of GO-GLU 100 was placed in five polypropylene tubes containing 25 mL of 0.01M NaCl. The pH of these solutions was then altered between 2 – 10 with 0.1 M HNO_3 as well as 0.1 M NaOH, giving each one a unique pH value. The suspensions were shaken horizontally for 24 hours. Each solution's final pH was plotted against its original pH, and the material's pH PZC was derived using the intersection points [46].

2.7 Water intake capacity (WIC)

The weight difference between the dry and wet TFC and TFN membranes was used to calculate WIC. To determine the dry weight (W_d), the membranes were oven-dried to remove any moisture thereafter weighed before being placed in distilled water (24 hours). The saturated membranes were gently patted prior to weighing to ascertain their wet weight (W_w) (**Equation 1**).

$$WIC\ (\%) = (W_w - W_d)/W_d \quad X\ 100 \qquad (1)$$

2.8 Membrane performance

The performance of all developed membranes was assessed by the use of a dead-end filtration system that is nitrogen-pressure driven (HP4750 Stirred Cell, Sterlitech) (**Scheme 1**). Membranes having an area of 0.00146 m^2 were compacted with DI water (transmembrane pressure = 600 kPa) until a steady flow was achieved. **Equation 2** was employed to compute the pure water flux at a pressure of 300 kPa with DI water as the feed solution.

$J_w = Q/ (A.\Delta t)$ (2)

Whereby: Q is the volume of permeated water (L); A is the membrane's effective area (m^2), Δt is the permeation time (h) and J_w is the pure water flux (L/m^2h);

A dead-end filtering cell was employed for dye rejection tests (single component), with continual magnetic stirring (**Scheme 1**). Two organic dyes of different electrostatic charges were used; Methyl orange (MO) and Methylene blue (MB) (**Table 2**). At 300 kPa, varying dye concentrations (20, 50, 80, 100 mg/L) and pH (2 – 7 – 11) were investigated (single component), these were run through the cell. River water samples were collected from South Africa's Vaal River to evaluate the potential use of the TFN membrane in environmental water systems. The physicochemical characteristics of the water samples were as follows: conductivity 834 µS/cm, pH 7.61, total dissolved solids (TDS) 417 ppm, and resistivity 1.20 KΩ.cm. The water samples were spiked with MB dye (50 mg/L). The change of the concentration of the MB and MO solution was monitored by means of UV–visible (UV–vis) spectroscopy at 664 and 464 nm, respectively.

The measured rejection (%R) was determined using **Equation 3**:

$\%R = (1 – (C_p / C_f)) \times 100$ (3)

where C_f and C_p denote the dye concentrations (mg/L) of the feed and permeate solutions.

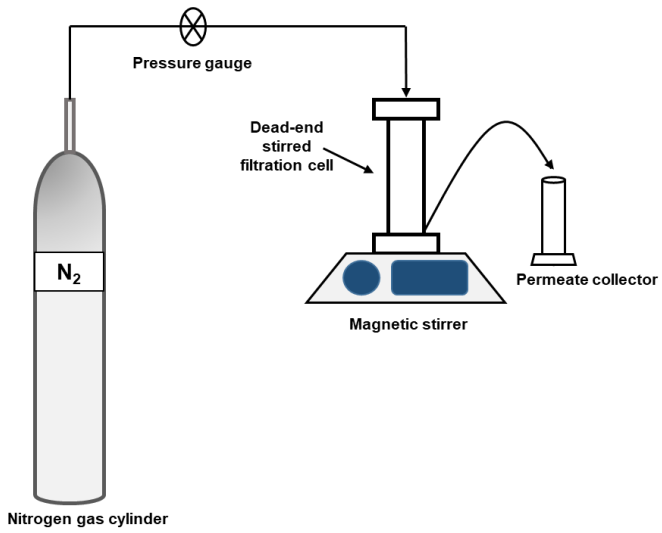

Scheme 1: Schematic illustration of a bench top dead-end filtration setup.

Table 2: The molecular structure, weight and charge of the dyes

Dyes	**MB**	**MO**
Molecular structure	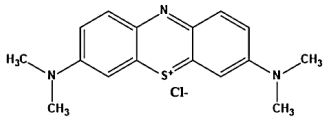	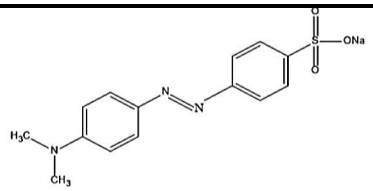
Charge	+	-
Molecular weight (MW) (g/mol)	**319.85**	**327.33**

2.9 Antifouling studies

BSA protein solution (concentration =1 g/L; pH = 7) was employed to evaluate the membranes fouling characteristics. Firstly, the pure water flux (J_{po}) was determined at a pressure of 300 kPa over a duration of 120 minutes. The pure water was subsequently substituted with the BSA solution and the permeate flow (J_{pt}) was measured every 15-minute for 120 minutes. The BSA solution was then substituted with pure water and the flux (J_{pf}) was measured again for 120 minutes. The following equations were used to determine the total fouling ratio (Rt), irreversible flux decline ratio (Rir), reversible flux decline ratio (Rr), and flux recovery ratio (FRR):

$$FRR\ (\%) = J_{pf}/J_{po} \times 100 \quad (4)$$

$$Rt\ (\%) = (J_{po} - J_{pt})/ J_{po} \times 100 \quad (5)$$

$$Rir\ (\%) = (J_{po} - J_{pf})/J_{po} \times 100 \quad (6)$$

$$Rr\ (\%) = (J_{pf} - J_{pt})/J_{po} \times 100 \quad (7)$$

3. Results and Discussion

3.1 Morphology of GO nanocomposites and membranes

Figure 1 reveals the morphological investigation of the GO nanocomposites using TEM. Pristine GO and GO-Br images revealed smooth, thin and laminar structure ranging from nano to micron scale nanosheets. **Figure 1 (b)** displayed no observable difference in the morphology of the nanosheets after modification with ATRP initiator α-bromoisobutyryl bromide. However, in **Figure 1 (c, d)**, GO is covered with nanosized poly(glutamic acid) brushes which are homogenously spread on the surface of GO. This is due to the collapsed chains on the surface of the GO sheets resulting in nanosized spots [47-48]. With the increase in the grafting amount of glutamic acid, there is an observable increase in the sizes of dark spots and the aggregation of these (**Figure 1**). EDS analysis of GO-Br was carried out (**Figure S1**). The EDS analysis of GO-Br verified the presence of C, O and Br at 0.27, 0.52 and 1.48 keV respectively, confirming the attachment of the Br containing initiator to the GO.

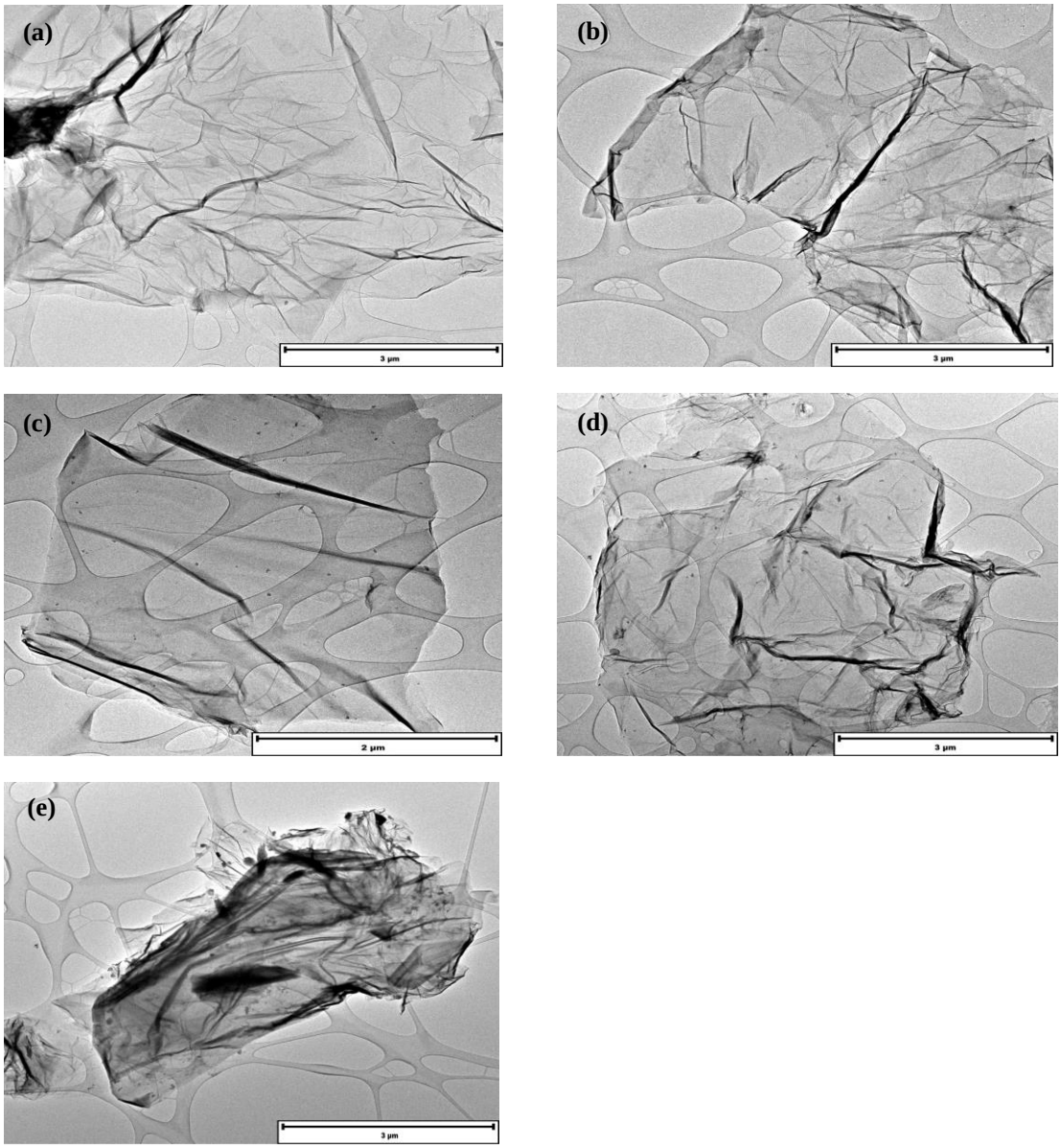

Figure 1: TEM images of pristine GO (a), GO-Br (b), GO-GLU 50 (c), GO-GLU 100 (d) and GO-GLU 200 (e).

Membrane morphology and AFM analysis

Figure 2 depicts the synthesized membranes' surface and cross-sectional morphologies. The pure PSF membrane (**Figure 2 (a, b)**) produced via phase inversion has an asymmetric spongy-like architecture comprising of a dense skin layer and a porous sub-layer. During phase inversion, the cast PSF polymer solution on a glass plate is immersed into a non-solvent bath (i.e. water) resulting in a rapid non-solvent/solvent replacement across the interface of non-solvent and casting film. Moreover, repulsive forces amid polymer and water sped up the precipitation of polymeric solution at the interface leading to the development of sub layer macro-voids and typical asymmetric structure together with a dense surface containing micro-pores [49-50]. The PSF support was used due to its favorable properties, which are crucial for enhancing membrane performance. The PSF

material exhibits superior chemical and thermal stability, enabling it to operate effectively across a wide range of temperatures and pH levels, as well as demonstrating excellent resistance to chlorine. [50] The cross sections morphology for all the membranes are similar exhibiting asymmetric structure that comprises of a macro-void containing porous sub-layer and a dense top layer (**Figure 2 (b, d, g, j, m)**). Upon IP, the surface morphology of TFC and TFN membranes displayed dense surfaces with the isolated distributed protrusions (**Figure 2 (c, f, i, l)**). At lower nanoparticle concentrations, the TFN membranes were similar to TFC membrane signifying that the nanoparticles produced no significant effect on the surface morphology of the TFN membranes. However, nanoparticles aggregated as concentrations increased. (**Figure 2 (l))** [51].

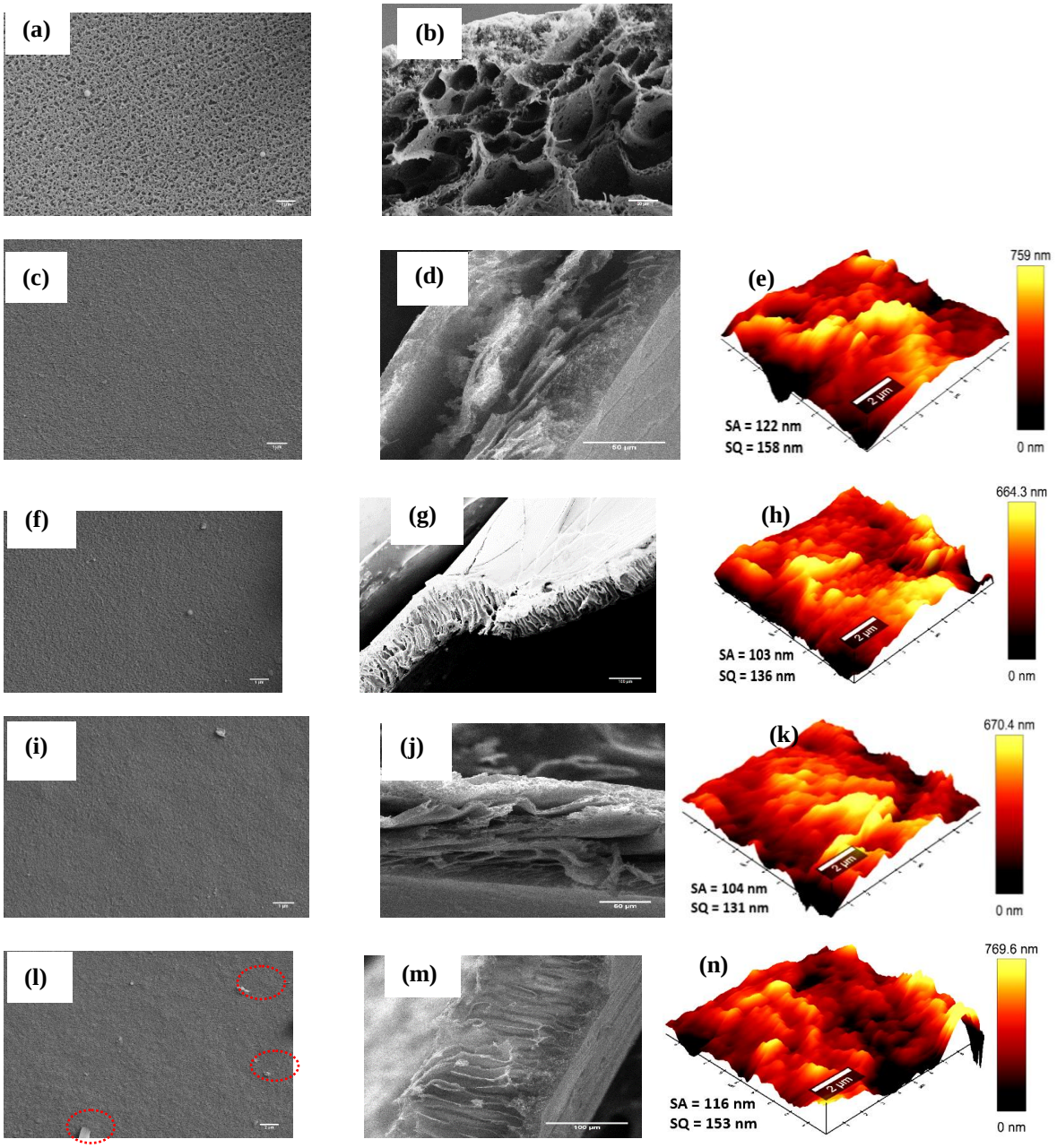

Figure 2: Surface, cross section morphologies and AFM images of PSF (a, b), TFC (c, d, e), TFN-1 (f, g, h) TFN-2 (i, j, k) and TFN-3 (l, m, n).

Surface roughness for TFN membranes investigations were conducted using AFM analysis as presented in **Figure 2**. As shown, the membrane surface structures are depicted as bright and dark areas, representing the peaks and valleys, respectively. As displayed in **Figure 2 (e, h, k, n)**, the TFC membrane displayed a rougher surface (Sa = 122 nm) compared to other membranes (103 – 116 nm). Lower concentrations of nanoparticles in the PA layer result in decreased surface roughness. This might be caused by the inclusion of hydrophilic nanofiller, which may increase the compatibility of organic and aqueous phases during IP [52]. In principle, membrane surfaces with low roughness and high hydrophilicity are expected to offer better fouling resistance [53]. On the other hand, there was an observed slight increase of roughness at TFN-3, and this could be attributed to surface-located clusters caused by the agglomeration of the GO. The morphological variation detected by AFM correlated with the SEM findings.

3.2 FTIR and elemental analysis of GO nanocomposites and membranes

Figure 3 illustrate the chemical transformation of GO, GO-Br and GO-GLU as confirmed by FTIR analysis. FTIR spectrum of pristine GO indicate a prominent peak at 3321 cm^{-1}, indicative of the stretching vibrations of OH groups present in GO (**Figure 3 (a)**). The GO spectrum additionally displayed peaks at 2978 cm^{-1} credited to CH_2, 1737 cm^{-1} attributed to the stretching vibration of -C=O bond from the carboxylic group, 1611 cm^{-1} corresponds to the presence of unoxidized sp^2 C=C bond in the graphitic lattice structure, 1420 cm^{-1} ascribed to the C-OH, 1226 cm^{-1} linked to stretching vibrations of C-O group, and 1027 and 863 cm^{-1} may be ascribed to epoxy groups [54]. Following the modification of GO with the ATRP initiator BIBB, there was a decrease in O-H signal signifying that the O-H groups on GO's surface underwent esterification with the initiator **(Figure 3(a))**. The substitution of the C-OH and C-O-C peaks of GO with a new peak at about 1180 cm^{-1} may be ascribed to the stretching vibrations of esters' C-O. In **Figure 3 (b)**, the GO-GLU 100 displayed peaks at 1714 cm^{-1} which correspond to the stretching vibration of -C=O bond due to the presence of the carboxylic group in glutamic acid. Other peaks include 1570 cm^{-1} for the N-H bend, 1371 and 1131 cm^{-1} corresponds to the -C-N- stretching in the secondary amide groups which confirms the amidation reaction. Notably, the peaks at 1610 and 1511 cm^{-1}, which are associated with primary amine groups in glutamic acid, are absent in the GO-GLU 100 sample. This FTIR analysis proves the successful covalent attachment of glutamic acid brushes to the GO nanosheets.

The elemental analysis also revealed the contents of C, H, N and S present in the GO and nanohybrids as shown in **Table 3**. As the glutamic acid grafting amount increased, similarly its Nitrogen content (3.57 – 5.7%). This correlates with the TEM analysis where the dark spots on the GO increased with the increase in glutamic acid amount grafted.

Table 3: Elemental analysis of GO, GO-GLU 50, GO-GLU 100 and GO-GLU 200

Elements (%)				
Sample	C	H	N	S
GO	37.7	2.894	0	3.783
GO-GLU 50	57.2	2.679	3.57	0.415
GO-GLU 100	56.78	2.804	3.9	0.412
GO-GLU 200	49.9	3.526	5.17	0.223

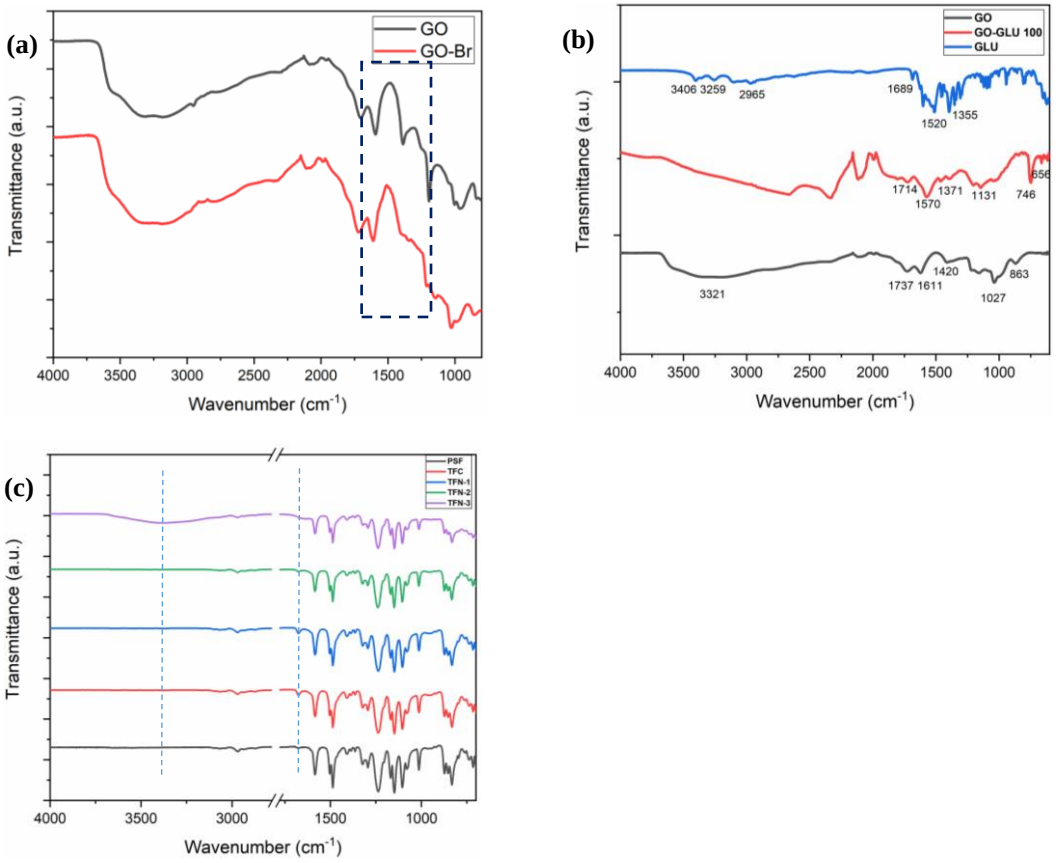

Figure 3: FTIR spectra for GO and GO-Br (a), GO, GO-GLU 100 and GLU (b), and for PSF, TFC, TFN-1, TFN-2 and TFN-3 (c).

FTIR analysis was performed to identify the chemical composition of virgin PSF, TFC, and TFN membranes (**Figure 3 (c)**). The FTIR spectra of the pristine PSF membrane exhibited distinct peaks at 2981, 1489, 1293, and 1322 cm^{-1} assigned to aliphatic C-H stretching, C=C stretching within the aromatic ring, S=O stretching, and asymmetric stretching of the C-SO_2-C group, respectively [55]. The aromatic rocking vibrations of C-H peaks can be detected at 1007 and 828 cm^{-1}. Following IP, the TFC and TFN membranes displayed spectra that differed from the virgin PSF membrane. The amide groups (C=O) at 1675 cm^{-1} are due to an interaction between MPD's amine groups and TMC's acyl chloride groups [56]. This proves that the PA layer was successfully formed via IP [56]. Regardless of the GO loading, the TFC and TFN spectra exhibited similar spectra with significant

peaks at 1675, 1241 cm^{-1} which are credited to C=O (Amide I) and C-N stretch [57]. Furthermore, TFN-3 exhibits a prominent band at 3372 cm^{-1} ascribed to the hydroxyl stretching from the TMCs incomplete hydrolyzed acyl chloride, this also attests to the effective synthesis of the PA layer [58].

3.3 TGA, XRD analysis and NMR analysis of GO nanocomposites

Figure 4 (a, b) depicts the TGA of GO and its functionalized hybrids. Functionalized GO displayed a distinct thermal degradation behavior than GO, indicating the successful modification of GO. The GO lost weight in three stages: loss of bound water at 30 - 150 °C, decomposition of labile epoxy, carboxylic, and hydroxyl groups (180 – 285 °C), and degradation of C-C backbone at ~285°C [59-60]. The final mass was approximately 30% of the initial weight. The GO-Br thermal degradation followed a similar trend but its final mass was slightly higher (~40%). This was due to the reduction of oxygenated groups thus less mass loss. Upon glutamic acid brushes grafting, GO-GLU 50 and 100 exhibited higher thermal stabilities with final masses of ~60%. This was attributed to the zwitterions shielding effect on oxygen-containing groups on GO sheets [61]. This also indicates that GO oxygenated functional groups were part of the organo-modification reaction with glutamic acid. However, with an increase in grafting density, GO-GLU 200 displays thermal instability with a major weight loss at 400 – 500 °C and a final mass of ~20%. This is attributable to the lowered van der Waals forces between GO layers as a result of the insertion of polymers between the sheets [60]. GO-GLU 100 was chosen as the optimal nanofiller due to its enhanced thermal stability and homogeneous distribution of glutamic acid brushes on GO nanosheets as observed in TEM analysis.

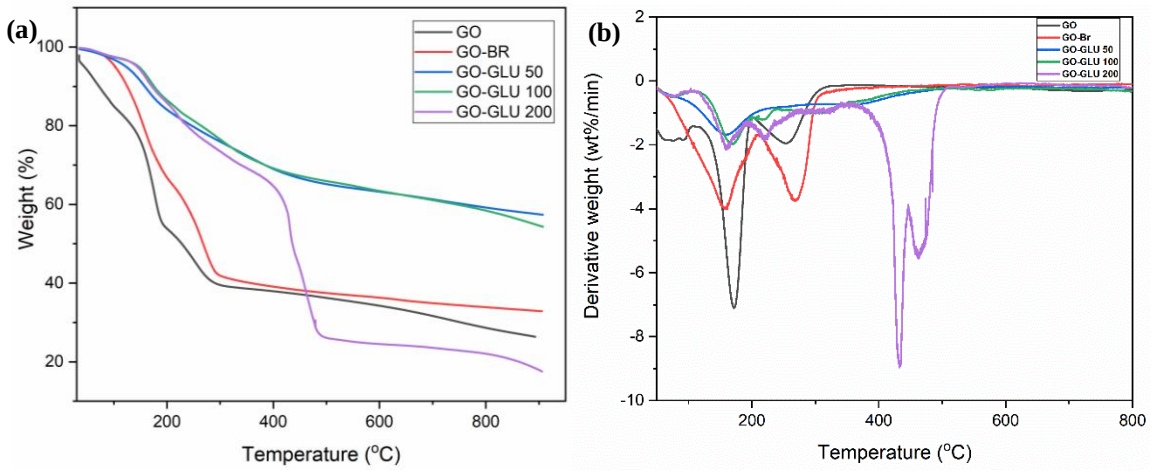

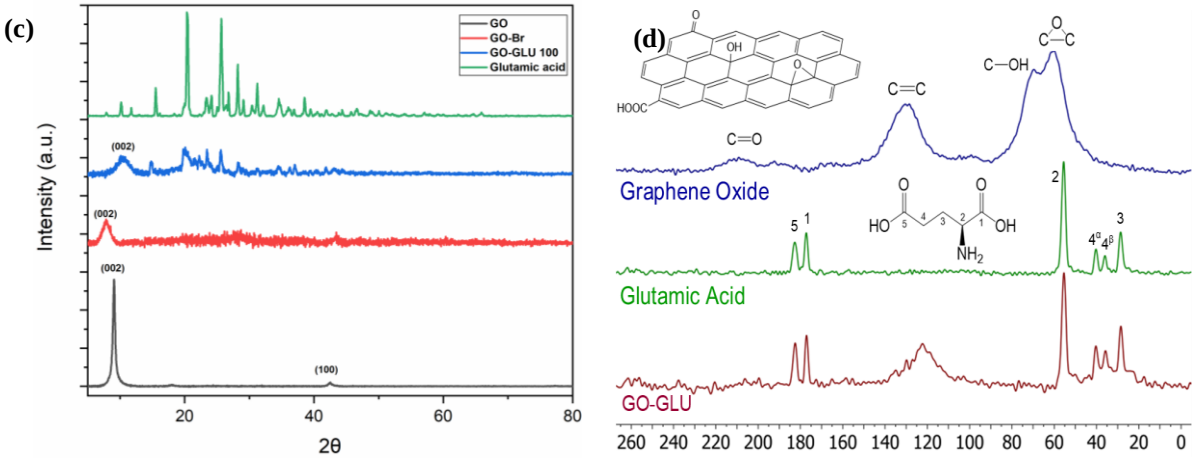

Figure 4: TGA thermograms of GO, GO-Br, GO-GLU 50, GO-GLU 100, and GO-GLU (200) (a) and corresponding derivative weight plot (b); XRD patterns of GO, GO-Br, GO-GLU 100 and GLU (c); ^{13}C MAS NMR spectrum of GO, GLU and GO-GLU (Pulse program = hpdec, MAS = 10 kHz) (d).

XRD analysis validated the synthesis of GO (**Figure 4 (c)**). GO diffraction patterns showed peaks at 9.2 and 43 at 2θ values, representing the (0 0 2) and (1 0 0) GO reflections, respectively. GO's interlayer spacing was 0.96 nm [22]. The diffraction angle of GO-Br is observed at 7.9° displaying a significant increase in interlayer distance (1.12 nm). This is credited to the reduced intercalated water molecules between the layers due to the decrease in oxygenated functional groups [61]. The XRD pattern for glutamic acid revealed its high crystallization. The GLU polymerized GO displayed a relatively weak peak at 10.5 2θ indicating an interlayer distance of 0.84 nm prompted by the presence of GLU polymer brushes. The GO-GLU XRD pattern proved the reaction between the GO and the GLU polymer brushes formed crystal complexes via chemical covalent bonds.

GO contains significant epoxide and hydroxyl functionality as shown by the ^{13}C MAS NMR spectrum (**Figure 4 (d)**). Upon grafting with GLU, these peaks seem to be significantly less prominent and an upfield shift is observed for the sp^2 carbons of the modified GO. Interestingly, the spectrum of GLU shows 2 peaks for the carbon at position 4. This can be attributed to the mixture of α and β polymorphs that exist in a typical GLU sample. All the carbons are expected to be unique for the α and β phases, but they are not resolved in this case. The higher resolution ^{13}C CP MAS NMR spectrum confirms the presence of both α and β polymorphs with all the signals resolved which is confirmed by the chemical shifts obtained by Wang et al. (2016) [62] (**Figure S2**).

3.4 Point of zero charge (PZC)

A substance's PZC in solution is the pH whereby its overall surface charge is zero [63]. The pH PZC of GO-GLU 100 was 5.45, meaning at a pH of the solution that exceeds 5.45, the surface charge is negative, neutral at a pH of 5.45, and positive when the pH is less (**Figure S3**) [64]. Incorporating GO-GLU 100 to the PA layer of membranes will inevitably influence their overall charge. This could indicate that the membrane's pH PZC is close to pH 5.45.

3.5 Water permeation studies

The membranes hydrophilicity was assessed using water intake capacity (WIC) and contact angle measurements (**Table 4**). The TFC membranes' contact angle was higher than the TFN membranes owing to the introduction of GO-GLU 100 in the PA layer. With an increase in GO-GLU 100 (0.025 – 0.10 wt%) in the PA layer, a decrease in water contact angle was noted (91.61 ± 6.53 – 83.18 ± 5.07 ^{o}). The membranes' hydrophilicity was slightly enhanced by the modified GO nanosheets that readily interacted with water molecules thus lowering the contact angle [65]. This was also confirmed by the WIC which is a bulk hydrophilicity assessment of membranes. The WIC was seen to increase proportionally to the GO-GLU 100 concentration as a result of increase of hydrophilic functional groups per unit area of the membranes. The TFC membrane exhibited the lowest WIC (60.11%) whilst the TFN membranes exhibited higher WIC (72.63 – 77.64%).

Table 4: Membrane pure water permeation studies

Membrane	WIC (%)	WCA (^{o})
TFC	60.11	94.29 ± 5.12
TFN-1	72.63	91.61 ± 6.53
TFN-2	77.64	89.37 ± 6.56
TFN-3	76.55	83.18 ± 5.07

3.6 Membrane filtration properties and antifouling studies

Water permeate flux was utilized to assess the effect of GO-GLU 100 on membrane efficiency (**Figure 5**). At 300 kPa, the concentration of GO-GLU in the PA layer led to an increase in pure water flux (PWF) from 7.69 ± 0.43 to 14.11 ± 0.22 L/m^{2}h. The membranes permeability increased as the nanocomposite increased with TFC having the least PWF and TFN-3 having the highest. The permeability of the membranes is linked to its internal structure and hydrophilicity. This membrane's water permeability and rejection efficacy are determined by the spacing between the layers GO nanosheets coupled with tortuosity of the transport channels. Growing polymer brushes on the GO nanosheets enhanced the lateral and vertical tortuous paths of the GO in the selective PA layer, hence boosting the PWF, as presented in **Scheme 2**. [66].

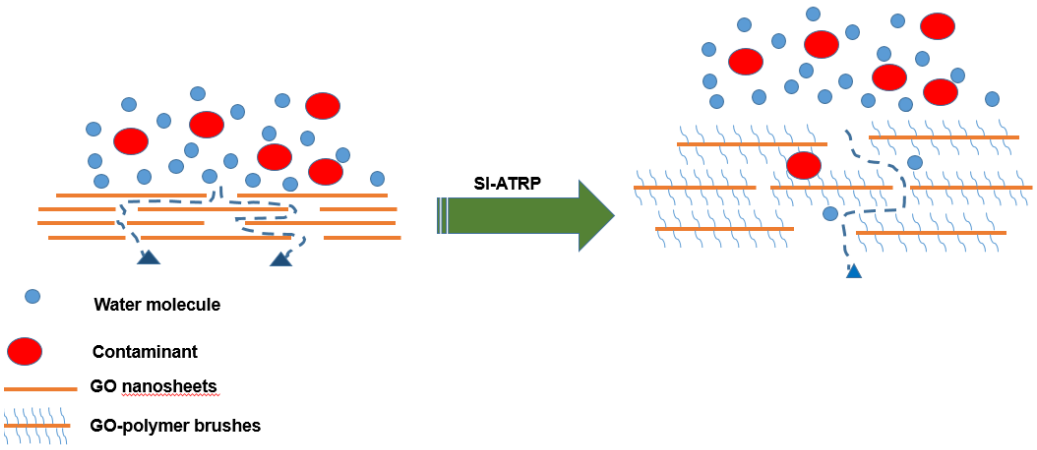

Scheme 2: Schematic illustration of diffusion pathways in GO and polymer brush modified GO.

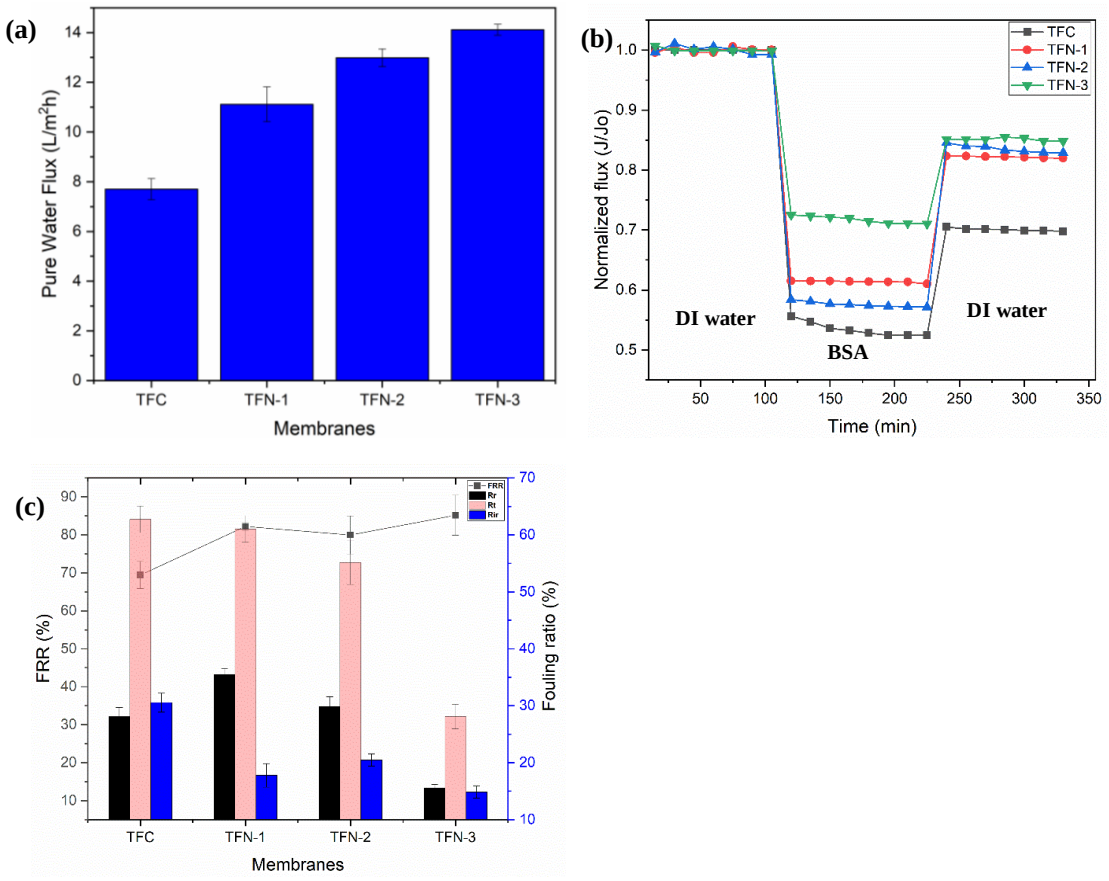

Figure 5: Pure water flux of membranes (300 kPa) (a), antifouling experiments for the filtration of BSA; The variation in flux over time (b); and fouling parameters (recovery ratio (FRR), fouling resistance ratios (Rt, Rr, Rir) for different membranes (c).

Fouling is unavoidable throughout NF operations, owing mostly to the hydrophobic qualities of the surface of NF membrane. The TFN membranes' antifouling characteristics were evaluated using separation experiments with BSA solution (foulant) and pure water as illustrated in **Figure 5 (b, c).** After 120 min running with BSA solution, the permeate fluxes of TFC, TFN-1, TFN-2 and TFN-3 were maintained at ~53%, ~61%, ~57%, and ~72% respectively. The reduction in flux is caused by membrane fouling, which is likely initiated by electrostatic and hydrophobic interactions, Van der Waals forces, and hydrogen bonding forces [67]. TFN membranes had greater BSA normalized flux than TFC membranes. Deionized water was utilized to clean the membranes, and their recovery rates for permeate flux were ~70%, ~82%, ~83% and ~85% respectively. TFN-3 exhibited the best antifouling performance with a recovery normalized flux of ~ 85%. TFC membranes have a lower flux recovery ratio (FRR) (70.12%) than TFN membranes (79.25-85.19%). The TFC membrane's fouling resistance ratio, Rir, was found to be 29.88%. However, Rir values for TFN membranes were substantially lower (14.82 - 20.79%). The decrease in BSA adsorption onto the surface of the membrane is most probably associated with an increase in the hydrophilicity of TFN membranes. BSA molecules are easily removed by backwashing since foulant-membrane interaction decreases as hydrophilicity increases [68].

3.7 Dye rejection studies

3.7.1 Dye concentration effect

To examine the dye removal capabilities of the membranes, tests were performed with varied concentrations of MB and MO (20 – 100 mg/L). MB and MO represent both cationic and anionic dye categories. This allows for a comprehensive evaluation of the adsorption/rejection performance of the TFN membranes across different charge types. Moreover, MB and MO dyes are prevalent in industrial wastewater, making them a relevant choice for this study. Among all the prepared membranes, TFC and TFN-3 selected for dye removal studies (**Figure 6 (a, b)**). **Table 2** displays the charge and molecular weight (MW) of the dyes under investigation. The surface charge and MW of dye molecules play a critical role in determining their adsorption and/or rejection by TFN membranes. The charge of the dye influences its electrostatic interactions with the membrane surface, thereby affecting whether the dye is retained or allowed to pass through. Meanwhile, the molecular weight dictates the size of the dye molecules relative to the membrane pores, which impacts their ability to be filtered out or permeate through the membrane. Together, these factors are essential for understanding and optimizing the separation performance of TFN membranes. TFC membrane rejection of MB dye ranged from 95.99 – 96.87%, whilst TFN-3 rejection ranged from 98.15 – 99.18% (**Figure 6 (a)**). MO dye rejections were lower for both TFC (38.47 - 50.46%) and TFN-3 (51.71 - 67.18%) (**Figure 6 (b)**). These results prove that the addition of modified GO nanosheets enhance dye separation owing to a rise in membrane electrostatic charge. The presence of carboxyl groups on the GO-GLU TFN membrane resulted in a negatively charged surface with a high electrostatic affinity to positively charge MB dye molecules. In contrast, the membrane's negatively charged surface causes electrostatic repulsion towards an anionic

dye. Consequently, the cationic dye (MB) displayed better rejection than the anionic dye (MO). Moreover, steric hindrance effects, sieving and the Donnan exclusion principle are useful in explaining the rejection behavior [69]. The increased rejection of MB is additionally credited to its larger hydrated radii of 5.04A as compared to MOs radii of 4.97A that causes sieving hindrances [70-71]. As indicated in **Figure 6 (c)**, the measured permeate fluxes were lower than those of pure water owing to the dye's sorption on the membrane.

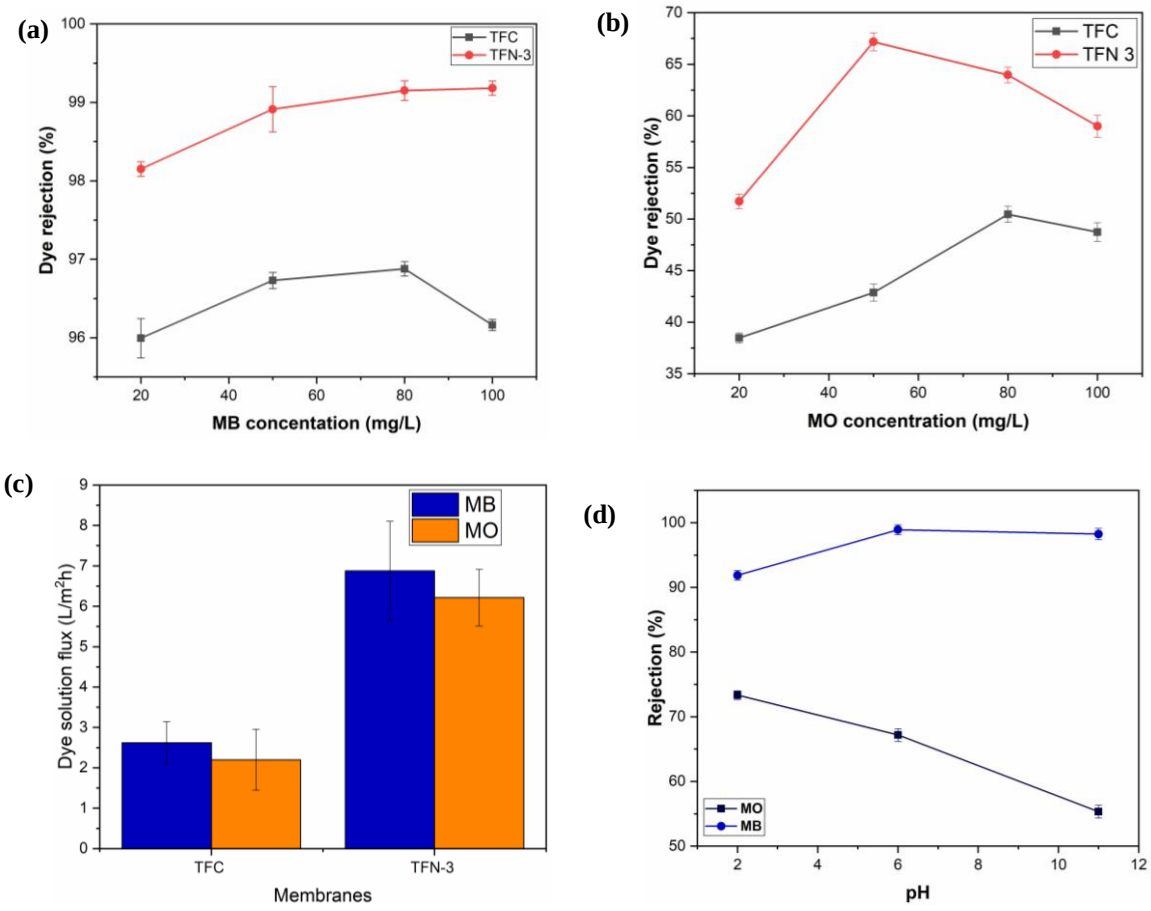

Figure 6: Dye rejection performance of TFC and TFN-3 membranes (300 kPa); MB (a) and MO (b); dye solution flux for TFC and TFN-3 membranes (300 kPa) (c); and TFN-3 dye rejection vs pH (300 kPa) (d).

3.7.2 Effect of feed solution pH

Similarly, interest was shown in investigating the influence of MB and MO dyes (50 mg/L) on pH-responsive behavior. Membrane separation efficiency can be efficiently altered because solution pH has a profound effect on the electrochemical characteristics of the dye molecules and membrane surface. **Figure 6 (d)** shows the pH-responsive separation performance of the dyes. The rate of MB rejection was above 90% at all pH ranges, with pH over 7 improving rejection to 98%. The membrane surface's negative charge lowers at lower pH levels, making it easier for negatively charged MO molecules to adsorb and

deposit on it. At pH 2, MO had the highest rejection rate of ~74%. As the solution pH increases, so does the membranes surface negative charge, and hence MO rejection reduces. Electrostatic repulsion reduced the ability of negatively charged MO dye molecules to adsorb on the membrane surface.

3.7.3 Reuse performances

Membrane reusability is critical for practical applications, particularly on a large scale. Accordingly, the membrane's efficiency and stability is key. As seen in **Figure S4**, the TFN-3 membrane presented excellent rejection performance for both MB and MO dyes (50 mg/L, solution pH) even after three cycles. The removal efficiency of MB dye decreased from 98 – 87% whilst MO rejection decreased from 67 – 54%. This could be due to membrane fouling or the cleaning process's inability to completely remove absorbed dye molecules. This will eventually lead to a deterioration in the membrane's removal effectiveness.

3.8 Dye removal from spiked river water

Spiked river water samples from South Africa's Vaal River were used to examine the possible applicability of the TFN membrane in environmental water systems. The physicochemical characteristics of the water samples were as follows: conductivity 834 µS/cm, pH 7.61, total dissolved solids (TDS) 417 ppm, and resistivity 1.20 KΩ.cm. The removal efficiencies are presented in **Figure S5**. TFN-3 membrane demonstrated higher removal efficiency for both MB (99.65%) and MO (71.72%) dyes than the control TFC membrane, which removed 95.73 and 49.85% for MB and MO, respectively. The increased removal observed for TFN-3 is due to the synergistic elimination caused by steric hindrance effects, sieving, and Donnan exclusion [69].

3.9 Performance Comparison of GO-based TFN Membranes

Table S1 provides a comparative analysis of the performance metrics for GO-based TFN membranes, specifically examining water permeability and dye rejection rates in relation to those developed in this study. Notably, the pressure applied in this research was lower than that typically reported in existing literature. Despite this, the water flux of the GO-GLU incorporated TFN membranes was found to be comparable to that of membranes discussed in previous studies. Most NF membranes operate at significantly higher pressures, which can lead to increased operational costs. The remarkable separation efficiency of the TFN-3 membranes at lower pressure indicates that GO-GLU could be an effective filler material for designing low-pressure TFN NF membranes. This finding highlights the potential for optimizing membrane performance while reducing energy expenditures.

4. Conclusion

This study successfully fabricated low pressure TFN membranes by incorporating GO-GLU nanosheets into the PA selective layer via interfacial polymerization. The results demonstrate that GO-GLU significantly enhances membrane hydrophilicity, negative charge density, surface roughness, and antifouling properties. At the optimal GO-GLU dosage of 0.10 wt%, the TFN-3 membrane achieved a water flux of 14.11 L/m2h at 300 kPa, with superior dye rejection rates of 99.18% for MB and 67.18% for MO. Furthermore, the TFN-3 membrane exhibited excellent antifouling resistance against BSA and maintained stable performance across three operational cycles. Real-world application testing revealed remarkable dye removal efficiency from river water samples, with rejection rates of 99.65% for MB and 71.75% for MO - outperforming conventional TFC membranes. These results highlight the potential of GO-GLU-based TFN membranes as a promising solution for sustainable wastewater treatment, paving the way for innovative approaches in NF technology.

References

[1] L. Wu, X. Liu, G. Lv, R. Zhu, L. Tian , M. Liu , Y. Li ,W. Rao, T. Liu , L. Liao. Study on the adsorption properties of methyl orange by natural one-dimensional nano-mineral materials with different structures. *Sci Rep*. 2021;11(1):1-11. doi:10.1038/s41598-021-90235-1

[2] J. Shakya, T. Mahanta, S. Kumar, T. Mohanty. Photocatalytic degradation of anionic and cationic dye by using nitrogen doped MoS_2. 2019, *AIP Conf Proc*. doi:10.1063/1.5113024

[3] N. Nikooe, E. Saljoughi. Preparation and characterization of novel PVDF nanofiltration membranes with hydrophilic property for filtration of dye aqueous solution. *Appl Surf Sci*. 2017;413:41-49. doi:10.1016/j.apsusc.2017.04.029

[4] M.T. Yagub, T.K. Sen, S. Afroze, H.M. Ang. Dye and its removal from aqueous solution by adsorption: A review. *Adv Colloid Interface Sci*. 2014;209:172-184. doi:10.1016/j.cis.2014.04.002

[5] R.S. Bangari, A. Yadav, J. Bharadwaj, N. Sinha. Boron nitride nanosheets incorporated polyvinylidene fluoride mixed matrix membranes for removal of methylene blue from aqueous stream. *J Environ Chem Eng*. 2022;10(1):107052. doi:10.1016/j.jece.2021.107052

[6] E. Pramono, K. Umam, F. Sagita,O.A. Saputra, R. Alfiansyah, R.S.S. Dewi, G.T.M. Kadja, M. Ledyastuti, D. Wahyuningrum, C.L. Radiman. The enhancement of dye filtration performance and antifouling properties in amino-functionalized bentonite/polyvinylidene fluoride mixed matrix membranes. *Heliyon*. 2023;9(1):e12823. doi:10.1016/j.heliyon.2023.e12823

[7] Q. Li, Y. Li, X. Ma, Q. Du, K. Sui, D. Wang, C. Wang, H. Li, Y. Xia. Filtration and adsorption properties of porous calcium alginate membrane for methylene blue removal from water. *Chem Eng J*. 2017;316:623-630. doi:10.1016/j.cej.2017.01.098

[8] P. Moradihamedani. Recent advances in dye removal from wastewater by membrane technology: a review. *Polym Bull*. 2022;79(4):2603-2631. doi:10.1007/s00289-021-03603-2

[9] Z. Liao, J. Zhu, X. Li, B. Van der Bruggen. Regulating composition and structure of nanofillers in thin film nanocomposite (TFN) membranes for enhanced separation performance: A critical review. *Sep Purif Technol*. 2021;266:118567. doi:10.1016/j.seppur.2021.118567

[10] Y. Mansourpanah, A. Ghanbari, H. Yazdani, A.G. Mohammadi, A. Rahimpour. Silver-polyamidoamine/graphene oxide thin film nanofiltration membrane with improved antifouling and antibacterial properties for water purification and desalination. *Desalination*. 2021;511:115109. doi:10.1016/j.desal.2021.115109

[11] P. Zhao, R. Li, W. Wu , J. Wang, J. Liu, Y. Zhang. In-situ growth of polyvinylpyrrolidone modified Zr-MOFs thin-film nanocomposite (TFN) for efficient dyes removal. *Compos Part B Eng*. 2019;176:107208. doi:10.1016/j.compositesb.2019.107208

[12] Y. Wang, H. Xu, M. Ding, L. Zhang, G. Chen, J. Fu, A. Wang, J. Chen, B. Liu, W. Yang. MXene-regulation polyamide membrane featuring with bubble-like nodule

for efficient dye/salt separation and antifouling performance. *RSC Adv*. 2022;12(17):10267-10279. doi:10.1039/d2ra00335j

[13] S.R. Mousavi, M. Asghari, N.M. Mahmoodi. Chitosan-wrapped multiwalled carbon nanotube as filler within PEBA thin film nanocomposite (TFN) membrane to improve dye removal. *Carbohydr Polym*. 2020;237:116128. doi:10.1016/j.carbpol.2020.116128

[14] T. Ormanci-Acar, F. Celebi, B. Keskin,O. Mutlu-Salmali, M. Agtas, T. Turken, A. Tufani, D.Y. Imer, G.O. Ince, T.U. Demir, Y.Z. Menceloglu, S. Unal, I. Koyuncu. Fabrication and characterization of temperature and pH resistant thin film nanocomposite membranes embedded with halloysite nanotubes for dye rejection. *Desalination*. 2018;429:20-32. doi:10.1016/j.desal.2017.12.005

[15] L. Yang, X. Liu, X. Zhang, T. Chen, Z. Ye, M.S. Rahaman. High performance nanocomposite nanofiltration membranes with polydopamine-modified cellulose nanocrystals for efficient dye/salt separation. *Desalination*. 2022;521:115385. doi:10.1016/j.desal.2021.115385

[16] R. Bi, Q. Zhang, R. Zhang, Y. Su, Z. Jiang. Thin film nanocomposite membranes incorporated with graphene quantum dots for high flux and antifouling property. *J Memb Sci*. 2018;553:17-24. doi:10.1016/j.memsci.2018.02.010

[17] T. Zhang, P. Li, S. Ding, X. Wang. High permeability composite nanofiltration membrane assisted by introducing TpPa covalent organic frameworks interlayer with nanorods for desalination and NaCl/dye separation. *Sep Purif Technol*. 2021;270:118802. doi:10.1016/j.seppur.2021.118802

[18] L. Yang, X. Zhang, W. Ma, B. Raisi, X. Liu, C. An, Z. Ye. Trimethylamine N-oxide-derived zwitterionic polyamide thin-film composite nanofiltration membranes with enhanced anti-dye deposition ability for efficient dye separation and recovery. *J Memb Sci*. 2023;665:121083. doi:10.1016/j.memsci.2022.121083

[19] D. Ma,S.B. Peh, G. Han, S.B. Chen. Thin-Film Nanocomposite (TFN) Membranes Incorporated with Super-Hydrophilic Metal-Organic Framework (MOF) UiO-66: Toward Enhancement of Water Flux and Salt Rejection. *ACS Appl Mater Interfaces*. 2017;9(8):7523-7534. doi:10.1021/acsami.6b14223

[20] L. Ge, H. Song, J. Zhu, Y. Zhang, Z. Zhou, B. Van der Bruggen. Metal/covalent-organic framework based thin film nanocomposite membranes for advanced separations. *J Mater Chem A*. Published online 2024. doi:10.1039/d4ta00578c

[21] W. Peng, H. Li, Y. Liu, S. Song. Comparison of Pb (II) adsorption onto graphene oxide prepared from natural graphites:Diagramming the Pb (II) adsorption sites. *Appl Surf Sci*. 2016;364:620-627. doi:10.1016/j.apsusc.2015.12.208

[22] A. Gopalakrishnan, R. Krishnan, S. Thangavel, G. Venugopal, S. Kim. Removal of heavy metal ions from pharma-effluents using graphene-oxide nanosorbents and study of their adsorption kinetics. *J Ind Eng Chem*. 2015;30:14-19. doi:10.1016/j.jiec.2015.06.005

[23] P. Li, Y. Li, Y. Wu, Z. Xu, H. Zhang, P. Gao, S. Xu. Thin-film nanocomposite NF membrane with GO on macroporous hollow fiber ceramic substrate for efficient heavy metals removal. *Environ Res*. 2021;197:111040.

doi:10.1016/j.envres.2021.111040

[24] Y. Kang, M. Obaid, J. Jang, I.S. Kim. Sulfonated graphene oxide incorporated thin film nanocomposite nanofiltration membrane to enhance permeation and antifouling properties. *Desalination*. 2019;470:114125. doi:10.1016/j.desal.2019.114125

[25] C.S. Lin, K.L. Tung, Y.L. Lin, D.C. Dong, C.W. Chen, C.H. Wu. Fabrication and modification of forward osmosis membranes by using graphene oxide for dye rejection and sludge concentration. *Process Saf Environ Prot*. 2020;144:225-235. doi:10.1016/j.psep.2020.07.007

[26] H. Abadikhah, E.N. Kalali, S. Khodi, X. Xu, S. Agathopoulos. Multifunctional Thin-Film Nanofiltration Membrane Incorporated with Reduced Graphene Oxide@TiO2@Ag Nanocomposites for High Desalination Performance, Dye Retention, and Antibacterial Properties. *ACS Appl Mater Interfaces*. 2019;11(26):23535-23545. doi:10.1021/acsami.9b03557

[27] H. Abadikhah, E.N. Kalali, S. Behzadi, S.A. Khan, X. Xu, M.E. Shabestari, S. Agathopoulos. High flux thin film nanocomposite membrane incorporated with functionalized TiO2@reduced graphene oxide nanohybrids for organic solvent nanofiltration. *Chem Eng Sci*. 2019;204:99-109. doi:10.1016/j.ces.2019.04.022

[28] N. Izadmehr, Y. Mansourpanah, M. Ulbricht, A. Rahimpour, M.R. Omidkhah. TETA-anchored graphene oxide enhanced polyamide thin film nanofiltration membrane for water purification; performance and antifouling properties. *J Environ Manage*. 2020;276:111299. doi:10.1016/j.jenvman.2020.111299

[29] D.L. Zhao, H. Jin, Q. Zhao, et al. Smart integration of MOFs and CQDs to fabricate defect-free and self-cleaning TFN membranes for dye removal. *J Memb Sci*. 2023;679:121706. doi:10.1016/j.memsci.2023.121706

[30] Y. Li, C. Li, S. Li, B. Su, L. Han, B. Mandal. Graphene oxide (GO)-interlayered thin-film nanocomposite (TFN) membranes with high solvent resistance for organic solvent nanofiltration (OSN). *J Mater Chem A*. 2019;7(21):13315-13330. doi:10.1039/c9ta01915d

[31] K. Tang, L.S. Zhu, P. Lan, Y. Chen, Z. Chen, Y. Lan, W. Lan et al. Regulating the thickness of nanofiltration membranes for efficient water purification. *Nanoscale Adv*. 2023;5(18):4770-4781. doi:10.1039/d3na00110e

[32] C. Zhang, K. Wei, W. Zhang, Y. Bai, Y. Sun, J. Gu. Graphene Oxide Quantum Dots Incorporated into a Thin Film Nanocomposite Membrane with High Flux and Antifouling Properties for Low-Pressure Nanofiltration. *ACS Appl Mater Interfaces*. 2017;9(12):11082-11094. doi:10.1021/acsami.6b12826

[33] H. Jee, J. Jang, Y. Kang, Y. Kang, T. Eisa, K. Chae, I.S. Kim, E. Yang. Enhancing the Dye-Rejection Efficiencies and Stability of Graphene Oxide-Based Nanofiltration Membranes via Divalent Cation Intercalation and Mild Reduction. *Membranes*. 2022;12(4). doi:10.3390/membranes12040402

[34] G. Zhao, R. Hu, Y. He, H. Zhu. Physically Coating Nanofiltration Membranes with Graphene Oxide Quantum Dots for Simultaneously Improved Water Permeability and Salt/Dye Rejection. *Adv Mater Interfaces*. 2019;6(5):1-11. doi:10.1002/admi.201801742

[35] R.R. Nair, H.A. Wu, P.N. Jayaram, I.V. Grigorieva, A.K. Geim. Unimpeded Permeation of Water Through Helium-Leak–Tight Graphene-Based Membranes. *Science* . 2012;335:442-444. doi:10.1126/science.1211694

[36] A. Anand, B. Unnikrishnan, J.Y. Mao, H.J. Lin, C.C. Huang. Graphene-based nanofiltration membranes for improving salt rejection, water flux and antifouling–A review. *Desalination*. 2018;429:119-133. doi:10.1016/j.desal.2017.12.012

[37] X. Feng, D. Peng, J. Zhu, Y. Wang, Y. Zhang. Recent advances of loose nanofiltration membranes for dye/salt separation. *Sep Purif Technol*. 2022;285:120228. doi:10.1016/j.seppur.2021.120228

[38] M.Q. Seah, W.J. Lau, P.S. Goh, A.F. Ismail. Greener synthesis of functionalized-GO incorporated TFN NF membrane for potential recovery of saline water from salt/dye mixed solution. *Desalination*. 2022;523:115403. doi:10.1016/j.desal.2021.115403

[39] O. Azzaroni. Polymer brushes here, there, and everywhere: Recent advances in their practical applications and emerging opportunities in multiple research fields. *J Polym Sci Part A Polym Chem*. 2012;50(16):3225-3258. doi:10.1002/pola.26119

[40] B. Zhao, L. Zhu. Mixed Polymer Brush-Grafted Particles : A New Class of Environmentally Responsive Nanostructured Materials. *Macromol*. 2009:9369-9383. doi:10.1021/ma902042x

[41] J.J. Keating IV, J. Imbrogno, G. Belfort. Polymer Brushes for Membrane Separations: A Review. *ACS Appl Mater Interfaces*. 2016. doi:10.1021/acsami.6b09068

[42] D.C. Marcano, D.V. Kosynkin, J.M. Berlin, A. Sinitskii, Z. Sun, A.S. Slesarev, L.B. Alemany, W. Lu, J.M. Tour. Correction to: Improved Synthesis of Graphene Oxide. *ACS Nano*. 2018;12(2):2078. doi:10.1021/acsnano.8b00128

[43] A. Kumar, A. Bansal, B. Behera, S.L. Jain, S.S. Ray. Ternary hybrid polymeric nanocomposites through grafting of polystyrene on graphene oxide-TiO_2 by surface initiated atom transfer radical polymerization (SI-ATRP). *Mater Chem Phys*. 2016;172:189-196. doi:10.1016/j.matchemphys.2016.01.064

[44] E.G. Masibi, T.A. Makhetha, R.M. Moutloali. Effect of the Incorporation of ZIF-8@GO into the Thin-Film Membrane on Salt Rejection and BSA Fouling. *Membranes*. 2022;12(4). doi:10.3390/membranes12040436

[45] Hoffman R. Solid-state chemical-shift referencing with adamantane. J Magn Reson. 2022;340:107231. doi:10.1016/j.jmr.2022.107231

[46] A. Etale, D. Nhlane, J. Mhlongo, A. Khan, K. Rumbold, Y.B. Nuapia. Synthesis and Application of Cationised Cellulose for Removal of Cr (VI) from Acid Mine-Drainage Contaminated Water. AAS Open Res. 2021;4. doi.org/10.12688/aasopenres.13182.1

[47] S. Zhu, J. Li, Y. Chen. Grafting of graphene oxide with stimuli-responsive polymers by using ATRP for drug release. *J Nanopart Res*, 2012. doi:10.1007/s11051-012-1132-x

[48] Y. Yang, J. Wang, J. Zhang, J. Liu, X. Yang, H. Zhao. Exfoliated Graphite Oxide

Decorated by PDMAEMA Chains and Polymer Particles. *Langmuir*. 2009;25(15):11808-11814. doi:10.1021/la901441p

[49] R.S. Hebbar, A.M. Isloor, B. Prabhu, Inamuddin, M. Abdullah. Removal of metal ions and humic acids through polyetherimide membrane with grafted bentonite. *Sci Rep*. 2018. doi:10.1038/s41598-018-22837-1

[50] Cristina B, Nechifor AC, Dimulescu IA, et al. Control of Nanostructured Polysulfone Membrane Preparation by Phase Inversion Method. *Nanomaterials.* 2020, 1-20. doi:10.3390/nano10122349

[51] W. Shao, C. Liu, H. Ma, Z. Hong, Q. Xie, Y. Lu. Fabrication of pH-sensitive thin-film nanocomposite nanofiltration membranes with enhanced performance by incorporating amine- functionalized graphene oxide. *Appl Surf Sci*. 2019;487:1209-1221. doi:10.1016/j.apsusc.2019.05.157

[52] Q. Xie, S. Zhang, Z. Xiao, X. Hu, R. Yi, W. Shao, Q. Wang. Preparation and characterization of novel alkali-resistant nanofiltration membranes with enhanced permeation and antifouling properties: the effects of functionalized graphene nanosheets. *RSC Adv*. 2017;7(30):18755-18764. doi:10.1039/c7ra00928c

[53] G. Natesan, K. Rajappan K. GO–CuO nanocomposites assimilated into CA–PES polymer membrane in adsorptive removal of organic dyes from wastewater. *Environ Sci Pollut Res*. 2023;30(15):42658-42678. doi:10.1007/s11356-022-21821-7

[54] Z. Hu, C. Li, R. Nie, Y. Li, J. Tang, X. Deng. Biomaterial functionalized graphene oxides with tunable work function for high sensitive organic. *RSC Adv*. 2015:99431-99438. doi:10.1039/c5ra19476h

[55] M. Wasim, A. Sabir, M. Sha, A. Islam, M. Azam, T. Jamil. Mixed matrix membranes: Two step process modified with electrospun (carboxy methylcellulose sodium salt/sepiolite) fibers for nanofiltration. *J Ind Eng Chem*. 2017. doi:10.1016/j.jiec.2017.02.011

[56] D. Chen, Q. Chen, T. Liu, J. Kang, R. Xu, Y. Cao, M. Xiang. Influence of L-arginine on performances of polyamide thin- film composite reverse osmosis membranes. *RSC Adv*. 2019:20149-20160. doi:10.1039/c9ra02922b

[57] K.C. Wong, P.S. Goh, A.F. Ismail. Highly permeable and selective graphene oxide-enabled thin film nanocomposite for carbon dioxide separation. *Int J Greenh Gas Control*. 2017;64:257-266. doi:10.1016/j.ijggc.2017.08.005

[58] W. Zhao, H. Liu, N. Meng, M. Jian, H. Wang, X. Zhang. Graphene oxide incorporated thin film nanocomposite membrane at low concentration monomers. *J Memb Sci*. 2018;565:380-389. doi:10.1016/j.memsci.2018.08.047

[59] M. Mahmoudian, M.G. Kochameshki, M. Hosseinzadeh. Modification of graphene oxide by ATRP : A pH-responsive additive in membrane for separation of salts, dyes and heavy metals. *J Environ Chem Eng*. 2018;6(2):3122-3134. doi:10.1016/j.jece.2018.04.056

[60] M. Namvari, C.S. Biswas, M. Galluzzi, Q. Wang, B. Du B, F.J. Stadler. Reduced graphene oxide composites with water soluble copolymers having tailored lower critical solution temperatures and unique tube-like structure. *Nat Publ Gr*. 2017;1-9.

doi:10.1038/srep44508

[61] S. Xabela, R.M. Moutloali. 2-(N-3-Sulfopropyl-N,N-dimethyl ammonium)ethyl methacrylate modified graphene oxide embedded into cellulose acetate ultrafiltration membranes for improved performance. *J. Appl. Polym. Sci.* 2022; 1-19. doi:10.1002/app.52336

[62] Wang Y, Wilson D, Harbison GS. Solid-State NMR and the Crystallization of Aspartic and Glutamic Acids. Cryst Growth Des. 2016;16(2):625-631. doi:10.1021/acs.cgd.5b01052

[63] M.C.D. Ngaha, L.G. Djemmoe, E. Njanja, I.T. Kenfack. Biosorption Isotherms and Kinetics Studies for the Removal of 2,6-Dichlorophenolindophenol Using Palm Tree Trunk (*Elaeis guineensis*). *J Encapsulation Adsorpt Sci*. 2018;08(03):156-177. doi:10.4236/jeas.2018.83008

[64] L.L. Borba, R.M.F. Cuba, F.J.C. Terán FJ, M.N. Castro, T.A. Mendes. Use of adsorbent biochar from pequi (Caryocar Brasiliense) husks for the removal of commercial formulation of glyphosate from aqueous media. *Brazilian Arch Biol Technol*. 2019;62. doi:10.1590/1678-4324-2019180450

[65] W. Shao, C. Liu, T. Yu, Y. Xiong, Z. Hong, Q. Xie. Constructing Positively Charged Thin-Film Nanocomposite Nanofiltration Membranes with enhanced performance. *Polymers.* 2020. doi:10.3390/polym12112526

[66] W. Zhang, H. Xu, F. Xie, B. Niu, M. Chen, H. Zhang, Y. Zhang, D. Long. General synthesis of ultra fine metal oxide/reduced graphene oxide nanocomposites for ultrahigh- flux nanofiltration membrane. *Nat Commun* (2022):1-10. doi:10.1038/s41467-022-28180-4

[67] F. Abdulraqeb, A. Ali, J. Alam, A.K. Shukla, M. Alhoshan, M.A. Ansari, W.A. Al-Masry, S. Rehman, M. Alam. Evaluation of antibacterial and antifouling properties of silver-loaded GO polysulfone nanocomposite membrane against Escherichia coli , Staphylococcus aureus , and BSA protein. *React Funct Polym*. 2019;140:136-147. doi:10.1016/j.reactfunctpolym.2019.04.019

[68] M. Yassari, A. Shakeri, H. Salehi, S. Reza. Enhancement in forward osmosis performance of thin-film nanocomposite membrane using tannic acid - functionalized graphene oxide. *J Polym Res*. 2022. doi:10.1007/s10965-022-02894-x

[69] R. Goswami, M. Gogoi, A. Borah, H. Sarmah, A.R. Borah, X. Feng, S. Hazarika. Quantum dot- β-Cyclodextrin nanofiller decorated thin film nanocomposite membrane for removal of cationic and anionic dyes from aqueous solution. *Mater Today Chem*. 2024;35:101871. doi:10.1016/j.mtchem.2023.101871

[70] B. Sapkota, W. Liang, A. VahidMohammadi, R. Karnik, A. Noy, M. Wanunu. High permeability sub-nanometre sieve composite MoS_2 membranes. *Nat Commun*. 2020;11(1):1-9. doi:10.1038/s41467-020-16577-y

[71] A. Akbari, P. Sheath, S.T. Martin, D.B. Shinde, M. Shaibani, P.C. Banerjee, R. Tkacz, D. Bhattacharyya, M. Majumeder. Large-area graphene-based nanofiltration membranes by shear alignment of discotic nematic liquid crystals of graphene oxide. *Nat Commun*. 2016;7. doi:10.1038/ncomms10891

Enhancing dye rejection and antifouling resistance of thin film nanocomposite nanofiltration membranes by the incorporation of glutamic acid functionalized graphene oxide

Khona Maziya, Izak Kotze, Heidi Lynn Richards

Molecular Sciences Institute, School of Chemistry, University of the Witwatersrand, Private Bag X3, Johannesburg, 2050, South Africa

Supplementary information

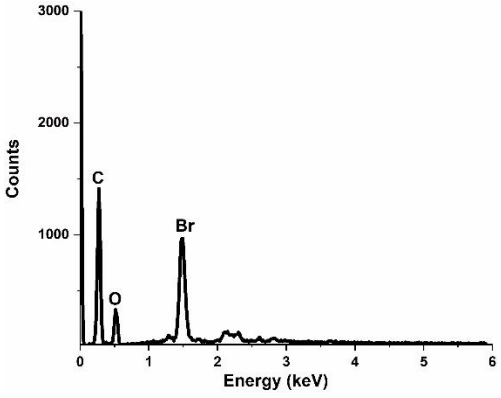

Figure S1: EDS of GO-Br

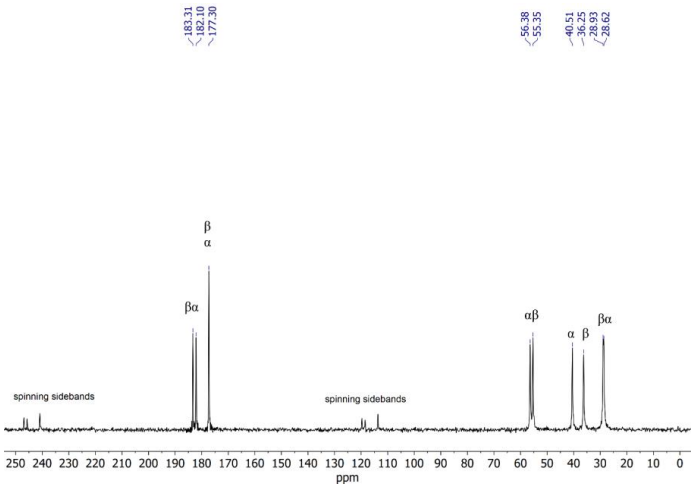

Figure S2: ^{13}C CP MAS NMR spectrum

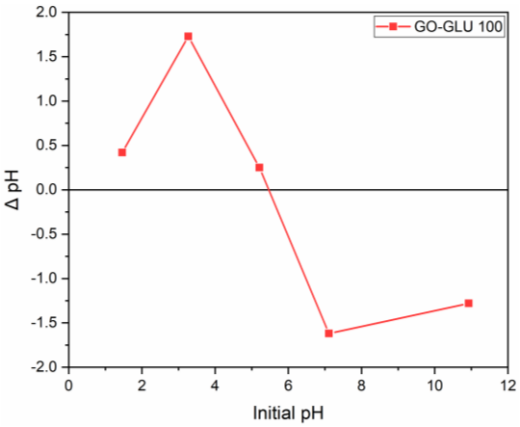

Figure S3: Point of zero charge (pH PZC) for GO-GLU 100.

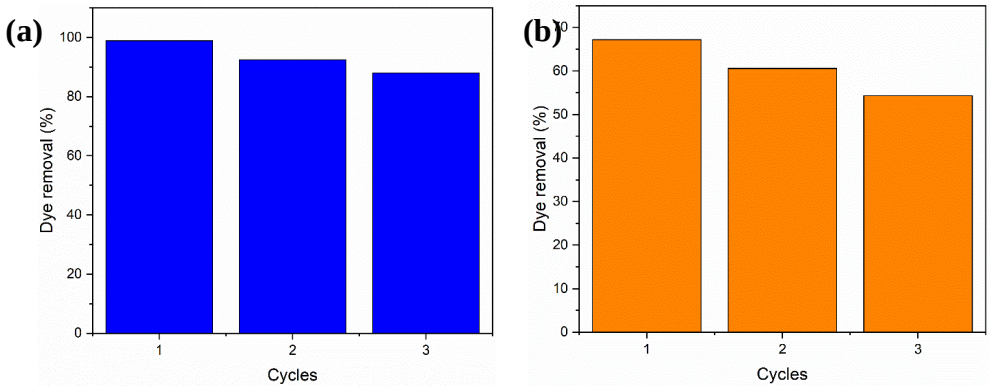

Figure S4: The cycles of reusability for TFN-3; MB (a) and MO (b).

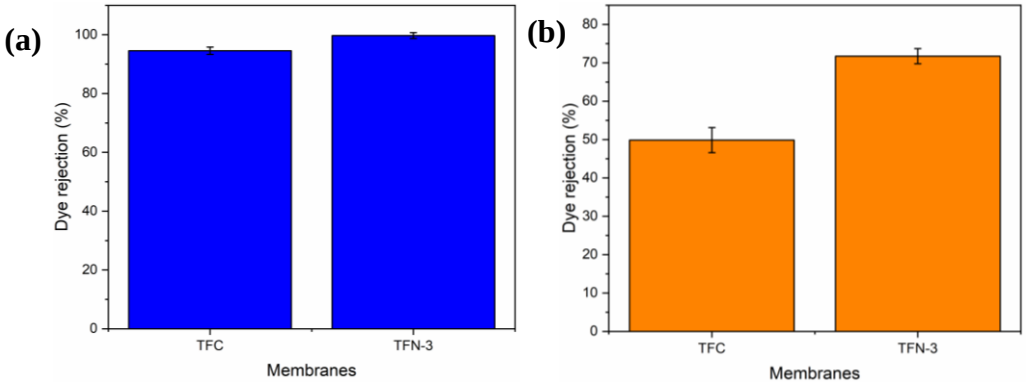

Figure S5: TFC and TFN-3 membranes application in real water remediation for MB (a) and MO (b).

Table S1: Comparison of Dye Separation Performance between GO-GLU TFN with Existing Studies.

Membrane	Loading concentration (wt%)	Dye	Permeability	Dye rejection (%)	Reference
GO-TETA TFN	0.03 wt% (GO-TETA)	direct red congo red	73 L/m^{2}h	99.6	[1]
f-GO PSU	2 wt% (GO-aminated heterocyclic compound; f-GO)	Congo red Methylene blue	~8 L/m^{2}h	>99	[2]
GO-TFN	10 mL (1 ppm GO solution)	Disperse Blue 1	40 L/m^{2}h.bar	99.97	[3]
MTFN	0.2 wt% (rGO@TiO2@Ag)	rose bengal	52 L/m^{2}h	98	[4]
TFN-AA/GO	0.03 g/m^2 (AA-functionalized GO)	Rhodamine B Acid red 1 Rose bengal	11.34 L/m^{2}h.bar	>98	[5]
PDA-rGOC3/HPAN	0.16 wt% (rGOC)	Reactive blue 2	22.8 L/m^{2}h.bar	99.4	[6]
CSGO-PEBA/PES	0.1 wt% 1 wt% (CSGO)	Malachite green	17.068 L/m^{2}h 8.58 L/m^{2}h	98.54 99.63	[7]
PA@GO-60	60 mg SA (GO/SA)	Trypan blue	75.7 L/m^{2}h.bar	99.8	[8]
TFN-3	0.10 wt% (GO-GLU 100)	MB MO	14.11 L/m^{2}h	99.18 67.18	This study

References

[1] N. Izadmehr, Y. Mansourpanah, M. Ulbricht, A. Rahimpour, M.R. Omidkhah. TETA-anchored graphene oxide enhanced polyamide thin film nanofiltration membrane for water purification; performance and antifouling properties. *J Environ Manage*. 2020;276:111299. doi:10.1016/j.jenvman.2020.111299

[2] A.E. Abdelhamid, A.A. El-Sayed, A.M. Khalil. Polysulfone nanofiltration membranes enriched with functionalized graphene oxide for dye removal from wastewater. J Polym Eng. 2020;40(10):833-841. doi:10.1515/polyeng-2020-0141

[3] H.F.M. Austria, J.O. Young, O. Setiawan, T-H. Huang, A.R. Caparanga, K.R.S. Pamintuan, W-S. Hung. Thin film nanocomposite loose nanofiltration membranes with graphene oxide interlayer for textile wastewater treatment. Sep Purif Technol. 2025;354:129053. doi:10.1016/j.seppur.2024.129053

[4] H. Abadikhah, E.N. Kalali, S. Khodi, X. Xu, S. Agathopoulos. Multifunctional Thin-Film Nanofiltration Membrane Incorporated with Reduced Graphene Oxide@TiO2@Ag Nanocomposites for High Desalination Performance, Dye Retention, and Antibacterial Properties. *ACS Appl Mater Interfaces*. 2019;11(26):23535-23545. doi:10.1021/acsami.9b03557

[5] M.Q. Seah, W.J. Lau, P.S. Goh, A.F. Ismail. Greener synthesis of functionalized-GO incorporated TFN NF membrane for potential recovery of saline water from salt/dye mixed solution. *Desalination*. 2022;523:115403. doi:10.1016/j.desal.2021.115403

[6] J. Zhu, J. Wang, A.A. Uliana, M. Tian, Y. Zhang, Y. Zhang, A. Volodin, K. Simoens, S. Yuan, J. Li, J. Lin, K. Bernaerts, B. Van der Bruggen. Mussel-Inspired Architecture of High-Flux Loose Nanofiltration Membrane Functionalized with Antibacterial Reduced Graphene Oxide-Copper Nanocomposites. ACS Appl Mater Interfaces. 2017;9(34):28990-29001. doi:10.1021/acsami.7b05930

[7] S.R. Mousavi, M. Asghari, N.M. Mahmoodi, I. Salahshoori. Water decolorization and antifouling melioration of a novel PEBA1657/PES TFC membrane using chitosan-decorated graphene oxide fillers. J Environ Chem Eng. 2023;11(3):109955. doi:10.1016/j.jece.2023.109955

[8] X. Zhan, R. Ge, T. Huo, J. Lu, J. Li. Highly permeable PA@GO loose nanofiltration membranes enabled by hierarchical transport channels for efficient dye removal. Chem Eng J. 2023;476:146831. doi:10.1016/j.cej.2023.146831

4.2 Paper 2

This paper entitled "**Enhancing dye/salt rejection and antifouling resistance of thin film nanocomposite nanofiltration membranes through the incorporation of BMEP grafted graphene oxide**" is yet to be submitted.

This article evaluated the potential of BMEP functionalized graphene oxide modified TFN membranes in the removal of dyes/ salt in water.

Khona Maziya – Principal author

Contribution: principal author, conceptualization, performed experiments, data collection/analysis, methodology, formal analysis, research, visualization and writing - original draft.

Enhancing dye/salt rejection and antifouling resistance of thin film nanocomposite nanofiltration membranes through the incorporation of BMEP grafted graphene oxide

Khona Maziya[a], Sphesihle Mzobe[a], O.T. Mahlangu[b], Heidi Lynn Richards[a*]

[a] *Molecular Sciences Institute, School of Chemistry, University of the Witwatersrand, Private Bag X3, Johannesburg, 2050, South Africa*

[b] *Institute for Nanotechnology and Water Sustainability, College of Science, Engineering and Technology, University of South Africa Florida Science Campus, 1709, Roodepoort, South Africa*

Graphical abstract

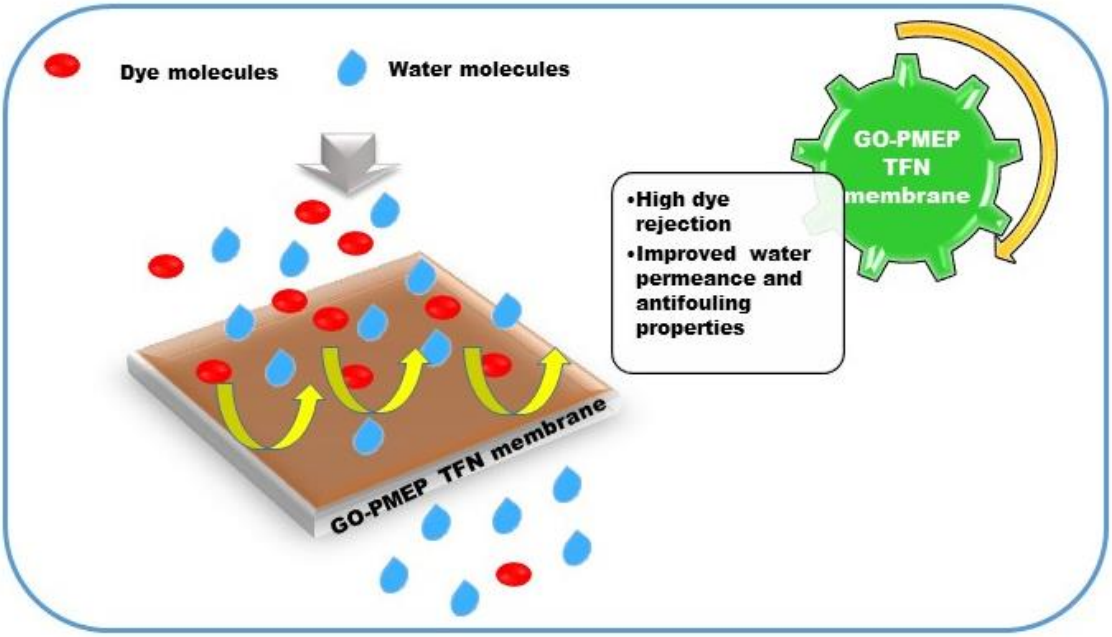

*Corresponding author: Email address: heidi.richards@wits.ac.za

Abstract

Thin-film nanocomposite (TFN) membranes made of graphene oxide (GO) are gaining traction in wastewater treatment applications. This work details the fabrication of TFN membranes through interfacial polymerization (IP), incorporating bis[2-(methacryloyloxy)ethyl] phosphate (BMEP)-grafted graphene oxide (GO-PMEP) into the selective polyamide (PA) layer. The incorporation of modified GO nanosheets into PA layer was successful, with no particle aggregation affecting structural integrity. FTIR, FESEM, and contact angle were used to assess the effects of GO-PMEP dosage on the physicochemical parameters of the PA layer. The results revealed that at an optimal GO-PMEP loading of 0.025 wt% (TFN-1), the membrane exhibited significantly enhanced wettability, hydrophilicity, and pure water permeability attributable to the increased level of oxygenated functional groups on the surface of the membrane, which promote higher affinity to water molecules. Furthermore, the TFN-1 membranes demonstrated superior performance under low-pressure conditions (400 kPa), achieving a water flux of 9.32 ± 0.89 L/m²h, representing a 1.5-fold increase relative to conventional thin-film composite (TFC) membranes. Furthermore, the TFN-1 demonstrated outstanding rejection rates, surpassing 80% for methyl orange (MO), achieving 100% for methylene blue (MB), and approximately 86% and 31% for $MgSO_4$ and NaCl, respectively. Moreover, the efficacy of these membranes were further validated using real water samples, confirming their potential for practical application in dye removal under environmental conditions. These findings underscore the significant potential of GO-PMEP modified TFN membranes for advanced wastewater treatment applications, particularly in enhancing flux performance and selective dye rejection at low operational pressures.

Keywords: Graphene oxide, polymer brushes, thin film nanocomposite membranes, dyes, salts.

1. Introduction

Dyes, commonly utilized in the paper and textile industries, are a significant source of water pollution [1 – 2]. Human health is significantly jeopardized by the massive outflow of wastewater from the paper and textile industries into the environment, which contains many types of dyes [3]. Among the most often utilized dyes, azo dyes, have been shown to convert into mutagenic and toxic compounds, hence the effective removal of dyes is crucial. Due to water scarcity, communities continues to rely on reuse of treated wastewater.

Traditional methods employed to treat dye-containing wastewater include oxidation, adsorption, biodegradation, coagulation, photocatalysis, and electrophoresis [4]. Nevertheless, there are drawbacks associated with these such as sludge formation, incomplete removal at low concentrations and a need for post treatment methods [5 – 6]. As such, membrane separation technologies, particularly nanofiltration (NF) membranes, have garnered significant attention among the plethora of wastewater treatment methods and is seen to be promising in removing dyes from water [7]. Membranes have numerous advantages, such as minimal usage of energy, low cost, ease of use, limited environmental pollution and ease of scale up [8 – 9].

Thin film nanocomposite (TFN) membranes produced through interfacial polymerization (IP) are one type of NF membrane that has demonstrated remarkable dye removal capabilities [10 – 12]. These membranes are made up of a thin polyamide (PA) layer constructed atop an ultrafiltration membrane, which serves as a support [13]. This multi-layered structure of TFN membranes allows for control and optimization of the ultrathin PA layer to improve selectivity and permeability while also providing great mechanical strength, allowing for the fabrication of membranes with desired features and performance [14]. One distinctive aspect of TFN membranes is the inclusion of nanoparticles in the ultrathin PA layer, which improve membrane performance without affecting crucial synthesis parameters.

The selection of nanoparticles is critical for the construction of TFN membranes since the primary separation processes are charge repulsion (Donnan exclusion), size exclusion, and/or solute-membrane affinity [6]. To boost membrane performance, the PA layer has been embedded with various nanoparticles such as halloysite nanotubes (HNTs), cellulose nanocrystals, carbon nanotubes, metallic organic frameworks (MOFs), and graphene quantum dots [12, 15 – 21]. Graphene oxide (GO) has sparked widespread interest due to its several appealing features. Its hydrophilic nature, large specific surface area (~2600 m^2g^{-1}), and presence of epoxy, ketones, hydroxyl, and carboxyl groups enable further functionalization of GO, enhancing pollutant removal [22 – 24]. Several studies have been published demonstrating the use of GO to improve membrane performance [25 – 35]. Seah et al. (2022) examined the impact of modified GO TFN membranes on salt and dye removal [36]. As a result, they developed a PA layer utilizing a mist-based IP technique in order to create a TFN membrane with superior characteristics. GO was treated with acrylic acid (AA) using plasma-enhanced chemical vapor deposition. The AA-modified GO

improved the TFNs pure water permeability (PWP) to 11.34 L/m^2h·bar compared to the control GO TFN. These membranes were evaluated for Rhodamine B, Acid Red, and Rose Bengal dye rejection, with rejection rates of greater than 98% [36].

The agglomeration and stacking of GO in the PA layer has an influence on membrane functionality by decreasing the membrane's hydrophilicity and water flow, hence lowering its permeability. These two key problems have hampered the use of GO-functionalized membranes in water treatment thus far [37 – 39]. As a result, addressing these difficulties and improving membrane performance involves modifying GO nanosheets through the addition of different functional groups preceding membrane construction. Izademhr et al. (2020) probed the impact of triethylenetetramine modified GO on membrane performance when inserted into TFN membrane [29]. There was an observable increase in flux (49.8 - 73.2 L/m^2h) with the introduction and rise of modified GO [29]. Furthermore, TFN membranes effectively removed various textile dyes (99.6%) [29]. Zhang et al. (2017) examined the effects of carboxyl-functionalized GO on TFN membrane efficacy [40]. At the ideal loading (0.07%), the permeation flux was 110.4 L/m^2h, with 25% NaCl retention and 95.1% dye (new coccine) removal [40].

Polymerization is one of the methods that can address this, it entails using the oxygenated groups situated on the surface of GO to enhance interlayer separation of the GO sheets while also binding the sheets together. GO modification via surface-initiated atom transfer radical polymerization (SI-ATRP) is a flexible polymerization method which allows for precise brush thickness and design and also high grafting density. This approach requires immobilizing an initiator on the substrate's surface, preceded by a growth phase in which monomers are repeatedly added to the expanding chain (polymerization), resulting in multifunctional materials with end group functions [41 – 43].

In this study, bis[2-(methacryloyloxy)ethyl] phosphate (BMEP) polymer brushes were grown on GO using SI-ATRP to improve contaminant rejection while also increasing GO compatibility with the membrane matrix. Polymer grafted GO can improve its dispersion ability within the PA layer as well as the hydrophilicity of the membrane. The effect of incorporating modified GO (GO-PMEP) into the PA layer on morphology, hydrophilicity, and membrane performance was examined. The structure of modified GO and TFN membranes was investigated by means of a variety of techniques, including XRD, FESEM, FTIR, EDX, and TEM. The effeciency of these membranes in removing methyl orange (MO) and methylene blue (MB) dyes, as well as salts such as sodium chloride (NaCl) and magnesium sulphate ($MgSO_4$), has not been explored. To our knowledge, GO-PMEP has not been utilized in TFN membranes for the removal of dyes and salts. This research addresses critical gaps in existing literature by providing a sustainable solution for wastewater treatment that reduces energy consumption and operational costs, thereby setting a new benchmark for future membrane applications.

2. Experimental section

2.1 Materials

Sodium chloride (NaCl), α-bromoisobutyryl bromide (BiBB) (98%), graphite powder, sulphuric acid (H_2SO_4), potassium permanganate ($KMnO_4$), magnesium sulphate ($MgSO_4$), phosphoric acid (H_3PO_4), dimethylformamide (DMF), hydrogen peroxide (H_2O_2), triethylamine (TEA, 99%), chloroform, tetrahydrofuran (THF), N,N,N′,N″,N‴-pentamethyldiethylenetriamine (PMDETA, 99%), methyl orange, methylene blue, trimesoyl chloride (TMC), copper(I) bromide (CuBr), Polysulphone (PSF) (MW= 35K g/mol), m-phenylenediamine (MPD), bis[2-(methacryloyloxy)ethyl] phosphate (BMEP) and Polyvinylpyrrolidone (PVP) (Mw = 30 – 70 K; 87 – 90%) were obtained from Sigma-Aldrich. The Milli-Q system (Millipore) produced de-ionized (DI) water which had a resistivity of 18 mΩ cm.

2.2 Surface-Initiated Atom-Transfer Radical Polymerization (SI-ATRP) of BMEP on the Surface of GO-Br

GO and initiator-functionalized GO (GO-Br) synthetic method is obtainable in the supplementary information (S.I.) (S1). The polymerization of GO-Br was performed using an altered approach described by Kumar et al., 2016 [44]. In brief, sonication was used to disperse 50 mg of GO-Br in 5 mL DMF. Cu(I)Br (30 mg, 0.2 mmol) and various concentrations of BMEP (50, 100, and 200 mmol) were put into sealed vials. Nitrogen purging was employed to degas vials. The reaction mixture was treated with 40 mL (0.2 mmol) of PMDETA ligand and polymerized for 24 hours at 70 ℃. The resultant mixture was then emptied into methanol for precipitation of the polymer composites. To eliminate any unused monomer, the product was washed multiple times with chloroform, centrifuged for 20 minutes, then vacuum dried for 24 hours.

2.3 Membrane synthesis

Preparation of polysulfone (PSF) substrate

The phase inversion procedure was used to create the PSF substrate. The casting solution for the PSF membrane was made by dissolving 16 wt% PSF and 1 wt% PVP in DMF solvent. To ensure homogeneity, the casting solution was agitated at 50 ℃ for 12 hours. Following degassing, the mixture was cast on a glass plate (100 μm thick) employing an Electrometer 4843 automatic film applicator (Manchester, UK). This was placed in a water coagulation bath at room temperature to facilitate solvent/non-solvent exchange (wet phase inversion). To eliminate any remaining DMF, the membrane film was rinsed with fresh distilled water and then stored in distilled water until ready for use.

Preparation of polyamide (PA) selective layer

The PA layer of membranes was synthesized on a PSF support membrane using the traditional interfacial polymerization (IP) process. Pre-treatment of the PSF support membranes involved soaking them in an overnight solution (0.5% sodium dodecyl sulphate (SDS)). The membranes were subsequently rinsed in distilled water for an hour. PSF membrane was then secured between a glass plate and a frame. 20 mL (2 w/v%) MPD

aqueous solution was emptied onto the porous substrate. Following a 2-minute contact period, surplus MPD solution was eliminated from the surface by placing it vertically for 1 minute. The PSF substrate was then exposed to the organic phase containing 0.2 wt% TMC-hexane solution for 1 minute before being withdrawn from the membrane surface. To promote crosslinking, the treated membrane was dried in the oven for 8 minutes at 60 °C before being rinsed with distilled water. The fabrication procedure for TFN membranes was comparable to that of TFC membranes, with one key difference that GO-PMEP nanosheets were initially added to an aqueous MPD solution (**Table 1**). Before affecting the interfacial polycondensation reaction, all MPD/additives solutions were sonicated for 30 minutes [45].

Table 1: TFN membranes GO-PMEP 100 loading

Membrane	GO-PMEP 100 loading (wt%)
TFC	-
TFN-1	0.025
TFN-2	0.050
TFN-3	0.100

2.4 Characterization

To examine the morphology of GO nanosheets, we employed a FEI Tecnai G2 Spirit transmission electron microscope operating at 120 kV. Fourier transform infrared (FTIR) spectroscopy (4000 – 500 cm^{-1}) was employed to analyze the chemical composition of the materials and membranes. X-ray diffraction (XRD) analysis on a Bruker D2 phaser diffractometer, provided information about the crystal structure of the GO nanosheets. The thermal stability of GO and its derivatives was evaluated utilizing thermogravimetric analysis (TGA), which involved heating samples from 35 – 900 °C at a rate of 20 °C/min under a nitrogen atmosphere. The cross-sectional and surface morphologies of the synthesized membranes were analyzed using field emission scanning electron microscopy (FESEM-EDS) (Carl Zeiss Sigma) (accelerating voltage = 20 kV). Prior to SEM analysis, the membranes were coated with carbon and Pd/Au. The membranes surface roughness was assessed through the utiliziation of a WITec α 300 atomic force microscope (AFM) (WITec, GmbH, Germany). Contact angle measurements, performed using a sessile-drop method, were used to determine the hydrophilicity or hydrophobicity of the membranes.

GO and derivatives' pH point of zero charge (pH PZC) was obtained by means of the salt titration method [46]. Briefly, 0.1g of GO-PMEP 100 was added to five polypropylene tubes comprising of 25 mL of 0.01M NaCl. The solutions pH was altered from 2 – 10 with 0.1 M HNO_3 and 0.1 M NaOH, giving each tube a unique pH value. The suspensions were shaken horizontally for 24 hours. Each solution's final pH was plotted against its initial pH and the pH PZC for each material was computed using the intersection points [46].

2.5 Water intake measurements

To ascertain the swelling capacity or water intake capacity (WIC), the weight differential between wet and dried TFN membranes was measured. Membrane samples each with an area of 0.00146 m^2 were initially weighed to establish their dry weight (W_d). These

samples were then submerged for 24 hours in distilled water. After removing the membranes and gently blotting them with absorbent paper, their wet weight (W_w) was recorded. The WIC was calculated using **Equation 1**;

$$WIC\ \% = (Ww - Wd)/Ww \text{ x } 100 \quad (1)$$

2.6 Membrane performance

To assess TFN membranes effectiveness, a nitrogen-pressure driven dead-end cell filtration system (Sterlitech, HP4750 Stirred Cell) was employed. The membrane samples (0.00146 m²) were initially conditioned by means of DI water at a transmembrane pressure of 600 kPa until a consistent filtration rate was achieved. Subsequently, the pure water flux was ascertained by passing DI water through the membranes at a pressure of 400 kPa. This flux was calculated using **Equation 2**.

$$Jw = \frac{Q}{A.\Delta t} \quad (2)$$

Where; J_w is the pure water flux (L/m^2.h), Q is the volume of the permeated water (L), A is the effective area of the membrane (m^2), Δt is the permeation time (h).

Dye and salt removal studies were performed on a dead-end filtration cell with continual stirring (time = 60 minutes). Two organic dyes of different electrostatic charges were used namely; Methylene blue (MB) and Methyl orange (MO) (**Table 2**). Varying dye concentrations (20, 50, 80, 100 mg/L) and pH were investigated, these were passed through the cell (transmembrane pressure = 400 kPa). The solute concentration was determined using UV–visible (UV–vis) spectroscopy. The feed also contained various salts (NaCl and $MgSO_4$) at concentrations of 2000 mg/L. Salts concentrations were detected by the conductivity meter (Hanna multimeter instrument, Hl 5522, South Africa).

Equation 3 was used to calculate the rejection rate (%R):

$$\%R = \left(1 - \frac{Cp}{Cf}\right) x100 \quad (3)$$

where C_f and C_p denote the dye concentrations (mg/L) of the feed and permeate solutions.

Table 2: The molecular structure, weight and charge of the dyes

Dyes	**MB**	**MO**
Molecular structure	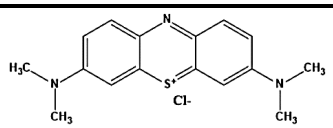	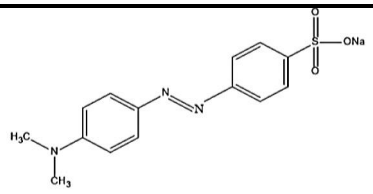
Charge	+	-
Molecular weight (MW) (g/mol)	**319.85**	**327.33**

3. Results and discussion

3.1 Physiochemical characterization of GO and derivatives

3.1.1 TEM analysis

TEM is an effective tool for visualizing the morphology of polymer-functionalized GO. **Figures 1(a-d)** depict TEM images of GO and hybrids with varying concentrations of BMEP. The bare GO and GO-Br images indicated a wrinkled, thin, and laminar structure. Modifying nanosheets with ATRP initiator α-bromoisobutyryl bromide had no effect on the morphology, as displayed in **Figure 1(b)**. However, in **Figure 1 (c)**, GO is covered with nanosized brushes that are evenly distributed on its surface. This is owing to the collapsed chains on the surface of the GO sheets that result in nanosized clusters [47 – 48]. With increasing grafting amount, the polymer created a compact layer on the GO surface, forming a dark sheet-like structure, implying notable thickness changes after polymer grafting. GO-PMEP 100 and 200, showed a more intense color (**Figure 1(d - e)**). These findings show that the polymer chains were effectively grown onto GO sheets using the SI-ATRP technique. Similar findings were observed by Kumar et al. (2016), who identified black patches on GO due to attached long alkyl polyacrylate chains tightly stacked on the surface [49]. EDS analysis, displayed in **Figure 1(f)**, reveals the presence of three primary peaks linked to the elements of C, O, and P. This also verifies the attachment of BMEP brushes on GO.

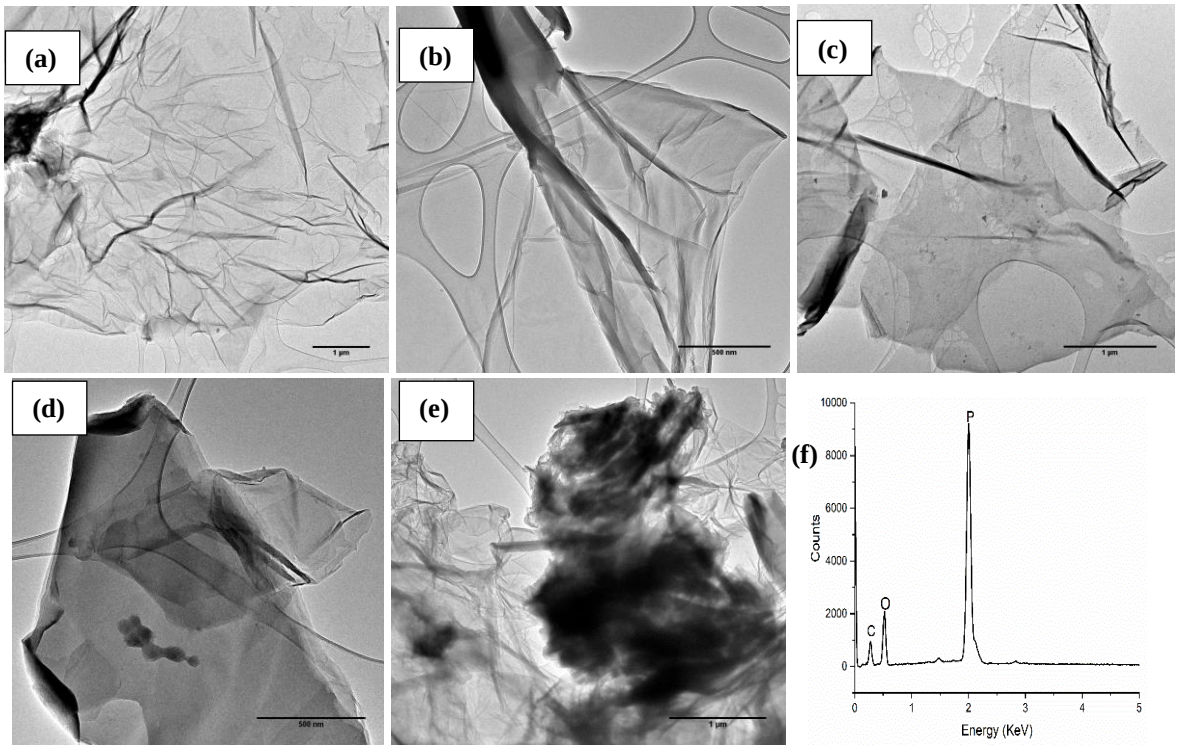

Figure 1: TEM images of pristine GO (a), GO-BR (b), GO-PMEP 50 (c), GO- PMEP 100 (d), GO- PMEP 200 (e) and GO-PMEP 100 EDS (f).

3.1.2 XRD, FTIR, TGA, PZC analysis

Subsequent FTIR evaluation of the samples confirmed that the grafting of BMEP brush on the initiator-modified GO surface was successful, as illustrated in **Figure 2 (a)**. The virgin GO FTIR spectrum displayed a significant peak at 3321 cm^{-1}, caused by stretching

vibrations of hydroxyl groups on GO (**Figure 2(a)**). The GO spectra also revealed characteristic peaks at 2978 cm^{-1}, 1737 cm^{-1}, 1611 cm^{-1}, 1420 cm^{-1}, 1226 cm^{-1}, 1027 cm^{-1}, and 863 cm^{-1}, indicating the presence of CH_2 groups, a carbonyl group, unoxidized sp^2 C=C bonds, hydroxyl groups, C-O bonds, and epoxy groups, respectively [50]. Following modification with α-bromoisobutyryl bromide, a new peak appeared at approximately 1180 cm^{-1}, suggesting the successful formation of an ester linkage. The FTIR spectrum of BMEP-grafted GO (GO-PMEP) exhibited additional peaks at 1180 and 938 cm^{-1}, attributed to the P=O and P-O-C stretching vibrations of BMEP groups, respectively [51]. These results confirm the successful grafting of PMEP brushes onto the GO surface.
TGA investigation was also conducted to assess the grafting of BMEP on GO (**Figure 2 (b)**). The polymer functionalized GO displayed different thermal degradation behavior when compared to GO, demonstrating the successful alteration of GO. The GO lost weight in three stages: loss of bound water at 30 - 150 °C, decomposition of labile carboxylic, epoxy, and hydroxyl groups at 180 - 285 °C, and disintegration of backbone (C-C bond) at ~285 °C [52 – 53]. The final mass was about 30% of the original weight. The thermal decomposition of GO-Br maintained a similar trend, but its final mass was significantly higher (~40%). This was associated with a decline of oxygenated groups, which resulted in less mass loss. GO-PMEP 50 and 100 displayed enhanced thermal stability with final weight of ~55%. This was accredited by the zwitterions' shielding action on the GO groups containing oxygen [54]. The modifications improved the nanocomposite's thermal stability. However, increasing grafting density causes thermal instability in GO-PMEP 200, resulting in a significant weight loss at 400 - 600 °C and a final mass of approximately 20%. This is owing to diminished van der Waals forces between graphene layers caused by the insertion of polymers between the sheets [53]. GO-PMEP 100 was chosen as the optimum nanofiller because of its improved thermal stability and homogenous distribution of PMEP brushes on GO nanosheets, as demonstrated in TEM investigation.

XRD analysis validated the synthesis of GO (**Figure 2 (c)**). The diffraction patterns of GO showed typical peaks at 9.2 and 43 at 2θ values, representing the (0 0 2) and (1 0 0) reflections of GO, respectively. Using Bragg's law, GOs interlayer spacing was 0.96 nm [23]. The diffraction angle of GO-Br is 7.9º, indicating a substantial rise in interlayer distance (1.12 nm). This is attributable to the decrease in water molecules intercalated amid the layers triggered by the decrease in oxygenated functional groups, as well as intercalation by functional groups introduced by the ATRP initiator, which allows for more loose stacking of the sheets [54 – 55]. There was a shift in peaks to 23.2º for GO-PMEP 100 due to the grafting of BMEP polymer chains. This, however reduced the d-spacing to 0.38 nm of GO-PMEP 100 and the peak was slightly broad due to the amorphous nature of polymer chains. During XRD investigation, the (002) peak moved significantly more than the (100) peak owing to fluctuations in interlayer spacing caused by polymer grafting, whereas the in-plane structure remains stable. This implies both structural changes at various levels and selective interactions among BMEP and GO.

A substance's PZC in solution is the pH at which its net surface charge equals zero [56]. As a result, when the pH PZC of GO-PMEP 100 was 6.68, the surface charge is negative

when the pH of the solution exceeds 6.68, neutral when the pH is 6.68, and positive when the pH is less than 6.68 (**Figure 2 (d)**) [57]. The inclusion of GO-PMEP 100 into the polyamide layer of TFN membranes will undoubtedly affect their overall charge. This may indicate that the membrane's pH PZC is close to 6.68.

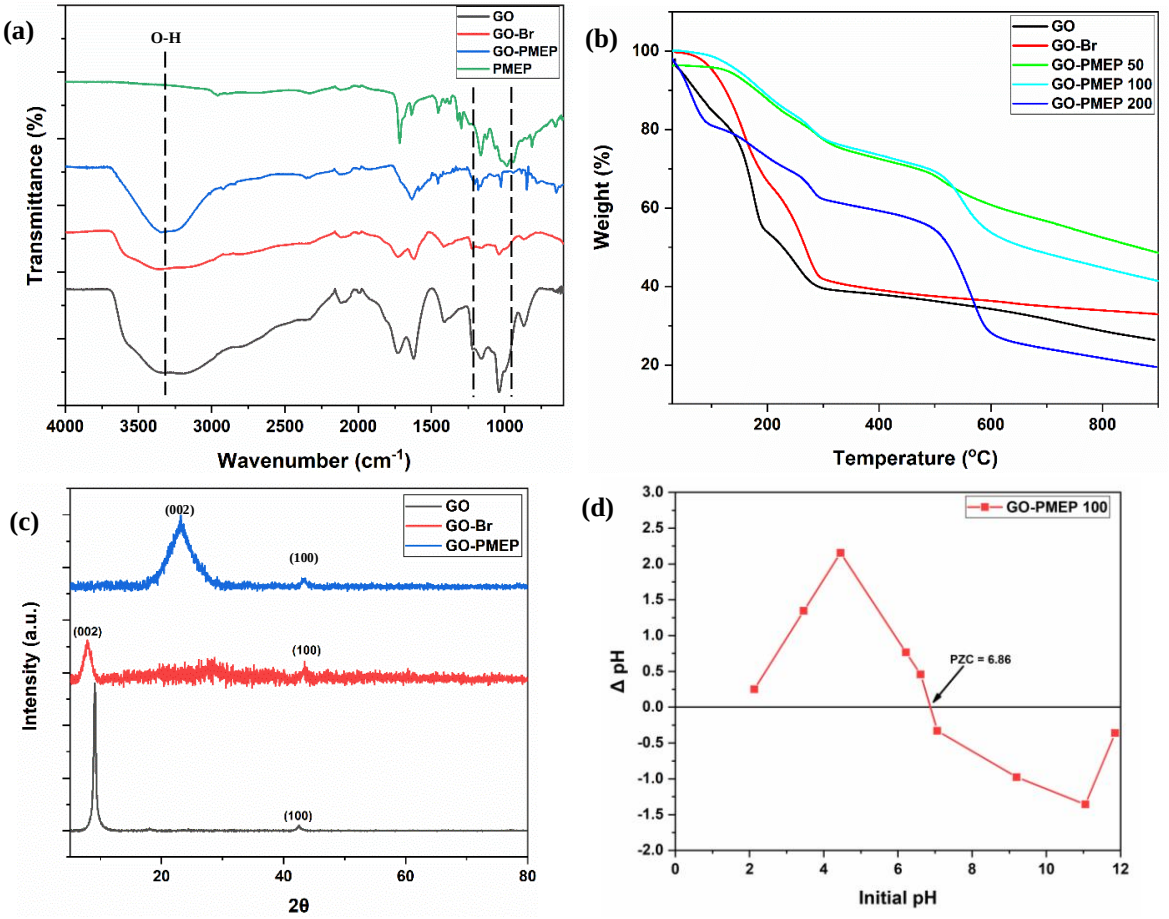

Figure 2: FTIR spectra (a), TGA thermograph (b), XRD patterns (c) and PZC (d) of GO, GO-Br, GO-PMEP.

3.2 Membrane characterization

3.2.1 Morphology and surface roughness of TFN membranes

The membranes surface and cross-section morphologies were characterized with FESEM and AFM imaging as portrayed in **Figure 3**. The pure PSF membrane (**Figure 3 (a, b)**) created by phase inversion has an asymmetric spongy-like shape comprising of a dense skin layer and a porous sub-layer. During phase inversion, casted PSF polymer solution on a glass plate is submerged in a non-solvent bath (water), causing a rapid non-solvent/solvent replacement across the interface of the non-solvent and casting film. Furthermore, repulsive forces between polymers and water accelerated the precipitation of polymeric solution at the interface, resulting in the creation of sublayer macro-voids and a typical asymmetric structure, as well as a dense surface containing micro-pores [58 – 59]. All the membranes displayed similar cross-section morphology, with an irregular construction comprising of a thick layer at the top and a spongy sub-layer containing macro-voids. The TFN membrane surfaces displayed typical nodular ridge valley structure

after IP, as is typical of nanofiltration membrane architectures prepared via IP of TMC and MPD (**Figure 3 (c – e)**) [60]. The characteristic nodular and spherical globule structure of the TFN membranes proved the formation of a polyamide layer atop the PSF substrate [61].

AFM analysis was employed to examine the morphology of the membranes surface following the incorporation of GO-PMEP 100 into the polyamide layer (**Figure 3**). The resulting images, characterized by contrasting bright and dark regions, represent the membrane surface features as peaks and valleys, respectively. As depicted in **Figure 3**, the TFC membrane exhibited a smoother surface (Sa = 50 nm) compared to the other membranes (65.9 – 129 nm). The higher surface roughness observed in TFN membranes relative to TFC verifies the presence of nanofillers, this is consistent with previous research [6, 12].

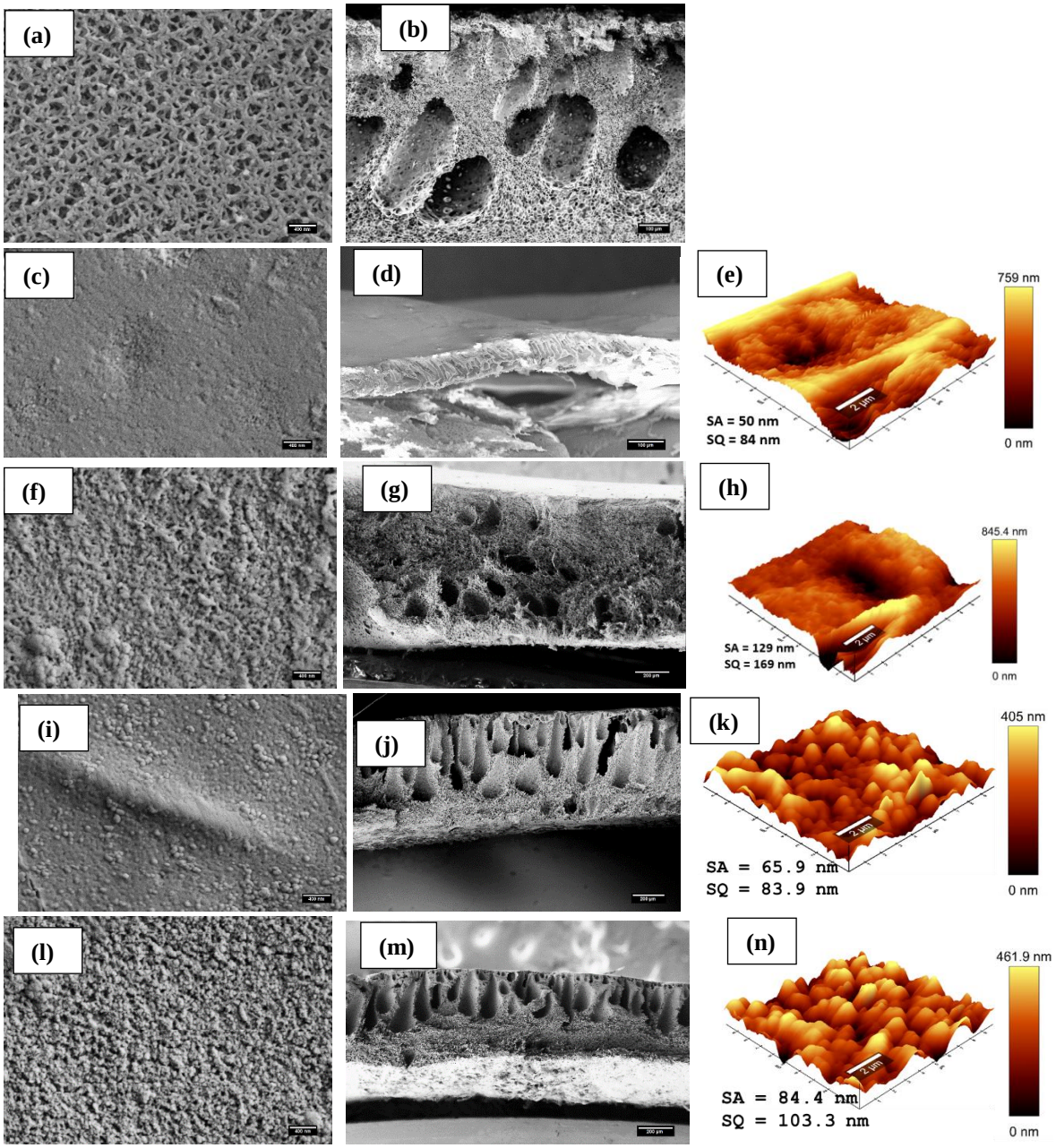

Figure 3: Surface cross section morphologies and AFM images of PSF (a, b), TFC (c, d, e), TFN-1 (f, g, h) TFN-2 (I, j, k) and TFN-3 (l, m, n).

3.2.2 FTIR of membranes

Figure 4 depicts the chemical characterization of PSF, TFC, and TFN membranes as examined by FTIR. The pristine PSF membrane exhibited distinctive peaks at 2981, 1489, 1293, and 1322 cm^{-1}, which corresponded to aliphatic C-H stretching, C=C stretching in the aromatic ring, S=O stretching, and asymmetric stretching of C-SO_2-C, respectively [62]. The PA active layer was effectively formed, as evidenced by the distinctive peaks 1653 cm^{-1} (N−H bending and C−N stretching vibrations of amide II), 1610 cm^{-1} (aromatic amide ring vibrations) and at 1543 cm^{-1} (C=O stretching vibrations of amide I bond), that correspond to PA functional groups [27]. Peaks at 3500 -3140 cm^{-1} may be observed as the amount of GO-PMEP 100 in the PA layer increases. The peaks were linked to the stretching of hydroxyl groups as well as the N-H vibration of free amine groups that remained after IP [13].

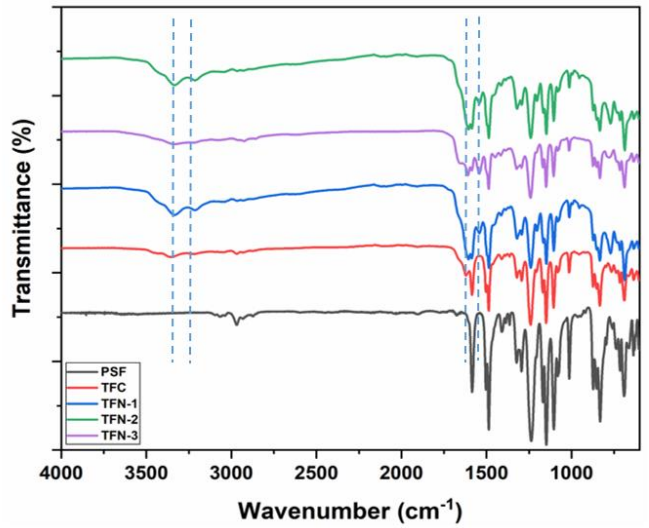

Figure 4: FTIR spectra for PSF (a), TFC (b), TFN-1 (c), TFN-2 (d) and TFN-3 (e).

3.3 Water permeability studies

The water contact angle qualitatively determines the membranes' hydrophilicity (**Table 3**). When the contact angle is decreased, the membrane surface's affinity for water improves, resulting in increased hydrophilicity [63]. The control membrane (TFC) contact angle was 86.81 ± 2.30°; however, incorporating of GO-PMEP 100 in the PA layer lowered the contact angle. The abundance of oxygen-rich functional groups in GO-PMEP 100 embedded in the membrane resulted in TFN-1 having the lowest contact angle (60.53 ± 3.82°) [64]. The contact angle of TFN-3 increased with increase in loading, achieving 80.29 ± 5.32°. The increased contact angles suggest hydrophobization of the PA layer due to nanoparticle aggregation. The moment nanoparticles aggregate, they can increase the membrane's tortuosity, which reduces water flow across it [65 – 66]. Optimization of nanoparticle loading in the PA layer is crucial since this may impact the membrane's

hydrophilicity [67]. Nambikkattu et al. (2021) noted that increasing $MgFe_2O_4$ and $ZnFe_2O_4$ nanoparticle loading (0.001 - 0.01 wt%) decreased the water contact angle (~50 °) owing to the abundance of hydroxyl groups present [67]. However, with loadings above 0.01wt%, contact angle increased because loadings above optimum levels caused agglomeration, which impeded the effective development of the PA layer and hence decreased hydrophilicity [67].

The bulk hydrophilicity measurement (WIC) was also carried out to assess membranes hydrophilicity (**Table 3**). The inclusion of GO-PMEP 100 improved the WIC since it contains hydrophilic functional groups that rapidly interface with water molecules, boosting hydrophilicity. The TFC membrane had the lowest WIC (55.41%), whereas the TFN membranes had a higher WIC (59.31 - 68.60%).

Table 3: Membrane Permeation studies and filtration properties.

Membrane	WIC (%)	WCA (°)	Pure water flux ($Lm^{-2}h^{-1}$)
TFC	55.41	86.81 ± 2.30	6.01 ± 0.38
TFN-1	68.60	60.53 ± 3.82	9.32 ± 0.89
TFN-2	60.98	63.83 ± 9.09	9.05 ± 1.03
TFN-3	59.31	80.29 ± 5.32	7.95 ± 0.52

Table 3 displays pure water flux (PWF) measurements for TFN membranes at 400 kPa. TFC, TFN-1, TFN-2, and TFN-3 had respective PWF values of 6.01 ± 0.38, 9.32 ± 0.89, 9.05 ± 1.03, and 7.95 ± 0.52 L/m^2h. As expected, the PWF increased when GO-PMEP 100 was incorporated into PA layer, increasing the membrane's hydrophilicity. However, since TFN-3 showed a drop in PWF, it is possible that the higher concentration of GO-PMEP 100 caused aggregation and a decrease in flux as compared to the optimal GO-PMEP 100 concentration in TFN-1. TFN-1 was selected for further testing because of its improved hydrophilicity as a result of optimal loading. Ang et al. (2020) obtained similar results when organo-modified montmorillonite (O-MMT) was added to TFNs PA layer [68]. The addition of O-MMT boosted water permeance, but increasing the quantity from 0.05 - 0.75 g/g in trimesoyl chloride reduced the flux from 53.15 ± 3.30 to 42.15 ± 3.98 L/m^2h [68].

3.4 Membrane separation performance

3.4.1 Influence of dye concentration and pH on removal capacity

To assess the membranes' dye removal capabilities, a rejection experiment was conducted with varying doses of MB and MO (20 – 100 ppm). TFC and TFN-1 were the favored membranes for dye removal experiments (**Figure 5**). TFC membrane rejection of MB dye varied between 95.99 – 96.87%, whereas TFN-1 rejection ranged between 97.35 - 100% (**Figure 5**). MO dye rejection rates were lower for both TFC (38.47 – 50.46%) and TFN-1 (66.62 – 83.92%).

These findings demonstrate that adding polymer modified GO nanosheets improves dye separation by increasing the membrane's electrostatic charge. Sieving, steric hindrance effects, and the Donnan exclusion principle can all be used to explain rejection behavior [7]. The high concentration of carboxyl and hydroxyl moieties located on the polymer

modified GO in the TFN membrane produces a negative surface charge thus causing the membrane to have a high electrostatic affinity for MB. In contrast, an anionic dye is repelled electrostatically by the membrane's negatively charged surface. As a result, the cationic MB dye displayed higher rejection than the anionic MO dye. MB's high rejection can also be ascribed to its greater hydrated radii of 5.04A as compared to MOs radii of 4.97A, resulting in sieving hindrances [69 – 70]. Yet, due to dye adsorption on membrane surfaces, the permeate fluxes measured were lower than those of pure water, as illustrated in **Figure 6**.

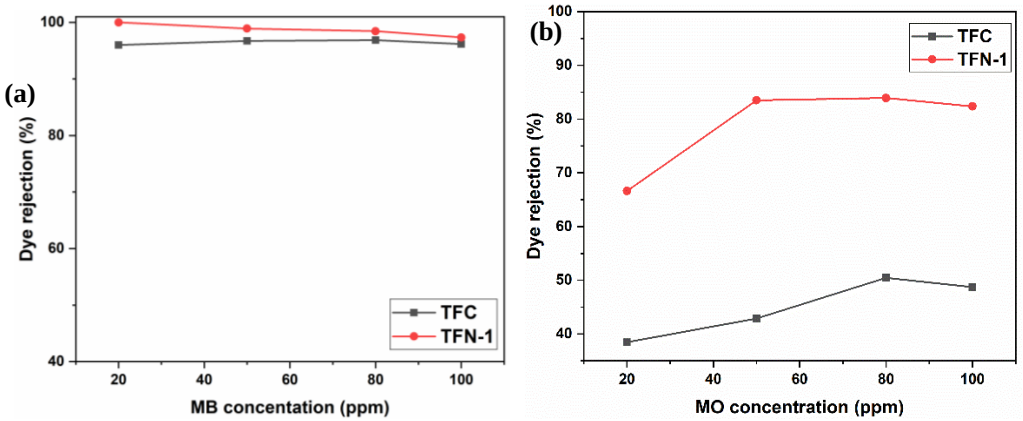

Figure 5: Dye rejection performance of TFC and TFN-1 membranes; MB (a) and MO (b).

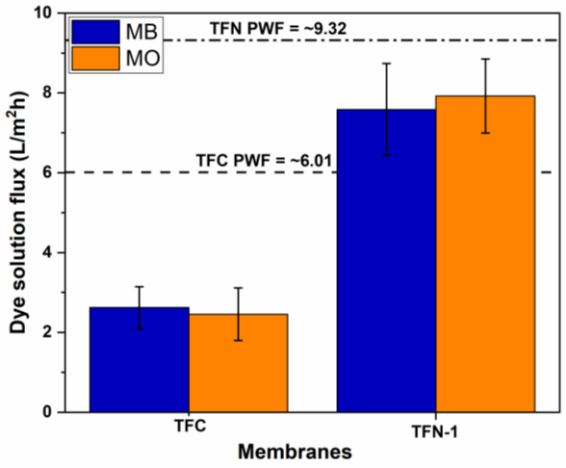

Figure 6: Dye solution flux for TFC and TFN-1 membranes.

Membrane separation efficiency may be efficiently altered because solution pH has a direct effect on the electrochemical characteristics of dye molecules and the membrane surface. In a similar vein, the effects of MB and MO dyes (50 ppm) on pH-responsive behavior were investigated (**Figure 7**). At all pH ranges, the rejection rate of MB was greater than 80%, with rejection increasing to 99% at pH levels above 11. At lower pH levels, the negative charge on the membrane surface weakens, which makes it simpler for negatively charged molecules of MO to adsorb and deposit on the membrane surface. At pH 2, MO showed a rejection rate of around 78%. As the solutions pH rises, so does the negative charge on the membrane surface, and MO rejection decreases at pH 11 (55.91%).

Negatively charged MO dye molecules' adsorption capacity on the membrane surface diminished due to electrostatic repulsion.

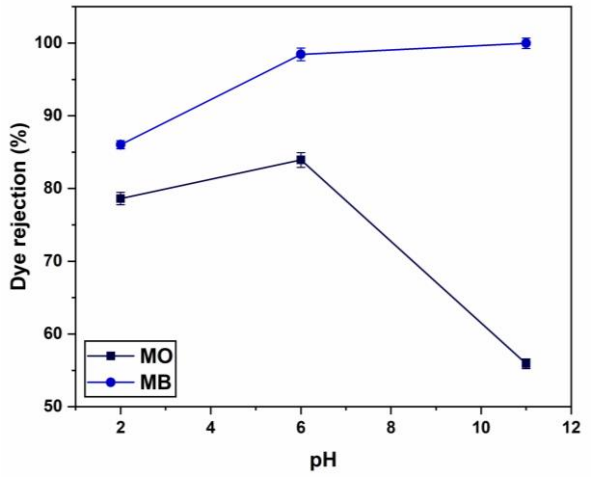

Figure 7: TFN-1 dye rejection vs pH.

3.4.2 Reuse performances

Membrane reuse is crucial for practical uses, especially on a large scale; hence, membrane efficiency and stability are critical. Following all three cycles, the TFN-1 membrane demonstrated outstanding rejection performance for both MB and MO dyes (50 ppm, solution pH), as seen in **Figure 8**. The MB dye removal efficiency declined from 98.91 to 94.99%, and the MO rejection reduced from 83.93 to 78.34%. This might be attributed to membrane fouling or the cleaning process's failure to entirely eliminate absorbed dye molecules. This will ultimately cause the membrane's removal efficacy to deteriorate.

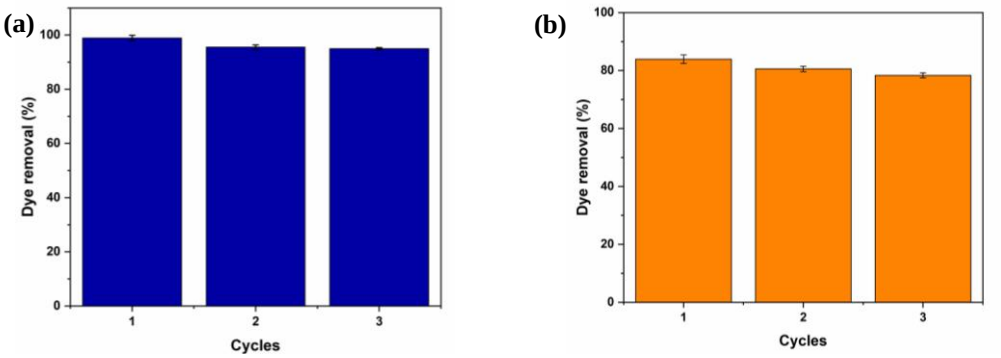

Figure 8: The cycles of reusability for TFN-1; MB (a) and MO (b).

3.4.3 Dye removal from spiked river water

Spiked river water samples from South Africa's Vaal River were utilized to investigate the TFN membrane's potential use in environmental water systems. The physicochemical characteristics of the water samples were the following: conductivity 834 µS/cm, pH 7.61, TDS 417 ppm, and resistivity 1.20 KΩ.cm. TFN-1 membrane had a better removal efficiency for MB (96.14%) and MO (74.93%) dyes than the control TFC membrane, which removed 95.73 and 49.85%, respectively. TFN-1 removal was enhanced due to synergistic elimination produced by steric hindrance effects, sieving, and Donnan exclusion [7].

3.4.4 Salt removal studies

Alongside dye removal studies, the investigation of salt rejection was also conducted. TFN-1 membrane was utilized to analyze the rejection rates of NaCl and $MgSO_4$ in a single-component system. TFN-1 exhibited increased $MgSO_4$ rejection rate (~86%) than NaCl (~31%), as exhibited in **Figure 9**. This observation is consistent with the expected features of negatively charged nanofiltration (NF) membranes, as documented in existing research [18, 21, 27]. The overall performance concerning rejection is influenced by both size exclusion and the Donnan exclusion effect. The superior rejection of sulphate ions over chloride ions is attributed to the larger hydrated radius and greater charge of sulphate ions ($SO4^{2-}$ at 0.38 nm) compared to chloride ions (Cl^- at 0.33 nm) [71]. Additionally, the divalent cation Mg^{2+} significantly affects the negatively charged surface of the membrane more than the monovalent Na^+, leading to an increased rejection rate for $MgSO_4$ relative to NaCl.

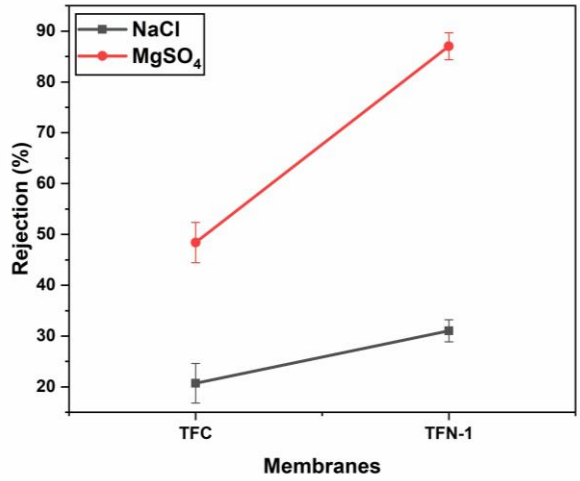

Figure 9: Salt rejection of the synthesized TFC and TFN-1 membranes (the test conditions: P = 400 kPa, C_f = 2000 mg/L).

4. Conclusion

In this present study, we utilized the IP approach to develop a TFN membrane containing polymer modified GO (GO-PMEP) nanoparticles. These TFN membranes were utilized for filtering dyes and salts during the water treatment process. The results reveal that the addition of 0.025 wt% GO-PMEP in the PA matrix greatly increases dye and salt separation capacity. Optimized parameters yielded a water flux of 9.32 ± 0.89 L/m^2h and a 100 % rejection rate for MB separation, whereas MO retained 83.92 %. Salt rejection was approximately 86% and 31% for $MgSO_4$ and NaCl, respectively. The results obtained indicate that TFN membranes fabricated with GO-PMEP integrated into the polyamide matrix exhibit enhanced efficacy in the removal of dyes and salts from aqueous solutions.

References

[1] Borpatra Gohain M, Karki S, Yadav D, Yadav A, Thakare NR, Hazarika S, Lee HK, Ingole PG. Development of Antifouling Thin-Film Composite/Nanocomposite Membranes for Removal of Phosphate and Malachite Green Dye. Membranes (Basel). 2022;12(8). doi:10.3390/membranes12080768.

[2] Liu B, Zhang S, Yao Z, Dong L, Bai Y, Zhang C. Carbon Nitride Quantum Dot-Based Thin-Film Nanocomposite Membranes for Efficient Dye Removal. ACS Appl Nano Mater. 2023;6(18):16297-16308. doi:10.1021/acsanm.3c02401.

[3] Mohammad Nejad S, Seyedpour SF, Aghapour Aktij S, et al. Loose nanofiltration membranes functionalized with in situ-synthesized metal organic framework for water treatment. Mater Today Chem. 2022;24:100909. doi:10.1016/j.mtchem.2022.100909

[4] Lin J, Ye W, Baltaru MC, Tang YP, Bernstein NJ, Gao P, Balta S, Vlad M, Volodin A, Sotto A, Luis P, Zydney AL, Van der Bruggen B. Tight ultrafiltration membranes for enhanced separation of dyes and Na_2SO_4 during textile wastewater treatment. J Memb Sci. 2016;514:217-228. doi:10.1016/j.memsci.2016.04.057.

[5] Ng HKM, Leo CP. Translucent and adsorptive PVA thin film containing microfibrillated cellulose intercalated with TiO_2 nanoparticles for dye removal. Colloids Surfaces A Physicochem Eng Asp. 2019;578. doi:10.1016/j.colsurfa.2019.123590.

[6] Ghaemi N, Safari P. Nano-porous SAPO-34 enhanced thin-film nanocomposite polymeric membrane: Simultaneously high water permeation and complete removal of cationic/anionic dyes from water. J Hazard Mater. 2018;358:376-388. doi:10.1016/j.jhazmat.2018.07.017.

[7] Goswami R, Gogoi M, Borah A, Sarmah H, Borah AR, Feng X , Hazarika S. Quantum dot- β-Cyclodextrin nanofiller decorated thin film nanocomposite membrane for removal of cationic and anionic dyes from aqueous solution. Mater Today Chem. 2024;35:101871. doi:10.1016/j.mtchem.2023.101871.

[8] Liao Z, Zhu J, Li X, Van der Bruggen B. Regulating composition and structure of nanofillers in thin film nanocomposite (TFN) membranes for enhanced separation performance: A critical review. Sep Purif Technol. 2021;266:118567. doi:10.1016/j.seppur.2021.118567.

[9] Moradihamedani P. Recent advances in dye removal from wastewater by membrane technology: a review. Polym Bull. 2022;79(4):2603-2631. doi:10.1007/s00289-021-03603-2.

[10] Mansourpanah Y, Ghanbari A, Yazdani H. Silver-polyamidoamine / graphene oxide thin film nanofiltration membrane with improved antifouling and antibacterial properties for water purification and desalination. Desalination. 2021;511:115109. doi:10.1016/j.desal.2021.115109.

[11] Zhao P, Li R, Wu W, Wang J, Liu J, Zhang Y. In-situ growth of polyvinylpyrrolidone modified Zr-MOFs thin-film nanocomposite (TFN) for efficient dyes removal. Compos Part B Eng. 2019;176:107208. doi:10.1016/j.compositesb.2019.107208.

[12] Mousavi SR, Asghari M, Mahmoodi NM. Chitosan-wrapped multiwalled carbon nanotube as filler within PEBA thin film nanocomposite (TFN) membrane to improve dye removal. Carbohydr Polym. 2020;237:116128. doi:10.1016/j.carbpol.2020.116128.

[13] Peyravi M, Jahanshahi M, Rahimpour A, Javadi A, Hajavi S. Novel thin film nanocomposite membranes incorporated with functionalized TiO2 nanoparticles for organic solvent nanofiltration. Chem Eng J. 2014;241:155-166. doi:10.1016/j.cej.2013.12.024.
[14] Lau WJ, Ismail AF, Misdan N, Kassim MA. A recent progress in thin film composite membrane: A review. Desalination. 2012;287:190-199. doi:10.1016/j.desal.2011.04.004.
[15] Bi R, Zhang Q, Zhang R, Su Y, Jiang Z. Thin film nanocomposite membranes incorporated with graphene quantum dots for high flux and antifouling property. J Memb Sci. 2018;553:17-24. doi:10.1016/j.memsci.2018.02.010.
[16] Zhang T, Li P, Ding S, Wang X. High permeability composite nanofiltration membrane assisted by introducing TpPa covalent organic frameworks interlayer with nanorods for desalination and NaCl/dye separation. Sep Purif Technol. 2021;270: 118802. doi:10.1016/j.seppur.2021.118802.
[17] Yang L, Zhang X, Ma W, Raisi B, Liu X, An C, Ye Z. Trimethylamine N-oxide-derived zwitterionic polyamide thin-film composite nanofiltration membranes with enhanced anti-dye deposition ability for efficient dye separation and recovery. J Memb Sci. 2023;665(October 2022):121083. doi:10.1016/j.memsci.2022.121083.
[18] Ormanci-Acar T, Celebi F, Keskin B, Mutlu-Salmanlı O, Agtas M, Turken T, Tufani A, Imer DY, Ince GO, Demir TU, Menceloglu YZ, Unal S, Koyuncu I. Fabrication and characterization of temperature and pH resistant thin film nanocomposite membranes embedded with halloysite nanotubes for dye rejection. Desalination. 2018;429:20-32. doi:10.1016/j.desal.2017.12.005.
[19] Ma D, Peh SB, Han G, Chen SB. Thin-Film Nanocomposite (TFN) Membranes Incorporated with Super-Hydrophilic Metal-Organic Framework (MOF) UiO-66: Toward Enhancement of Water Flux and Salt Rejection. ACS Appl Mater Interfaces. 2017;9(8):7523-7534. doi:10.1021/acsami.6b14223.
[20] Ge L, Song H, Zhu J, Zhang Y, Zhou Z, Van der Bruggen B. Metal/covalent-organic framework based thin film nanocomposite membranes for advanced separations. J Mater Chem A. 2024; 12: 7975 – 8013. doi:10.1039/d4ta00578c.
[21] Yang L, Liu X, Zhang X, Chen T, Ye Z, Rahaman MS. High performance nanocomposite nanofiltration membranes with polydopamine-modified cellulose nanocrystals for efficient dye/salt separation. Desalination. 2022;521:115385. doi:10.1016/j.desal.2021.115385.
[22] Peng W, Li H, Liu Y, Song S. Comparison of Pb (II) adsorption onto graphene oxide prepared from natural graphites: Diagramming the Pb (II) adsorption sites. Appl Surf Sci. 2016;364:620-627. doi:10.1016/j.apsusc.2015.12.208.
[23] Gopalakrishnan A, Krishnan R, Thangavel S. Removal of heavy metal ions from pharma-effluents using graphene-oxide nanosorbents and study of their adsorption kinetics. J Ind Eng Chem. 2015;30:14-19. doi:10.1016/j.jiec.2015.06.005.
[24] Li P, Li Y-X, Wu Y-Z, Xu Z-L, Zhang H-Z, Gao P, Xu S-J. Thin-film nanocomposite NF membrane with GO on macroporous hollow fiber ceramic substrate for efficient heavy metals removal. Environ Res. 2021;197:111040. doi:10.1016/j.envres.2021.111040.

[25] Kang Y, Obaid M, Jang J, Kim IS. Sulfonated graphene oxide incorporated thin film nanocomposite nanofiltration membrane to enhance permeation and antifouling properties. Desalination. 2019;470(May):114125. doi:10.1016/j.desal.2019.114125.
[26] Lin CS, Tung KL, Lin YL, Dong C Di, Chen CW, Wu CH. Fabrication and modification of forward osmosis membranes by using graphene oxide for dye rejection and sludge concentration. Process Saf Environ Prot. 2020;144:225-235. doi:10.1016/j.psep.2020.07.007.
[27] Abadikhah H, Naderi Kalali E, Khodi S, Xu X, Agathopoulos S. Multifunctional Thin-Film Nanofiltration Membrane Incorporated with Reduced Graphene Oxide@TiO2@Ag Nanocomposites for High Desalination Performance, Dye Retention, and Antibacterial Properties. ACS Appl Mater Interfaces. 2019;11(26):23535-23545. doi:10.1021/acsami.9b03557.
[28] Abadikhah H, Kalali EN, Behzadi S, Khan SA, Xu X, Shabestari ME, Agathopoulos S. High flux thin film nanocomposite membrane incorporated with functionalized TiO2@reduced graphene oxide nanohybrids for organic solvent nanofiltration. Chem Eng Sci. 2019;204:99-109. doi:10.1016/j.ces.2019.04.022.
[29] Izadmehr N, Mansourpanah Y, Ulbricht M, Rahimpour A, Omidkhah MR. TETA-anchored graphene oxide enhanced polyamide thin film nanofiltration membrane for water purification; performance and antifouling properties. J Environ Manage. 2020;276:111299. doi:10.1016/j.jenvman.2020.111299.
[30] Zhao DL, Jin H, Zhao Q, Xu Y, Shen L, Lin H, Chung T-S. Smart integration of MOFs and CQDs to fabricate defect-free and self-cleaning TFN membranes for dye removal. J Memb Sci. 2023;679(January):121706. doi:10.1016/j.memsci.2023.121706.
[31] Li Y, Li C, Li S, Su B, Han L, Mandal B. Graphene oxide (GO)-interlayered thin-film nanocomposite (TFN) membranes with high solvent resistance for organic solvent nanofiltration (OSN). J Mater Chem A. 2019;7(21):13315-13330. doi:10.1039/c9ta01915d.
[32] Tang K, Zhu LS, Lan P, Chen YQ, Chen Z, Lan Y, Lan WG. Regulating the thickness of nanofiltration membranes for efficient water purification. Nanoscale Adv. 2023;5(18):4770-4781. doi:10.1039/d3na00110e.
[33] Zhang C, Wei K, Zhang W, Bai Y, Sun Y, Gu J. Graphene Oxide Quantum Dots Incorporated into a Thin Film Nanocomposite Membrane with High Flux and Antifouling Properties for Low-Pressure Nanofiltration. ACS Appl Mater Interfaces. 2017;9(12):11082-11094. doi:10.1021/acsami.6b12826.
[34] Jee H, Jang J, Kang Y, Eisa T, Chae K-J, Sim IS, Yang E. Enhancing the Dye-Rejection Efficiencies and Stability of Graphene Oxide-Based Nanofiltration Membranes via Divalent Cation Intercalation and Mild Reduction. Membranes (Basel). 2022;12(4). doi:10.3390/membranes12040402.
[35] Zhao G, Hu R, He Y, Zhu H. Physically Coating Nanofiltration Membranes with Graphene Oxide Quantum Dots for Simultaneously Improved Water Permeability and Salt/Dye Rejection. Adv Mater Interfaces. 2019;6(5):1-11. doi:10.1002/admi.201801742.
[36] Seah MQ, Lau WJ, Goh PS, Ismail AF. Greener synthesis of functionalized-GO incorporated TFN NF membrane for potential recovery of saline water from salt/dye mixed solution. Desalination. 2022;523:115403. doi:10.1016/j.desal.2021.115403.

[37] Nair RR, Wu HA , Jayaram PN, Grigorieva IV, and Geim AK. Unimpeded Permeation of Water Through Helium-Leak–Tight Graphene-Based Membranes. Science. 2012;335: 6067) 442-444. doi:10.1126/science.1211694.

[38] Anand A, Unnikrishnan B, Mao JY, Lin HJ, Huang CC. Graphene-based nanofiltration membranes for improving salt rejection, water flux and antifouling–A review. Desalination. 2018;429 :119-133. doi:10.1016/j.desal.2017.12.012.

[39] Feng X, Peng D, Zhu J, Wang Y, Zhang Y. Recent advances of loose nanofiltration membranes for dye/salt separation. Sep Purif Technol. 2022;285:120228. doi:10.1016/j.seppur.2021.120228.

[40] Zhang H, Bin Li, Pan J, et al. Carboxyl-functionalized graphene oxide polyamide nanofiltration membrane for desalination of dye solutions containing monovalent salt. J Memb Sci. 2017;539 :128-137. doi:10.1016/j.memsci.2017.05.075.

[41] Azzaroni O. Polymer brushes here, there, and everywhere: Recent advances in their practical applications and emerging opportunities in multiple research fields. J Polym Sci Part A Polym Chem. 2012;50(16):3225-3258. doi:10.1002/pola.26119.

[42] Zhao B, Zhu L. Mixed Polymer Brush-Grafted Particles : A New Class of Environmentally Responsive Nanostructured Materials. Macromolecules 2009, 42, 24, 9369–9383. doi:10.1021/ma902042x.

[43] Iv JJK, Imbrogno J, Belfort G. Polymer Brushes for Membrane Separations: A Review. ACS Appl Mater Interfaces. 2016; 8 (42). doi:10.1021/acsami.6b09068.

[44] Kumar A, Bansal A, Behera B, Jain SL, Ray SS. Ternary hybrid polymeric nanocomposites through grafting of polystyrene on graphene oxide-TiO_2 by surface initiated atom transfer radical polymerization (SI-ATRP). Mater Chem Phys. 2016;172:189-196. doi:10.1016/j.matchemphys.2016.01.064.

[45] Masibi EG, Makhetha TA, Moutloali RM. Effect of the Incorporation of ZIF-8@GO into the Thin-Film Membrane on Salt Rejection and BSA Fouling. Membranes (Basel). 2022;12(4). doi:10.3390/membranes12040436.

[46] Etale A, Nhlane D, Mhlongo J, Khan A. Synthesis and Application of Cationised Cellulose for Removal of Cr (VI) from Acid Mine-Drainage Contaminated Water. 2020;(October):0-18. doi:10.20944/preprints202009.0708.v1

[47] Yang Y, Wang J, Zhang J, Liu J, Yang X, Zhao H. Exfoliated Graphite Oxide Decorated by PDMAEMA Chains and Polymer Particles. Langmuir. 2009;25(15):11808-11814. doi:10.1021/la901441p.

[48] Zhu S, Li J, Chen Y. Grafting of graphene oxide with stimuli-responsive polymers by using ATRP for drug release. 2012; 14 (1132). doi:10.1007/s11051-012-1132-x.

[49] Kumar A, Behera B, Thakre GD, Ray SS. Covalently Grafted Graphene Oxide/Poly(Cn-acrylate) Nanocomposites by Surface-Initiated ATRP: An Efficient Antifriction, Antiwear, and Pour-Point-Depressant Lubricating Additive in Oil Media. Ind Eng Chem Res. 2016;55(31):8491-8500. doi:10.1021/acs.iecr.6b00848.

[50] Hu Z, Li C, Nie R, Li Y, Tang J, Deng X. RSC Advances Biomaterial functionalized graphene oxides with tunable work function for high sensitive organic. 2015:99431-99438. doi:10.1039/c5ra19476h.

[51] Oktay B, Uğur MH, Apohan NK. Preparation of poly (bis[2-(methacryloyloxy)ethyl] phosphate) crosslinked polymer brushes on Poly(vinylidene fluoride) nanofibers. Mater Chem Phys. 2018;217 168-174. doi:10.1016/j.matchemphys.2018.06.044.
[52] Mahmoudian M, Kochameshki MG, Hosseinzadeh M. Modification of graphene oxide by ATRP: A pH-responsive additive in membrane for separation of salts, dyes and heavy metals. J Environ Chem Eng. 2018;6(2):3122-3134. doi:10.1016/j.jece.2018.04.056.
[53] Namvari M, Biswas CS, Galluzzi M, Wang Q, Du B, Stadler FJ. Reduced graphene oxide composites with water soluble copolymers having tailored lower critical solution temperatures and unique tube-like structure. Nat Publ Gr. 2017;(7) 44508. doi:10.1038/srep44508.
[54] Xabela S, Moutloadi RM. 2-(N-3-Sulfopropyl-N,N-dimethyl ammonium)ethyl methacrylate modified graphene oxide embedded into cellulose acetate ultrafiltration membranes for improved performance. 2022;139 (24). doi:10.1002/app.52336.
[55] Rajender N, Suresh KI. Surface-Initiated Atom Transfer Radical Polymerization (SI-ATRP) From Graphene Oxide: Effect of Functionalized Graphene Sheet (FGS) on the Synthesis and Material Properties of PMMA Nanocomposites. 2016:9-11. doi:10.1002/mame.201500256.
[56] Ngaha MCD, Djemmoe LG, Njanja E, Kenfack IT. Biosorption Isotherms and Kinetics Studies for the Removal of 2,6-Dichlorophenolindophenol Using Palm Tree Trunk (Elaeis guineensis). J Encapsulation Adsorpt Sci. 2018;08(03):156-177. doi:10.4236/jeas.2018.83008.
[57] Borba LL, Cuba RMF, Cuba Terán FJ, Castro MN, Mendes TA. Use of adsorbent biochar from pequi (Caryocar Brasiliense) husks for the removal of commercial formulation of glyphosate from aqueous media. Brazilian Arch Biol Technol. 2019;62. doi:10.1590/1678-4324-2019180450.
[58] Hebbar RS, Isloor AM, Prabhu B, Inamuddin, Abdullah AM, Ismail AF. Removal of metal ions and humic acids through polyetherimide membrane with grafted bentonite. Sci Rep. 2018;(8) 4665. doi:10.1038/s41598-018-22837-1.
[59] Cristina B, Nechifor AC, Dimulescu IA, Oprea O, Nechifor G, Totu E.E., Isildak I, Albu P.C., Bungău S.G. Control of Nanostructured Polysulfone Membrane Preparation by Phase Inversion Method. Nanomaterials (Basel). 2020; 10(12): 2349. doi.org/10.3390%2Fnano10122349.
[60] Bai L, Liu Y, Bossa N, Ding A, Ren N, Li G, Liang H, Wiesner W.R. Incorporation of Cellulose Nanocrystals (CNCs) into the Polyamide Layer of Thin-Film Composite (TFC) Nanofiltration Membranes for Enhanced Separation Performance and Antifouling Properties. Environ Sci Technol. 2018;52(19):11178-11187. doi:10.1021/acs.est.8b04102.
[61] Xu C, Chen W, Gao H, Xie X, Chen Y. Cellulose nanocrystal/silver (CNC/Ag) thin-film nanocomposite nanofiltration membranes with multifunctional properties. Environ Sci Nano. 2020;7(3):803-816. doi:10.1039/c9en01367a.
[62] Wasim M, Sabir A, Sha M, Islam A, Azam M. Mixed matrix membranes: Two step process modified with electrospun (carboxy methylcellulose sodium salt/sepiolite) fibers for nanofiltration. J Ind Eng Chem. 2017; 50: 172 – 182. doi:10.1016/j.jiec.2017.02.011.

[63] Maiti S, Samantaray PK, Bose S. In situ assembly of a graphene oxide quantum dot-based thin-film nanocomposite supported on de-mixed blends for desalination through forward osmosis. Nanoscale Adv. 2020;2(5):1993-2003. doi:10.1039/c9na00688e.
[64] Shao W, Liu C, Yu T, Xiong Y, Hong Z, Xie Q. Constructing Positively Charged Thin-Film Nanocomposite Nanofiltration Membranes with enhanced performance. Polymers (Basel). 2020;12 (11), 2526. https://doi.org/10.3390/polym12112526.
[65] Hussainzadeh M, Mighani H, Shakeri A. High permeable and anti-fouling forward osmosis membranes modified with Grafted Graphene Oxide to Polyacrylamide (GO - PAAm). J Polym Res. 2022;29 (169). doi:10.1007/s10965-022-03018-1.
[66] Balcik C, Ozbey-Unal B, Sahin B, Keyikoğlu R, Khataee A. Loose Nanofiltration Membrane Incorporating CeZnFe Layered Double Hydroxide with Enhanced Dye/Salt Separation Performance and Self-Cleaning Ability. Membranes (Basel). 2023;13(8). doi:10.3390/membranes13080711.
[67] Nambikkattu J, Kaleekkal NJ, Jacob JP. Metal ferrite incorporated polysulfone thin-film nanocomposite membranes for wastewater treatment. Environmental and Energy Management 2021, 28:11915-11927. doi.org/10.1007/s11356-020-08024-8.
[68] Ang MBMY, Deang ABG, Aquino RR, et al. Assessing the Performance of Thin-Film Nanofiltration Membranes with Embedded Montmorillonites. MDPI Membranes 2020;10(79):1-21. http://dx.doi.org/10.3390/membranes10050079.
[69] Sapkota B, Liang W, VahidMohammadi A, Karnik R, Noy A, Wanunu M. High permeability sub-nanometre sieve composite MoS_2 membranes. Nat Commun. 2020;11(1):1-9. doi:10.1038/s41467-020-16577-y.
[70] Akbari A, Sheath P, Martin ST, et al. Large-area graphene-based nanofiltration membranes by shear alignment of discotic nematic liquid crystals of graphene oxide. Nat Commun. 2016;7. doi:10.1038/ncomms10891.
[71] Nightingale E.R. Phenomenological theory of ion solvation. Effective radii of hydrated ions, J. Phys. Chem. 1959; 63: 1381–1387.

Supplementary Information (S.I.)

S1: Experimental section

S1.1: Synthesis of GO nanosheets

GO was synthesized using improved Hummers method [1]. Briefly, graphite powder (1 g) was combined with $KMnO_4$ (6g) in a concentrated solution of H_2SO_4 and H_3PO_4 in a 9:1 ratio. For 12 hours, the mixture was stirring in an oil bath set to 50 ℃. After the reaction was completed, the mixture was allowed to cool to ambient temperature before being transferred to 400 mL of ice with 1 mL of 30% hydrogen peroxide (H_2O_2). When the mixture had reached room temperature, it was centrifuged at 4000 rpm for 30 minutes and the supernatant was carefully removed. The remaining precipitate underwent two washes with DI water before being rinsed with 30% HCl and ethanol. After this thorough washing, the residual material was coagulated with diethyl ether (200 mL). The resulting solid was then placed under vacuum and dried overnight at ambient temperature. Finally, the dried solid was pulverized with a mortar and pestle.

S1.2: Preparation of initiator-functionalized GO-Br

The modification of GO was achieved using an amended method reported by Kumar et al. in 2016 [2]. In a typical procedure, 250 mg of GO were added to a round-bottomed flask comprising of 30 mL of dimethylformamide (DMF). In order to make a colloidal suspension, the solution was sonicated for one hour and thereafter, 4 mL of triethylamine (TEA) was added to the flask, followed by the slow addition of 5 mL of α-bromoisobutyryl bromide. The mixture in an ice bath was stirred for 24 hours. The functionalized GO (GO-Br) was recovered via centrifugation, underwent numerous washes with chloroform and deionized water, and finally dried under vacuum for 12 hours.

References

[1] Marcano DC, Kosynkin DV, Berlin JM, Sinitskii A, Sun Z, Slesarev AS, Alemany LB, Lu W, Tour JM. Correction to: Improved Synthesis of Graphene Oxide. ACS Nano (2010) 4: 8 (4806-4814). doi: 10.1021/nn1006368.

[2] Kumar A, Bansal A, Behera B, Jain SL, Ray SS. Ternary hybrid polymeric nanocomposites through grafting of polystyrene on graphene oxide-TiO_2 by surface initiated atom transfer radical polymerization (SI-ATRP). Mater Chem Phys. 2016; 172:189-196. doi:10.1016/j.matchemphys.2016.01.064.

4.3 Paper 3

This paper entitled "**Low Pressure Thin Film Membranes with Cellulose Nanocrystals derived from Cannabis sativa for Enhanced Dye and Salt Removal**" has been published in Separation and Purification Technology.

This article evaluated the potential of glutamic acid functionalized cellulose nanocrystals modified TFN membranes in the removal of dye/salt in water.

Volume 366, 2025, 132829.

https://doi.org/10.1016/j.seppur.2025.132829

Khona Maziya – Principal author

Contribution: principal author, conceptualization, performed experiments, data collection/analysis, methodology, formal analysis, research, visualization and writing - original draft.

Low Pressure Thin Film Membranes with Cellulose Nanocrystals derived from Cannabis sativa for Enhanced Dye and Salt Removal

Khona Maziya[a], Izak Kotze[a], Oranso T. Mahlangu[b], Heidi Lynn Richards[a]

[a] Molecular Sciences Institute, School of Chemistry, University of the Witwatersrand, Private Bag X3, Johannesburg, 2050, South Africa

[b] University of South Africa, Nanotechnology and Water Sustainability Research Unit, College of Engineering, Science and Technology, Florida Science Campus, Roodepoort, South Africa

Graphical abstract

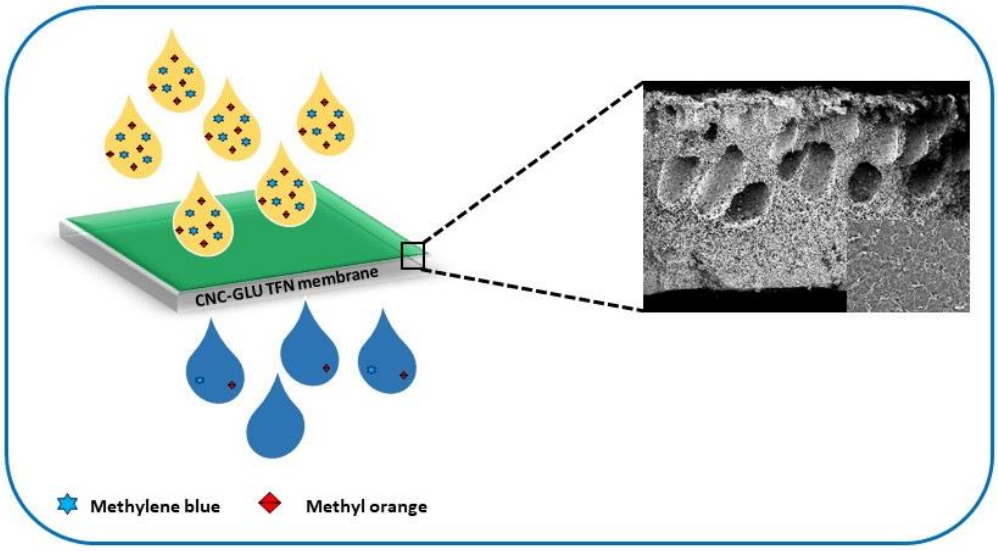

*Corresponding author: Email address: heidi.richards@wits.ac.za

Abstract

Cellulose nanocrystals (CNCs) are gaining popularity as nanomaterials in membrane-based separation processes due to their environmental friendliness and sustainability. Thin film nanocomposite (TFN) membranes containing glutamic acid modified CNCs dispersed within a polyamide (PA) film were produced in this study using an interfacial polymerization (IP) reaction over a polysulfone (PSF) substrate for low-pressure nanofiltration (NF). To characterize the membranes, FTIR, SEM, AFM, and contact angle analysis were utilized. The resulting CNC-GLU TFN membranes (0.10 wt%) were more hydrophilic and smoother than the comparable thin film composite (TFC) membrane. The CNC-GLU TFN membrane outperformed pristine TFC membranes with a pure water flux of 15.45 ±1.03 L/m^2h (400 kPa), high dye rejection (99.83% for methylene blue, 90.63% for methyl orange) and salt removal ($MgSO_4$ = 86%; NaCl = 38%). This was attributed to the increased hydrophilic active layer, Donnan exclusion, and steric hindrance. Furthermore, the TFN membrane effectively removed MB and MO dyes from wastewater and demonstrated good operational stability after six cycles. These findings revealed the enormous potential of these membranes in wastewater treatment, separation, and purification in a wide range of industrial applications.

***Keywords*:** Cellulose nanocrystals, Glutamic acid, Thin film nanocomposite membranes, dyes.

1. Introduction

Dyes used in the paper and textile sectors are one of the principal water pollutants, with over 10,000 tons discharged globally each year [1 – 3]. Dye wastewater contains elevated biological oxygen demand (BOD), chemical oxygen demand (COD), heightened color and contains organic compounds which are carcinogenic and mutagenic [4 – 5]. It is vital to remove dyes from textile and dyeing industries wastewater prior to being released to the environment. Dyes, even at low concentrations are toxic, and highly visible thus degrading the visual appeal of waterbodies and reducing the photosynthetic activities of aquatic flora [6 – 7].

Membrane separation technologies outshine conventional removal methods (adsorption, coagulation, flocculation, ozonation, etc.) due to their low operational costs, simple operation, smaller footprint and excellent selectivity [8 – 10]. However, conventional polymeric membranes are disposed to fouling thus reducing its lifespan [11 – 12]. Furthermore, the balance that exists amidst permeability and selectivity restricts the applicability of polymeric membranes [13 – 14]. To address these limitations, thin film nanocomposite (TFN) membranes with selective polyamide (PA) layer atop a support layer was developed. TFN membranes can be designed and controlled to regulate its separating abilities [15]. Considering only a small number of nanoparticles are required, including them into the selective PA layer lowers costs [15]. TFN membranes prepared via interfacial polymerization (IP) method on a porous support have demonstrated a high level of dye removal in water [15 – 18].

The integration of advanced nanomaterials into TFN membrane has been seen to significantly enhance water permeability and dye rejection performance. Ghaemi et al. (2018) investigated the effects of introducing nano-porous SAPO-34 (silicoaluminophosphate nano-porous zeolite) nanoparticles into the active layer of TFN membranes on membrane permeability and performance [19]. Upon the introduction and growth of nanoparticles in the active layer, the pure water flux increased from 10.9 – 35.2 kg/m^2h. The membrane's performance was evaluated in the removal of 50 mg/L of dyes (acid blue 193, methyl violet 6B, and reactive blue 4) in water, and the modified membranes efficiently removed 100% of all dyes [19]. Zhao et al. (2019) evaluated the impact of graphene oxide (GO) quantum dots on membrane performance [20]. Surface coating was used to incorporate GO quantum dots into the TFN PA layer, and membrane rejection against methyl orange (MO) and methylene blue (MB) was investigated. Electrostatic repulsion boosted MO rejection from 89.2 to 97% after modifying the PA layer with GO quantum dots [20]. However, there was a drop in MB rejection (75.4 – 71%), which was caused by positively charged MB adsorption onto the membrane, which reduced water flux and rejection [20].

Various materials have been incorporated during polyamide layer fabrication process to enhance water flux, selectivity and mechanical strength [21]. These include graphene oxide (GO), halloysite nanotubes (HNTs), carbon nanotubes, metallic organic frameworks (MOFs), titanium dioxide (TiO_2), etc. [18, 20, 22 – 28]. Nevertheless, some materials

incorporated into TFN membranes have been documented to be toxic to humans and the environment, thus limiting their usage in water treatment [29]. Cellulose nanocrystals (CNCs) from the cellulose nanomaterial family address these concerns. CNCs are made from sustainable and renewable resources, resulting in reduced health, environmental, and safety impact [30 – 31]. Acid hydrolysis is one of the methods of producing rod-shaped CNCs from plant sources such as hemp, wood, wheat, etc. CNCs have several impressive attributes such as large negative surface charge density, high aspect ratio, excellent mechanical properties and hydrophilicity due to the abundance of hydroxyl groups [32 – 34]. These features make CNCs appealing candidates for increasing membrane performance. Furthermore, because of cellulose biomass abundance in nature and the CNC synthesis process being straightforward, CNC production is extremely cost effective, making them an attractive choice [32]. Several researchers have reported the use of CNCs in TFN membranes to enhance performance. Bai et al. (2019) investigated membrane performance following the incorporation of CNCs (0.005 – 0.200 wt%) in polyamide layer generated via interfacial polymerization in TFC membranes [29]. The developed membranes demonstrated excellent divalent salt rejection of 98% and 97.5% for $MgSO_4$ and Na_2SO_4. The membranes also demonstrated superior dye removal (Rose Bengal, Crystal violet, Congo red, Methyl orange and Methylene blue), with the 0.150 wt% CNC membrane surpassing the others with 99.0% removal for all dyes [29].

Despite being shown to increase membrane performance, the aggregation of CNCs (stemming from hydrogen bonding interactions at the surface) remains a barrier to their widespread implementation in water treatment [33, 35]. CNCs modification is crucial to address this issue. Abedi et al. (2023) demonstrated that incorporating modified CNCs into TFN membranes significantly enhanced water permeability [36]. L-cysteine-functionalized CNCs (CysCNCs) and acetylated CNCs (ACNCs) were synthesized and integrated into the membranes [36]. Among the tested membranes, CysCNC-TFN0.2 (0.2 wt% CysCNCs) achieved the highest water permeability at 16 $L/m^2h.bar$, followed by ACNC-TFN0.1 (14.5 $L/m^2h.bar$), CNC-TFN0.1 (11.5$L/m^2h.bar$), and unmodified TFC membranes (6 $L/m^2h.bar$) [36].

Polymerization is one strategy that can be utilized to modify CNCs. This technique entails exploiting the oxygenated groups located on the CNCs surface to enhance interlayer distance. Surface-initiated atom transfer radical polymerization (SI-ATRP) serves as a flexible polymerization process which produces excellent grafting density and control over the brush design and thickness. This process requires immobilizing an initiator on the substrates surface followed by the growth phase characterized by the recurrent addition of monomers on the growing chain (polymerization) [37 – 38]. This functionalization produces multifunctional materials with end group functionalities [39]. Modifying the surface characteristics of CNCs serves dual purposes: it elevates membrane functionality by enhancing resistance to fouling and improving separation efficiency, while simultaneously enhancing compatibility with the polymer matrix through better dispersion and reduced particle clustering.

In this work, CNCs were modified with glutamic acid brushes through SI-ATRP to develop novel TFN membranes that display improved water permeability and dye/salt rejection capabilities. A range of characterization techniques including SEM, FTIR, NMR, XRD, TGA and AFM were employed to assess the physicochemical attributes of both the CNCs and the resulting TFN membranes, thereby elucidating the influence of the modified CNCs on membrane performance. Furthermore, permeation flux and dye removal tests were used to gauge the filtration and fouling resistance of the membranes. This research represents a groundbreaking approach in applying glutamic acid-modified CNCs to boost the efficacy of TFN membranes for dye and salt removal, proposing novel and effective methodologies for producing high-performance nanofiltration membranes. Ultimately, the efficacy of the TFN membranes was evaluated in real-world applications, specifically targeting water samples contaminated with dyes.

2. Materials and methods

2.1 Materials

Sodium hydroxide (NaOH), N,N,N ,N ,N‴- pentamethyldiethylenetriamine (PMDETA, 99%), glacial acetic acid (CH_3COOH), sodium chlorite ($NaClO_2$), trimesoyl chloride (TMC), sodium chloride (NaCl), sulphuric acid (H_2SO_4), tetrahydrofuran (THF), dimethylformamide (DMF), α-bromoisobutyryl bromide (BiBB) (98%), magnesium sulphate ($MgSO_4$), triethylamine (TEA, 99%), 4-(Dimethylamino)pyridine (DMAP), copper(I) bromide (CuBr), glutamic acid (GLU), ethanol, polysulphone (PSF) pellets (MW= 35 000 g/mol), m-phenylenediamine (MPD), Methyl orange (MO), Methylene blue (MB) and Polyvinylpyrrolidone (PVP) (MW = 30 – 70 K; 87 – 90%) were obtained from Sigma-Aldrich. By employing a Milli-Q system (Millipore), de-ionized (DI) water was produced with a resistivity of 18 mΩ cm. Hemp fibers were obtained locally.

2.2 Extraction of cellulose from cannabis sativa and CNC synthesis

The extraction of cellulose fibers was performed following a method reported by Mhlongo et al, 2022 [40]. To soften the bark, hemp branches and stems were immersed in water for a whole night then peeled from the woody core. The extracted bark was treated 4 wt% NaOH at 80℃ (2 hours). This step was done three times to ensure complete delignification. The fibers were then bleached with a solution containing equal parts of acetate buffer (pH 4.8) and $NaClO_2$ (1.7 wt%) at 100℃ for 1 hour, or till the fibers became white. Finally, the bleached fibers were rinsed with distilled water and air-dried.

Synthesis of cellulose nanocrystals from hemp cellulose fibers

Sulphuric acid (60 wt%) was added to bleached fibers. In summary, cellulose fibers were hydrolyzed with sulfuric acid (20 mL/g acid/pulp ratio). Dropwise, sulphuric acid was added with vigorous stirring while keeping the temperature below 30℃. The reaction mixture temperature was increased to 45 ℃ once the acid addition was finished. The reaction was kept at this temperature for an hour while being constantly stirred. The hydrolysis process was terminated by introducing 200 mL of cold water (about 2x the volume of acid solution). To obtain a precipitate, the diluted sample was centrifuged for 10 minutes at 11,000 rpm. After thorough agitation, the precipitate was re-suspended in water

and centrifuged. This procedure was continued until the pH of the suspension reached 5, at which point dialysis was performed for three days to ensure that the pH remained constant. In order to disperse the nanocellulose in water, the suspension was sonicated using an ultrasonic homogenizer [41].

2.3 Synthesis of ATRP initiator grafted CNC (CNC-Br)

CNCs were modified by BIBB to prepare brominated CNCs (CNC-Br) prior to SI-ATRP reaction with glutamic acid. This was done following a modified approach described by Zhang et al (2019) [42]. After sonicating the CNCs into the 50 mL of DMF, DMAP (2 g) and TEA (4 mL) were added. The suspension was stirred for 24 hours after adding 4 mL of BIBB dropwise at 0°C. The reaction was terminated with ethanol, rinsed with acetone 3 times, and dialyzed for 5 days in water. Finally, the CNC-Br was produced through freeze-drying.

2.4 Grafting GLU from CNC-Br by SI-ATRP

This was done following a comparable method described by Zhang et al (2017) [43]. In a typical reaction, CNC-Br was evenly dispersed in DMF using sonication and magnetic stirring. The mixture was then moved to a 250 mL round-bottom flask, where PMDETA and GLU monomer were introduced. These components were combined in a molar ratio of 100:1:1 for GLU, PMDETA, and CuBr. Before adding CuBr, the suspension was purged with nitrogen gas for 10 minutes. It was then degassed for an additional 10 minutes before being placed in an oil bath (70°C) under magnetic stirring, allowing the reaction to proceed for 24 hours. The reaction was concluded by exposing the mixture to air. To isolate CNC-GLU 100, the resulting mixture was washed with THF and ethanol, followed by centrifugation to eliminate any unreacted chemicals and free polymer, and finally freeze-dried.

2.5 Preparation of TFN membranes

Preparation of polysulfone (PSF) substrate

The PSF support membrane was produced via the phase inversion method. To create the casting solution for the PSF membrane, a mixture consisting of 1 wt% PVP and 16 wt% PSF was dissolved in DMF solvent. This solution was stirred for 12 hours at a temperature of 50°C to ensure it was homogeneous. Following degassing, the solution was applied onto a glass plate to achieve a thickness of 100 μm, utilizing an Electrometer 4843 automatic film applicator from Manchester, UK. The coated plate was then submerged in a water coagulation bath at room temperature to enable solvent/non-solvent exchange through the wet phase inversion process. Afterward, the membrane film was thoroughly washed with fresh distilled water to eradicate any remaining DMF and was stored in distilled water until it was ready for use.

Preparation of polyamide (PA) selective layer

The membranes PA layer was synthesized on a PSF support membrane using the traditional IP process. Pre-treatment of the PSF support membranes involved soaking them in an overnight solution (0.5% sodium dodecyl sulphate (SDS)). Following that, distilled

water was used to rinse the membranes for an hour. The substrate (PSF support) was subsequently secured between a frame and a glass plate. 2 w/v% MPD aqueous solution (20 mL) was poured onto the porous PSF substrate. After a 2-minute contact period, surplus MPD solution was removed from the sub-layer surface by placing it vertically (1 minute). The PSF substrate was then contacted with the organic phase that contained 0.2 wt% TMC-hexane solution (1 minute) before being removed from the membrane surface. Thereafter, the membrane was oven-dried for 8 minutes at 60°C to increase crosslinking and washed with distilled water. The technique to fabricate CNC-GLU TFN membranes resembled that used for TFC membranes, with the exception that CNCs (modified) were first introduced to an aqueous solution of MPD (**Table 1**). Prior to affecting the interfacial polycondensation reaction, all MPD/additives solutions were sonicated for 30 minutes [44].

Table 1: TFN membranes CNC-GLU 100 loading

Membrane	CNC-GLU 100 loading (wt%)
TFC	-
TFN	0.10

2.6 Characterization

The morphology of CNCs was analyzed with a FEI Tecnai G2 Spirit transmission electron microscope (TEM) (Hillsboro, USA) operating at an acceleration voltage of 120 kV. The Image J software was used to measure the diameter of CNCs. The chemical changes in CNCs and membranes were investigated using Fourier transform infrared (FTIR) spectroscopy, with spectra recorded between 4000 to 500 cm^{-1} using a Tensor 27 Infrared Spectrometer (Massachusetts, USA). X-ray diffraction (XRD) analysis was performed using a Bruker D2 Phaser diffractometer (Cu-Kα) (Johannesburg, South Africa) scanning from 5 to 90° (2θ), with a step size of 0.026 and a step time of 37 seconds. The solid-state ^{13}C nuclear magnetic resonance (^{13}C MAS NMR) spectra for CNC and CNC-GLU were obtained on an AVANCE-III-500 spectrometer (Bruker, Germany) using cross-polarization MAS with 4mm zirconium rotors at a spin rate of 8 or 10 kHz. ^{13}C NMR chemical shifts were externally referenced to adamantane following Hoffman's method [45]. Elemental analysis of carbon, hydrogen, nitrogen, and sulfur (CHNS) was performed using a varioELcube v4.0.13 analyzer (Elementar, Germany). The thermal resistance of CNC and its derivatives was measured via thermogravimetric analysis (TGA), conducted with a thermogravimetric analyzer over a temperature range of 35 – 900°C in a nitrogen atmosphere at a heating rate of 20°C/ minute (Perkin Elmer). The surface and cross-sectional morphologies of the synthesized membranes were analyzed using field emission scanning electron microscopy (FESEM-EDS) (Carl Zeiss Sigma) at an accelerating voltage of 20 kV. Prior to imaging, the TFN membranes were coated with carbon and Pd/Au. Contact angle measurements were performed employing the sessile-drop method using a

DataPhysics Optical Contact Angle apparatus (Germany). For each membrane sample, ten measurements were recorded at different locations.

CNC derivatives' pH point of zero charge (pH PZC) was ascertained using the salt titration method [45]. In short, 0.1g of CNC-GLU 100 was added to five polypropylene tubes containing 25 mL of 0.01M NaCl. The pH of these solutions was then adjusted between 2 and 10 with 0.1 M NaOH and 0.1 M HNO_3, giving each tube its own pH value. The suspensions were shaken horizontally for 24 hours. The ultimate pH of each solution was plotted against the initial pH of the solutions, and the pH PZC for each material was computed using the intersection points [46].

2.7 Water uptake measurements

Water uptake of the TFN membranes was ascertained by measuring the change between their dry and wet weights. Membrane samples with an area of 0.00146 m² were first dried to remove moisture then weighed to determine their dry weight (W_d) before being immersed for 24 hours in distilled water. After soaking, the membranes were lightly dabbed with paper to eliminate extra water, and then their wet weight (W_w) was measured (**Equation 1**).

$$WIC\ (\%) = (W_w - W_d)/ W_w \times 100 \quad (1)$$

2.8 Membrane performance

The efficacy of all fabricated membranes was assessed using a nitrogen-driven dead-end filtration system (Sterlitech, HP4750 Stirred Cell). Membrane samples (0.00146 m^2) were compacted with DI water under a transmembrane pressure of 600 kPa until a stable flux was reached. The pure water flux was then calculated at a pressure of 400 kPa using deionized water as the feed solution, following **Equation 2**.

$$J_w = V/(A.\Delta t) \quad (2)$$

Where; J_w is the pure water flux ($L/m^2.h$),

V is the volume of the permeated water (L),

A is the effective area of the membrane (m^2),

Δt is the permeation time (h).

Salt and dye rejection tests were carried out on a dead-end filtration cell with continual magnetic stirring. Two organic dyes with varying electrostatic properties were used: methylene blue (MB) and methyl orange (MO) (**Fig. 1**). Various dye concentrations (20, 50, 80, and 100 mg/L) and pH were tested, and they were circulated through the cell at 400 kPa transmembrane pressure. The solute concentration was determined using UV-visible (UV-vis) spectroscopy. The feed also contained various salts (NaCl and $MgSO_4$) at concentrations of 2000 mg/L. Salts concentrations were detected by the conductivity meter (Hanna multimeter instrument, Hl 5522, South Africa).

The observed rejection (%R) was calculated using **Equation 3**:

$$\%R = (1 - C_p/C_f) \text{ X } 100 \quad (3)$$

where C_p and C_f denote the dye concentrations (mg/L) of the feed and permeate solutions.

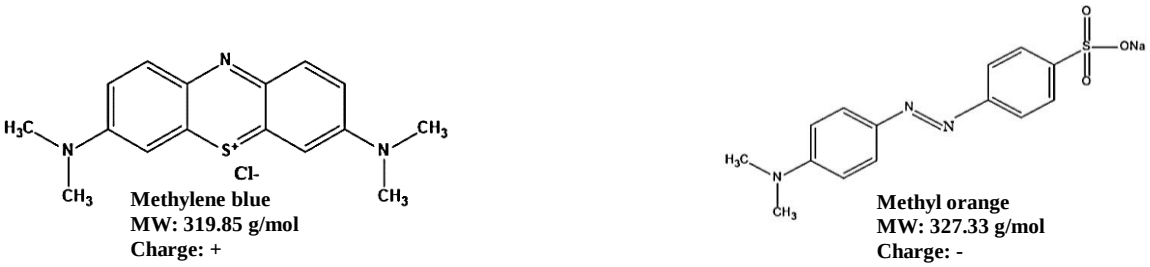

Fig. 1. The molecular structure, weight and charge of the dyes.

3. Results and discussion

3.1 Physiochemical characterization of CNC and derivatives

3.1.1 TEM analysis

By hydrolyzing hemp fibers with sulfuric acid, the CNCs used in this work were isolated, following a typical process published in the literature [41]. The morphology of CNCs and its derivatives was visualized using TEM (**Fig. 2**). Synthesized CNCs were rod-shape with a mean diameter of 4.9 ± 1.6 nm. The CNCs exhibits laterally aggregated rods due of its large specific area and strong hydrogen bonding between nanocrystals [47]. Upon attachment with the initiator, the CNCs still maintained a rod-shaped morphology with no change in diameter (**Fig. 2 (b, b')**). EDS analysis of CNC-Br was carried out (**Fig. S1**). The EDS analysis of CNC-Br confirmed the presence of Br, C, and O at 1.48, 0.26, and 0.51 keV respectively, verifying the attachment of the Br containing initiator to the CNC.

However, growing glutamic acid chains on the surface of the CNCs exhibits an opaque layer around the CNCs, with an increase in diameter (9.4 ± 1.7 nm) (**Fig. 2 (c, c')**). The difference in the structural integrity prior to and following grafting modification could be used to indicate the presence of GLU brushes [48]. Kiriakou et al. (2021) observed comparable results in their study, wherein CNCs were grafted with Poly (butyl acrylate) synthesized in either toluene or DMF, along with a free polymer derived from a sacrificial initiator [49]. The initiator-attached CNCs maintained their rod-shaped structure and resembled their unaltered precursors according to TEM imaging, while the DMF polymerized CNCs displayed increased width but similar lengths, which was consistent with polymer grafting [49].

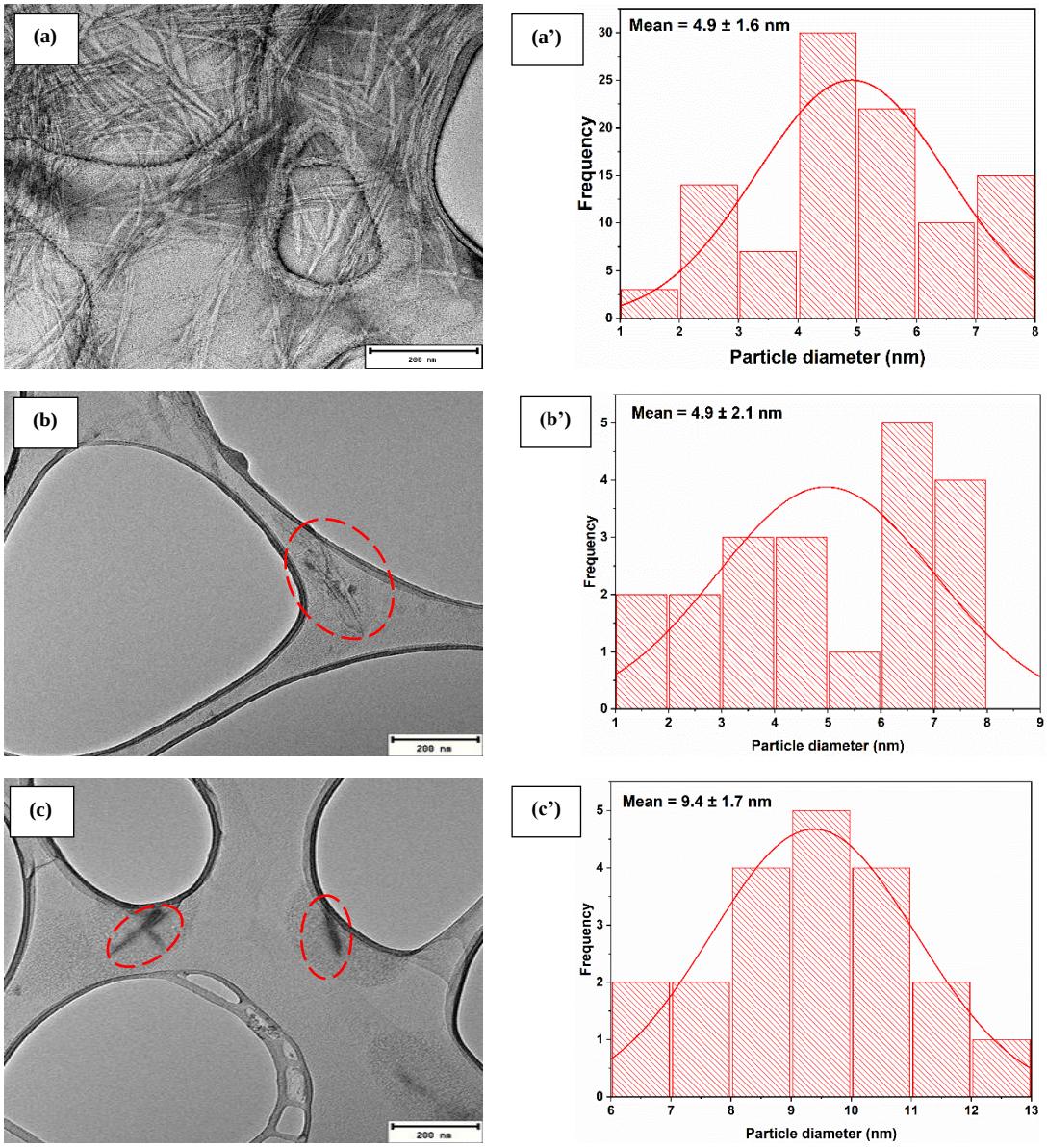

Fig. 2. TEM image of pristine CNC, CNC-Br and CNC-GLU 100 (a - c), and corresponding size distribution histogram (a' – c').

3.1.2 FTIR, XRD, CP/MAS ^{13}C NMR, CHNS, TGA, PZC analysis

The CNCs and derivatives were characterized using FTIR, XRD, CP/MAS ^{13}C NMR, CHNS and pH PZC as depicted in **Fig. 3**. The FTIR spectroscopy revealed the effective grafting of the BIBB initiator on the surface of CNCs. **Fig. 3(a)** displays the spectra of pure CNCs, CNC-Br and CNC-GLU 100. The CNC spectrum exhibits significant bands at 3319 cm^{-1} ascribed to the O-H groups. The bands at 2897, 1368 and 1640 cm^{-1} are due to the C-H stretching and bending, and carboxyl groups stretching vibrations, respectively. Compared to the CNC, CNC-Br samples revealed an additional FTIR peak at around 1724 cm^{-1} owing to the ester carbonyl group of ATRP initiator attached to the CNCs [50 – 51]. There was a decrease in peak at 3319 cm^{-1} after ATRP initiator attachment, indicating that some surface O-H groups were replaced [52]. Upon growing the glutamic acid brushes on CNCs, the spectra displayed peaks at 1728 cm^{-1} allotted to the stretching vibration of -C=O

bond due to the presence of the carboxylic group in glutamic acid. The peaks at 1570, 1371 and 1131 cm^{-1} are ascribed to the N-H bend, -C-N- stretching in the secondary amide groups, respectively suggesting that amidation reaction was successful.

XRD analysis was used to explore alterations in the crystalline structure of CNCs after acidic hydrolysis, esterification with BIBB, and polymerization with glutamic acid (**Fig. 3 (b)**). The CNC diffractograms exhibited a broad amorphous hump with distinct crystalline peaks, characteristic of a semi-crystalline material. Three crystalline peaks typical of cellulose I were present at approximately $2\theta = 15.5^{o}$,16.5^{o} (110), 22.7^{o} (002) and 34.6^{o} (004) [53 – 54]. Upon attachment with BIBB initiator, there was no observable difference in the pattern suggesting that the CNCs maintained their structure during the reaction. The XRD pattern for glutamic acid demonstrated the high crystallization imparted on the CNC-GLU 100 following its polymer growth on CNCs.

The thermal resistance of CNC and derivatives was investigated by means of TGA analysis as shown in **Fig. 3(c)**. The pure CNCs thermogram correlates with the thermal behavior commonly detected for CNCs produced by sulfuric acid hydrolysis [55]. The minor weight loss observed below 150°C is due to the absorbed moisture content of the samples. The CNCs exhibited major weight loss at 210 – 430°C due to cellulose chain degradation which includes dehydration, depolymerization, and decomposition of glycosidic units. CNC-Br showed a similar weight loss pattern, however it exhibited its main loss between 182 – 400°C. The CNC-Br exhibited lower thermal stability due to the labile bromine, upon heating it forms HBr which can speed the degradation of cellulose [56 – 57]. Upon grafting the CNC-Br with glutamic acid brushes, there was an increase in Tonset (~180°C), and the main weight loss step shifted to 194 – 362 °C. This was due to the presence of glutamic acid chains that minimize exposure to high temperature thus increasing resistance to thermal degradation.

The pH at which a material has zero net surface charge in a particular solution is referred to as its PZC [58]. It was observed that the pH PZC of CNC-GLU 100 was 5.13, this implies that at pHs lower than 5.13 the surface charge is positive, neutral at 5.13 and negatively charged at higher pHs (**Fig. 3(d)**) [59]. Adding CNC-GLU 100 to the PA layer of TFN membranes unavoidably impacts their overall charge. This might suggest that the membrane's PZC pH might be close to 5.13.

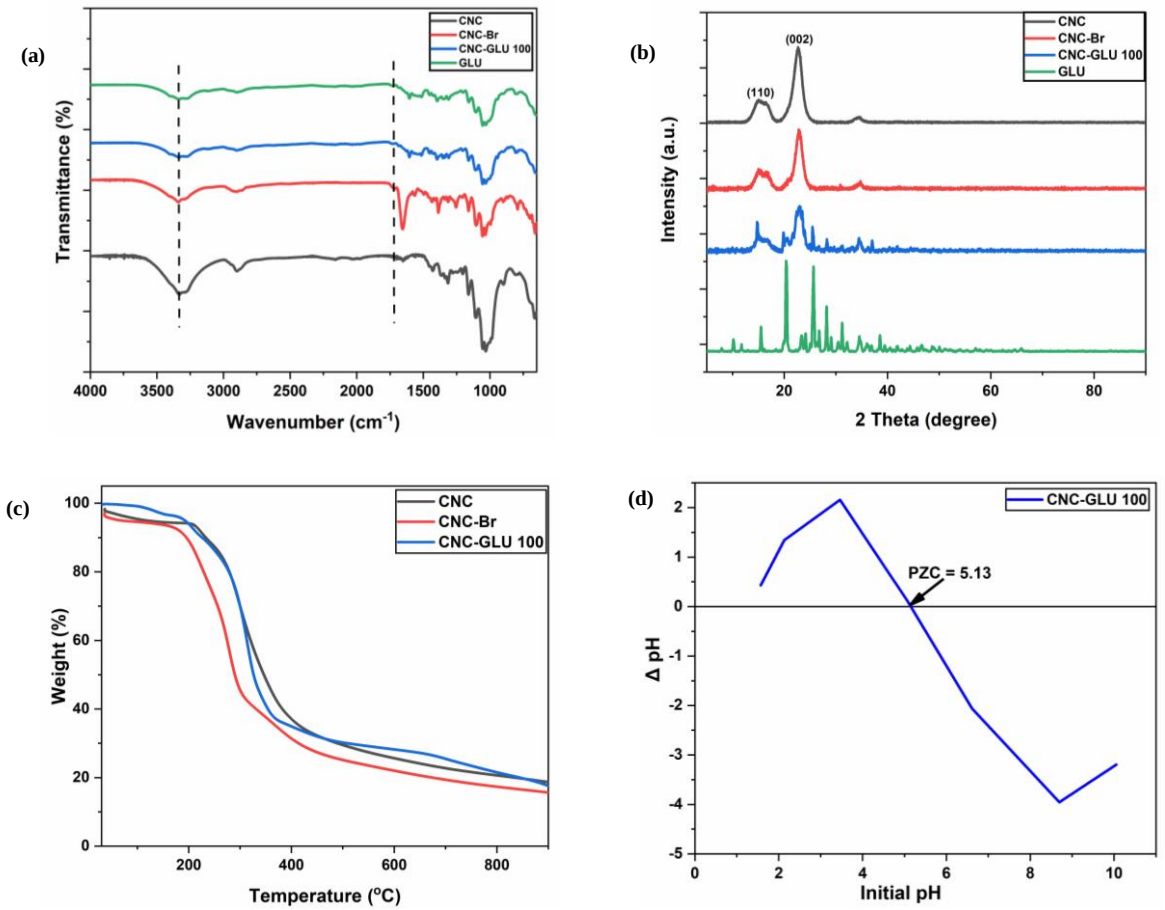

Fig. 3. FTIR spectra (a), TGA thermograph (b), XRD patterns (c) and PZC (d) of CNC, CNC-Br, CNC-GLU 100.

The elemental analysis also revealed the contents of C, H, N and S present in the CNC and derivatives as shown in **Table 2**. The Nitrogen content increased with the grafting of the glutamic acid brushes (0.54 – 2.76%). This correlates with the TEM analysis where a dense layer is observed around CNCs after growing glutamic acid brushes.

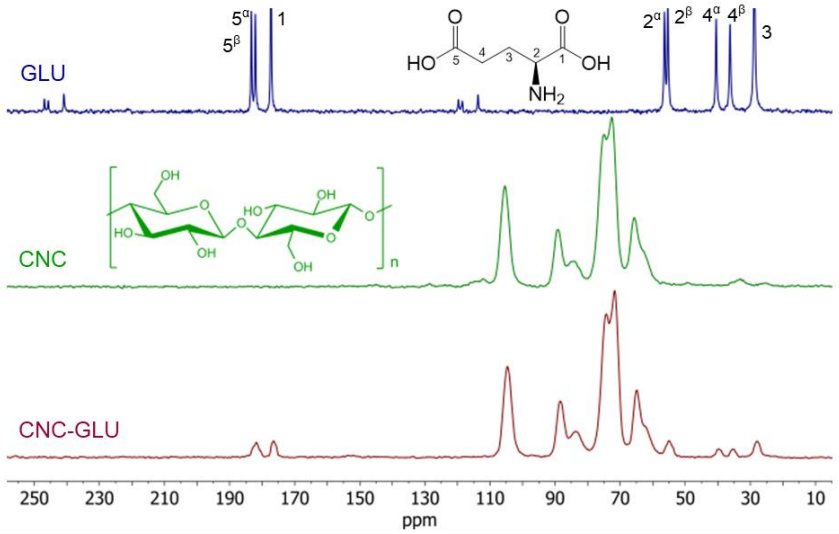

Fig. 4. 13C CP/MAS NMR spectrum of CNC, GLU, and CNC-GLU 100 (Pulse program: CP/MAS; MAS rate: 8–10 kHz).

The high-resolution ^{13}C CP/MAS NMR spectrum of GLU confirms the presence of both α and β polymorphs, with all signals clearly resolved **(Fig. 4)**. This is consistent with the chemical shifts reported by Wang and colleagues [60]. After grafting GLU onto CNC, the signals from GLU broaden, as expected for polymerised GLU on the CNC surface (**Fig. 4**). No significant changes in the peak width or chemical shift of the CNC were observed, suggesting that the structure of the CNC is largely preserved, corroborating our findings from other characterisation techniques.

Table 2: Elemental analysis of CNC, CNC-GLU 100 and GLU.

Sample	C (%)	H (%)	N (%)	S (%)
CNC	**35.76**	**4.348**	**0.54**	**0.185**
CNC-Br	**42.29**	**5.791**	**0.15**	**0.319**
CNC-GLU 100	**37.13**	**5.221**	**2.76**	**0.036**
GLU	**32.18**	**4.974**	**7.57**	**0**

3.2 Characterization of CNC-GLU -Functionalized TFN Membranes

3.2.1 Morphology of TFN membranes

The membranes surface and cross-section morphologies were characterized with FESEM and AFM imaging as depicted in **Fig. 5**. The TFC membrane exhibits spherical globules and rough nodules credited to the crosslinking in between MPD and TMC (**Fig. 5 (a)**). This also shows that the PA layer completely covers the substrate layer [34]. This typical ridge valley structure is observed in polyamide layers prepared via interfacial polymerization [31]. However, upon CNC-GLU 100 incorporation, more leaf-like nodules

are observed (**Fig. 5 (b)**). This might have occurred owing to the presence of hydrophilic CNCs, which can facilitate the IP procedure by improving the compatible mixing of the aqueous and organic phases and the diffusion of MPD into the organic phase [30, 61]. Shamar et al (2022) noted similar findings after the formation of PA layer with Co-Zn based mixed metal-organic frameworks (mMOFs) incorporated in MPD and TMC [62]. Both TFC and TFN membrane after diffusion reaction of monomers (TMC and MPD) exhibited a typical ring and leaf shape structure. However, a prominent leaf-like structure was observed in TFN membrane, this is due to the occurrence of highly porous evenly distributed mMOFs. This results in improved containment of gases (resultant CO_2 gasses that are IP by-products trapped in PA layer resulting in ridge valley morphology), therefore a leaf-like PA formation is favored [62]. Furthermore, **Fig. S2** demonstrates the successful formation of a PA layer atop the PSF substrate for both TFC and CNC-GLU TFN membranes as indicated by the visible PA layer.

The surface roughness analysis is presented in **Fig. 5 (a')** and **(b')**. As illustrated, the architecture of the membrane surfaces appears in the form of dark and light areas illustrating valleys and peaks, respectively. The TFC membrane exhibited a greater surface roughness (Sa = 103 nm) than the TFN membrane (Sa = 63 nm). This is likely caused by the formation of hydrogen bonds in between CNCs and MPD coupled with the presence of hydroxyl and polar functional groups of the CNC-GLU which can hinder the formation of the PA layer thus causing the membrane to smoothen [63]. In theory, membrane surfaces with low roughness and high hydrophilicity have the potential to provide improved fouling resistance [64]. The change in both morphology and surface roughness proves the proper dispersion and distribution of CNC-GLU 100 embedded in the PA layer.

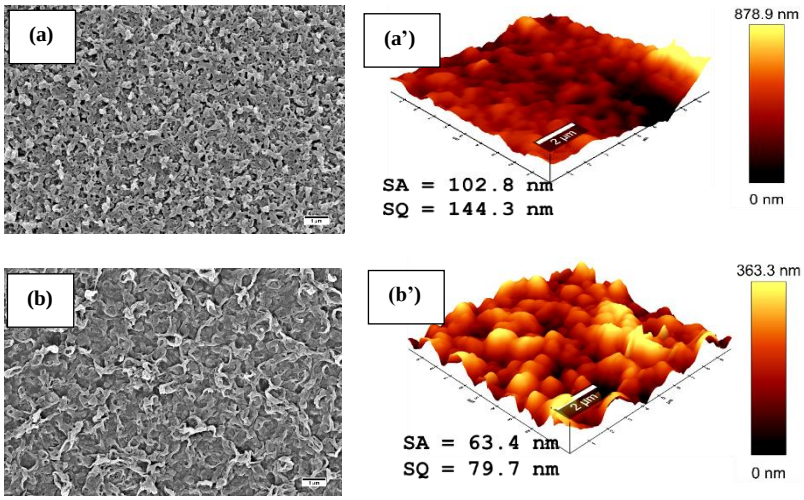

Fig. 5. Surface (a, b), and AFM images (a', b') of TFC and CNC-GLU TFN membranes.

3.2.2 FTIR of membranes

The surface functional groups of PSF, TFC and CNC-GLU TFN membranes were analyzed using FTIR as illustrated in **Fig. 6**. The pure PSF membrane exhibited distinctive

peaks at 1322, 1293, 1489, and 2981 cm^{-1} which are corresponding to the following molecular vibrations: asymmetric stretching of C-SO_2-C, S=O stretching, C=C stretching present in the aromatic ring and aliphatic C-H stretching respectively [65]. The peaks at 828 and 1007 cm^{-1} are ascribed to the aromatic rocking vibrations of the C-H bonds. Upon the formation of the active PA layer on the PSF, different spectra is observed for both TFC and TFN membrane. The appearance of the peak at 1658 cm^{-1} is ascribed to the reaction between the acryl chloride groups of TMC and the amine groups found in MPD solution [66]. The peak at 1542 cm^{-1} relates to N-H bending and C-N stretching vibrations associated with the amide II band. These peaks confirm the successful synthesis of the polyamide layer via IP [32, 66]. Regardless of the CNC incorporation, both TFC and TFN display similar spectra with noteworthy peaks at 1658, 1241 cm^{-1} which are credited to C=O (Amide I) and C-N stretch [67]. Furthermore, TFN exhibits a broad band at 3372 cm^{-1} ascribed to the O–H stretching from the partially hydrolyzed acyl chloride of TMC and the CNC-GLU 100 [68 – 69].

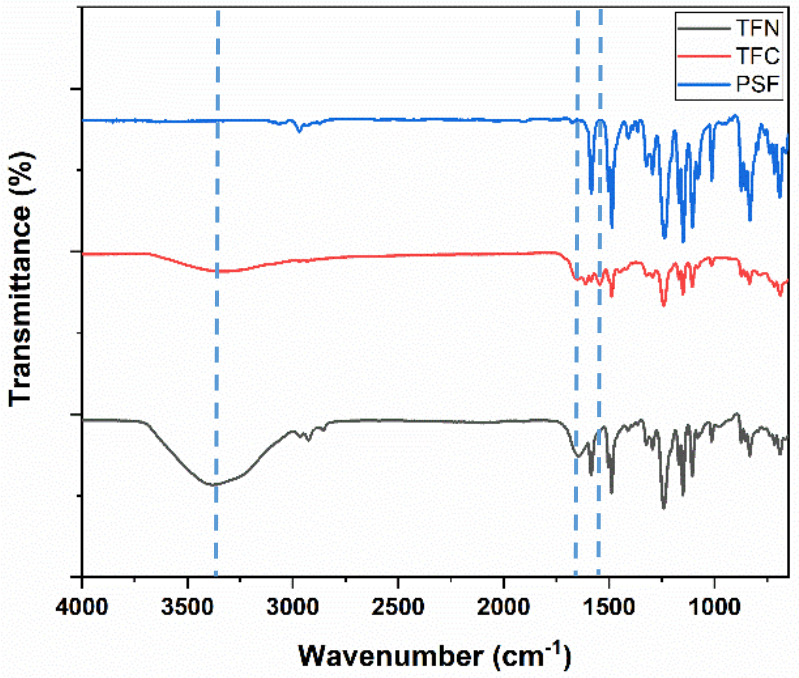

Fig. 6. FTIR spectra for PSF, TFC and CNC-GLU TFN membrane.

3.2.3 Water permeability studies

The hydrophilicity of the TFC and CNC-GLU TFN membranes was assessed using water intake capacity (WIC) and contact angle measurements (**Table 3**). The swelling capacity or WIC of a membrane is a measurement of its bulk hydrophilicity. The WIC increased upon the addition of CNC-GLU 100 into the PA layer. The TFN membrane exhibited a higher WIC (70.63%) as opposed to the TFC membrane (59.62%). These results correlated with the contact angle measurements whereby TFN membrane proved to be more hydrophilic by exhibiting a lower CA (76 ± 4º) as compared to the TFC membrane (95 ± 2º). The CNC-GLU 100 enhanced the hydrophilicity of the membranes due to the presence of

hydrophilic carboxyl and hydroxyl groups [70 – 71]. The increase in hydrophilicity suggests an increased water flux and antifouling properties [71].

Table 3: Membrane pure water permeation studies.

Membrane	WIC (%)	WCA (^{o})
TFC	59.62	95 ± 2
CNC-GLU TFN	70.63	76 ± 4

3.3 Membrane performance

3.3.1 Pure water flux

Fig. 7 demonstrates the pure water flux of the TFC and CNC-GLU TFN membranes at 400 kPa. Upon the introduction of CNC-GLU 100 into the PA layer, there was an observable increase in permeate water flux from 7.11 ± 0.63 – 15.45 ±1.03 L/m^{2}h. The inclusion of CNC-GLU 100 into the PA layer dramatically enhances pure water flux owing to the rise in hydrophilicity resulting from the addition of hydrophilic groups to the polyamide film [29]. The CNC-GLU 100 exhibits a high surface density of functional groups, including hydroxyl, carboxyl, and amine moieties, which confer a hydrophilic nature to the membrane. The enhanced surface area of CNC-GLU 100, coupled with the electrostatic effects arising from functionalization, led to an increase in membrane flux. Moreover, the free volume created by the restricted phase separation stemming from the tight interfacial bonding between functionalized CNCs and the polyamide matrix mimics water conduits, thus boosting water transport efficiency.

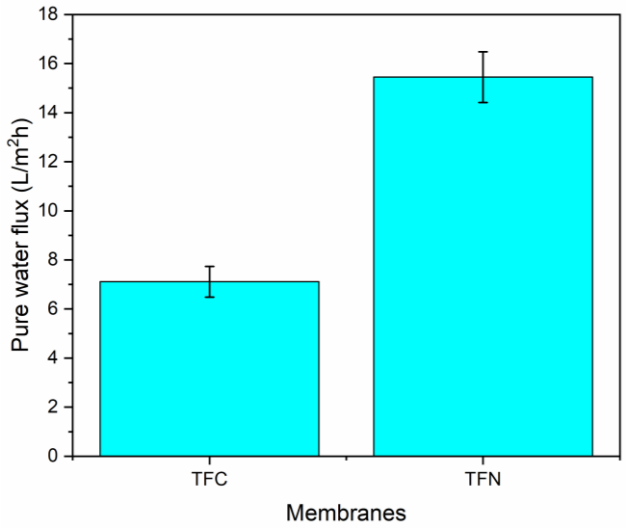

Fig. 7. Pure water flux for TFC and CNC-GLU TFN membranes.

3.3.2 Membrane separation performance

Influence of dye concentration and pH on removal capacity

The separation efficiency of the membranes for the rejection of dyes was assessed by varying both the dye concentrations and pHs of MO and MB. The concentration of the dyes ranged from 20 – 100 mg/L as shown in **Fig. 8**. The TFC membrane rejection of MB dye ranged from 83.63 – 96.29%, whilst CNC-GLU TFN rejection ranged from 93.91 - 99.83%. MO dye rejections were lower for both TFC (54.83 – 60.16%) and TFN (74.15 – 90.63%). These results demonstrate that the inclusion of modified CNC enhances dye separation by increasing the electrostatic charge of the membrane. The rejection behavior can be due to sieving, steric hindrances and the Donnan exclusion principle [72]. MB's enhanced rejection can be ascribed to its larger hydrated radii of 5.04A as compared to MOs radii of 4.97A, which produces sieving hindrances [73 – 74]. The abundance of carboxyl groups on the glutamic acid modified CNCs in the TFN membrane generates a negative surface charge causing the membrane to have substantial electrostatic attraction to MB. Conversely, electrostatic repulsion towards the anionic MO dye is caused by the membrane's negatively charged surface thus improved rejection was observed for the cationic MB dye. **Fig. 9** reveals that dye solutions (50 mg/L) showed lower permeate fluxes than pure water due to dye adsorption on membrane surfaces.

Fig. 9 further indicates that the dye flux is higher in MB than in MO. The incorporation of negatively charged CNC-GLU 100 imparts a negative surface charge. As a result, this surface is likely to repel anionic dyes more effectively than cationic dyes, leading to a decrease in the flux of anionic dyes due to electrostatic repulsion. Conversely, cationic dyes may encounter less repulsion or even electrostatic attraction, resulting in an increased flux.

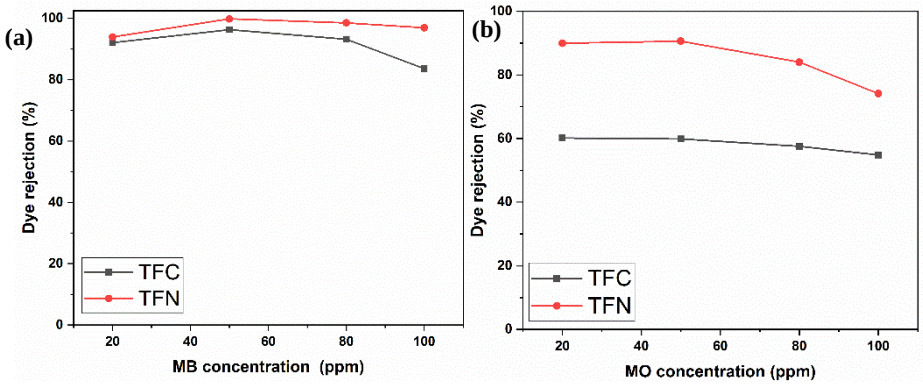

Fig. 8. Dye rejection performance of TFC and CNC-GLU TFN membranes; MB (a) and MO (b).

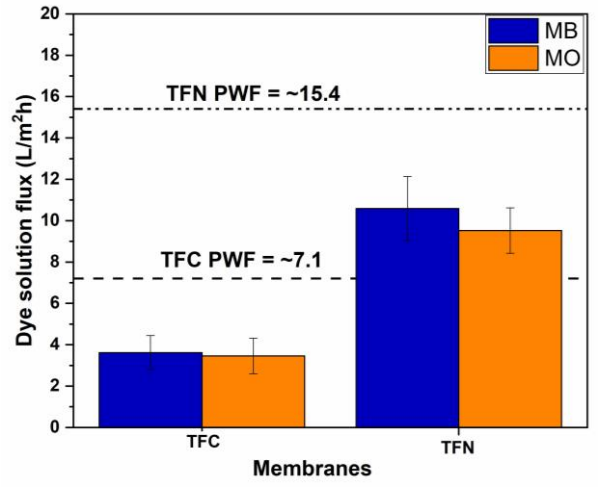

Fig. 9. Dye solution flux for TFC and CNC-GLU TFN membranes.

pH studies were carried out at pH 2, 6.5, and 11 using dye filtration with TFC and TFN membranes, with results shown in **Fig. 10 (a)** and **(b)** for MB and MO, respectively. Given that solution pH has a direct impact on the electrochemical attributes of the dye molecules and membrane surface, membrane separation efficiency can be successfully regulated. At all pH ranges, the rejection rate of MB was greater than 85%, with rejection increasing to 96% at pH levels above 7. At lower pH levels, the negative charge on the membrane surface weakens, making it easier for negatively charged MO molecules to adsorb and deposit. At pH 2, MO had the highest rejection rate (~90%). A decrease in MO rejection is caused by an increase in the membranes surface negative charge when the pH of the solution rises. Electrostatic repulsion hindered the ability of negatively charged MO dye molecules to adsorb on the membrane surface.

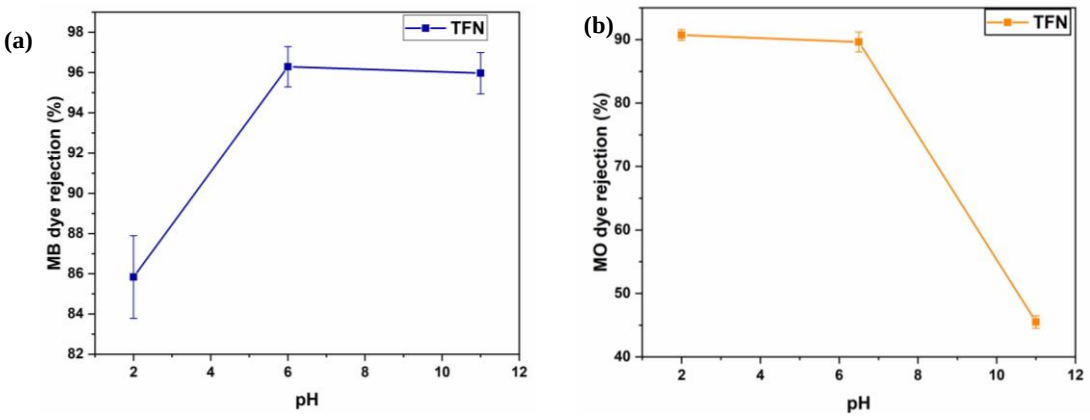

Fig. 10. TFN dye rejection vs pH; MB (a) and MO (b).

3.3.3 Membrane recyclability and long-term performance studies

Membrane reusability is crucial for practical applications, especially on a large scale; hence, membrane effectiveness and durability are critical. Even after six cycles (30 minute per cycle), **Fig. 11** shows that the CNC-GLU TFN membrane demonstrated outstanding

rejection ability for both MB and MO dyes (50 mg/L, solution pH). After six cycles, both dyes showed a decline in their removal efficiency. MB dye removal effectiveness reduced from 97.98 to 88.26% whilst MO rejection decreased from 88.97 to 79.98%. This could be explained by membrane fouling or the cleaning process's failure to eliminate absorbed dye molecules. This will eventually lead to a reduction in the membrane's removal efficacy.

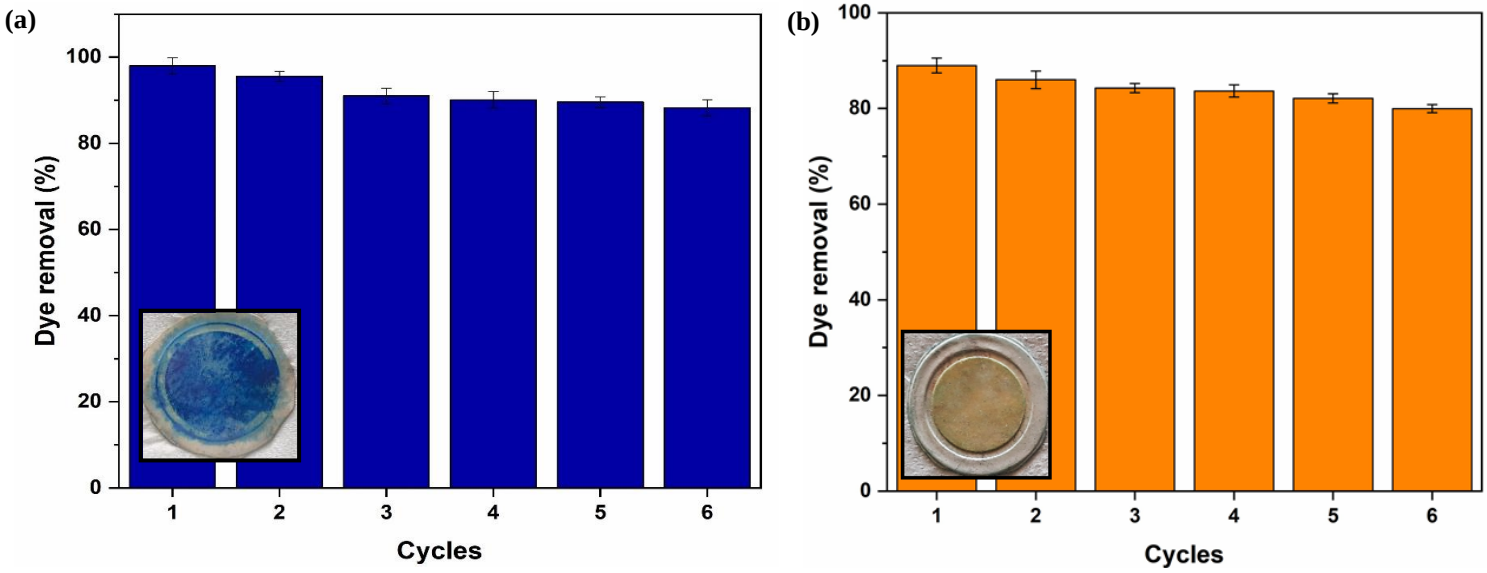

Fig. 11. The cycles of reusability for CNC-GLU TFN; MB (a) and MO (b). (Insert: Photos of CNC-GLU TFN after filtration cycles).

3.3.4 Long-term performance studies

The long-term operational durability of the CNC-GLU TFN membrane was also assessed. The normalized permeate flux and dye rejection performance of the CNC-GLU TFN membrane when filtering a 50 mg/L MB solution at 400 kPa are illustrated in **Fig. 12**. The CNC-GLU TFN membrane retained a dye rejection above 99% during continuous operation spanning over 400 minutes. However, its permeate flux toward MB exhibited a gradual decline over time. This performance degradation was linked to progressive fouling mechanisms, including the formation of a dense cake layer on the membrane surface and associated pore occlusion. These factors contributed to increased concentration polarization effects, ultimately reducing membrane permeability.

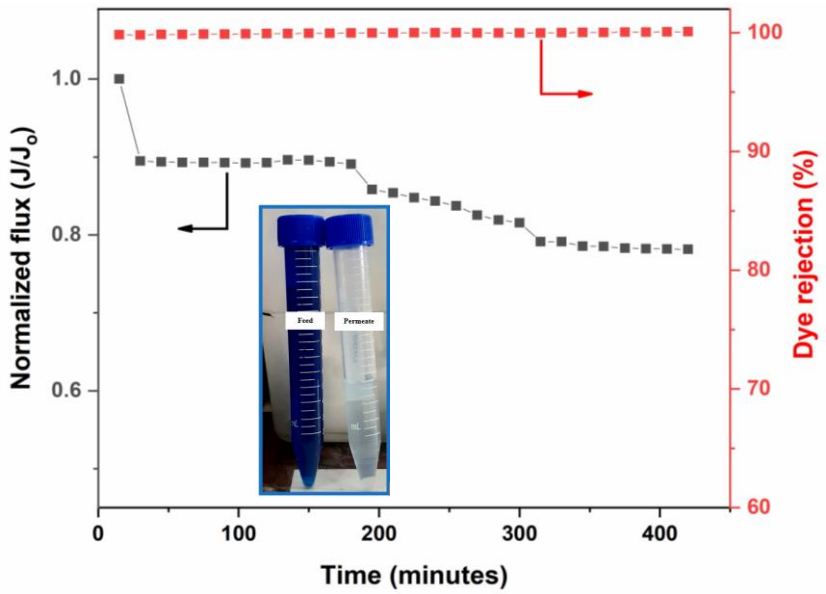

Fig. 12. Long-term performance studies for CNC-GLU TFN membrane (Insert: Digital photographs of the feed and the permeate).

An examination of macro- and microscopic images of the CNC-GLU TFN membranes (**Fig.13**) revealed the extent of fouling during membrane filtration. After >400 minutes of filtration with MB dye at a concentration of 50 mg/L, the membrane surface was fully covered by dye molecules. The impact of this fouling was evident in the decline of filtrate flux over time, which compromised the overall filtration performance. This phenomenon is likely influenced by multiple factors, including the formation of a cake layer, adsorptive fouling, and pore blockage. These mechanisms can modify the membrane's characteristics, leading to increased resistance during filtration.

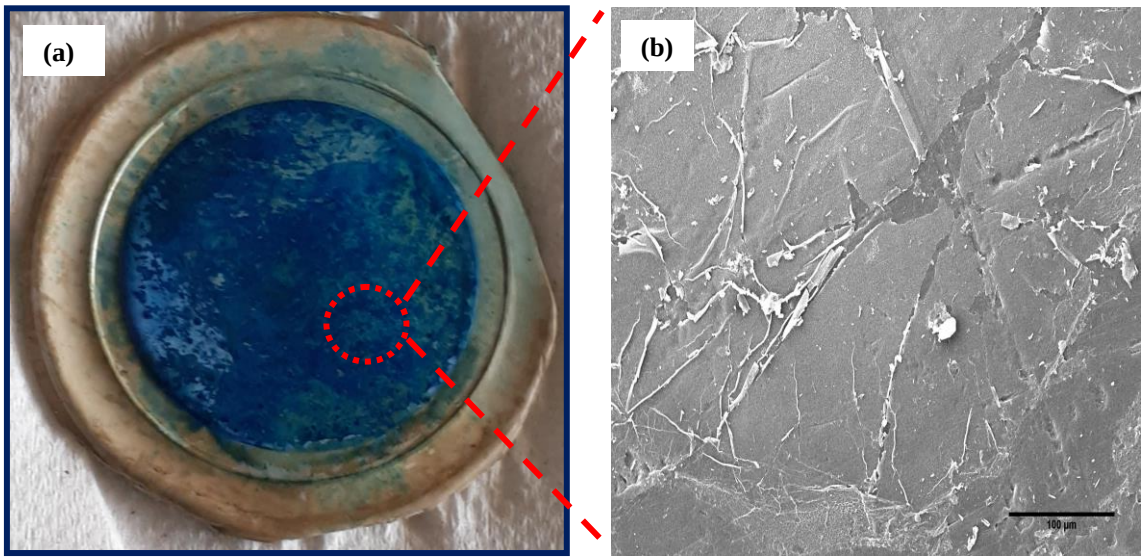

Fig. 13. Digital photograph (a) and SEM image (b) of fouled CNC-GLU TFN membrane after long-term filtration studies with MB dye (50 mg/L; 420 minutes).

3.4 Dye removal from spiked river water

River water samples from South Africa's Vaal River were spiked (50 mg/L) and tested for the prospective utilization of these membranes in environmental water bodies. The water samples had the following physicochemical characteristics: conductivity 834 µS/cm, pH 7.61, resistivity 1.20 KΩ.cm and total dissolved solids (TDS) 417 ppm. The TFN membrane exhibited higher removal efficiency for both MB (99.26%) and MO (82.62%) dyes than the control TFC membrane, which removed 94.56 and 49.85% for MB and MO, respectively. The increased removal observed for the TFN is due to the synergistic elimination caused by steric hindrance effects, sieving, and Donnan exclusion [72].

3.5 Salt removal studies

In addition to dye removal studies, salt rejection was also examined. In a single component system, the rejection of NaCl and $MgSO_4$ was studied using a TFN membrane. The rejection of salts was found to be greater for $MgSO_4$ than for NaCl, as depicted in **Fig. 14**. This aligns with the typical behavior of negatively charged nanofiltration (NF) membranes, as reported in the literature [25, 75, 76]. Overall, the rejection performance is influenced by both size exclusion and the Donnan exclusion effect. The enhanced rejection of sulfate ions compared to chloride ions is primarily due to the larger hydrated radius and higher charge of SO_4^{2-} (0.38 nm) relative to Cl^- (0.33 nm) [77]. Furthermore, the divalent cation Mg^{2+} has a more significant impact on the negatively charged membrane surface compared to Na^+. As a result, $MgSO_4$ exhibits a higher rejection rate than NaCl.

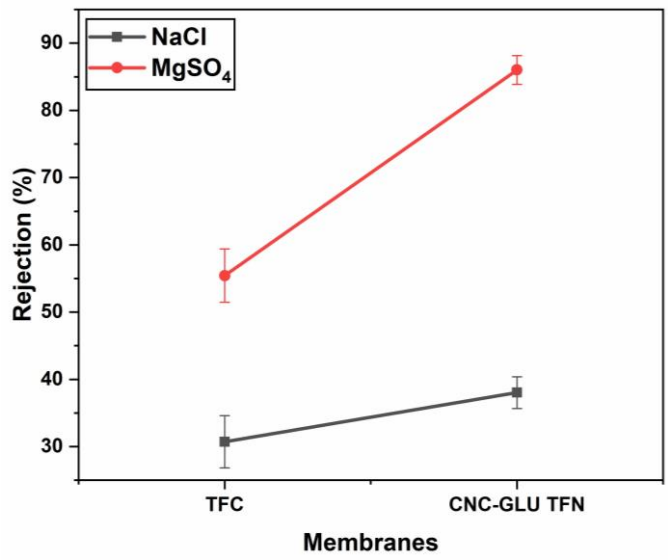

Fig. 14. Salt rejection of the synthesized TFC and TFN membranes (the test conditions: P = 400 kPa, C_f = 2000 mg/L).

3.6 Performance comparison to other reports

Table 4 presents a comparison of TFN membrane performance in terms of dye rejection and permeability, specifically contrasting them with those developed in this research. The

CNC-GLU TFN membranes exhibited a good water flow and comparable dye rejection capabilities at low operating pressures. In contrast, most NF membranes typically function at significantly higher pressures, which substantially increases operational costs. The impressive separation efficacy of CNC-GLU TFN membranes under reduced pressure conditions suggests that cellulose nanocrystals (CNCs) serve as effective filler materials for the creation of low-pressure TFN NF membranes.

Table 4: Comparison of Dye Separation Performance between CNC-GLU TFN and existing Studies.

Membrane	Types of dyes	Permeability	Dye rejection (%)	Pressure (Bar)	References
TFN (CNQDs 0.08 wt%)	Methyl Blue	13.8 $Lm^{-2}h^{-1}bar^{-1}$	96.1	5	[78]
TFN (UiO-66-NH_2 0.02 wt%)	Malachite green (MG)	13.32 ± 0.6 $Lm^{-2}h^{-1}$	91.90 ± 3	10	[79]
TFN (GO-TiO_2-Ag 0.2 wt%)	Rose bengal	52 $Lm^{-2}h^{-1}$	98	7	[75]
TFN (HNT 0.04 wt%)	Setazol red Reactive orange	~28 $Lm^{-2}h^{-1}$	99.7 99.7	9	[25]
TFN (polydopamine modified CNCs)	Congo red/NaCl	128.4 $Lm^{-2}h^{-1}bar^{-1}$	99.91	2	[76]
TFN-1 (MOFs)	Rhodamine B	20.6 $Lm^{-2}h^{-1}bar^{-1}$	99.9	4	[80]
TFN (COFs-polyester)	Congo red	105 $Lm^{-2}h^{-1}bar^{-1}$	98.5	2	[81]
TFN (CNF-CNTs/ZIF-67)	Methyl blue	207.8 $Lm^{-2}h^{-1}bar^{-1}$	95.1	1	[82]
TFN (CNC-GLU 100)	MB MO	15.4 $Lm^{-2}h^{-1}$	99.83 90.63	4	**This study**

4. Conclusion

Utilizing interfacial polymerization (IP), TFN membranes containing glutamic acid-modified cellulose nanocrystals (CNC-GLUs) were developed in this study. CNCs were synthesized from hemp fibers, and glutamic acid brushes were grown through SI-ATRP. These modified CNCs were characterized using a series of characterization tests (XRD, CP/MAS ^{13}C NMR spectroscopy, CHNS, TEM, and FTIR). Subsequently, varying ratios of CNC-GLUs, specifically 0 wt% (TFC) and 0.10 wt% (CNC-GLU TFN), were added to the aqueous phase during membrane construction. Given that the CNCs added hydrophilic groups to the polyamide film, the hydrophilicity of the PA layer significantly improved. The TFN membrane exhibited the highest PWF (15.45 ±1.03 L/m^2h) and a lower contact angle (76 ± 4°). TFN membranes also demonstrated outstanding rejection of both MB and

MO dyes from water, as well as the ability to reject these dyes from environmental water samples (99.26% and 82.62%, respectively). The TFN membranes further displayed enhanced salt rejection making it a capable choice in wastewater treatment. The improved membrane performance and durability of these CNC-GLU TFN membranes is promising for dye removal applications and other industrial separation processes since CNCs are environmentally friendly, produced from sustainable materials, and modification using SI-ATRP is a straightforward procedure.

References

1. Forgacs E, Cserháti T, Oros G. Removal of synthetic dyes from wastewaters: A review. *Environ Int*. 2004;30(7):953-971. doi:10.1016/j.envint.2004.02.001.

2. Zeng G, Ye Z, He Y, Yang X, Mang J, Shi H, Feng Z. Application of dopamine-modified halloysite nanotubes/PVDF blend membranes for direct dyes removal from wastewater. *Chem Eng J*. 2017;323:572-583. doi:10.1016/j.cej.2017.04.131.

3. Gowriboy N, Kalaivizhi R, Ganesh MR, Aswathy KA. Development of thin film polymer nanocomposite membrane (ZIF-8@PSf/CS) for removal of textile pollutant and evaluating the effect of water samples on human monocytic cell lines (THP-1) using flow cytometer. *J Clean Prod*. 2022;377:134399. doi:10.1016/j.jclepro.2022.134399.

4. Xu L, Du LS, Wang C, Xu W. Nanofiltration coupled with electrolytic oxidation in treating simulated dye wastewater. *J Memb Sci*. 2012;409-410:329-334. doi:10.1016/j.memsci.2012.04.001.

5. Meng J, Xie Y, Gu YH, Yan X, Chen Y, Guo XJ, Lang WZ. PVDF-CaAlg nanofiltration membranes with dual thin-film-composite (TFC) structure and high permeation flux for dye removal. *Sep Purif Technol*. 2021;255:117739. doi:10.1016/j.seppur.2020.117739.

6. de Luna LAV, da Silva THG, Nogueira RFP, Kummrow F, Umbuzeiro GA. Aquatic toxicity of dyes before and after photo-Fenton treatment. *J Hazard Mater*. 2014;276:332-338. doi:10.1016/j.jhazmat.2014.05.047.

7. Punzi M, Nilsson F, Anbalagan A, Anbalagan A, Svensson BM, Jönsson K,Mattiasson B, Maria Jonstrup. Combined anaerobic-ozonation process for treatment of textile wastewater: Removal of acute toxicity and mutagenicity. *J Hazard Mater*. 2015;292:52-60. doi:10.1016/j.jhazmat.2015.03.018.

8. Yu W, Liu Y, Xu Y, Li R, Chen J, Liao BQ, Shen L, Lin H. A conductive PVDF-Ni membrane with superior rejection, permeance and antifouling ability via electric assisted in-situ aeration for dye separation. *J Memb Sci*. 2019;581:401-412. doi:10.1016/j.memsci.2019.03.083.

9. Halakarni MA, Polisetti V, Samage AA, Mahto A, Svagan AJ, Hedenqvist MS, Nataraj SK. Design of selective and self-cleaning iron aminoclay thin film nanocomposite membranes. *Chem Eng J*. 2023;456:140941. doi:10.1016/j.cej.2022.140941.

10. Mohammad Nejad S, Seyedpour SF, Aghapour Aktij S, Dadashi Firouzjaei M, Elliott M, Tiraferri A, SadrzadehM, Rahimpour A. Loose nanofiltration membranes functionalized with in situ-synthesized metal organic framework for water treatment. *Mater Today Chem*. 2022;24:100909. doi:10.1016/j.mtchem.2022.100909.

11. Karami P, Aktij SA, Khorshidi B, Firouzjaei MD, Asad A, Elliott M, Rahimpour A,. Soares J.B.P, Sadrzadeh M. Nanodiamond-decorated thin film composite membranes with antifouling and antibacterial properties. *Desalination*. 2022;522:115436. doi:10.1016/j.desal.2021.115436.

12. Firouzjaei MD, Seyedpour SF, Aktij SA, Giagnorio M, Bazrafshan N, Mollahosseini A, Samadi F, Ahmadalipour S, Firouzjaei FD, Esfahani MR, Tiraferri A, Elliott M, Sangermano M, Abdelrasoul A, McCutcheon JR, Sadrzadeh M, Esfahani AR, Rahimpour A. Recent advances in functionalized polymer membranes for biofouling

control and mitigation in forward osmosis. *J Memb Sci*. 2020;596:117604. doi:10.1016/j.memsci.2019.117604.

13. Ismail AF, Goh PS, Sanip SM, Aziz M. Transport and separation properties of carbon nanotube-mixed matrix membrane. *Sep Purif Technol*. 2009;70(1):12-26. doi:10.1016/j.seppur.2009.09.002.

14. Rahimi-Kashkouli Y, Rahbari-Sisakht M, Ghadami Jadval Ghadam A. Thin film nanocomposite nanofiltration membrane incorporated with cellulose nanocrystals with superior anti-organic fouling affinity. *Environ Sci Water Res Technol*. 2020;6(3):715-723. doi:10.1039/c9ew00963a.

15. Zhao P, Li R, Wu W, Wang J, Liu J, Zhang Y. In-situ growth of polyvinylpyrrolidone modified Zr-MOFs thin-film nanocomposite (TFN) for efficient dyes removal. *Compos Part B Eng*. 2019;176:107208. doi:10.1016/j.compositesb.2019.107208.

16. Mansourpanah Y, Ghanbari A, Yazdani H, Mohammadi GA, Rahimpour A. Silver-polyamidoamine/graphene oxide thin film nanofiltration membrane with improved antifouling and antibacterial properties for water purification and desalination. *Desalination*. 2021;511:115109. doi:10.1016/j.desal.2021.115109.

17. Zhao DL, Jin H, Zhao Q, Xu Y, Shen L, Lin H, Chung T-S. Smart integration of MOFs and CQDs to fabricate defect-free and self-cleaning TFN membranes for dye removal. *J Memb Sci*. 2023;679:121706. doi:10.1016/j.memsci.2023.121706.

18. Mousavi SR, Asghari M, Mahmoodi NM. Chitosan-wrapped multiwalled carbon nanotube as filler within PEBA thin film nanocomposite (TFN) membrane to improve dye removal. *Carbohydr Polym*. 2020;237:116128. doi:10.1016/j.carbpol.2020.116128.

19. Ghaemi N, Safari P. Nano-porous SAPO-34 enhanced thin-film nanocomposite polymeric membrane: Simultaneously high water permeation and complete removal of cationic/anionic dyes from water. *J Hazard Mater*. 2018;358:376-388. doi:10.1016/j.jhazmat.2018.07.017.

20. Zhao G, Hu R, He Y, Zhu H. Physically Coating Nanofiltration Membranes with Graphene Oxide Quantum Dots for Simultaneously Improved Water Permeability and Salt/Dye Rejection. *Adv Mater Interfaces*. 2019;6(5):1801742. doi:10.1002/admi.201801742.

21. Lai GS, Lau WJ, Goh PS, Ismail AF, Tan YH , Chong CY , Krause-Rehberg R, Awad S. Tailor-made thin film nanocomposite membrane incorporated with graphene oxide using novel interfacial polymerization technique for enhanced water separation. *Chem Eng J*. 2018;344:524-534. doi:10.1016/j.cej.2018.03.116.

22. Bi R, Zhang Q, Zhang R, Su Y, Jiang Z. Thin film nanocomposite membranes incorporated with graphene quantum dots for high flux and antifouling property. *J Memb Sci*. 2018;553:17-24. doi:10.1016/j.memsci.2018.02.010.

23. Zhang T, Li P, Ding S, Wang X. High permeability composite nanofiltration membrane assisted by introducing TpPa covalent organic frameworks interlayer with nanorods for desalination and NaCl/dye separation. *Sep Purif Technol*. 2021;270:118802. doi:10.1016/j.seppur.2021.118802.

24. Yang L, Zhang X, Ma W, Raisi B, Liu X, An C, Ye Z. Trimethylamine N-oxide-

derived zwitterionic polyamide thin-film composite nanofiltration membranes with enhanced anti-dye deposition ability for efficient dye separation and recovery. *J Memb Sci*. 2023;665:121083. doi:10.1016/j.memsci.2022.121083.

25. Ormanci-Acar T, Celebi F, Keskin B, Mutlu-Salmanlı O, Agtas M, Turken T, Tufani A, Imer DY, Ince GO, Demir TU, Menceloglu YZ, Unal S, Koyuncu I. Fabrication and characterization of temperature and pH resistant thin film nanocomposite membranes embedded with halloysite nanotubes for dye rejection. *Desalination*. 2018;429:20-32. doi:10.1016/j.desal.2017.12.005.

26. Ma D, Peh SB, Han G, Chen SB. Thin-Film Nanocomposite (TFN) Membranes Incorporated with Super-Hydrophilic Metal-Organic Framework (MOF) UiO-66: Toward Enhancement of Water Flux and Salt Rejection. *ACS Appl Mater Interfaces*. 2017;9(8):7523-7534. doi:10.1021/acsami.6b14223.

27. Ge L, Song H, Zhu J, Zhang Y, Zhou Z, Van der Bruggen B. Metal/covalent-organic framework based thin film nanocomposite membranes for advanced separations. *J Mater Chem A*. 2024; 12:7975-8013. doi:10.1039/d4ta00578c.

28. Peyravi M, Jahanshahi M, Rahimpour A, Javadi A, Hajavi S. Novel thin film nanocomposite membranes incorporated with functionalized TiO_2 nanoparticles for organic solvent nanofiltration. *Chem Eng J*. 2014;241:155-166. doi:10.1016/j.cej.2013.12.024.

29. Bai L, Liu Y, Ding A, Ren N, Li G, Liang H. Fabrication and characterization of thin-film composite (TFC) nanofiltration membranes incorporated with cellulose nanocrystals (CNCs) for enhanced desalination performance and dye removal. *Chem Eng J*. 2019;358:1519-1528. doi:10.1016/j.cej.2018.10.147.

30. Moon RJ, Martini A, Nairn J, Simonsen J, Youngblood J. Cellulose Nanomaterials Review: Structure, Properties and Nanocomposites. *Chem. Soc. Rev*. 2011;40:3941-3994. doi:10.1039/c0cs00108b.

31. Bai L, Liu Y, Bossa N, Ding A, Ren N, Li G, Liang H, Wiesner MR. Incorporation of Cellulose Nanocrystals (CNCs) into the Polyamide Layer of Thin-Film Composite (TFC) Nanofiltration Membranes for Enhanced Separation Performance and Antifouling Properties. *Environ Sci Technol*. 2018;52(19):11178-11187. doi:10.1021/acs.est.8b04102.

32. Asempour F, Emadzadeh D, Matsuura T, Kruczek B. Synthesis and characterization of novel Cellulose Nanocrystals-based Thin Film Nanocomposite membranes for reverse osmosis applications. *Desalination*. 2018;439:179-187. doi:10.1016/j.desal.2018.04.009.

33. Liu Y, Bai L, Zhu X, Xu D, Li G, Liang H, Wiesner MR. The role of carboxylated cellulose nanocrystals placement in the performance of thin-film composite (TFC) membrane. *J Memb Sci*. 2021;617:118581. doi:10.1016/j.memsci.2020.118581.

34. Xu C, Chen W, Gao H, Xie X, Chen Y. Cellulose nanocrystal/silver (CNC/Ag) thin-film nanocomposite nanofiltration membranes with multifunctional properties. *Environ Sci Nano*. 2020;7(3):803-816. doi:10.1039/c9en01367a.

35. Peltzer M, Pei A, Zhou Q, Berglund L, Jiménez A. Surface modification of cellulose nanocrystals by grafting with poly(lactic acid). *Polym Int*. 2014;63(6):1056-1062. doi:10.1002/pi.4610.

36. Abedi F, Dubé MA, Emadzadeh D, Kruczek B.Improving nanofiltration performance using modified cellulose nanocrystal-based TFN membranes. *J Memb Sci.* 2023; 670: 121369. doi.org/10.1016/j.memsci.2023.121369.

37. Azzaroni O. Polymer brushes here, there, and everywhere: Recent advances in their practical applications and emerging opportunities in multiple research fields. *J Polym Sci Part A Polym Chem*. 2012;50(16):3225-3258. doi:10.1002/pola.26119.

38. Zhao B, Zhu L. Mixed Polymer Brush-Grafted Particles : A New Class of Environmentally Responsive Nanostructured Materials. *Macromol*. 2009; 42, 24: 9369–9383. doi:10.1021/ma902042x.

39. Iv JJK, Imbrogno J, Belfort G. Polymer Brushes for Membrane Separations: A Review. *ACS Appl Mater Interfaces*. *ACS Appl. Mater. Interfaces* 2016; 8, 42: 28383–28399. doi:10.1021/acsami.6b09068.

40. Mhlongo JT, Dlamini ML, Nuapia Y, Etale A. Synthesis and application of cationized cellulose for adsorption of anionic dyes. *Mater Today Proc*. 2022;62:S133-S140. doi:10.1016/j.matpr.2022.02.100.

41. Fahma F, Iwamoto S, Hori N, Iwata T, Takemura A. Isolation, preparation, and characterization of nanofibers from oil palm empty-fruit-bunch (OPEFB). *Cellulose*. 2010;17(5):977-985. doi:10.1007/s10570-010-9436-4.

42. Zhang Z, Wang X, Tam KC, Sèbe G. A comparative study on grafting polymers from cellulose nanocrystals via surface-initiated atom transfer radical polymerization (ATRP) and activator re-generated by electron transfer ATRP. *Carbohydr Polym*. 2019;205:322-329. doi:10.1016/j.carbpol.2018.10.050.

43. Zhang X, Zhang J, Dong L, Ren S, Wu Q, Lei T. Thermoresponsive poly(poly(ethylene glycol) methylacrylate)s grafted cellulose nanocrystals through SI-ATRP polymerization. *Cellulose*. 2017;24(10):4189-4203. doi:10.1007/s10570-017-1414-7.

44. Masibi EG, Makhetha TA, Moutloali RM. Effect of the Incorporation of ZIF-8@GO into the Thin-Film Membrane on Salt Rejection and BSA Fouling. *Membranes (Basel)*. 2022;12(4): 436. doi:10.3390/membranes12040436.

45. Hoffman R. Solid-state chemical-shift referencing with adamantane. *J Magn Reson*. 2022;340:107231. doi:10.1016/j.jmr.2022.107231

46. Etale A, Nhlane D, Mhlongo J, Khan A, Rumbold K, Nuapia YB. Synthesis and Application of Cationised Cellulose for Removal of Cr (VI) from Acid Mine-Drainage Contaminated Water. *AAS Open Res*. 2021;4:4. doi:10.20944/preprints202009.0708.v1.

47. Abousalman-rezvani Z, Eskandari P, Roghani-mamaqani H, Mardani H, Salami-Kalajahi M. Grafting light- , temperature , and CO_2 -responsive copolymers from cellulose nanocrystals by atom transfer radical polymerization for adsorption of nitrate ions. *Polymer*. 2019;182:121830. doi:10.1016/j.polymer.2019.121830.

48. Wu W, Huang F, Pan S, Mu W, Meng X , Yang H, Xu Z, Ragauskas AJ and Deng Y. Thermo-Responsive and Fluorescent Cellulose Nanocrystals Grafted with Polymer Brushes. *J Mater Chem A*. 2015;3:1995 – 2005. doi:10.1039/b000000x.

49. Kiriakou M V., Berry RM, Hoare T, Cranston ED. Effect of Reaction Media on

Grafting Hydrophobic Polymers from Cellulose Nanocrystals via Surface-Initiated Atom-Transfer Radical Polymerization. *Biomacromolecules*. 2021;22(8):3601-3612. doi:10.1021/acs.biomac.1c00692.

50. Hemraz UD, Lu A, Sunasee R, Boluk Y. Structure of poly(N-isopropylacrylamide) brushes and steric stability of their grafted cellulose nanocrystal dispersions. *J Colloid Interface Sci*. 2014;430:157-165. doi:10.1016/j.jcis.2014.05.011.

51. Yi J, Xu Q, Zhang X, Zhang H. Temperature-induced chiral nematic phase changes of suspensions of poly(N,N-dimethylaminoethyl methacrylate)-grafted cellulose nanocrystals. *Cellulose*. 2009;16(6):989-997. doi:10.1007/s10570-009-9350-9.

52. Zeinali E, Haddadi-Asl V, Roghani-Mamaqani H. Nanocrystalline cellulose grafted random copolymers of N- isopropylacrylamide and acrylic acid synthesized by RAFT polymerization: Effect of different acrylic acid contents on LCST behavior. *RSC Adv*. 2014;4(59):31428-31442. doi:10.1039/c4ra05442c.

53. Huang S, Zhou L, Li MC, Wu Q, Zhou D. Cellulose nanocrystals (CNCs) from corn stalk: Activation energy analysis. *Materials (Basel)*. 2017;10(1). doi:10.3390/ma10010080.

54. Hemmati F, Jafari SM, Kashaninejad M, Barani Motlagh M. Synthesis and characterization of cellulose nanocrystals derived from walnut shell agricultural residues. *Int J Biol Macromol*. 2018;120:1216-1224. doi:10.1016/j.ijbiomac.2018.09.012

55. Planes M, Brand J, Lewandowski S, Remaury S, Solé S, Le Coz C, Carlotti S, Sèbe G. Improvement of the Thermal and Optical Performances of Protective Polydimethylsiloxane Space Coatings with Cellulose Nanocrystal Additives. *ACS Appl Mater Interfaces*. 2016;8(41):28030-28039. doi:10.1021/acsami.6b09043

56. Sui X, Yuan J, Zhou M, Zhang J, Yang H, Yuan W, Wei Y, Pan C. Synthesis of cellulose-graft-poly(N,N-dimethylamino-2-ethyl methacrylate) copolymers via homogeneous ATRP and their aggregates in aqueous media. *Biomacromolecules*. 2008;9(10):2615-2620. doi:10.1021/bm800538d

57. Zhang Z, Sèbe G, Wang X, Tam KC. UV-Absorbing Cellulose Nanocrystals as Functional Reinforcing Fillers in Poly(vinyl chloride) Films. *ACS Appl Nano Mater*. 2018;1(2):632-641. doi:10.1021/acsanm.7b00126

58. Ngaha MCD, Djemmoe LG, Njanja E, Kenfack IT. Biosorption Isotherms and Kinetics Studies for the Removal of 2,6-Dichlorophenolindophenol Using Palm Tree Trunk ((Elaeis guineensis) *J Encapsulation Adsorpt Sci*. 2018;8(3):156-177. doi:10.4236/jeas.2018.83008

59. Borba LL, Cuba RMF, Cuba Terán FJ, Castro MN, Mendes TA. Use of adsorbent biochar from pequi (Caryocar Brasiliense) husks for the removal of commercial formulation of glyphosate from aqueous media. *Brazilian Arch Biol Technol*. 2019;62. doi:10.1590/1678-4324-2019180450

60. Wang Y, Wilson D, Harbison GS. Solid-State NMR and the Crystallization of Aspartic and Glutamic Acids. *Cryst Growth Des*. 2016;16(2):625-631. doi:10.1021/acs.cgd.5b01052

61. Xie Q, Zhang S, Xiao Z, Hu X, Hong Z, Yi R, Shao W, Wang Q. Preparation and

characterization of novel alkali-resistant nanofiltration membranes with enhanced permeation and antifouling properties: the effects of functionalized graphene nanosheets. *RSC Adv*. 2017;7(30):18755-18764. doi:10.1039/c7ra00928c

62. Sharma U, Pandey R, Basu S, Saravanan P. Facile monomer interlayered MOF based thin film nanocomposite for efficient arsenic separation. *Chemosphere*. 2022;309(P1):136634. doi:10.1016/j.chemosphere.2022.136634

63. Bagherzadeh M, Nikkhoo M, Ahadian MM, Amini M. Novel Thin-Film Nanocomposite Forward Osmosis Membranes Modified with WS_2/CuAl LDH Nanocomposite to Enhance Desalination and Anti-fouling Performance. *J Inorg Organomet Polym Mater*. 2023;33(4):956-968. doi:10.1007/s10904-023-02547-6

64. Natesan G, Rajappan K. GO–CuO nanocomposites assimilated into CA–PES polymer membrane in adsorptive removal of organic dyes from wastewater. *Environ Sci Pollut Res*. 2023;30(15):42658-42678. doi:10.1007/s11356-022-21821-7

65. Wasim M, Sabir A, Shafiq M, Islam A, Azam M, Jamil T. Mixed matrix membranes: Two step process modified with electrospun (carboxy methylcellulose sodium salt/sepiolite) fibers for nanofiltration. *J Ind Eng Chem*. 2017; 50: 172-182. doi:10.1016/j.jiec.2017.02.011.

66. Chen D, Chen Q, Liu T, Kang J, Xu R, Cao Y, Xiang M. Influence of L-arginine on performances of polyamide thin- film composite reverse osmosis membranes. *RSC Adv*. 2019; 9: 20149-20160. doi:10.1039/c9ra02922b.

67. Wong KC, Goh PS, Ismail AF. Highly permeable and selective graphene oxide-enabled thin film nanocomposite for carbon dioxide separation. *Int J Greenh Gas Control*. 2017;64:257-266. doi:10.1016/j.ijggc.2017.08.005.

68. Zhao W, Liu H, Meng N, Jian M, Wang H, Zhang X. Graphene oxide incorporated thin film nanocomposite membrane at low concentration monomers. *J Memb Sci*. 2018;565:380-389. doi:10.1016/j.memsci.2018.08.047.

69. Liu S, Low ZX, Hegab HM, Xie Z, Ou R, Yang G, Simon GP, Zhang X, Zhang L, Wang H. Enhancement of desalination performance of thin-film nanocomposite membrane by cellulose nanofibers. *J Memb Sci*. 2019;592: 117363. doi:10.1016/j.memsci.2019.117363.

70. Hoang MT, Pham TD, Verheyen D, Nguyen MK, Pham TT, Zhu J, Van der Bruggen B. Fabrication of thin film nanocomposite nanofiltration membrane incorporated with cellulose nanocrystals for removal of Cu (II) and Pb (II). *Chem Eng Sci*. 2020;228:115998. doi:10.1016/j.ces.2020.115998.

71. Kadhom M, Albayati N, Salih S, Al-Furaiji M, Bayati M, Deng B. Role of cellulose micro and nano crystals in thin film and support layer of nanocomposite membranes for brackish water desalination. *Membranes (Basel)*. 2019;9(8). doi:10.3390/membranes9080101.

72. Goswami R, Gogoi M, Borah A, Sarmah H, Borah AR, Feng X, Hazarika S. Quantum dot- β-Cyclodextrin nanofiller decorated thin film nanocomposite membrane for removal of cationic and anionic dyes from aqueous solution. *Mater Today Chem*. 2024;35:101871. doi:10.1016/j.mtchem.2023.101871.

73. Sapkota B, Liang W, VahidMohammadi A, Karnik R, Noy A, Wanunu M. High permeability sub-nanometre sieve composite MoS_2 membranes. *Nat Commun*. 2020;11(1):2747. doi:10.1038/s41467-020-16577-y.

74. Akbari A, Sheath P, Martin ST, Shinde DB, Shaibani M, Banerjee PC, Tkacz R, Bhattacharyya D, Majumder M. Large-area graphene-based nanofiltration membranes by shear alignment of discotic nematic liquid crystals of graphene oxide. *Nat Commun*. 2016;7: 10891. doi:10.1038/ncomms10891.

75. Abadikhah H, Kalali EN, Khodi S, Xu X, Agathopoulos S. Multifunctional Thin-Film Nanofiltration Membrane Incorporated with Reduced Graphene Oxide@TiO_2@Ag Nanocomposites for High Desalination Performance, Dye Retention, and Antibacterial Properties. *ACS Appl Mater Interfaces*. 2019;11(26):23535-23545. doi:10.1021/acsami.9b03557.

76. Yang L, Liu X, Zhang X, Chen T, Ye Z, Rahaman MS. High performance nanocomposite nanofiltration membranes with polydopamine-modified cellulose nanocrystals for efficient dye/salt separation. *Desalination*. 2022;521:115385. doi:10.1016/j.desal.2021.115385.

77. Nightingale E.R. Phenomenological theory of ion solvation. Effective radii of hydrated ions, *J. Phys. Chem*. 1959; 63: 1381–1387.

78. Liu B, Zhang S, Yao Z, Dong L, Bai Y, Zhang C. Carbon Nitride Quantum Dot-Based Thin-Film Nanocomposite Membranes for Efficient Dye Removal. *ACS Appl Nano Mater*. 2023;6(18):16297-16308. doi:10.1021/acsanm.3c02401.

79. Borpatra Gohain M, Karki S, Yadav D, Yadav A, Thakare NR, Hazarika S, Lee HK, Ingole PG. Development of Antifouling Thin-Film Composite/Nanocomposite Membranes for Removal of Phosphate and Malachite Green Dye. *Membranes (Basel)*. 2022;12(8): 768. doi:10.3390/membranes12080768.

80. Jia M-M, Feng J-H , Shao W , Chen Z , Yu J-R, Sun J-J, Wu Q-Y, Li Y, Xue M, Chen X-M. In-situ interfacial synthesis of metal-organic framework/polyamide thin-film nanocomposite membranes with elevated nanofiltration performances. *J Memb Sci*. 2024; 694: 122418. doi.org/10.1016/j.memsci.2024.122418.

81. Zhou C, Li H, Wang L, Fu T, Liu G, Shen X, Zhao H. High-flux and stability nanofiltration membranes prepared with β-cyclodextrin and in-situ co-polymerized of TpPa COFs for dye desalination. *J. Environ. Chem. Eng*. 2025; 13: 116096. doi.org/10.1016/j.jece.2025.116096.

82. Qin Z, Xiang S, Jing Z, Deng M, Jiang W, Yao L, Yang L, Deng L, Dai Z. Thin film nanocomposite membranes fabricated via 2D ZIF-67 nanosheets and 1D nanofibers with ultrahigh water flux for dye removal from wastewater. *Sep Purif Technol*. 2025; 330: 125308. doi.org/10.1016/j.seppur.2023.125308.

Low Pressure Thin Film Membranes with Cellulose Nanocrystals derived from Cannabis sativa for Enhanced Dye and Salt Removal

Khona Maziya[a], Izak Kotze[a], Oranso T. Mahlangu[b], Heidi Lynn Richards[a]

[a] Molecular Sciences Institute, School of Chemistry, University of the Witwatersrand, Private Bag X3, Johannesburg, 2050, South Africa

[b] University of South Africa, Nanotechnology and Water Sustainability Research Unit, College of Engineering, Science and Technology, Florida Science Campus, Roodepoort, South Africa

Supplementary Information

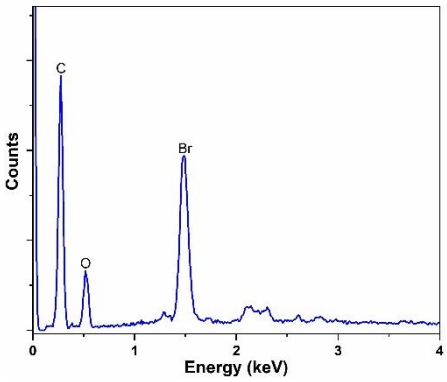

Figure S1: EDS of CNC-Br.

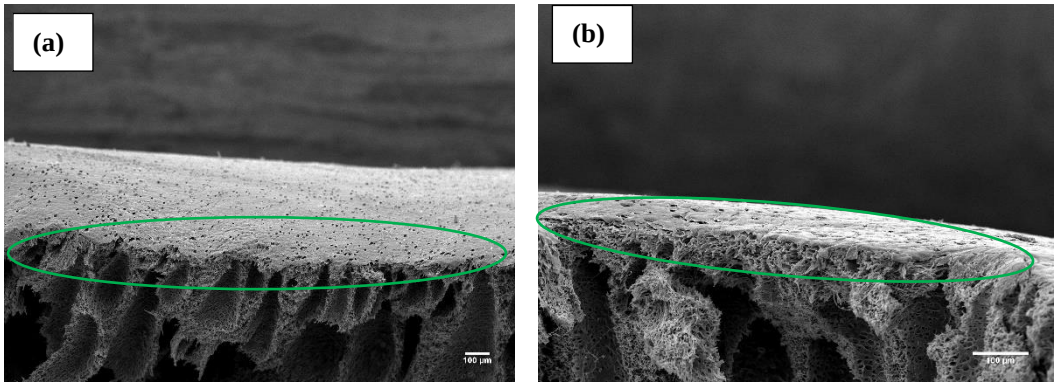

Figure S2: Cross sectional morphologies of TFC (a) and CNC-GLU TFN (b).

4.4 Paper 4

This paper entitled "**Polyvinyl Alcohol Cross-linked Graphene Oxide with Grafted Glutamic Acid Aerogels for Enhanced Methylene Blue Adsorption**" has been submitted to Journal of Polymer Research.

This article evaluated the potential of glutamic acid functionalized graphene oxide modified aerogels in the removal of dyes in water.

Khona Maziya – Principal author

Contribution: principal author, conceptualization, performed experiments, data collection/analysis, methodology, formal analysis, research, visualization and writing - original draft.

Polyvinyl Alcohol Cross-linked Graphene Oxide with Grafted Glutamic Acid Aerogels for Enhanced Methylene Blue Adsorption

Khona P Maziya, Mbongiseni L Dlamini, Heidi L Richards*
Molecular Sciences Institute, School of Chemistry, University of the Witwatersrand, Private Bag X3, Johannesburg, 2050, South Africa

Graphical Abstract

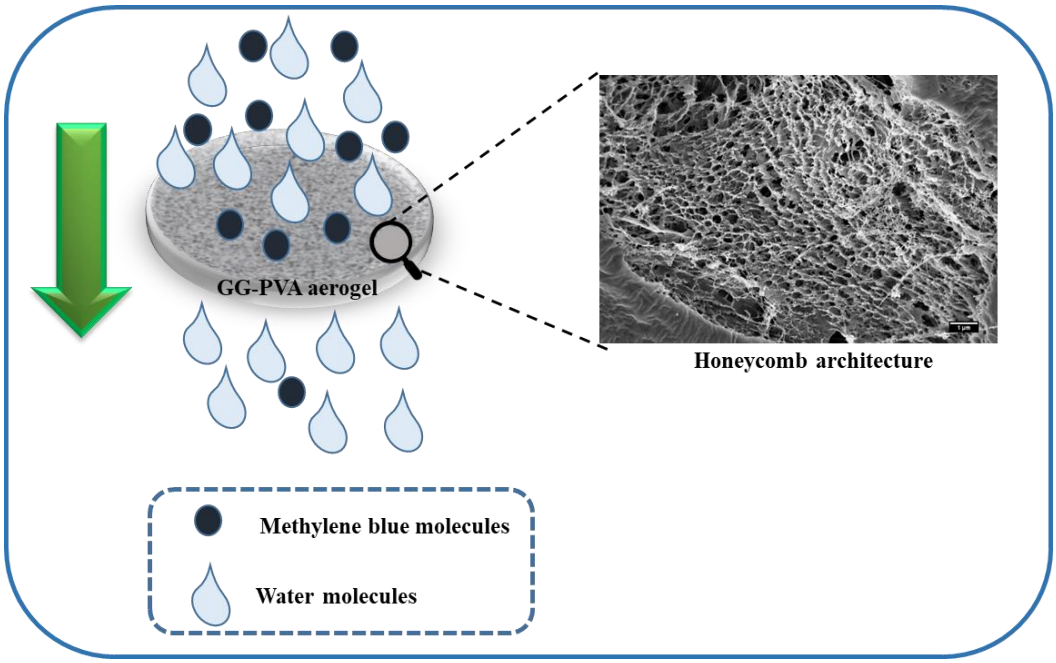

*Corresponding author: Email address: heidi.richards@wits.ac.za

Abstract

In this present work, glutamic acid modified graphene oxide (GG-PVA) aerogels were fabricated through a simplistic sol gel and freeze-drying process utilizing polyvinyl alcohol (PVA) as a cross-linker. The aerogels were extensively explored in the abatement of methylene blue (MB) dye from aqueous solutions. Successful synthesis of the aerogels was confirmed by field emission scanning electron microscopy (FESEM), Fourier transform infrared (FTIR), Brunauer-Emmett-Teller (BET), and Thermogravimetric analysis (TGA), yielding relatively homogeneous honeycomb and porous surfaces, with 3.4326 m^2 g^{-1} surface area and high thermal stability. The MB removal followed monolayer adsorption on the homogeneous surfaces of the GG-PVA, thus defined by the Langmuir Isotherm model, possessing a maximum adsorption capacity (q_{max}) of 121.95 mg g^{-1}. Maximum adsorption of the MB was favored by near neutral to alkaline conditions, reaching 88.4% efficiency and equilibrium reached in the first 30 minutes of the adsorption process. The kinetics of the MB removal followed the pseudo-second order model. Furthermore, thermodynamic studies displayed endothermic (ΔH^o = 80.598 kJ mol^{-1}) and spontaneous (ΔG^o = -8.219 kJ mol^{-1}) nature of the adsorption process. The overall adsorption process was principally influenced by the charge and size of the MB molecule, as well as the surface-active sites, porosity, and charge of aerogels among other factors. This study underscores the facile synthesis and effective application of GG-PVA aerogels in MB dye removal, highlighting their potential as effective materials for textile wastewater remediation.

***Keywords*:** Aerogels; Graphene Oxide; Methylene Blue; Glutamic Acid; Polyvinyl alcohol

1. Introduction

The rise in industrial activities and swift urban development has led to a significant increase in water pollution.[1] Untreated effluents are being emitted in greater quantities as a result of the extensive use of synthetic colors in the textile, paper, tannery, food, paint, and cosmetic industries.[2,3] The development of treatment techniques for wastewater including colored effluents is imperative owing to the wastewater's toxicity and its potential to induce mutagenic, teratogenic, and carcinogenic effects on humans and aquatic organisms.[4–6] Colored effluents are usually a clear sign of textile dyes in the water system. One of the extensively employed synthetic cationic dyes in the textile and printing sectors is methylene blue (MB),[7] due to its high affinity for natural fibers and intense blue color. MB dye containing effluents may end in the water column, posing a severe threat to aquatic life, water quality and humankind. Typically, several adverse effects may arise from exposure to such polluted wastewater, including skin irritation, burns to the eyes, and potential digestive tract irritation.[8] MB-containing wastewaters cause major environmental difficulties, as well as being mutagenic and carcinogenic.[58] Eliminating dye pollutants from water sources and the environment is therefore crucial for improving environmental safety and safeguarding and the health of living organisms.

Nowadays, dye effluents are treated utilizing a range of biological, chemical, and physical techniques, such as membrane separation techniques, biodegradation, ion exchange, precipitation, adsorption, chemical oxidation and so on.[9–11] Adsorption is a particularly appealing and advantageous technique among these measures because of its broad range of applications, ease of use, and economic feasibility.[12–14] Efficient MB contaminated wastewater treatment commonly involves the use of adsorbents with a large surface area and porous structure.[15] Numerous novel adsorbents have recently been developed, with excellent results in the treatment of colored wastewater.[16] Nonetheless, producing simple and efficient adsorbents remains a difficult task due to constraints such as tedious synthetic approaches, low adsorption capacity, and recyclability.[17] Accordingly, the fabrication of novel adsorbents with exceptional adsorption capacity is crucial in tackling the challenge of dye-induced environmental pollution.

Graphene oxide (GO) and GO based materials have been explored in the elimination of dyes from water.[18–21] GO, a two-dimensional sp^2 hybridized monolayer carbon atoms arranged in a honeycomb pattern, has recently gained prominence due to its numerous benefits. The large specific surface area (~2600 m^2g^{-1}), hydrophilic nature, and presence of epoxy, ketones, hydroxyl, and carboxyl groups allow for further functionalization of GO, improving pollutant removal.[22–25] Several functionalization approaches have been investigated to improve the application efficacy of the GO. One promising modification approach is the surface-initiated atom transfer radical polymerization (SI-ATRP). This technique utilizes the oxygen-rich groups located on the surface of GO. This principally results in materials that are multifunctional with end group functionalities.[26] This approach offers customization of polymer brush's thickness and design, while also resulting in high grafting density. This process necessitates the anchoring of an initiator on the substrate's

surface, subsequently followed by a growth phase in which monomers are added to the extending chain repeatedly (polymerization).[27,28]

Furthermore, GO is prone to agglomeration, resulting in diminished adsorption efficacies, and has a high colloidal stability, which limits its practicability and reuse.[20,29] The utilization of three-dimensional (3D) graphene-based materials, specifically aerogels, may alleviate the constraints associated with pristine GO usage to treat wastewater. Aerogels are 3D materials that possess an impressive nano pore architecture and distinctive attributes including high surface area, porosity, and low density.[30] These benefits qualify their common utilization in water treatment. For instance, Zamani *et al*. (2014) explored the efficacy of GO aerogel (GOA) produced by unidirectional freezing in removing MB in water.[31] This aerogel possessed an impressive adsorption capacity for MB removal, reaching a maximum of 416.6667 mgg^{-1}.[31] The Langmuir isotherm model accurately characterized the MB removal process using GOA.[31] GO aerogel has been prepared for wastewater treatment using a variety of synthetic processes, including ice crystal templating, bio-assembly, self-assembly, and unidirectional freezing.[32,33] Nonetheless, these GO aerogels in water typically disintegrate, resulting in secondary contamination and preventing effective aerogel reuse.[34,35] To counter this limitation, incorporating various forms of reinforcing agents such as polyvinyl alcohol (PVA) during the preparation process has been examined as a potential way to boost the mechanical stability and strength of the GO aerogel.[36] PVA is a non-toxic, relatively affordable, and water-soluble polymer which can enhance the stability of graphene's self-assembly structure thereby boosting its mechanical strength.[37–39]

In this present study, we explore the fabrication of glutamic acid-modified graphene oxide (GO-GLU) aerogel in the presence of PVA using a simple sol-gel approach combined with freeze-drying. PVA was used to reinforce the GO-GLU nanosheets, minimize aggregation, and improve the mechanical strength of the porous aerogels. The resulting aerogels (GG-PVA) exhibited outstanding adsorption capacity toward MB. The influence of varied adsorption conditions on the MB removal by the GG-PVA was thoroughly investigated. The equilibrium data was characterized using sorption isotherms and kinetics models.

2. Materials and methods

2.1 Materials

Graphite powder, 25% glutaraldehyde, phosphoric acid (H_3PO_4), methylene blue (MB), potassium permanganate ($KMnO_4$), dimethylformamide (DMF), α-bromoisobutyryl bromide (BiBB) (98%), hydrogen peroxide (H_2O_2), Poly (vinyl alcohol) (PVA, Mw = 30 – 70K, 99% hydrolyzed), triethylamine (TEA, glutamic acid, copper (I) bromide (CuBr), sulphuric acid (H_2SO_4), N,N,N ,N ,N‴- pentamethyldiethylenetriamine (PMDETA, 99%), 99%), were attained from Sigma-Aldrich. A Milli-Q system (Millipore) (resistance = 18 mΩ.cm) produced de-ionized (DI) water utilized.

2.2 Preparation of GG-PVA aerogels

GO, GO-Br and GO-GLU nanosheets were synthesized following procedures presented in the supplementary information (S.I.) (S1). For the preparation of aerogels, 20 mL GO-GLU (10 mg mL^{-1}) solution was sonicated for an hour. In parallel, a 10 wt% aqueous solution of PVA was created by mixing PVA powder with deionized water at 90 °C for three hours, ensuring that the PVA was fully dissolved through continuous stirring. The PVA solution was added dropwise into the aqueous dispersion of GO-GLU, together with 25 µL of 25% glutaraldehyde. The resulting mixture was allowed to stir overnight to facilitate the gelatinization. Samples were transferred to a refrigerator (-20 °C) for pre-freezing. Finally, these samples were kept freeze-drying for 48 hours. This resulted to the development of the porous structure water sublimated. Ultimately, PVA-supported GO-GLU (GG-PVA) aerogels were obtained. Moreover, for comparison, PVA and G-PVA (Graphene oxide-PVA) aerogels were also prepared through the same process.

2.3 Instrumentation

An FEI Tecnai G2 Spirit transmission electron microscope (Hillsboro, USA) with a 120 kV acceleration voltage was utilized to study the morphological characteristics of GO nanosheets. A Bruker D2 phaser diffractometer (Cu-Kα) (Johannesburg, South Africa) was utilized for X-ray diffraction investigations, with a scanning range of 5 - 90 (2θ). A Tensor 27 Infrared Spectrometer (Massachusetts, USA) was employed to acquire Fourier transform infrared (FTIR) spectra in a range of 4000 – 500 cm^{-1} for the GO nanosheets and aerogels. The magic-angle solid state ^{13}C nuclear magnetic resonance (^{13}C MAS NMR) spectra of GO and GO-GLU were recorded on an AVANCE-III-500 (Bruker, Germany) machine. Direct polarization high power broad band ^{1}H decoupling and cross-polarization MAS was acquired using 4 mm zirconium rotors with 8 or 10 kHz MAS spin-rate. ^{13}C NMR chemical shifts were externally referenced with adamantane as described by Hoffman (2022).[40] VarioELcube version 4.0.13 (Elementar, Germany) was used for the elemental study of carbon, hydrogen, nitrogen, and sulfur (CHNS). The thermal properties of GO and its derivatives was studied using thermogravimetric analysis (TGA), run in an inert (nitrogen) environment on a thermogravimetric analyzer through a temperature ranging from 35 – 900 °C (heating rate = 20 °C/min) (Perkin Elmer). Morphologies of aerogels were analyzed using field emission scanning electron microscopy (FESEM-EDS) (Carl Zeiss Sigma) at an accelerating voltage of 20 kV. N_2 adsorption–desorption isotherm was recorded using Brunauer-Emmett-Teller (BET) Micrometrics Tristar II Plus 3.03 to estimate the pore volume and surface area.

2.4 Adsorption Experiments

Batch experiments were performed to investigate the influence of adsorption parameters which include adsorbent dosage (10 – 50 mg), pH (2 – 11), contact time (0 – 300 minutes), initial dye concentration (10 – 50 mg L^{-1}), and temperature (25 – 45 °C (298.15 – 318.15 K)), on the adsorption of MB (**Scheme 1**). For these tests, 10 mg of aerogel adsorbent was placed to 50 mL centrifuge tubes having 30 mL (20 mg L^{-1}) of dye solution. Utilizing a pH meter, the pH of the dye solution was modified through the addition of 0.1 M HCl or

NaOH. At room temperature, the solutions were placed on a horizontal automated shaker set to 120 rpm. A UV-Vis spectrophotometer was employed to analyze for the equilibrium concentration of the dye solution at 664 nm wavelength. The equations that follow were used to compute the quantity of dye adsorbed by GG-PVA aerogel per gram of the adsorbent as well as the percentage of dye removal efficiency**.** Accordingly, **equations (1)** and **(2)** were employed to compute the equilibrium adsorption capacity (q_e, (mg g^{-1})) and the percentage removal (% R):

$q_e = (C_o - C_e)/M \times V$ (1)

$\% R = (C_o - C_e)/C_o \times 100$ (2)

Where q_e is the quantity of dye adsorbed by the aerogel (mg g^{-1}) at equilibrium, C_0 (mg L^{-1}) and C_e (mg L^{-1}) are the initial and equilibrium concentrations of the dye in solution, respectively, V (L) is the solution volume and M (g) is the adsorbent mass.

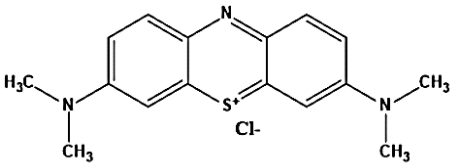

Molecular weight (MW) = 319.85 g mol^{-1}

Scheme 1: Molecular structure and weight of Methylene blue (MB).

3. Results and discussion

3.1 Characterization of GO and derivatives

3.1.1 TEM analysis

The morphological investigation of GO and its derivatives was analyzed using TEM. **Figure 1(a)** displayed thin and smooth structures of GO, there were no observable morphological differences upon attachment of ATRP initiator α-bromoisobutyryl bromide (**Figure S1 (a)**). EDS analysis further confirmed the incorporation of ATRP initiator by the presence of C, O, and Br at 0.26, 0.51, and 1.48 keV (**Figure S1 (b)**), respectively, certifying the attachment of the Br-containing initiator to the GO. Spots on the surface of GO emerged after grafting poly(glutamic acid) brushes, which are attributed to collapsed chains on the GO sheets' surface **(Figure 1(b))**. [41,42]

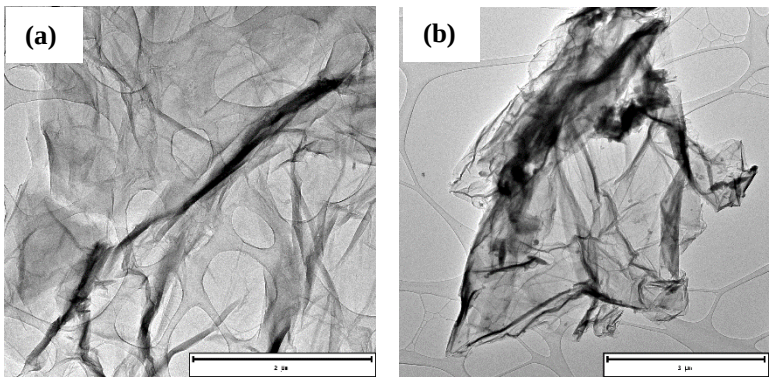

Figure 1: TEM images of pristine GO (a) and GO-GLU 100 (b).

3.1.2 FTIR, XRD, ^{13}C NMR, CHNS, TGA, PZC analysis

Figure 2 (a) depicts the TGA of GO and its functionalized hybrids. The glutamic acid modified GO displayed a distinct thermal breakdown behavior than GO, indicating that GO has been effectively modified. GO lost weight in three stages: loss of bound water at 30 - 150 ℃, decomposition of labile epoxy, carboxylic, and hydroxyl groups at 180 - 285 ℃, and breakdown of backbone (C-C bond) at ~285 ℃. [43,44] The final mass was around 30% of the original weight. The thermal deterioration of GO-Br followed a similar trend, but its final mass was significantly higher (~40%). This was attributable to a reduction in oxygenation groups, which resulted in less mass loss. After grafting glutamic acid brushes, GO-GLU showed improved thermal stability with a final mass of ~60%. This was due to the zwitterions' shielding action on the oxygenated functional groups of GO sheets.[45] This also suggests that GO oxygenated functional groups participated in the organo-modification process with glutamic acid.

XRD analysis verified the synthesis of GO. GO diffraction patterns show peaks at 9.2 and 43 at 2θ values, representing the (0 0 2) and (1 0 0) reflections, respectively as shown in **Figure 2 (b)**. GO's interlayer spacing was 0.96 nm.[23] The diffraction angle of GO-Br is 7.9^{o}, indicating a significant increase in interlayer distance (1.12 nm). This is related to the reduction in intercalated water molecules between the layers due to the decrease in oxygenated functional groups.[45] The glutamic acid's XRD pattern showed a significant degree of crystallization. GLU polymerized GO showed a weak peak at 10.5^{o} (2θ), indicating a 0.84 nm interlayer distance due to GLU polymer brushes. The GO-GLU XRD pattern demonstrated that the reaction between the GO and GLU polymer brushes resulted in crystal complexes produced through chemical covalent bonding.

A substance's point of zero charge (PZC) in solution is the pH where the surface overall charge is zero.[46] The PZC of GO-GLU was obtained to be 5.45, implying that the material's surface charge is positive at pHs less than 5.45, negative at pHs more than 5.45, and neutral at pH 5.45 (**Figure 2 (c)**).[47] The integration of GO-GLU into the aerogels would just be an anchor, providing mechanical support to it, with limited structural changes of the composite, therefore, a significant change in the surface charges is not anticipated. The C, H, and N elemental analysis showed the composition of the GO and hybrids, as indicated in **Table 1**. The nitrogen content rose when the polymer was grafted (0 to 3.9%). These findings are consistent with the TEM investigation, which showed the evolution of dark patches on the GO following polymer grafting.

FTIR analysis was performed to assess the structural modifications in GO after modification (**Figure 2 (d)**). A broad peak at 3321 cm^{-1} was detected in the GO spectra, owing to O-H stretching vibrations. Peaks at 1731, 1611, 1420, 1226, 1027, and 863 cm^{-1} correspond to stretching vibrations of the carboxylic group's -C=O bond, unoxidized sp^2 C=C bond in the graphitic lattice structure, stretching vibrations of C-OH and the C-O group, and epoxy groups, respectively.[48] The synthesized GO was modified with α-bromoisobutyryl bromide, an ATRP initiator. The O-H groups on the GO surface were esterified with the initiator, as seen by the reduction in the O-H peak (**Figure 2(d**). The

emergence of a peak at approximately 1180 cm^{-1} could be credited to the ester's C-O stretching. **Figure 2 (d)** displays GO-GLU spectra with peaks at 1714, 1570, 1396, and 1140 cm^{-1}, which accredited to the stretching vibration of the -C=O bond resulting from the presence of the carboxylic group in glutamic acid, the N-H bend, and the -C-N- stretching in the secondary amide groups, confirming the amidation reaction. On the GO-GLU sample, the peaks at 1610 and 1511 cm^{-1}, which were attributable to the stretching vibration of primary amine groups in glutamic acid, disappeared. This FTIR investigation affirms the glutamic acid brushes' covalent attachment to the GO.

Solid state NMR characterization was utilized to provide insights into the transformation of GO to GO-GLU (**Figure 2 (e)**). GO exhibits significant epoxide and hydroxyl functionalities, as demonstrated by peaks between 50 and 80 ppm in its ^{13}C MAS NMR spectrum, as well as unoxidized sp^2 carbon (C=C,130 ppm).[49,50] These peaks appear to be substantially less pronounced after grafting with GLU, and the modified GO's sp^2 carbons shift up-field. Furthermore, the GLU spectrum reveals two peaks for the carbon at position 4. This is due to the presence of both α and β polymorphs in typical GLU samples. The carbons in the α and β phases should be distinct, however this is not the case. The ^{13}C CP MAS NMR spectrum reveals the presence of both α and β polymorphs, with all signals resolved, as corroborated by Harbison *et al*'s (2015) chemical shifts (**Figure S2**).[51] These findings confirm that the GLU is successfully grafted onto the GO. These findings are congruent with the results of FTIR, XRD, and TGA.

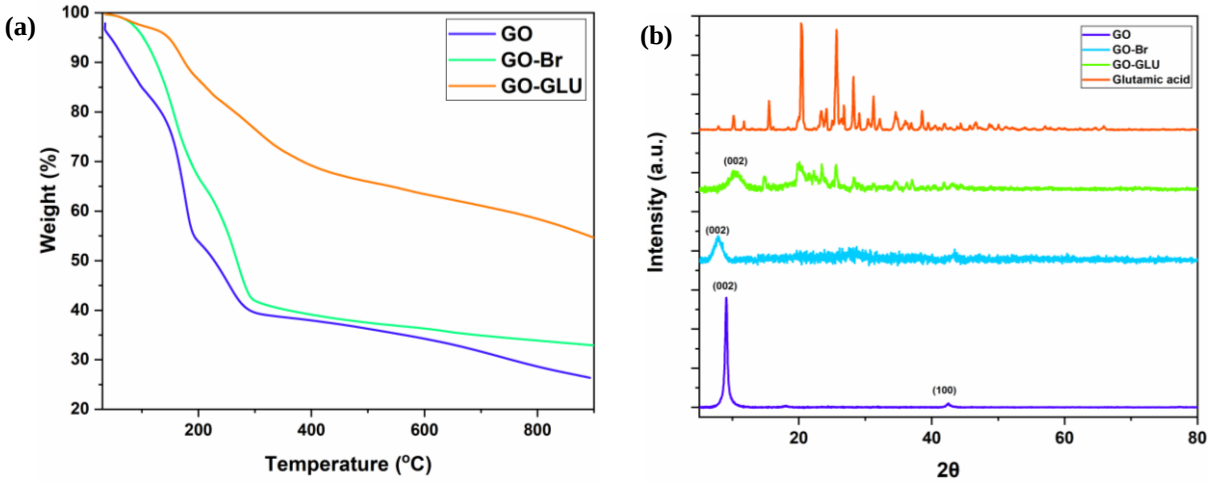

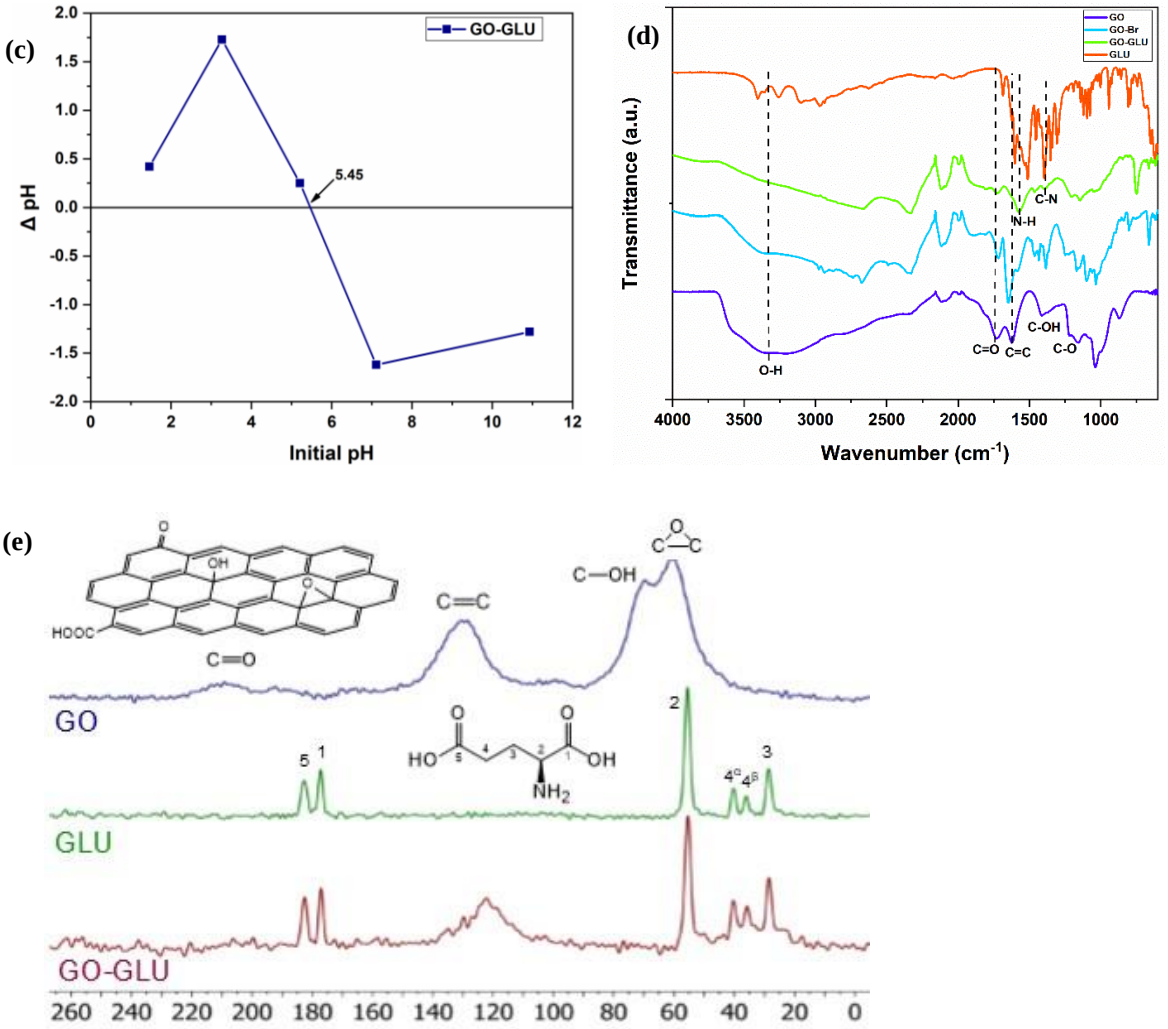

Figure 2: TGA (a), XRD patterns (b), PZC (c), FTIR (d) and NMR (e) spectra for GO, GO-Br, GO-GLU and GLU.

Table 1: Elemental analysis of GO and GO-GLU.

Sample	C	H	N
GO	37.7	2.894	0
GO-GLU	56.78	2.804	3.9

3.2 Characterization of Aerogels

3.2.1 Morphology of aerogels

Figure 3 depicts optical images and micro-morphologies (FESEM analysis) of PVA, G-PVA, and GG-PVA aerogels. The pictorial photographs show that the aerogels exhibited a white color for the PVA aerogel and brown colors for G- PVA/ GG-PVA aerogels, due to the introduction of GO/GO-GLU. Prior to synthesis, GO/GO-GLU and PVA solutions were mixed to allow for hydrogen bonding amongst GO/GO-GLU sheets and PVA chains, which was followed by freezing. The freezing water crystals were removed during the lyophilization process, leaving behind a porous interconnecting crinkly-layered structure.[52] PVA aerogel revealed reticulated networks with regular fibres in the nanometer range (**Figure 3 (b) and (c)**), however G-PVA and GG-PVA exhibited notable voids with a

honeycomb architecture as shown in **Figure 3 (d) – (g)**. The strong hydrogen connections between GO/GO-GLU and PVA may be responsible for this unique structure. Furthermore, the local orientation of the pore structure in PVA aerogel is consistent, reflecting the development direction of ice crystals when frozen.[53]

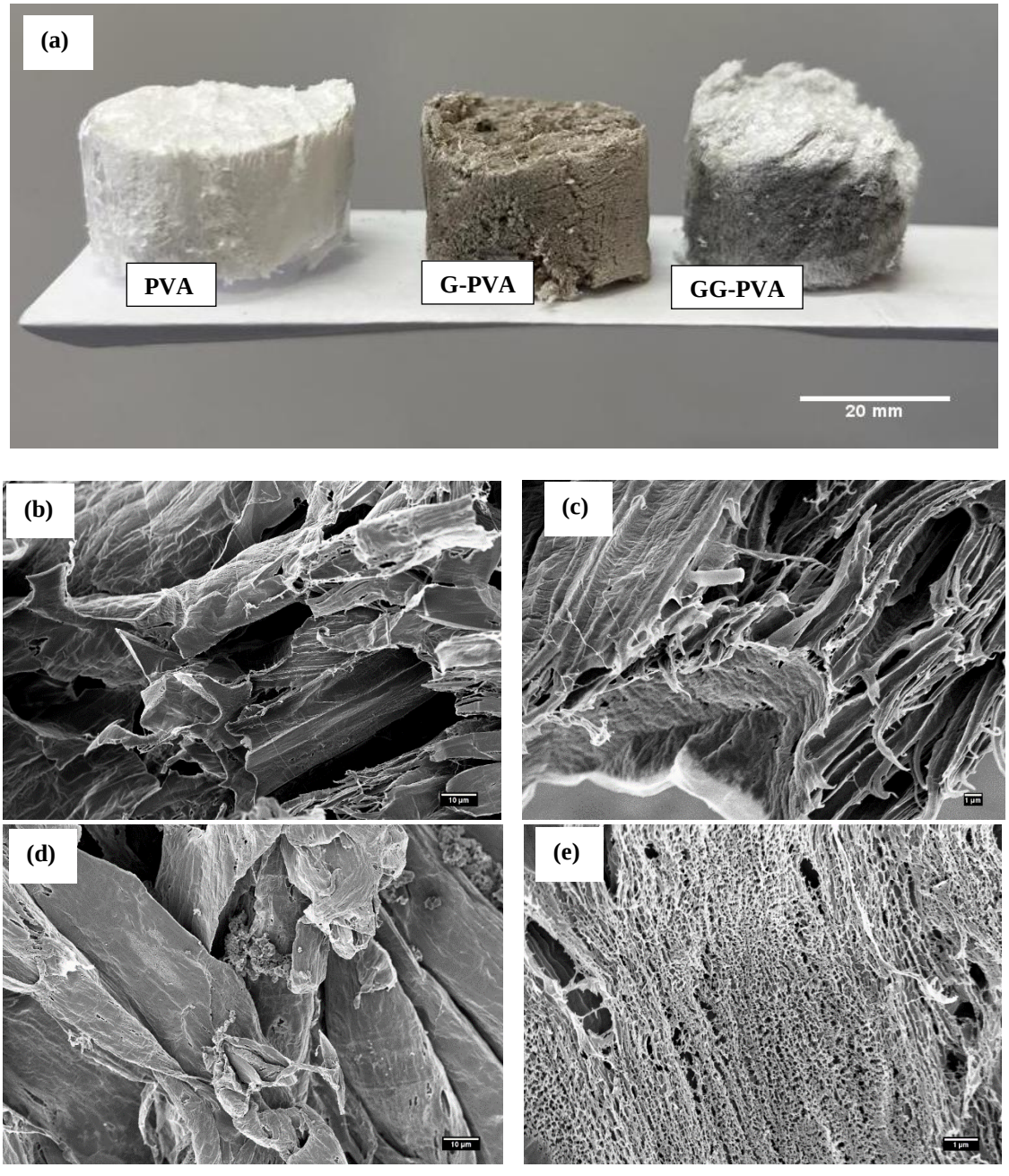

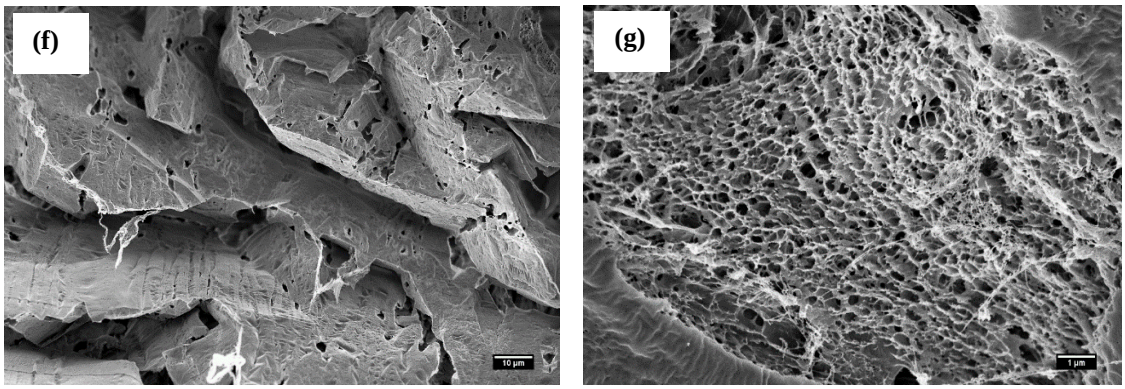

Figure 3: Optical photographs of aerogels (a); SEM images of PVA (b) & (c), G-PVA (d) & (e) and GG-PVA (f) & (g).

3.2.2 PVA, G-PVA, GG-PVA aerogels BET, FTIR and TGA analysis.

Figure 4 depicts the nitrogen adsorption–desorption isotherm and pore size distribution of PVA, G-PVA, and GG-PVA and the values were summarized in **Table 2**. The isotherm plots (**Figure 4 (a))** illustrate curves corresponding to a type-IV isotherm with a hysteresis loop at P/P_o of 0.4 – 1.0, indicating a well-formed mesoporous nature with significant adsorbent-adsorbate interaction. [36,52] The BET specific surface areas for PVA, G-PVA, and GG-PVA were 4.2240, 6.6324, and 3.4326 m^2 g^{-1}, respectively. The pore size distribution obtained from the nitrogen adsorption data using BJH calculations is presented in **Figure 4(b)**. The figure depicts that the aerogels' pore diameter distribution is largely concentrated between 2 – 20 and 80 – 160 nm, with average pore diameters of 58.19, 32.43, and 57.46 nm for PVA, G-PVA, and GG-PVA respectively. These results correspond well with dye molecule adsorption, where probable Knudsen diffusion is the main contributing effect. The reduced surface area of GG-PVA is credited to the presence of glutamic acid brushes, which promotes GO-GLU restacking and so decreases the aerogel's surface area.

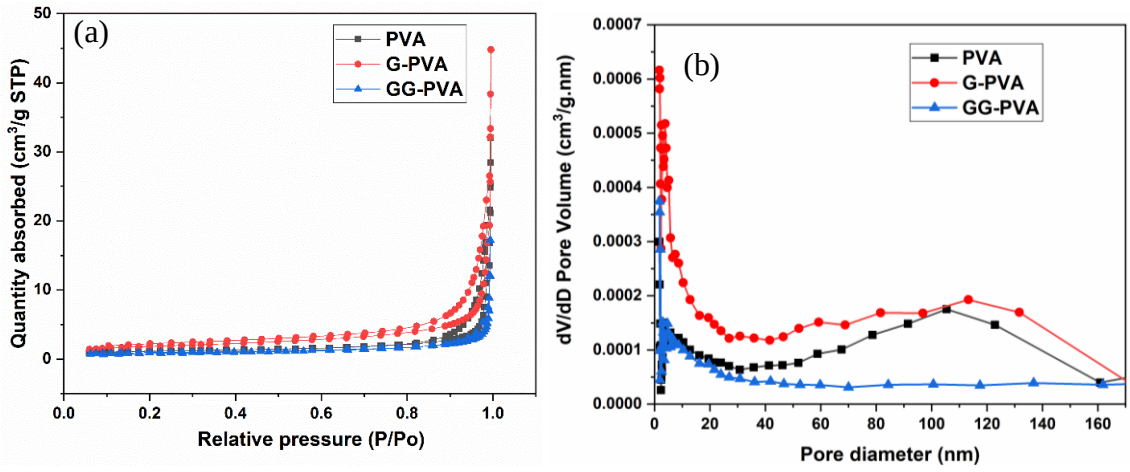

Figure 4: N_2 adsorption–desorption isotherm (a) and pore size distribution of PVA, G-PVA and GG-PVA (b).

Table 2: Properties of PVA, G-PVA and GG-PVA aerogels based on the N_2 adsorption/desorption isotherms depicted in Figure 4.

Sample	S_{BET} (m^2/g)	V_{TOTAL} ($cm^3 g^{-1}$)	Pore size (nm)
PVA	4.2240	0.031751	58.19
G-PVA	6.6324	0.038597	32.43
GG-PVA	3.4326	0.025945	57.46

Chemical functionalities of PVA, G-PVA and GG-PVA were analyzed using FTIR (**Figure 5(a)**). PVA, G-PVA and GG-PVA exhibited similar spectra with peaks at 3313 cm^{-1} (O–H stretching vibration), 2926 cm^{-1} (saturated CH_2/CH_3 groups, stretching vibration), 1732 cm^{-1} (C=O stretching), 1429 cm^{-1} (CH stretching), 1086 cm^{-1} (C–O–C stretching vibrations) and 845 cm^{-1} (C-C stretching) which are PVA characteristic peaks.[54] The link via hydrogen bonds amid GO/ GO-GLU and PVA can be found due to the shift of the O-H peak from 3313 – 3293 cm^{-1}.[34] Peaks at 1573 cm^{-1} due to the graphene's carbonyl moieties are observed.[55]

The thermal stability of PVA, G-PVA, and GG-PVA aerogels were evaluated using TGA (**Figure 5(b)**). Pure PVA and its composite aerogels exhibit three-stage deterioration processes. The deterioration due to the release of water from the aerogel is allocated to the initial point at temperatures below 100 °C.[56] The degradation of the main PVA chains is responsible for the majority of the mass loss stage, which happens within 180 and 400 °C. The last mass loss stage ranges from 400 – 480 °C, which is attributed to the continued pyrogenic disintegration of the unstable residue formed in the main stage.[57] Following heating from room temperature to 800 °C, the GG-PVA aerogel preserved a higher weight of ~20% due to the grafting of glutamic acid brushes. The addition of GO-GLU improved the aerogel's thermal stability.

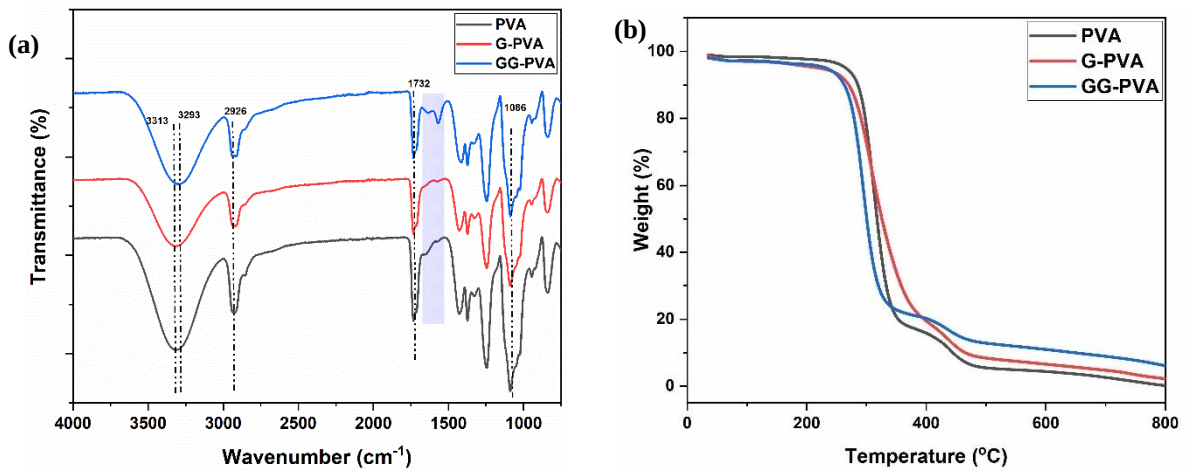

Figure 5: FTIR (a) and TGA (b) for PVA, G-PVA and GG-PVA aerogels.

3.3 Methylene blue dye adsorption

The adsorptive removal of cationic dye (MB) from simulated wastewater using GG-PVA is being investigated. The influence of adsorbent dosage, pH, temperature, and contact time is explored.

3.3.1 Effect of solution pH

Monitoring the pH of a solution is essential because it plays a key role in the adsorption process. It influences both the charge of the adsorbent surface species present in the solution and the adsorbates level of ionization.[59] The influence of pH on adsorption was examined at 25 °C using a pH range of 2 – 11 and a dye concentration of 20 mg L^{-1}; the findings are presented in **Figure 6**. The figure displays the dye removal efficiency rises from 75.72 – 88.44% with the increase of pH. In water, the MB dye is cationic and interacts with the adsorbate electrostatically.[60] The GG-PVA aerogel was protonated in the acid solution, resulting in a reduced removal efficiency due to extra H^+ ions on the aerogel's surface competing with the MB molecules.[30] The amount of adsorption rapidly increased in the alkaline solution owing to the electrostatic interaction amongst deprotonated aerogel and cationic MB molecules. For subsequent studies, all dye solutions were adjusted to pH 7, which is an environmentally relevant condition.

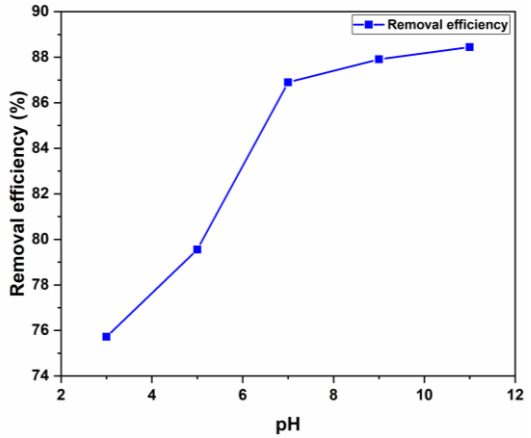

Figure 6: The effect of solution pH on adsorption of MB on GG-PVA aerogel.

3.3.2 Effect of Adsorbent Dosage and Temperature

Figure 7 (a) depicts the impact of adsorbent mass on MB dye removal efficacy. As the mass of GG-PVA aerogel increased from 10 – 50 mg, the MB removal efficiency improved from 93 to 95%. The enhanced dye removal was as a result of increased surface area and active sites for the adsorption of dye at higher dosages. At an excessive dosage, however, the adsorbent tends to aggregate, lowering the overall surface area and accessibility of active sites, thus adversely affecting the adsorption effectiveness.[20] Furthermore, in contrast to the positive trend noted for removal efficiency, adsorption capacity decreased from 61.85 to 12.33 mg g^{-1} as adsorbent mass rose, signifying that a significant number of active sites remained unsaturated at fixed dye concentration and solution volume. Consequently, the optimum adsorbent mass for removing MB dye was chosen to be 10 mg, which was used in subsequent investigations.

Temperature may significantly affect the adsorption process, in this sense, the temperature effects on MB absorption were studied at a range of 298.15 to 318.15 K and dye concentrations (10 to 50 mg L^{-1}). As displayed in **Figure 7 (b)**, the adsorption capacity improved with increasing temperature, implying that MB adsorption by GG-PVA aerogel is kinetically controlled by an endothermic process.

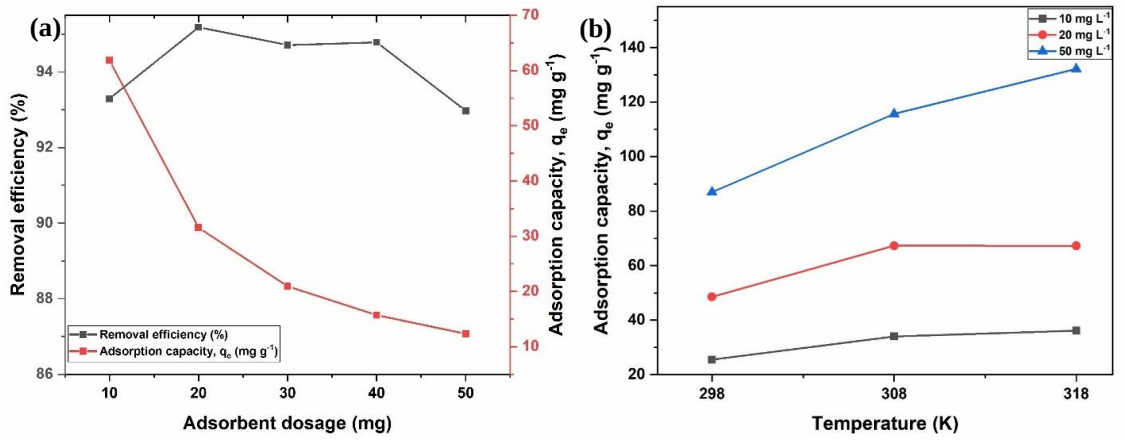

Figure 7: The Effect of adsorbate dosage (a) and temperature (b) on MB adsorption (20 mg L^{-1} initial concentration, 25 °C temperature, 60 min contact time).

3.3.3 Effect of contact time

The duration of interaction between adsorbent and dye is of great interest in the adsorption process. **Figure 8** shows the effect of contact time on the adsorption of MB dye onto GG-PVA at various starting concentrations (10 – 50 mg L^{-1}). The uptake of MB dye rose with the contact time and initial dye concentration, and remained stable after adsorption equilibrium was reached. The interaction between the numerous active sites of the adsorbent and dye molecules resulted in a swift dye adsorption in the first 25 minutes of the process. After 30 minutes, the dye adsorption rate becomes constant owing to the filling of active sites on adsorbent surfaces. This time period is called the dynamic equilibrium time. [61] Mhlongo *et al* (2022) reported on similar findings while studying methylene blue and methyl orange dye adsorption onto GT-cellulose adsorbent.[62]

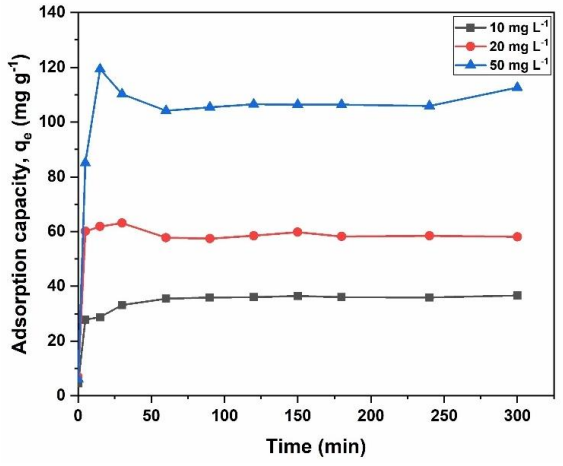

Figure 8: Effect of contact time on the removal efficiency of MB.

3.4 Adsorption isotherms

Three isotherm models, namely Langmuir, Temkin and Freundlich isotherms were used to characterize the adsorption behavior of MB dye onto GG-PVA aerogel. Adsorption isotherms can provide detailed information regarding adsorption mechanisms, surface

characteristics, and an adsorbent's affinity for an adsorbate. The Langmuir isotherm model posits that the process of adsorption on the surface of adsorbent is governed by homogeneous monolayer adsorption and the number of binding sites is limited.[63] The Langmuir equation is expressed in **equation (3)**.

$$1/q_e = 1/(K_L q_m C_e) + 1/q_m \quad (3)$$

where q_e and C_e are the adsorption amount (mgg^{-1}) and concentration of dye in the solution at equilibrium ($mg\ L^{-1}$), respectively, q_m is the maximum adsorption amount of monolayer adsorption on the adsorbent ($mg\ g^{-1}$), and K_L is the Langmuir constant ($L\ mg^{-1}$) utilized to verify the angle and linear coefficient attained from fitting, which is associated to adsorption site affinity.

According to the Freundlich model, this adsorption can be summarized as multilayer adsorption processes on a heterogeneous adsorbent surface with non-uniform distribution of adsorption affinity and heat.[1] The Freundlich equation is expressed as follows:

$$\log(q_e) = \log(K_f) + \log(C_e/n) \quad (4)$$

where K_F and n (dimensionless) are Freundlich constants associated with adsorption intensity and capacity, respectively. The n values reflect the adsorption process's favorability. A plot of $\log q_e$ vs $\log C_e$ can be used to calculate K_F and n.

The Temkin model analyzes the thermodynamic information in the adsorption process, pressuming that the heat of adsorption reduces linearly with increasing dye adsorption.[64] The equation is expressed as follows:

$$q_e = RT/B_T \ln(K_T) + RT/B_T \ln(C_e) \quad (5)$$

where B is the Temkin constant linked to the heat of adsorption ($kJ\ mol^{-1}$), R is gas constant ($8.314\ J\ (mol\ K)^{-1}$), T is temperature (K), and K_T denotes the empirical Temkin constant associated to the equilibrium binding constant related to the maximum binding energy ($L\ mg^{-1}$).

The adsorption data was fitted on the three isotherm models and **Table 3** lists all of the parameters obtained from the fittings. According to the correlation coefficients (R^2), the adsorption fits better the Langmuir isotherm model (R^2 = 0.9884 – 0.9950) than the Freundlich model (R^2 = 0.6476 – 0.9451), indicating that the process is monolayer adsorption on the surface of the GG-PVA aerogel.[4] This implies that GG-PVA's adsorption surface is homogenous, with a maximum removal effectiveness of 121.95 $mg\ g^{-1}$ at 25 °C. Furthermore, from the Freundlich parameters, 1/n quantifies adsorption favorability as well as surface heterogeneity. The evaluated 1/n values were less than 1 indicating a positive adsorption process.[13] **Table 3**'s correlation factors (R^2) reveal that the Temkin isotherm fits the adsorption data as well. The rise in values at elevated temperatures insinuates that the adsorption process becomes more favorable as the temperature increases.[65]

Table 3: Isotherm parameters for the adsorption of MB onto GG-PVA aerogel.

Equilibrium model	Temperature (°C)		
	25	**35**	**45**
Langmuir			
q_{max} (mg g^{-1})	121.95	117.65	144.92
K_L (L mg^{-1})	0.10	3.05	1.02
R^2	0.9912	0.9950	0.9884
Freundlich			
1/n	0.5403	0.2242	0.2751
K_F (L mg^{-1})	15.79	64.61	64.65
R^2	0.9451	0.8100	0.6476
Temkin			
B_T (J mol^{-1})	28.08	16.03	23.142
K_T (L mg^{-1})	0.88	93.65	24.15
R^2	0.9958	0.9246	0.8035

3.5 Adsorption Kinetics

Kinetic investigations were performed at 25 °C to examine the adsorption mechanism. The experimental data was fitted using the pseudo-first-order and pseudo-second-order kinetic models. These models are presented in **equations (6)** and **(7)**, respectively;

$$\ln (q_e - q_t) = \ln(q_e) - k_1 t \quad (6)$$

$$t/q_t = 1/k_2 q_{e2}^2 + t/q_e \quad (7)$$

where q_e and q_t (mg g^{-1}) are the amount of solute adsorbed at equilibrium and time *t*, respectively, k_1 is the first order kinetic constant (min^{-1}) and k_2 denotes the pseudo-second order rate constant (mg/(g·min)).[66] **Table 4** lists the derived kinetic constants and correlation coefficients. Based on the coefficient of determination, R^2, the experimental and calculated values of q_e attained from the linear fit align more closely with the pseudo-second-order kinetics model. The pseudo-second-order model achieved a high R^2 value of 0.9979, significantly surpassing the 0.5545 obtained from the pseudo-first-order model. These findings indicate that the removal of methylene blue (MB) follows the pseudo-second-order kinetic model, implying that the adsorption process is primarily driven by chemical interactions between MB and the polar functional groups present on the surfaces of the GG-PVA aerogel.[67]

Table 4: Kinetic parameters for MB adsorption on GG-PVA aerogels.

Absorbate	q_e (exp) (mg g^{-1})	**Pseudo-first-order model**			**Pseudo-second-order model**		
		K_1 (min^{-1})	q_e (mg g^{-1})	R^2	K_2 (mg (g min)$^{-1}$)	q_e (mg g^{-1})	R^2
MB	63.917	0.0000257	6.3314	0.556	0.008377	58.824	0.998

3.6 Adsorption Thermodynamics

Temperature has a significant influence on adsorption, and studying thermodynamics can indicate the degree of adsorption as well as the driving force behind the process. The adsorption isotherms of GG-PVA aerogel for MB at various temperatures were examined. From this data, the Van't Hoff equation can be employed to calculate the enthalpy change

(ΔH°), Gibbs free energy change (ΔG°), and entropy change (ΔS°) of the adsorption process[68]:

$$\Delta G° = -RT \ln(K_L) \quad (8)$$

$$\ln K_L = \Delta S°/R - \Delta H°/RT \quad (9)$$

where K_L is the Langmuir equilibrium constant (L mol^{-1}), R and T are the universal gas constant (8.314 J $(mol\ K)^{-1}$) and absolute solution temperature (K), respectively. **Table 5** presents the values calculated at various temperatures. **Table 5** shows negative values of ΔG° for MB removal, indicating spontaneous adsorption onto GG-PVA aerogel within the examined temperature and concentration ranges. Furthermore, the growing negative value of ΔG° at higher temperatures indicates that adsorption becomes more favorable as temperature rises.[30] The positive value of ΔH° (80.598 kJ mol^{-1}) validates the endothermic nature of MB adsorption, showing that MB's adsorption capability increased at higher temperatures. The positive value of ΔS° (300.568 J $(mol\ K)^{-1}$) indicates the affinity of GG-PVA aerogel for MB and the growing unpredictability at the solid-liquid interface during adsorption process.[69]

Table 5: Thermodynamic parameters for the adsorption of MB on GG-PVA aerogel.

Thermodynamic parameters	**Temperature (K)**		
	298.15	**313.15**	**328.15**
ΔG^o (kJ mol^{-1})	-8.219	-13.583	-14.126
ΔH^o (kJ mol^{-1})	80.598		
ΔS^o [J $(mol\ K)^{-1}$]	300.568		

4. Conclusion

In this research, the GG-PVA aerogel was fabricated via a combined approach of sol-gel and freeze-dry strategies, in which strong hydrogen bonds between PVA and GO-GLU were identified as the key factor. FTIR examination validated the successful synthesis of the aerogels and it yielded honeycomb architectures with relatively uniform pore diameters. Batch equilibrium adsorption of MB dye and kinetics studies using the aerogels were performed, and the Langmuir model fitted the experimental data best (R^2 = 0.9912 at 25 ℃). Accordingly, the q_{max} was evaluated to be 121.95 mg g^{-1}, and the reaction kinetics were characterized by the pseudo-second order kinetic model. Furthermore, thermodynamic studies revealed a spontaneous and endothermic adsorption process, as witnessed by the negative ΔG^o and positive ΔH^o values. Finally, the results indicate that GG-PVA aerogels are effective adsorbents for MB dye abatement. These results suggest that GG-PVA could be utilized to successfully remove toxic dyes from industrial effluents originating from the cosmetic, paper, textile, food, and textile industries.

Acknowledgements

This work was supported by Margaret Macnamara Education grants (2023).

References

1. Ilgin P, Ozay H, Ozay O. The efficient removal of anionic and cationic dyes from aqueous media using hydroxyethyl starch-based hydrogels. *Cellulose*. 2020;27(8):4787-4802. doi:10.1007/s10570-020-03074-0

2. Wu L, Liu X, Lv G, et al. Study on the adsorption properties of methyl orange by natural one-dimensional nano-mineral materials with different structures. *Sci Rep*. 2021;11(1):1-11. doi:10.1038/s41598-021-90235-1

3. Wang Y, Xie Y, Zhang Y, et al. Anionic and cationic dyes adsorption on porous poly-melamine-formaldehyde polymer. *Chem Eng Res Des*. 2016;114:258-267. doi:10.1016/j.cherd.2016.08.027

4. Cl L, Silva S, Castro D, Cavalcanti E. Hyperbranched Cellulose for Dye Removal in Aqueous Medium. Published online 2024:399-421.

5. Pramono E, Umam K, Sagita F, et al. The enhancement of dye filtration performance and antifouling properties in amino-functionalized bentonite/polyvinylidene fluoride mixed matrix membranes. *Heliyon*. 2023;9(1):e12823. doi:10.1016/j.heliyon.2023.e12823

6. Li Q, Li Y, Ma X, et al. Filtration and adsorption properties of porous calcium alginate membrane for methylene blue removal from water. *Chem Eng J*. 2017;316:623-630. doi:10.1016/j.cej.2017.01.098

7. Yu Z, Hu C, Dichiara AB, Jiang W, Gu J. Cellulose nanofibril/carbon nanomaterial hybrid aerogels for adsorption removal of cationic and anionic organic dyes. *Nanomaterials*. 2020;10(1):1-20. doi:10.3390/nano10010169

8. Tan IAW, Ahmad AL, Hameed BH. Adsorption of basic dye using activated carbon prepared from oil palm shell: batch and fixed bed studies. *Desalination*. 2008;225(1-3):13-28. doi:10.1016/j.desal.2007.07.005

9. Zhu J, Wang Y, Liu J, Zhang Y. Facile one-pot synthesis of novel spherical zeolite-reduced graphene oxide composites for cationic dye adsorption. *Ind Eng Chem Res*. 2014;53(35):13711-13717. doi:10.1021/ie502030w

10. Gupta VK, Suhas. Application of low-cost adsorbents for dye removal - A review. *J Environ Manage*. 2009;90(8):2313-2342. doi:10.1016/j.jenvman.2008.11.017

11. Yin M, Pan Y, Pan C. Adsorption properties of graphite oxide for Rhodamine B. *Micro Nano Lett*. 2019;14(11):1192-1197. doi:10.1049/mnl.2018.5820

12. Chinoune K, Mekki A, Boukoussa B, et al. Adsorption behavior of MB dye on alginate-sepiolite biocomposite beads: Adsorption, kinetics, and modeling. *Inorg Chem Commun*. 2024;165(May):112558. doi:10.1016/j.inoche.2024.112558

13. Gong Y, Qin C, He W, et al. Solar light assisted green synthesis of photoreduced graphene oxide for the high-efficiency adsorption of anionic dyes. *RSC Adv*. 2017;7(84):53362-53372. doi:10.1039/c7ra10009d

14. Mittal A, Mittal J, Malviya A, Gupta VK. Adsorptive removal of hazardous anionic dye "Congo red" from wastewater using waste materials and recovery by desorption. *J Colloid Interface Sci*. 2009;340(1):16-26. doi:10.1016/j.jcis.2009.08.019

15. Nguyen VT, Ha LQ, Nguyen TDL, Ly PH, Nguyen DM, Hoang D. Nanocellulose and Graphene Oxide Aerogels for Adsorption and Removal Methylene Blue from an

Aqueous Environment. *ACS Omega*. 2022;7(1):1003-1013. doi:10.1021/acsomega.1c05586

16. Tiwari JN, Mahesh K, Le NH, et al. Reduced graphene oxide-based hydrogels for the efficient capture of dye pollutants from aqueous solutions. *Carbon N Y*. 2013;56:173-182. doi:10.1016/j.carbon.2013.01.001

17. Xiao J, Lv W, Xie Z, Song Y, Zheng Q. L-Cysteine-Reduced Graphene Oxide/Poly(Vinyl Alcohol) Ultralight Aerogel As a Broad-Spectrum Adsorbent for Anionic and Cationic Dyes. *J Mater Sci*. 2017;52(10):5807-5821. doi:10.1007/s10853-017-0818-y

18. Liu T, Aniagor CO, Ejimofor MI, et al. Recent developments in the utilization of modified graphene oxide to adsorb dyes from water: A review. *J Ind Eng Chem*. 2023;117:21-37. doi:10.1016/j.jiec.2022.10.008

19. Yang J, Shojaei S, Shojaei S. Removal of drug and dye from aqueous solutions by graphene oxide: Adsorption studies and chemometrics methods. *npj Clean Water*. 2022;5(1):1-10. doi:10.1038/s41545-022-00148-3

20. Lai KC, Hiew BYZ, Lee LY, et al. Ice-templated graphene oxide/chitosan aerogel as an effective adsorbent for sequestration of metanil yellow dye. *Bioresour Technol*. 2019;274(August 2018):134-144. doi:10.1016/j.biortech.2018.11.048

21. Sun J, Yu M, Kang R, Sun H, Zhang Y, Wang N. Self-assembled graphene aerogels for removal of methylene blue and copper from aqueous solutions. *J Hazard Mater Adv*. 2021;4(October):100026. doi:10.1016/j.hazadv.2021.100026

22. Peng W, Li H, Liu Y, Song S. Comparison of Pb (II) adsorption onto graphene oxide prepared from natural graphites : Diagramming the Pb (II) adsorption sites. *Appl Surf Sci*. 2016;364:620-627. doi:10.1016/j.apsusc.2015.12.208

23. Gopalakrishnan A, Krishnan R, Thangavel S. Journal of Industrial and Engineering Chemistry Removal of heavy metal ions from pharma-effluents using graphene-oxide nanosorbents and study of their adsorption kinetics. *J Ind Eng Chem*. 2015;30:14-19. doi:10.1016/j.jiec.2015.06.005

24. Li P, Li Y, Wu Y, et al. Thin-film nanocomposite NF membrane with GO on macroporous hollow fiber ceramic substrate for efficient heavy metals removal. *Environ Res*. 2021;197(November 2020):111040. doi:10.1016/j.envres.2021.111040

25. Mao B, Sidhureddy B, Thiruppathi AR, Wood PC, Chen A. Efficient dye removal and separation based on graphene oxide nanomaterials. *New J Chem*. 2020;44(11):4519-4528. doi:10.1039/c9nj05895h

26. Iv JJK, Imbrogno J, Belfort G. Polymer Brushes for Membrane Separations: A Review. *ACS Appl Mater Interfaces*. Published online 2016. doi:10.1021/acsami.6b09068

27. Azzaroni O. Polymer brushes here, there, and everywhere: Recent advances in their practical applications and emerging opportunities in multiple research fields. *J Polym Sci Part A Polym Chem*. 2012;50(16):3225-3258. doi:10.1002/pola.26119

28. Zhao B, Zhu L. Mixed Polymer Brush-Grafted Particles : A New Class of Environmentally Responsive Nanostructured Materials. Published online 2009:9369-9383. doi:10.1021/ma902042x

29. Hiew BYZ, Lee LY, Lai KC, et al. Adsorptive decontamination of diclofenac by three-dimensional graphene-based adsorbent: Response surface methodology, adsorption equilibrium, kinetic and thermodynamic studies. *Environ Res*. 2019;168(September 2018):241-253. doi:10.1016/j.envres.2018.09.030
30. Jiao C, Li T, Wang J, et al. Efficient Removal of Dyes from Aqueous Solution by a Porous Sodium Alginate/gelatin/graphene Oxide Triple-network Composite Aerogel. *J Polym Environ*. 2020;28(5):1492-1502. doi:10.1007/s10924-020-01702-1
31. Zamani S, Tabrizi NS. Removal of methylene blue from water by graphene oxide aerogel: Thermodynamic, kinetic, and equilibrium modeling. *Res Chem Intermed*. 2015;41(10):7945-7963. doi:10.1007/s11164-014-1868-2
32. Lv Y, Xing B, Zheng M, et al. Hydrothermal synthesis of ultra-light coal-based graphene oxide aerogel for efficient removal of dyes from aqueous solutions. *Nanomaterials*. 2018;8(9):1-17. doi:10.3390/nano8090670
33. Liu H, Qiu H. Recent advances of 3D graphene-based adsorbents for sample preparation of water pollutants: A review. *Chem Eng J*. 2020;393(January):124691. doi:10.1016/j.cej.2020.124691
34. Dai J, Huang T, Tian S qi, et al. High structure stability and outstanding adsorption performance of graphene oxide aerogel supported by polyvinyl alcohol for waste water treatment. *Mater Des*. 2016;107:187-197. doi:10.1016/j.matdes.2016.06.039
35. Ding Y, Tian Z, Li H, Wang X. Efficient removal of organic dyes using a three-dimensional graphene aerogel with excellent recycling stability. *New Carbon Mater*. 2019;34(4):315-324. doi:10.1016/s1872-5805(19)30020-4
36. Han M, Xu B, Zhang M, et al. Preparation of biologically reduced graphene oxide-based aerogel and its application in dye adsorption. *Sci Total Environ*. 2021;783:147028. doi:10.1016/j.scitotenv.2021.147028
37. Chen Y, Yang L, Xu S, et al. Ultralight aerogel based on molecular-modified poly(: M -phenylenediamine) crosslinking with polyvinyl alcohol/graphene oxide for flow adsorption. *RSC Adv*. 2019;9(40):22950-22956. doi:10.1039/c9ra04207e
38. Zhu Y, Hu J, Wang J. Removal of Co2+ from radioactive wastewater by polyvinyl alcohol (PVA)/chitosan magnetic composite. *Prog Nucl Energy*. 2014;71:172-178. doi:10.1016/j.pnucene.2013.12.005
39. Yi X, Sun F, Han Z, et al. Graphene oxide encapsulated polyvinyl alcohol/sodium alginate hydrogel microspheres for Cu (II) and U (VI) removal. *Ecotoxicol Environ Saf*. 2018;158(April):309-318. doi:10.1016/j.ecoenv.2018.04.039
40. Hoffman R. Solid-state chemical-shift referencing with adamantane. *J Magn Reson*. 2022;340:107231. doi:10.1016/j.jmr.2022.107231
41. Zhu S, Li J, Chen Y. Grafting of graphene oxide with stimuli-responsive polymers by using ATRP for drug release. Published online 2012. doi:10.1007/s11051-012-1132-x
42. Yang Y, Wang J, Zhang J, Liu J, Yang X, Zhao H. Exfoliated Graphite Oxide Decorated by PDMAEMA Chains and Polymer Particles. 2009;25(15):11808-11814. doi:10.1021/la901441p

43. Mahmoudian M, Kochameshki MG, Hosseinzadeh M. Modification of graphene oxide by ATRP : A pH-responsive additive in membrane for separation of salts , dyes and heavy metals. *J Environ Chem Eng*. 2018;6(2):3122-3134. doi:10.1016/j.jece.2018.04.056
44. Namvari M, Biswas CS, Galluzzi M, Wang Q, Du B, Stadler FJ. Reduced graphene oxide composites with water soluble copolymers having tailored lower critical solution temperatures and unique tube-like structure. *Nat Publ Gr*. 2017;(December 2016):1-9. doi:10.1038/srep44508
45. Xabela S. 2-(N-3-Sulfopropyl-N,N-dimethyl ammonium)ethyl methacrylate modified graphene oxide embedded into cellulose acetate ultrafiltration membranes for improved performance. 2022;(November 2021):1-19. doi:10.1002/app.52336
46. Ngaha MCD, Djemmoe LG, Njanja E, Kenfack IT. Biosorption Isotherms and Kinetics Studies for the Removal of 2,6-Dichlorophenolindophenol Using Palm Tree Trunk (Elaeis guineensis). *J Encapsulation Adsorpt Sci*. 2018;08(03):156-177. doi:10.4236/jeas.2018.83008
47. Borba LL, Cuba RMF, Cuba Terán FJ, Castro MN, Mendes TA. Use of adsorbent biochar from pequi (Caryocar Brasiliense) husks for the removal of commercial formulation of glyphosate from aqueous media. *Brazilian Arch Biol Technol*. 2019;62. doi:10.1590/1678-4324-2019180450
48. Hu Z, Li C, Nie R, Li Y, Tang J, Deng X. RSC Advances Biomaterial functionalized graphene oxides with tunable work function for high sensitive organic. Published online 2015:99431-99438. doi:10.1039/c5ra19476h
49. Johra FT, Lee JW, Jung WG. Facile and safe graphene preparation on solution based platform. *J Ind Eng Chem*. 2014;20(5):2883-2887. doi:10.1016/j.jiec.2013.11.022
50. Park GT, Chang JH. Comparison of properties of PVA nanocomposites containing reduced graphene oxide and functionalized graphene. *Polymers (Basel)*. 2019;11(3). doi:10.3390/polym11030450
51. Harbison GS, Wang Y, Wilson D. Solid-State NMR and the Crystallization of Aspartic and Glutamic Acids. *Cryst Growth Des*. 2015;16(2):625-631. doi:10.1021/acs.cgd.5b01052
52. Huo JB, Yu G. Hexacyanoferrate-modified polyvinyl alcohol/graphene oxide aerogel as an efficient and retrievable adsorbent for cesium. *J Mater Sci*. 2022;57(1):351-365. doi:10.1007/s10853-021-06573-y
53. Zheng Q, Cai Z, Gong S. Green synthesis of polyvinyl alcohol (PVA)-cellulose nanofibril (CNF) hybrid aerogels and their use as superabsorbents. *J Mater Chem A*. 2014;2(9):3110-3118. doi:10.1039/c3ta14642a
54. Rapisarda M, Malfense Fierro GP, Meo M. Ultralight graphene oxide/polyvinyl alcohol aerogel for broadband and tuneable acoustic properties. *Sci Rep*. 2021;11(1). doi:10.1038/s41598-021-90101-0
55. Xu Z, Zhou H, Tan S, et al. Ultralight super-hydrophobic carbon aerogels based on cellulose nanofibers/poly(vinyl alcohol)/graphene oxide (CNFs/PVA/GO) for highly effective oil-water separation. *Beilstein J Nanotechnol*. 2018;9(1):508-519. doi:10.3762/bjnano.9.49

56. Wang YT, Liao SF, Shang K, et al. Efficient approach to improving the flame retardancy of poly(vinyl alcohol)/clay aerogels: Incorporating piperazine-modified ammonium polyphosphate. *ACS Appl Mater Interfaces*. 2015;7(3):1780-1786. doi:10.1021/am507409d
57. Sheng X, Li S, Zhao Y, Zhai D, Zhang L, Lu X. Synergistic effects of two-dimensional mxene and ammonium polyphosphate on enhancing the fire safety of polyvinyl alcohol composite aerogels. *Polymers (Basel)*. 2019;11(12):1-17. doi:10.3390/polym11121964
58. Arabzadeh A, Salimi A. One dimensional CdS nanowire@TiO2 nanoparticles core-shell as high performance photocatalyst for fast degradation of dye pollutants under visible and sunlight irradiation. *J Colloid Interface Sci*. 2016;479:43-54. doi:10.1016/j.jcis.2016.06.036
59. Li Y, Liu H, Nie R, et al. Highly efficient adsorption of anionic dyes on a porous graphene oxide nanosheets/chitosan composite aerogel. *Ind Crops Prod*. 2024;220(January):119146. doi:10.1016/j.indcrop.2024.119146
60. Nie ZJ, Guo QF, Xia H, et al. Cyclodextrin self-assembled graphene oxide aerogel microspheres as broad-spectrum adsorbent for removing dyes and organic micropollutants from water. *J Environ Chem Eng*. 2021;9(2):104749. doi:10.1016/j.jece.2020.104749
61. Muhammad A, Shah A ul HA, Bilal S. Comparative study of the adsorption of acid blue 40 on polyaniline,magnetic oxide and their composites: Synthesis, characterization and application. *Materials (Basel)*. 2019;12(18). doi:10.3390/ma12182854
62. Mhlongo JT, Dlamini ML, Nuapia Y, Etale A. Synthesis and application of cationized cellulose for adsorption of anionic dyes. *Mater Today Proc*. 2022;62(February):S133-S140. doi:10.1016/j.matpr.2022.02.100
63. Zhan Y, Guan X, Ren E, Lin S, Lan J. Fabrication of zeolitic imidazolate framework-8 functional polyacrylonitrile nanofibrous mats for dye removal. *J Polym Res*. 2019;26(6). doi:10.1007/s10965-019-1806-5
64. Li Y, Liu H, Nie R, et al. Highly efficient adsorption of anionic dyes on a porous graphene oxide nanosheets/chitosan composite aerogel. *Ind Crops Prod*. 2024;220(June):119146. doi:10.1016/j.indcrop.2024.119146
65. Aljeboree AM, Alkaim AF, Al-Dujaili AH. Adsorption isotherm, kinetic modeling and thermodynamics of crystal violet dye on coconut husk-based activated carbon. *Desalin Water Treat*. 2015;53(13):3656-3667. doi:10.1080/19443994.2013.877854
66. He Z, Qin M, Han C, et al. Pectin/graphene oxide aerogel with bamboo-like structure for enhanced dyes adsorption. *Colloids Surfaces A Physicochem Eng Asp*. 2022;652(June):129837. doi:10.1016/j.colsurfa.2022.129837
67. Sadegh H, Ali GAM, Agarwal S, Gupta VK. Surface Modification of MWCNTs with Carboxylic-to-Amine and Their Superb Adsorption Performance. *Int J Environ Res*. 2019;13(3):523-531. doi:10.1007/s41742-019-00193-w
68. Feng J, Ding H, Yang G, et al. Preparation of black-pearl reduced graphene oxide–sodium alginate hydrogel microspheres for adsorbing organic pollutants. *J Colloid Interface Sci*. 2017;508:387-395. doi:10.1016/j.jcis.2017.07.113

69. Kuo CY, Wu CH, Wu JY. Adsorption of direct dyes from aqueous solutions by carbon nanotubes: Determination of equilibrium, kinetics and thermodynamics parameters. *J Colloid Interface Sci*. 2008;327(2):308-315. doi:10.1016/j.jcis.2008.08.038

Supplementary Information (S.I.)

S1: Experimental section

S1.1: Synthesis of GO nanosheets

The improved Hummers method was utilized to synthesize GO [1]. A mixture of graphite powder (1 g) and $KMnO_4$ (6 g) was combined with 120 mL of concentrated H_2SO_4 and 13 mL of H_3PO_4 in a 9:1 ratio. This blend was stirred in an oil bath maintained at 50 °C for a duration of 12 hours. Once the reaction mixture had cooled to room temperature, it was poured into 400 mL of ice containing 1 mL of 30% hydrogen peroxide (H_2O_2). The mixture was allowed to reach room temperature again and then centrifuged at 4000 revolutions per minute (rpm) for 30 minutes. The supernatant was carefully removed, and the resulting precipitate was washed in succession with deionized water, followed by 30% hydrochloric acid (HCl), and then with ethanol (two washes for each solvent). Diethyl ether (200 mL) was combined with the remaining material to induce coagulation. The obtained solid was dried under vacuum at ambient temperature overnight. Finally, the dried solid was pulverized with a mortar and pestle.

S1.2: Synthesis of initiator-functionalized GO-Br

The modification of GO was achieved using a revised method described by Kumar et al. in 2016 [2]. In a typical procedure, in a round-bottomed flask comprising of 30 mL of dimethylformamide (DMF), 250 mg of GO was added and sonicated for one hour to produce a colloidal suspension. 4 mL of triethylamine (TEA) were added to the flask, followed by the slow addition of 5 mL of α-bromoisobutyryl bromide. The resultant mixture was kept stirring in an ice bath for 24 hours. Centrifugation was used to collect functionalized GO (GO-Br), which was then washed with chloroform and deionized water before being vacuum dried for 12 hours.

S1.3 Surface-Initiated Atom-Transfer Radical Polymerization (SI-ATRP) of glutamic acid on the surface of GO-Br

The polymerization of GO-Br was conducted using a modified procedure detailed by Kumar et al., 2016 [2]. In this process, 50 mg of GO-Br was initially dispersed in 5 mL of dimethylformamide (DMF) through sonication. A mixture of 30 mg (0.2 mmol) of Cu(I)Br and 100 mmol of glutamic acid was then placed into sealed vials, which were subsequently purged with nitrogen to remove any air. Following this, ~ 40 mL (0.2 mmol) of the ligand PMDETA was introduced into the reaction mixture, and the polymerization was allowed to proceed at 70 °C for a duration of 24 hours. After the reaction, the solution was poured into methanol to precipitate the polymer composites. The resultant product underwent multiple washes with chloroform to eliminate any unreacted monomer, followed by centrifugation for 20 minutes and drying under vacuum for a period of 24 hours.

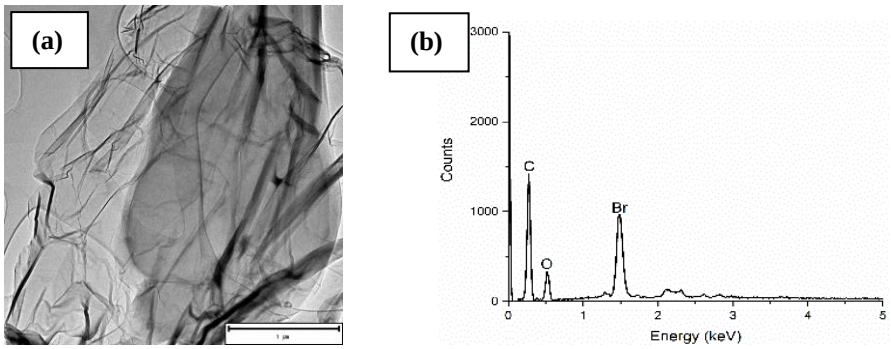

Figure S1: GO-Br TEM image (a), and EDS (b)

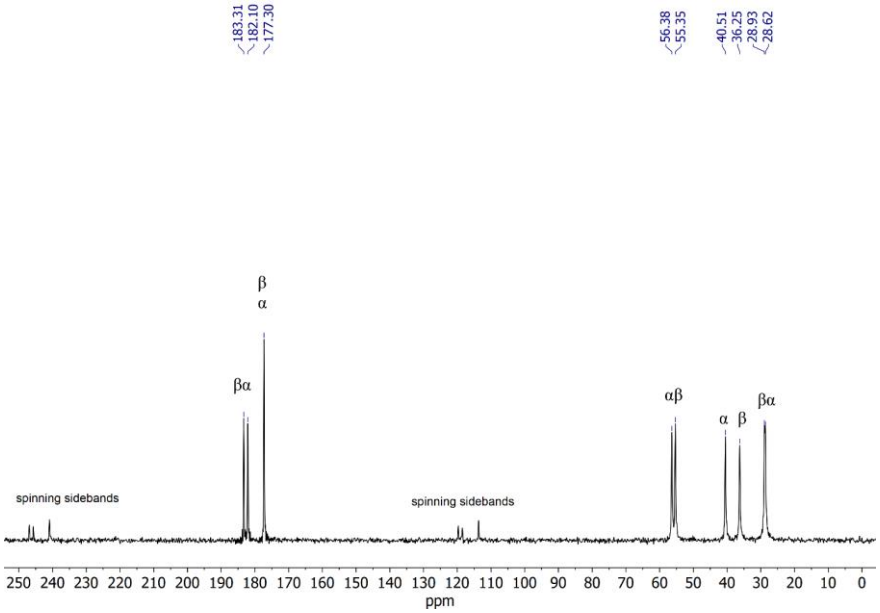

Figure S2: ^{13}C CP MAS NMR spectrum

References

[1] Marcano DC, Kosynkin DV, Berlin JM, Sinitskii A, Sun Z, Slesarev AS, Alemany LB, Lu W, Tour JM. Correction to: Improved Synthesis of Graphene Oxide. ACS Nano (2010) 4: 8 (4806-4814). doi: 10.1021/nn1006368.

[2] Kumar A, Bansal A, Behera B, Jain SL, Ray SS. Ternary hybrid polymeric nanocomposites through grafting of polystyrene on graphene oxide-TiO_2 by surface initiated atom transfer radical polymerization (SI-ATRP). Mater Chem Phys. 2016; 172:189-196. doi:10.1016/j.matchemphys.2016.01.064.

CHAPTER 5
CONCLUSIONS AND RECOMMENDATIONS

Conclusions

In this research, we explored the development and performance evaluation of various TFN membranes enhanced with different nanomaterials to improve water treatment efficiency. The findings revealed significant advancements in membrane technology, particularly under low-pressure conditions (≥ 400 kPa), showcasing their potential for practical applications in dye removal. Several conclusions can be derived from the studies that were carried out in relation to the study's specific aims.

The first part of the study demonstrated that the GO-GLU TFN membrane, optimized at a loading of 0.10 wt%, achieved remarkable ~2-fold increase in water permeance (14.11 ± 0.22 L/m^2h) along with impressive rejection rates of 99.18% for methylene blue (MB) and 67.18% for methyl orange (MO) when compared to pristine TFC membrane. In the second part, the results indicated that the TFN-1 membrane, optimized at a GO-PMEP loading of 0.025 wt%, displayed significantly improved wettability and hydrophilicity due to an increased presence of oxygenated functional groups on its surface. This enhancement resulted in a remarkable ~1.5-fold increase in water flux (9.32 ± 0.89 L/m²h) as compared to the conventional TFC membranes. The TFN-1 membrane also achieved outstanding rejection rates, with complete removal of MB and over 80% for MO, alongside effective salt rejection of approximately 86% and 31% for $MgSO_4$ and NaCl, respectively. The last set of TFN membranes, CNC-GLU TFN membrane (0.10 wt%) exhibited a pure water flux of 15.45 ± 1.03 L/m²h (~2-fold increase) and high rejection rates of 99.83% for MB and 90.63% for MO. All TFN membranes exhibited superior antifouling characteristics compared to the traditional TFC membranes maintaining good operational stability over three cycles. The hydrophilic nature of the GO-GLU, GO-PMEP and CNC-GLU NPs effectively mitigated hydrophobic interactions between dye molecules and the membrane, enhancing its antifouling performance during filtration. Moreover, the efficacy of these membranes was further validated using real water samples, confirming their potential for practical application in dye removal under environmental conditions.

This research not only demonstrates the potential of novel nanofillers for improving membrane performance but also sets a new standard in the field of water treatment by showcasing the viability of using functionalized, renewable nanomaterials to tackle one of the most pressing environmental issues - dye pollution in wastewater. The innovative combination of GLU/PMEP polymer brushes and GO/CNCs NPs opens up new avenues for developing advanced, efficient, and sustainable membranes for applications in dye removal and wastewater treatment. Furthermore, in contrast to most reported NF membranes which typically function at significantly higher pressures, the low operation pressures will substantially decrease operational costs.

Moreover, the potential application of GO-GLU NPs (GG-PVA) aerogels fabricated through a simplistic sol gel and freeze-drying process utilizing PVA as a cross-linker in dye removal was also investigated achieving a maximum adsorption capacity of 121.95 mg/g for MB. The optimal removal efficiency was 88.4% under near-neutral to alkaline conditions, with equilibrium reached in 30 minutes. The adsorption process was found to be endothermic and spontaneous. The adsorption capacity is comparable to other materials reported in literature and the study supports previous findings that highlight the significant role of surface chemistry and structural properties in adsorption efficiency. This indicates that while the GG-PVA aerogels are effective, however, there is room for improvement or optimization to reach higher capacities. The use of a simple sol-gel and freeze-drying process to fabricate the aerogels is a notable strength, as it suggests scalability and cost-effectiveness, aligning with the need for practical environmental solutions.

Recommendations

Based on the outcomes of this thesis research, the following suggestions are made for further research on the fabrication of high performing TFN membranes:

- Further characterization of nanocomposites and membranes need to be done in order to gain understanding of surface chemistry and membrane surface charge. Nanocomposite characterization such as X-ray photoelectron spectroscopy (XPS) needs to be done to assess the high resolution core spectra. This will identify the bonding and oxidation states of chemical elements. Zeta potential also needs to be done to assess the surface charge of the membrane, this will assist in understanding the rejection studies.
- To improve dye adsorption/rejection, the stimuli responsiveness of nanocomposites needs to be investigated. Nanocomposites depending on the results can be utilized in different fields such as sensors, drug delivery, etc.
- The use of computational simulations would be important to consider as they also provide extended use in understanding processes e.g. optimization of high performing membranes, water samples and quality of treated wastewater. Many scenarios can be modelled from which important information about the dye treatment process can be gleaned and used for process improvement or other innovation.
- Textile industry wastewaters typically contain a wide range of pollutants. As a result, performance evaluation of the membranes synthesized in this study against real wastewaters from these industries is required to evaluate their prospective applications under harsh circumstances.
- For a more realistic evaluation of membrane stability and leaching, long-term performance under continuous operation is required. Following that, additional membrane characterization and testing, including SEM-EDX, can be carried out to analyse changes in morphology on the membrane surface and gain a better understanding of fouling mechanisms.
- The membranes can be tested for rejection of other organic and inorganic contaminants found in water.

- Research into the synthesis and application of CNC-PMEP TFN and aerogel for dye removal from water was not performed. Such findings would allow for a comparison of the efficiency of modified CNCs versus GOs nanocomposites in dye rejection.